Université de Lille / Institut Français des Sciences et Technologies des Transports, de l'Aménagement et des Réseaux (IFSTTAR)

École doctorale: SPI
Unités de recherche: Laboratoire de Mécanique Multiphysique et Multiéchelle (LaMcube - FRE CNRS 2016) - Unité Mixte de Recherche en Acoustique Environnementale IFSTTAR - CEREMA

Thèse présentée par: LAI Van-Vuong

Pour obtenir le grade de docteur de l'université de Lille

Discipline / Spécialité: **Mécanique des solides, des matériaux, des structures et des surfaces**

Titre de la thèse :

DYNAMIC MODEL OF WHEEL-RAIL CONTACT FOR CURVE SQUEAL SIMULATION

SIMULATION DYNAMIQUE DU CONTACT ROUE/RAIL EN COURBE APPLICATION AU BRUIT DE CRISSEMENT

Thèse dirigé par:

M. Philippe DUFRÉNOY	Directeur de thèse	Professeur, LaMcube, Université de Lille
M. Jean-François BRUNEL	Encadrant	Maître de conférences, LaMcube, Université de Lille
M. Olivier CHIELLO	Encadrant	Chargé de recherche, UMRAE, IFSTTAR

Jury:

M. Gael CHEVALIER	Rapporteur	Professeur, FEMTO, Université de Franche Comté
M. Jean- Jacques SINOU	Président du jury	Professeur, LTDS, Ecole Centrale de Lyon
Mme. Béatrice FAVERJON	Examinatrice	Maître de conférences HdR, LaMCoS, INSA Lyon
Mme. Astrid PIERINGER	Examinatrice	Assistant professor, Chalmers University of Technology
Mr. Huajiang OUYANG	Examinateur	Professor, University of Liverpool

Abstract

Squeal noise of railbound vehicles emitted in tight curves (radius lower than 200m) is characterized by high sound pressure levels at pure medium and high frequencies. In urban areas where tight curves are numerous, squeal may affect many passengers and local residents and it is necessary to reduce this noise. State-of-the-art abounds with models trying to simulate curve squeal. They can be distinguished according to the mechanisms leading to squeal (negative damping introduced in the system due to the decrease of friction coefficient with the sliding velocity or mode coupling in the case of constant friction coefficient) but also wheel-rail contact models and solution types (time or frequency domain, linear or nonlinear analysis) according to. However the instability mechanisms are still controversial. In addition, existing curve squeal models are often simplified (analytical frictional contact laws or elastic half-space assumption).

The first aim of the thesis is to contribute to a clarification of the possible generation mechanisms. For this purpose, a stability analysis of wheel/rail rolling contact in the case of lateral full sliding is perfomed by using a point-contact model and wheel/rail modal bases. It is found that, even with a constant Coulomb friction coefficient, instabilities can occur because of the coupling between normal and tangential dynamics in wheel/rail system. However, this coupling may involve two wheel modes or only one wheel mode when the rail dynamics is included. The last case corresponds to a specific original mechanism. The rail vertical flexibility is notably found to play an important role on the instability occurrence without "falling friction" nor without "mode-coupling". This role is clarified by proposing a simple model including a single wheel mode and an analytical rail model. It is thus showed how the imaginary part of the complex stiffness of the rail, induced by the phase shift of the propagating wave but also by track damping (supporting pad, rail) plays an critical role in the instability mechanism . The combination of friction and phase shift induces a negative damping which may destabilize the system, leading to self-sustained vibration and squeal noise. Finally it is shown that the results obtained with the model are rather coherent with experimental observations.

The second aim of the thesis is to develop a full Finite Element model of wheel/rail contact in order to compute reference solutions and especially to verify the effects of the simplifications carried out in the point-contact model of Part I. A finite element formulation around the stationary position in an Eulerian reference frame is derived with a fine discretization of the contact surfaces. Unilateral contact and Coulomb friction with constant friction coefficient are assumed in the contact zone. This formulation, already used in other problems of structures destabilized by friction, is adapted here to a rolling case. Appropriate numerical techniques are used in order to solve the nonlinear discrete equations in quasi-static and dynamic conditions. In addition to the transient approach, a stability analysis performed around the full sliding equilibrium position allows to determine unstable modes and corresponding frequencies. In order to reduce the computational effort, reduction strategies are proposed for both domains. The first technique uses a classical reduction basis including free-interface normal modes and static contact attachments modes. A second original technique consists in simply adding a residual static contact flexibility to the free-interface normal modes when solving the frictional contact equations (Contact Static Approximation). The method is then tested in the case of frictional rolling contact between two annular cylinders. The quasi-static results show a good agreement with the ones obtained with Kalker's CONTACT software which is the reference method for the quasi-static wheel/rail contact analysis. In

case of full sliding, the stability analysis brings out a mode coupling when the contact zone is laterally shifted from the center of the cylinders. In the unstable configuration, the numerical integration provides solutions in the time domain which are coherent with the stability results. Concerning the performance of the reduction strategies, the approximate results show a good agreement with the reference ones in both transient and stability analyses. The methods are then applied in a realistic wheel/rail model in curve. It is found that the discretization of the contact zone does not stubstantially modify the instability mechanisms in comparison with the results obtained in the first part. However due to a stronger coupling between the normal contact degrees of freedom, the divergence rates of the unstable modes are greater for the finite element-contact model than for the point-contact model. The results of transient dynamics are consistent with the stability analysis and show localized stick/slip oscillations in the contact zone. The average global friction coefficient during stick-slip cycles is lightly smaller than the constant local friction coefficient. Thus, the decrease of the global friction coefficient could be interpreted as a consequence (and not a cause) of the friction-induced vibrations. Moreover, an hysteresis is observed in the average dynamic saturation curve provided with the finite element model. This result is is significantly different from those obtained with quasi-static curves. This could be due to the high lateral stiffness resulting from transient contact effects at squeal frequencies. Nonlinear dynamic analyses with point contact models should thus take into account this effect in order to provide correct limit cycles.

Keywords: Railway noise, Curve squeal, Dynamic instability, Finite Element Method, Wheel/rail contact, Nonlinear dynamics, Transient calculation.

Résumé

Le bruit de crissement émis par les véhicules guidés sur rail dans les courbes serrées (rayon inférieur à 200 m) est caractérisé par un niveau de pression acoustique élevé et un spectre de raies à moyennes et hautes fréquences. Dans les zones urbaines où les courbes sont nombreuses, le crissement peut affecter de nombreux passagers et résidents et il est nécessaire de réduire ce bruit. La littérature est riche en modèles de simulation du crissement en courbe. Ils se distinguent principalement au niveau des mécanismes d'instabilité conduisant au crissement (amortissement négatif introduit dans le système dû à la diminution du coefficient de frottement avec la vitesse de glissement ou couplage de modes dans le cas d'un coefficient de frottement constant), mais aussi au niveau des modèles de contact roue/rail et des types de solution (domaine temporel ou fréquentiel, analyse linéaire ou non linéaire). Cependant, le mécanisme d'instabilité est toujours controversé. De plus, les modèles de crissement en courbe existants sont souvent simplifiés (lois de pseudo-glissement analytiques ou hypothèse de massif semi-infini élastique).

Le premier objectif de la thèse est de contribuer à la compréhension du mécanisme de génération. Pour ce faire, une analyse de stabilité du contact de roulement roue/rail dans le cas du glissement latéral total est réalisée en utilisant un modèle de contact ponctuel et des bases modales roue et rail. On constate que même avec une hypothèse de coefficient de frottement de Coulomb constant, des instabilités peuvent se produire en raison du couplage entre la dynamique normale et tangentielle dans les systèmes roue/rail. Ce couplage peut faire intervenir deux modes de roue (couplage de modes classique) ou un seul mode de roue lorsque la dynamique du rail est incluse. Il s'agit alors d'un mécanisme spécifique. La flexibilité verticale du rail joue notamment un rôle important dans l'occurrence d'instabilité sans "décroissance du coefficient de frottement" ni sans "couplage de modes". Ce rôle est ensuite clarifié par un modèle simple comprenant un mode de roue et un modèle analytique de rail. On constate alors que la partie imaginaire de la raideur complexe du rail, induite par le déphasage de l'onde de propagation mais aussi par l'amortissement des semelles et du rail, joue un rôle critique dans le mécanisme d'instabilité. La combinaison du frottement et de ce déphasage induit un amortissement négatif qui peut alors déstabiliser le système, conduisant à des vibrations auto-entretenues et au bruit de crissement. Il est finalement montré que les résultats de la modélisation sont cohérents avec les constatations expérimentales.

Le second objectif de la thèse est de développer un modèle élément finis complet de contact roue/rail pour calculer des solutions de référence. Une formulation par éléments finis autour de la position stationnaire dans un repère eulérien est proposée avec une discrétisation fine de la surface de contact. Des lois non régularisées de contact unilatéral et de frottement avec un coefficient de frottement constant sont utilisées. Cette formulation déjà utilisée dans d'autres types de structures frottantes est ici adaptée au cas avec roulement. Des techniques numériques appropriées sont développées pour résoudre les équations discrètes non linéaires dans des conditions quasi-statiques ou dynamiques. Outre l'approche transitoire, une analyse de stabilité réalisée autour de la position d'équilibre en glissement total permet de déterminer les modes et les fréquences instables. Afin de réduire le temps de calcul, des méthodes de réduction sont proposées pour la stabilité et le calcul temporel. La première technique utilise une base réduite classique de sous-structuration dynamique (Component Mode Synthesis ou CMS) comprenant des modes normaux et des modes statiques d'attache au contact. Une deuxième technique consiste simplement à ajouter une flexibilité de contact statique résiduelle aux modes normaux lors de la résolution des équations de contact par frottement (approximation statique du contact). La méthode est ensuite testée dans le cas d'un contact

roulant et frottant entre deux cylindres annulaires. Les résultats quasi statiques montrent un bon accord avec ceux obtenus avec le logiciel CONTACT de Kalker, qui constitue la méthode de référence pour le contact roue/rail quasi-statique. Dans le cas de glissement total, l'analyse de stabilité fait apparaître une instabilité du couplage de modes lorsque la zone de contact est décalée latéralement du plan moyen des cylindres. Dans la configuration instable, la solution transitoire est cohérente avec les résultats de stabilité. En ce qui concerne les performances des modèles de réduction, les résultats obtenus montrent un bon accord avec ceux de référence dans l'analyse de stabilité et dans les calculs transitoires. Ces méthodes sont ensuite appliquées à un modèle réaliste de contact roue/rail en courbe. On constate que la discrétisation de la zone de contact ne modifie sensiblement pas les mécanismes d'instabilité. Cependant, en raison du couplage plus fort entre les degrés de liberté de contact normaux, les taux de divergence des modes instables sont plus élevés avec le modèle éléments finis que pour le modèle de contact ponctuel. Les résultats de la simulation dynamique transitoire sont cohérents avec l'analyse de stabilité et montrent des oscillations localisées adhérence/ glissement dans la zone de contact. Le coefficient de frottement global moyenné pendant les cycles stabilisés est légèrement inférieur au coefficient de frottement local constant. Ainsi, la diminution du coefficient de frottement global pourrait être interprétée comme une conséquence (et non une cause) des vibrations auto-entretenues. La courbe de saturation dynamique moyenne obtenue avec le modèle éléments finis montre un hystérésis qui est n'est pas obtenu avec les courbes quasi-statiques. Ce phénomène pourrait être du à l'importante rigidité latérale liée aux effets transitoires dans la zone de contact. Des analyses non linéaires avec des modèles de contact ponctuels devraient ainsi prendre en compte cette cette rigidité pour améliorer la prédiction des cycles limites.

Mots clés: Bruit ferroviaire, Crissement en courbe, Instabilité dynamique, Méthode éléments finis, Contact roue/rail, Dynamique non linéaire, Calcul transitoire, Frottement

Acknowledgment

This work was carried out in Laboratoire de Mécanique Multiphysique Multiéchelle (LaMcube) of the University of Lille, in collaboration with L'Unité Mixte de Recherche en Acoustique Environnementale (UMRAE-IFSTTAR). I want to thank them for having offered me this topic and for their welcome and help in this work.

The supervision was done by Mr Philippe DUFRÉNOY, Mr Jean-François BRUNEL in LaMcube and Mr Olivier CHIELLO in UMRAE, whom I thank for their advice, their help and the time spent throughout this work, especially when writing.

I thank:

- to Mr Jean-Jacques SINOU and Mr Gaël CHEVALLIER for agreeing to report this work, and to Mr Huajiang OUYANG, Mrs Astrid PIERINGER and Béatrice FAVERJON for examining this work,
- to Mr Fabien LETOURNEAUX (SNCF) for having participated in the jury,
- to the permanent employees and PhD students in LaMcube and UMRAE, administrative staff of the University of Lille,
- to my family and friends.

Contents

List of Figures

List of Tables

General introduction

Industrial and environmental context

In order to qualify and certify railway transport systems, the railway industry continues to rely on physical tests, which are often very expensive . To reduce these tests, optimized numerical simulations would allow a considerable gain in cost and development time. For instance, during the last decade, aeronautics and automotive industries have succeeded in replace more than 50% of physical tests with virtual computer tests, and have reduced the development time of new vehicles by at least 50%. Thus, the time and cost reductions on the certification operations would allow the French railway industry to gain in competitiveness compared to its competitors around the world. In this context, the CERVIFER project (Certification Virtuelle Ferroviaire) aims, by 2020, to:

- limit as much as possible the number of prototypes and physical tests with an objective of replacing 50% of the physical tests by virtual computer tests,
- reduce at least 50% of the certification duration of the railway components,
- increase the life duration of the components and reduce the maintenance cost of railway systems in the order of 10 to 15% .

This project which has been financed by ADEME (French Environment and Energy Management Agency) started in October 2013 and was completed in December 2017. This project was a cooperative project involving private and public partners including University of Lille, UTC, IFSTTAR, Alstom Transport, RATP, SNCF, Vossloh Cogifer, Hutchinson, Vibratec, CETIM, IRT Railenium and was managed by ESI Group. The project was divided into five Work Packages (WPs) described in Tab. 1.

WP 1	WP 2	WP 3	WP 4	WP 5
Analysis of the existing and technical specifications	Safety, reliability and safety of the vehicle-track interaction	Wear and fatigue of wheel/rail contact	Reduction of noise pollution	Integration of virtual prototyping tools

Table 1: Work packages of the CERVIFER project

The thesis is devoted to the task 4.2 "Parametric modeling of curve squeal with regular contact geometry" of WP 4. This work package aimed to develop virtual prototyping softwares in order to propose efficient and inexpensive solutions for the reduction of the noise emitted by rail-bound vehicles. Railway noise includes wheel/rail noise due the wheel/rail contact, "traction" noise due to the traction equipments on the vehicles (motors, electrical auxiliary devices, etc..) and aerodynamic noise. In a wide speed range, the main contributions come from wheel/rail noise which include two very different sources: rolling noise and squeal noise. Rolling noise is a broadband noise generated in almost every situation by stationary random irregularities of wheel and rail running surfaces (acoustic roughness) whereas curve

squeal is emitted in the tight curves of the rail network and is due to the sliding of wheels on the rail head. This noise is charaterized by intense levels and pure tones in the the medium or high frequency range. The tramway and metro networks are strongly concerned.

In CERVIFER WP4, tasks related to rolling noise directly concerned the development of an operational software allowing virtual certification. This was possible since knowledge about rolling noise is very advanced and problem is more about the developement of precise track or wheel models as well as implementation and test of technological solutions within the software. Considering that the modeling of curve squeal noise is less advanced, the goal of the related task was quite different. The modeling of curve squeal still faces a number of scientific obstacles at the origin of the thesis. These difficulties are essentially related to the vibration generation mechanism of squeal noise. The sound radiation part of the mechanism is not directly adressed in the thesis since project partners developed efficient virtual softwares to estimate the sound radiation for rolling noise. These developements have been re-used for the estimation of the sound radiation for curve squeal.

General scientific issues

Squeal remains a complex scientific problem because of the many physical interactions involved (mechanical, acoustic, tribological,...) and the difficulty in identifying and controlling the excitation source. Many studies have been performed to understand the mechanisms responsible for this curve squeal noise. In particular, it is established that squeal is due to friction-induced vibrations in relation with lateral sliding of wheel/rail contact in curve. Bibliography allows to identify influential parameters, especially kinematic parameters such as the angle of attack or the lateral contact position as well as structural characteristics such as wheel damping. It also provides different mitigation solutions with more or less success due to the approximative control of source mechanisms. However, several questions remain open and some parts of the generation mechanisms are still controversial, partly because of the difficulty of experimental validation and because models are often restricted and not always quantitative. In this scientific context, the general objectives of the thesis are:

- to review and enlighten the mechanisms leading to curve squeal in order to propose efficient and mitigation solutions,
- to develop a model able to evolve towards a quantitative tool for squeal prediction by taking into account more complexity which are not included for the moment in the different models of curve squeal: particularly the phenomena of plastic deformation, contact surface defects that can affect the wheel/rail contact area.

Outline of the manuscript

The organization of the document roughly corresponds to these general objectives. In, Chapter 1, an extensive literature review about curve squeal is proposed, covering a quite broad scope, with some sections dealing specifically with friction-induced vibrations or wheel/rail contact modeling. At thE end of this fundamental chapter, the detailed objectives and strategy of the thesis are presented, emphasizing the main originalities of the work. The first part includes Chapters 2 and 3 and is entirely dedicated to the instability mechanisms occurring at the onset of curve squeal. The second part, including Chapter 4 and 5, focuses on the development and the validation of a nonlinear finite element model for the dynamics of wheel/rail systems in curve with an application to curve squeal.

Literature review

Contents

This chapter aims to situate this work in relation to existing studies dealing with a type of friction-induced vibration: curve squeal of rail-bound vehicles. This chapter is organized as follows:

Firstly, the phenomenon of curve squeal is described and compared with other noises emitted by railway systems. General observations about curve squeal, potential excitations at wheel/rail contact and wheel and rail vibro-acoustic behaviors during squealing are also presented.

Then, from literature, existing instability mechanisms enlighting contact-friction induced vibrations are presented and separated into two types: mechanisms of tribological origin and those of geometric origin. The main methods for determining self-sustained vibration of nonlinear systems are outlined: stability analysis for predicting the occurrence of instabilities and nonlinear methods for the determination of self-sustained vibrations levels and spectra.

Considering that curve squeal results from phenomena occurring in the wheel/rail interaction, a review of wheel/rail rolling contact models is given. Several types of contact models relevant to distinguish wheel/rail contact situations are presented including point-contact models, surface-contact models based on influence functions and full finite element models.

Curve squeal models are then examined and classified according to the following criteria: wheel and rail dynamics, contact models including friction characteristic and dynamic interaction combined with solution computation. From an analysis of the main results of these curve squeal models together with primary experimental observations , the strategy of the thesis is proposed.

1.1 The phenomenon of curve squeal

There are many sources of noise and vibration in the railway systems. They can be distinguished in two categories:

- *Wheel/rail noise* is caused by excitations occurring mainly inside the wheel/rail contact zone. It includes : rolling noise, impact noise and curve squeal noise. Rolling noise is brought on by stationary random irregularities of wheel and rail running surfaces (acoustic roughness). The roughness acts as a dynamic imposed relative displacement and induces vertical vibration of wheel, rail and other neighboring structures. Rolling noise acoustic levels (in dB) vary with train speed V according to an approximate law of about $30\log_{10}V$ [3]. Impact noise is generated by localized irregularities such as wheel flats, rail joints. Impact noise is similar to rolling noise as it is due to a forced vertical broadband excitation. Curve squeal noise is emitted during curving and is discussed later in this thesis.

- *Other railway noises* include bridge noise, aerodynamic noise, ground-borne noise and vibrations, traction noise and brake noise. Bridge noise is emitted when a train runs over a bridge. The bridge is excited by dynamic forces acting on it from the track. Aerodynamic noise is caused by air flowing over the running train. Ground-borne noises are due to ground vibration excited by the track at low frequency, between about 2 and 80 Hz. Ground-borne noise may be radiated in buildings from the vibration of walls, floors and ceilings of rooms at higher frequency from about 30 to 250 Hz. Traction noise comes from from diesel engines, exhaust systems, electric traction equipments, fans, gearboxes or turbochargers. Brake noise is emitted during braking generally at low speed.

Within the audible frequency range from 20 to 20000 Hz, bridge noise and ground-bornenoise are concentrated at low frequencies whereas brake squeal noise can occur at very high frequencies.

1.1.1 General observations

When a railway vehicle negotiates with a tight curve (Fig. 1.1), a strong noise called curve squeal may be emitted. The sound pressure levels can reach to 130 dB close to the wheel, and up to 110 dB at 7.5 m from the track center in the frequency range 250 Hz - 10 kHz [4]. The predominating part of squeal noise energy is concentrated in one or several pure tone frequencies [5]. The occurrence probability of

this noise depends on the vehicle dynamics in the curve and consequently on some typical geometric parameters like the bogie wheelbase (Fig. 1.1). The curve radius/bogie wheelbase ratio R/W is thus a good indicator. According to Rudd [6] and Remington [7], an occurrence is expected if $R/W < 100$ but according to Thompson [3], this noise can occur sporadically if $R/W < 500$ and commonly if $R/W < 200$.

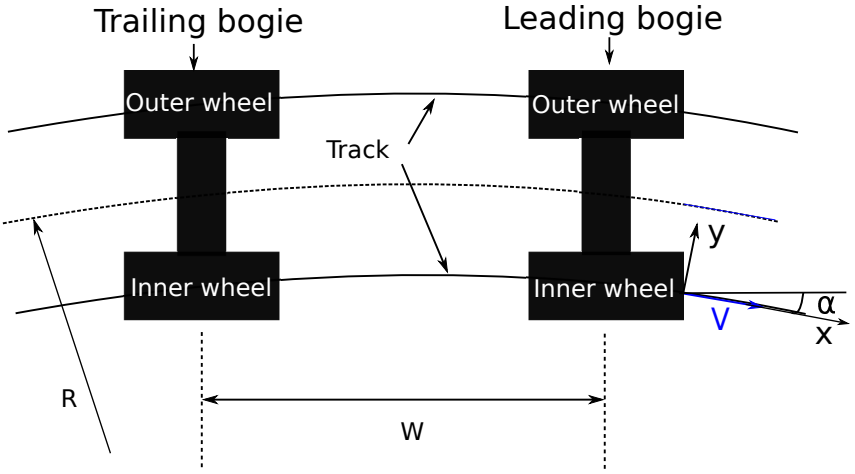

Figure 1.1: Behavior of a bogie in curve

Experimental observations (cf. for instance [8]) show that curve squeal is strongly influenced by the following parameters:

- local kinematic parameters at wheel/rail contact,
- friction at contact interface,
- wheel vibro-acoustic characteristics.

The local kinematic parameters at wheel/rail contact include the rolling speed V, the angle of attack α and the lateral position of the contact across the wheel tread. The angle of attack and lateral position parameters depend on the bogie and track design features through the vehicle dynamics in the curve. The critical attack angle, above which squeal noise appears, corresponds well with the criteria based on the R/W ratio (a R/W value of 100 gives a W/R value of about 10 mrad) [5]. Squeal seems to strongly depend on the lateral position as indicated for instance in the measurements of De Beer *et al.* [9]. Experimental results found by Liu and Meehan [10], Vincent *et .al* [5] and Koch *et .al* [8] showed that squeal noise levels increase with rolling speed and angle of attack.

The friction at contact interface is a key factor and is influenced by weather conditions, track polluants and eventual lubrication. Friction modifiers can reduce curve squeal but does not eliminate definitively this noise [4, 11]. This can be an additional lubricant focused on the wheel flange during curving, rail watering.

The measurements described by Rudd [6], Vincent *et .al* [5], Koch *et .al* [8] and Glocker *et .al* [12] show that the wheel radiates squeal noise at frequencies close to the wheel natural frequencies. In addition, the highest noise levels is most often radiated by the inner leading wheel. However, squeal noise is occasionally observed on the outer wheel [12].

That is the reason why the addition of damping devices on wheels may reduce or eliminate the squeal noise in many cases.These include resilient wheels commonly used on trams or friction systems added on the wheel like constrained layer systems and dynamic absorbers [11].

Global observations about curve squeal are mentioned above. To further explore the issue, it is necessary to examine the main features of the squeal generation mechanism in the next section.

1.1.2 Excitation at wheel/rail contact

In rail terminology, the "imposed creepage" is defined as as the relative velocity between wheel and rail normalized with the rolling velocity V in the rigid case, i.e. without deformations of the wheel and the rail in the contact zone. Depending on the motion of the wheel on the rail, there are three imposed creepages which may happen in the wheel/rail contact area: longitudinal creepage s_{xo}, lateral creepage s_{yo} and spin creepage s_{wo} given by:

$$\begin{cases} s_{xo} = \dfrac{\Delta V_x}{V} \\ s_{yo} = \dfrac{\Delta V_y}{V} \\ s_{wo} = \dfrac{\Delta \Omega_z}{V} \end{cases} \tag{1.1}$$

where $\Delta V_x = V_x - V$ is the relative longitudinal velocity of the wheel in comparison with the rolling velocity, $\Delta V_y = V_y$ is the relative lateral velocity of the wheel and $\Delta\Omega_z$ is the rotation velocity of the wheel around the vertical axis. These quasi-static creepages are imposed by the relative motion of the wheel on the rail.

When the vehicle negotiates the curve, three different cases can be distinguished according to Rudd [6]:

- flange rubbing,
- differential longitudinal creepage,
- lateral creepage.

The flange rubbing happens when the wheel flange is in contact with the rail gauge corner (Fig. 1.2). As a result, this mainly concerns the outer wheel of the leading bogie in the curve. In accordance with field observations and laboratory measurements [7, 8], squeal level is reduced when this occurs. According to [5], in most cases, the flanging contact seems to bring a positive effect on squeal control. Specific flange noise is observed by Glocker 's measurements [12]. Unlike squeal noise, the flange noise is characterized by a wide-band frequency spectrum. A railway operator such as RATP found that squeal control is efficient by only watering the inner rail in the curve whereas the outer wheel of the leading bogie forms a flanging contact with the rail [5]. Thus, for all these reasons this flange rubbing can be neglected as a primary cause of squeal generation.

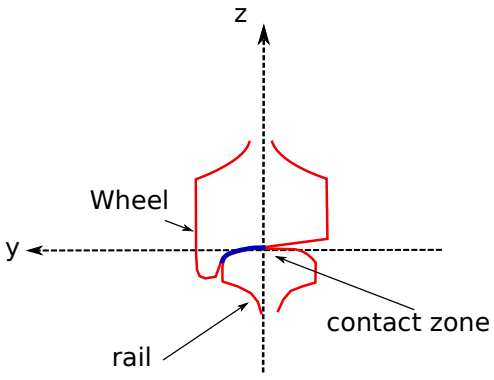

Figure 1.2: Flange rubbing

Differential longitudinal creepage occurs in the curve since the longitudinal velocity of the outer wheel is generally higher than the velocity of the inner wheel. In the frequent cases where the left and right wheels are rigidly connected via the axle, the rotation velocities of both wheels are identical. The

outer wheel therefore slides in the longitudinal direction. This phenomenon was cited as a possible cause of squeal but was also is discredited by tests in which only one rail on a curve has been lubricated and there is no squeal noise [13].

Finally, in the curve, the wheel forms an angle of attack α with the rail in the longitudinal direction that induces a lateral velocity of the wheel relatively to the rail (Fig. 1.1). For small angles, this lateral velocity is given by:

$$\Delta V_y = V \tan(\alpha) \simeq V\alpha \tag{1.2}$$

Consequently, the wheel slides on the rail in the lateral direction. Considering this last hypothesis, the remaining question concerns the mechanism by which quasi-static friction forces in the curve may lead to high-frequency vibrations and squeal noise. A widespread assumption is that friction induces structural instability of the quasi-static equilibrium and self-sustained vibrations of the wheel-rail system. These "friction-induced vibrations" are not uncommon in the field of structural dynamics but require a special attention since they have to be analyzed with specific tools (stability analysis and nonlinear dynamics) and will be discussed in more detail in subsection 1.2. This assumption is corroborated by the typical line spectra observed in acoustic and vibratory responses (cf. section below) which are specific to self-sustained vibrations.

For many authors, a key feature of this instability mechanism can be found in the relation between friction forces and lateral creepages and especially in the supposed weakening of the friction curve for high creepages. Indeed, in some measurements [8–10, 14], the apparent friction coefficient, which is defined as the time-averaged ratio of the resulting lateral force over the resulting vertical contact force for each angle of attack , shows a clear region of negative slope for angles corresponding to squeal noise occurrences. On the other hand, in the experimental observations made by Koch [8] sfor instance, the same "apparent" friction curve does not show any region of negative slope even in case of squeal noise.

Without going into detail, at this point it is necessary to introduce the distinction between this apparent friction coefficient and the local instantaneous friction coefficient at contact level because they can differ from each other, especially in non stationary squealing cases. Generally, only the apparent friction curve is measured.

This topic is crucial and deserves clarification firstly with generalities on instabilities related to friction in section 1.2 and then with the results of existing models in section 1.5.

1.1.3 Wheel and track vibro-acoustic behavior

1.1.3.1 Wheel vibro-acoustic behavior

Most railway wheels are axi-symmetric having a constant cross-section around the azimuthal direction [3]. A typical wheel geometry is showed in Fig. 1.3. At the hub, the wheel is connected to the axle. The flange is designed to avoid derailment.

Like all finite structures, all wheels can be characterized by a series of normal modes and associated natural frequencies. The wheel modes are generally classified according to their predominant motion (out-of-plane (axial) modes, in-plane (radial or circumferential) modes) , their number of nodal diameters n_d and their number of nodal circles n_c. This classification refers to the classical natural mode shapes of a disc as illustrated in Fig. 1.4.

Railway wheels are made of metal material. Consequently, wheels have a light damping and their vibratory responses are strongly marked by mode resonances. Damping modal factors are usually measured by the half frequency bandwidth at which the power amplitude level is 3dB below that at the resonance peaks of the wheel mobility [3]. For rolling noise, Thompson [3] uses for instance the following nominal wheel modal damping factors:

$$\begin{cases} \xi_w = 10^{-3} & \text{if} \quad n_d = 0 \\ \xi_w = 10^{-2} & \text{if} \quad n_d = 1 \\ \xi_w = 10^{-4} & \text{if} \quad n_d \geq 2 \end{cases} \tag{1.3}$$

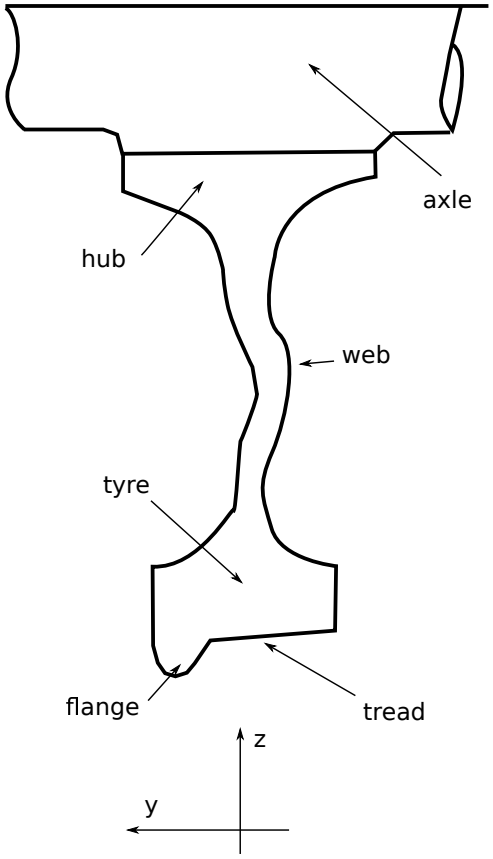

Figure 1.3: An example of typical wheel geometry

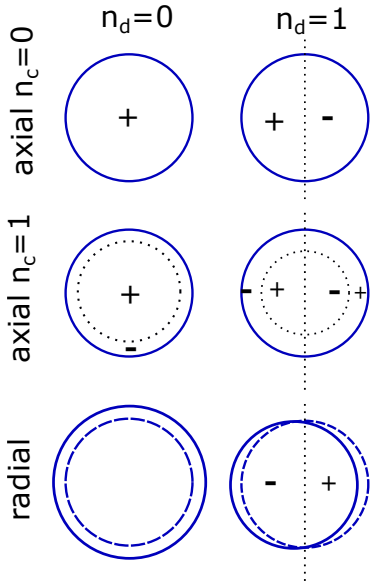

Figure 1.4: Classification of the first mode shapes of an ideal "disc" wheel: $+/-$ indicate the relative phase of the motion in each area. $-$, deformed shape; $--$, undeformed shape; $\cdots$, node lines

In the case of curve squeal, the wheel contribution in vibration response and sound radiation generally dominates over that of the rail [6, 7]. It is often related to the higher lateral mechanical receptance of the wheel at the contact in the frequency range of interest. Vibro-acoustic responses are characterized by line spectra with one one or a few fundamental frequencies with harmonics. In many cases, the fundamental frequencies correspond to the natural frequencies of wheel axial modes with no nodal circles n_c=0 [5, 8, 15]. However, in Glocker's measurements [12], the fundamental squeal frequency is close to three wheel modes including one axial mode and two radial modes at similar frequencies. Less classical observations were recently reported in the works of Ding and al. [16], Fourie *et .al* [17] or Jiang *et .al* [18] where some squealing frequency is different from the natural frequencies of the involved modes and there is a phase shift between the radial and axial wheel vibrations.

1.1.3.2 Track vibro-acoustic behavior

Fig. 1.5 shows a typical railway geometry. The rails are fixed on transverse sleepers, which may be made of wood or concrete (combined with steel in bi-bloc concrete sleepers). These sleepers are supported by ballast, which is a layer of crushed stones. Between the rails and the sleepers, we find the rail pads, which may be made of rubber or synthetic rubber. These pads are originally designed to protect sleepers and ballast from high impact quasi-static load but their stiffness is critically important in the vibratory behavior of the track. In particular, they can significantly affect the rolling noise produced by the track. Some other tracks are designed using concrete slabs instead of ballast. In France, this is especially the case in light rail networks like trams. In such tracks, the sleepers are often embedded in the slabs.

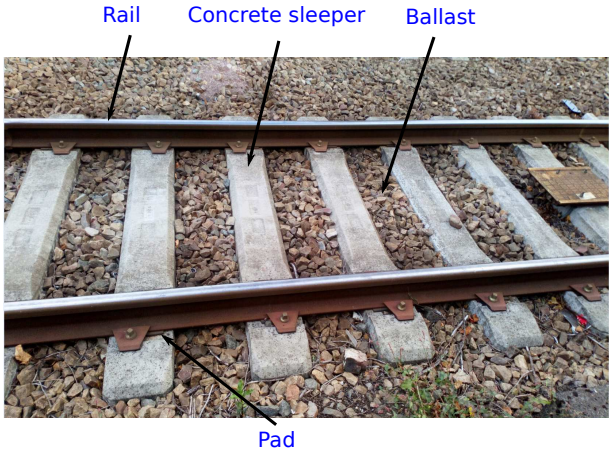

Figure 1.5: Typical ballasted track structure

Unlike the wheel which is a finite structure, the track can be considered as an infinite structure because of its very high length in comparison with its cross-section dimensions. The rail does not have a modal behavior as the wheel but rather a waveguide behavior allowing structural waves to propagate along it from the excitations with very limited reflexions. At a given frequency a number of different structural waves can exist in the rail. At low frequencies, these are vertical and lateral bending, torsional and longitudinal waves. However, at high frequencies, these are rail cross-section deformation waves [3].

Important features of the rail vibro-acoustic behavior are the wave attenuations (or track decay rates) since weakly attenuated waves may radiate a lot of noise. This is often the case in the medium frequency range (between 500 and 1500 Hz) according to the rail pad stiffness. These phenomena have been thoroughly investigated in rolling noise studies where rail and wheel contributions may be very similar. In the case of squeal noise, the historical measurements of Rudd and Remington [6, 7] showed a low track contribution in sound radiation in comparison with that of the wheel. In subsequent works, very few experimental data have been published about the track behavior in squealing conditions. Only recent

works addressed the issue but rather in order to explore the excitation mechanism than to assess the acoustic contribution of the rail (cf. Ding and al [19], Fourie and al [17], Jiang *et .al* [18]).

1.2 Instability and friction-induced vibrations

As mentioned in subsection 1.1.2, according to a widely shared assumption based on experimental observations, curve squeal noise is related to structural instability and friction-induced vibrations. For that reason, this section firstly attempts to answer how the frictional contact can induce instabilities by examine the literature concerning the frictional contact models and the instability mechanisms due to friction in academic simple models. Secondly, the modeling tools commonly used to study this kind of problem are presented, especially for the stability analysis of the mechanical frictional systems and the simulation of resulting non-linear friction-induced vibrations.

1.2.1 Classical contact and friction models

Contact models

Contact modeling has been developed due to the occurrence of fatigue problems resulting from industrial systems (wheel-rail contact for trains, plane-sphere contact for bearings). For instance, normal contact was studied in the XIXth century by Hertz [20] for the non-conform surface contact of elastic bodies as it will be exposed in section 1.3.2 dealing with wheel/rail contact. These kind of specific contact laws are based on some assumptions on the effective contact area (bilateral contact). In many cases, this area is unknown and unilateral contact laws have to be used at each point of the interface. Non-smooth Signorini's law [21, 22] is the classical law, which deals with unilateral contact on the interface. It is given by:

$$\begin{cases} g_n \leq 0 & (i) \\ r_n \leq 0 & (ii) \\ g_n r_n = 0 & (iii) \end{cases} \tag{1.4}$$

where $g_n = u_n - g_o$ is the gap between the two solids, u_n is the relative normal displacement of the two solids in contact, g_o is the initial gap between the two solids (cf. Fig. 1.6a) and r_n is the normal contact reaction. This law simply conveys that (i) there is no inter-penetration between the two bodies, (ii) the interface only undergoes compression and (iii) it respects the condition of complementarity.

A equivalent semi-smooth form of non-smooth Signorini's law uses the projection [23] on the real level set:

$$r_n = \text{Proj}_{\mathbb{R}^-}(r_n - \rho_n g_n) \qquad \forall \rho_n > 0 \tag{1.5}$$

where $\text{Proj}_{\mathbb{R}^-}(x) = \min(x, 0)$ and ρ_n is a positive real number called normal augmentation parameter.

This law is however not "one to one" between relative normal displacement and normal contact pressure. To avoid this difficulty, some authors propose to regularize the relation. In addition, smooth laws are commonly introduced not only to make a compromise between the verification of non-inter-penetration condition but also to account for a physical problem: there are always surface asperities crushed by contact pressure so that interpenetration is present at a macroscopic level. However, input parameters of these smooth laws are not easy to measure and are often chosen arbitrarily. A graph of typical contact laws [24] is proposed in Fig. 1.6b.

Friction models

Modeling friction is earlier than contact modeling. Leonard de Vinci studied friction in the XVIth century. Amontons [25] studied the origin of resistance in machines in 1699. Friction is important

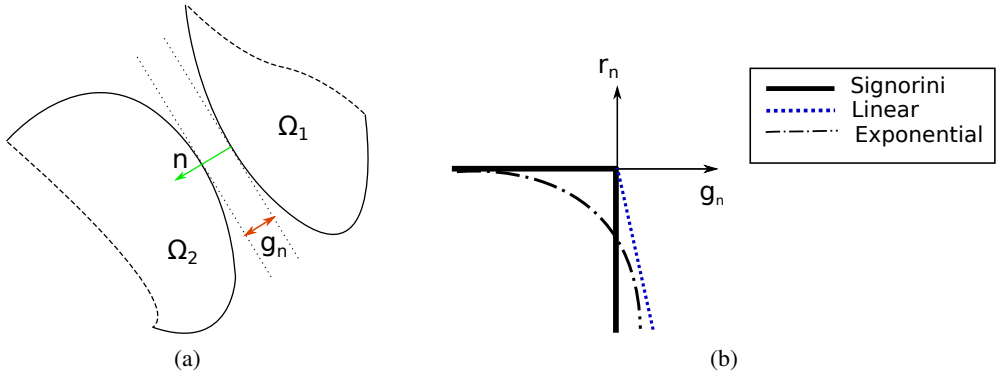

Figure 1.6: Contact normal direction n and gap g_n definition for two solids Ω_1 and Ω_2 (a) and graph of typical unilateral contact laws (b)

because it is opposed to movement and can be a important factor in the conception or the deterioration of frictional rolling systems. The most commonly used friction law is Coulomb's law which is based on the observations of Leonard de Vinci and of Amontons observations. This law is given by:

$$\begin{cases} ||r_t|| \leq -\mu r_n \\ ||r_t|| = -\mu r_n \quad \text{if} \quad \exists \lambda > 0, w_t = -\lambda r_t \\ ||r_t|| < -\mu r_n \quad \text{if} \quad w_t = 0 \end{cases} \tag{1.6}$$

where r_n, r_t are the normal and tangential contact reactions respectively and w_t is the relative tangential velocity between the two solids at contact surface. The two contact points are sticking if $w_t = 0$ and sliding if $w_t \neq 0$. In addition, μ is friction coefficient and mainly depends on contacting materials and surface conditions .

This law states that the frictional reaction cannot be greater than a limit $-\mu r_n$. If it reaches the limit, the material particle slides and has a direction opposed to the direction of the reaction (slip state). In other cases, the relative velocity is null (stick state).

A equivalent semi-regularized form of the law uses the projection on the Coulomb cone ([23]):

$$r_t = \text{Proj}_{\mathcal{C}}(r_t - \rho_t w_t) \qquad \forall \rho_t > 0 \tag{1.7}$$

where $\text{Proj}_{\mathcal{C}}(\mathbf{x}) = \min(\frac{\mu|r_n|}{\|\mathbf{x}\|}, 1)\mathbf{x}$ and ρ_t is a positive real number called tangential augmentation parameter.

Like Signorini's law, friction Coulomb's law is non-smooth and not one-to-one. To regularize this law, several propositions were made [26, 27]. For instance, one can set a threshold of the tangential velocity and make the transition between the two directions over the interval $[-\delta, \delta]$ or to use Arctangent law in order to get close to Coulomb's law as well as possible. The graph of these laws are represented in Fig. 1.7.

1.2.2 Instability mechanisms

This section is dedicated to the origins of dry friction-induced vibrations and especially self-sustained vibrations due to instabilities. A number of instability mechanisms have been proposed in the literature to explain the appearance of friction-induced vibrations [28, 29]. Four instability mechanisms stand out which can be separated in two categories.

In the first category, the origin of friction-induced vibrations is considered as tribological. Two instability mechanisms belong to this category: "stick-slip" mechanism and friction laws characterized by a decrease of friction coefficient depending on the relative tangential velocity.

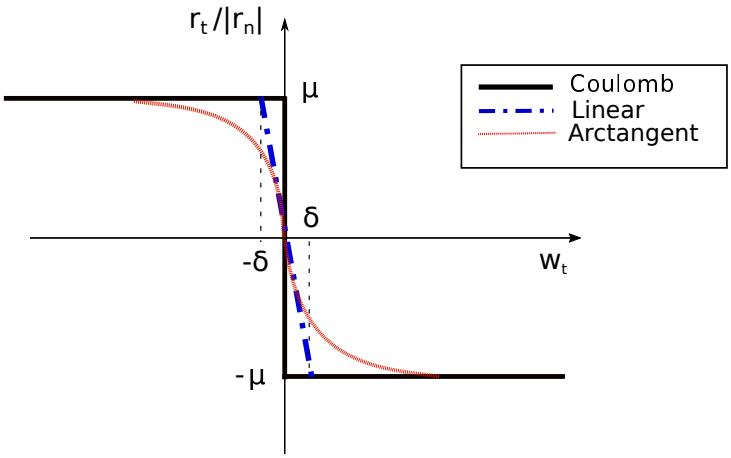

Figure 1.7: Graph of Coulomb's law

The second category highlights the importance of the geometry of the mechanical system on the appearance of the friction-induced vibrations. In this case, the friction coefficient is assumed constant. Two instability mechanisms belong to this category: "sprag-slip" mechanism and mode-coupling.

1.2.2.1 Tribological origin

In the literature, many studies deal with the mechanisms presented below. The developments proposed in [28, 30] are re-used. For these developments, a one degree of freedom (DOF) model is considered in Fig. 1.8 where a mass m supports a constant vertical charge **N** and is maintained in position by one linear springs k. V is the constant velocity of the conveyor belt. $R_n = -N$ is the normal contact reaction of the conveyor belt on the mass. $\Delta V_x = \dot{u}_x - V$ denotes the relative tangential velocity between the mass and the conveyor belt. u_x is the displacement of the mass. R_t is nonlinear and depends on ΔV_x. The notation $\dot{u} = \frac{\partial u}{\partial t}$ refers to the time partial derivative.

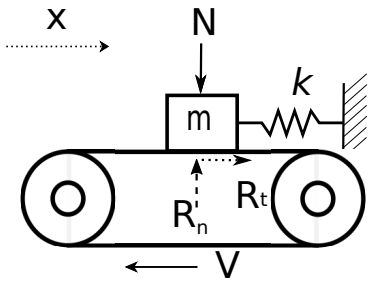

Figure 1.8: Model of one degree of freedom

The equation of motion is written by:

$$m\ddot{u}_x + ku_x = R_t(\Delta V_x) \tag{1.8}$$

Stick-slip mechanism

For this mechanism, the key factor is the discontinuity of the friction coefficient between the adhesion state (static friction coefficient μ_s) and the slip state (dynamic friction coefficient μ_d) of the mechanical system. It is considered as an origin of friction-induced vibrations (cf. Fig. 1.9).

Using this law, the frictional force $R_t(\Delta V_x)$ can be written by:

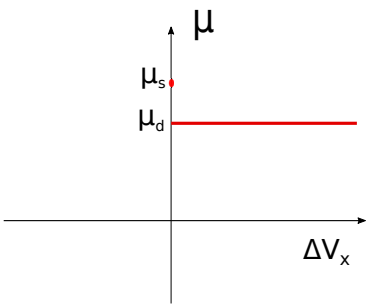

Figure 1.9: Difference between the static and dynamic friction coefficients as a function of the creep velocity

$$\begin{array}{ll} & R_t \leq \mu_s R_n \\ R_t = -\mu_d R_n \ \text{sign}(\Delta V_x) & \text{if} \quad \Delta V_x \neq 0 \end{array} \tag{1.9}$$

where sign$(\bullet)$ is the sign of $\bullet$.

If the mass is initially considered in the adhesion state with the conveyor belt ($\Delta V_x = \dot{U}_x - V = 0$), the displacement of the mass induces an augmentation of the frictional force R_t until it reaches the limit value $R_t = \mu_s R_n$. At this moment, the mass starts to slide on the conveyor belt with the frictional force $R_t = -\mu_d R_n \ \text{sign}(\Delta V_x)$. The mass is again in the adhesion state with the conveyor belt until the frictional force R_t reaches again the static limit value $\mu_s R_n$.

The limit of adhesion U_{xa} is defined by: $U_{xa} = \mu_s R_n / k$ and the position of the quasi-static equilibrium is defined by : $U_{xe} = \mu_d R_N / k$. In the space $(U_x, \dot{U}_x)$, the adhesion state is described by the segment $([-U_{xa}, U_{xa}], V)$. If the velocity V is positive, the system describes elliptic trajectories centered on $U_{xe}, 0$. If V is negative, these trajectories are centered on $(-U_{xe}, 0)$.

The case with V positive is considered here. According to the initial conditions, we can distinguished 3 cases which represent the dynamic behavior of the system (cf. Fig. 1.10):

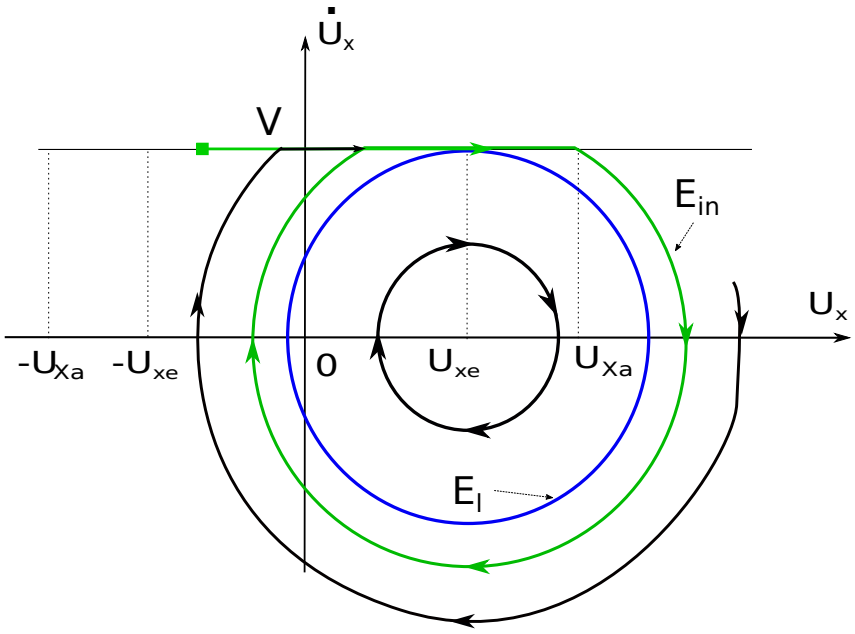

Figure 1.10: Evolution in the phase space for stick-slip phenomena

- If the initial conditions are inside the ellipse $\mathbf{E}_l$ of center $(U_{xe}, 0)$ and tangent to the adhesion segment $([-U_{xa}, U_{xa}], V)$, there is no stick-slip phenomenon.

- If the initial conditions are in the adhesion segment $([-U_{xa}, U_{xa}], V)$, the trajectory follows the segment to the point (U_{xa}, V) then becomes an ellipse of center $(U_{xe}, 0)$ until intercepting the adhesion segment again. This trajectory is the curve $\mathbf{E}_{in}$ in Fig. 1.10.
- For all other initial conditions, the trajectory of the system has an elliptical portion until intercepting the adhesion segment. Then it describes the curve $\mathbf{E}_{in}$.

If the system is damped, all trajectories in Fig. 1.10 become spirals converging to the center point $(U_{xe}, 0)$ which will be the steady solution. Thus, this historical model is interesting to describe the friction-induced vibrations of type stick-slip but is not very useful to explain the occurrence of instability in the system.

Friction coefficient decreasing with the relative tangential velocity

The same system as the previous case (Fig. 1.8) is considered here. However, the considered friction law is different (Fig. 1.11). In this case, friction coefficient μ decreases as a function of the relative tangential velocity ΔV_x.

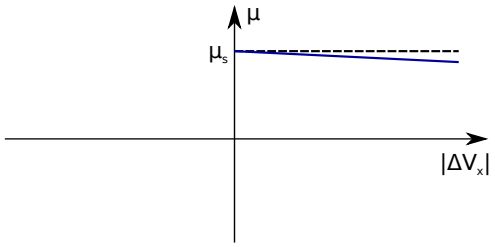

Figure 1.11: Variation of friction coefficient with the relative tangential velocity

The nonlinear friction force is defined by:

$$\begin{aligned} R_t &\leq \mu_s R_n \\ R_t &= -\mu_s(1-\alpha_\mu|\Delta V_x|)R_n \ \mathrm{sign}(\Delta V_x) \quad \text{if} \quad \Delta V_x \neq 0 \end{aligned} \tag{1.10}$$

where α_μ is positive.

The quasi-static sliding equilibrium is defined by:

$$U_{xe} = \mu_s(1-\alpha_\mu V)R_n/k \tag{1.11}$$

In the sliding state, the equation of motion Eq. (1.8) linearized around the quasi-static equilibrium of the mechanical system can be written:

$$\begin{aligned} m\ddot{U}_x + kU_x &= \mu_s\alpha_\mu\dot{U}_x R_n \\ m\ddot{U}_x - \mu_s\alpha_\mu R_n\dot{U}_x + kU_x &= 0 \end{aligned} \tag{1.12}$$

Eq. (1.12) shows that the decrease of the friction coefficient with the relative tangential velocity can introduce a negative damping in the system. If the damping of the system is inferior to the negative damping, the quasi-static equilibrium is consequently unstable. This negative damping is responsible for the self-sustained vibrations.

According to the initial conditions, we can distinguished 3 cases which represent the dynamic behavior of the system (cf. Fig. 1.12):

- If the initial conditions are inside the ellipse $\mathbf{E}_{in}$, the trajectory is a spiral diverging until intercepting the adhesion segment $([-U_{xa}, U_{xa}], V)$ then follows the segment until the point (U_{xa}, V). This trajectory then follows the curve $\mathbf{E}_{in}$.

- If the initial conditions are in the adhesion segment $([-U_{xa}, U_{xa}], V)$, the trajectory follows the segment to the point (U_{xa}, V) then describes the same behavior $\mathbf{E}_{in}$ as that of the "stick-slip" case.
- For all other initial conditions, the trajectory of the system has a elliptical portion until intercepting the adhesion segment and then it describes the curve $\mathbf{E}_{in}$.

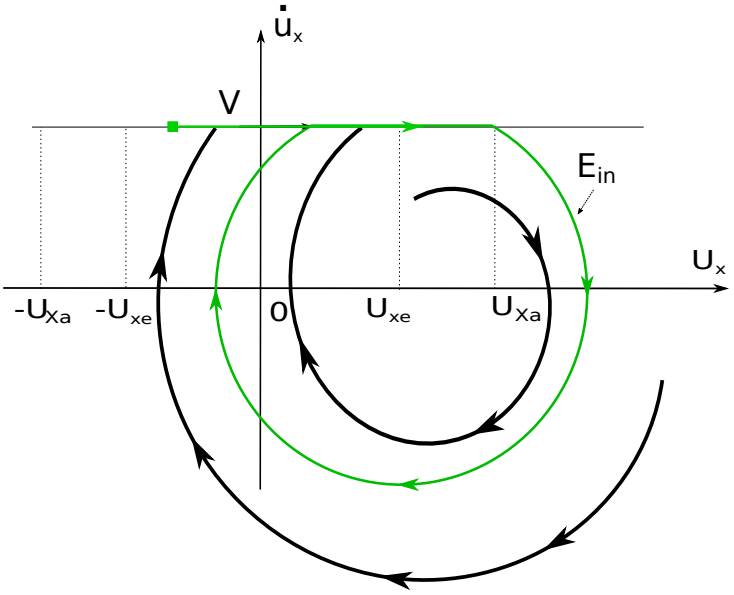

Figure 1.12: Evolution in the phase space with the decrease of friction coefficient depending on the relative tangential velocity

Thus, by considering this simple 1-DOF model, it is found that by introducing a negative damping in the mechanical system, the decrease of the friction coefficient with the relative tangential velocity can destabilize the mechanical system and the instability of the system and lead to self-sustained vibrations characterized by stick-slip cycles.

1.2.2.2 Geometric origin

In this section, one takes an interest in the occurrence of friction-induced vibrations of the mechanical system induced by geometrical phenomena. By considering the two mechanisms presented below, it is thus found that even if the friction coefficient is constant with the relative tangential velocity, friction-induced vibrations may happen.

"Sprag/slip" case

This mechanism was introduced by Spurr [31] by considering the mechanical system illustrated in Fig. 1.13. The system is composed of two rigid beams with a pivot connection at point O. The first beam is clamped at O'. The beam OP is loaded against a moving belt by a vertical force N at point P. V is the constant velocity of the conveyor belt. R_n is the normal contact reaction of the conveyor belt at point P. $\Delta V_x = \dot{U}_x - V$ is noted as the relative tangential velocity between P and the conveyor belt. U_x is the displacement of point P. R_t is the friction force applying on the beam and depends on ΔV_x. The friction coefficient is supposed to be constant.

By assuming $R_t = \mu R_n$ and taking moments about point O, it is shown in Fig. 1.13 :

$$R_t = \frac{\mu N}{1 - \mu \tan(\gamma)} \tag{1.13}$$

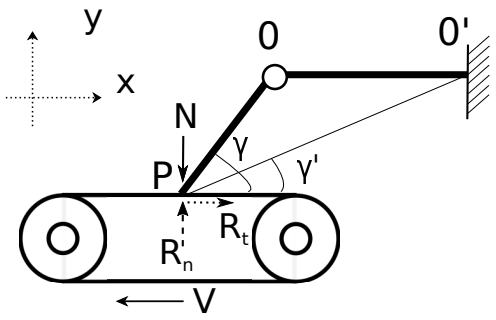

Figure 1.13: model sprag

When angle γ approaches the value $\arctan(1/\mu)$, the force R_t becomes consequently very high: beam O'P sprags and motion is impossible. Due to spragging, there is no slip between P and the conveyor belt. In order for motion to continue, point O' becomes a pivot connection and angle γ takes the value of angle γ' which is smaller than γ. Consequently, the friction force R_t suddenly decreases and point P slides again on the conveyor belt.

This model is useful to illustrate that the occurrence of self friction-induced vibrations can be obtained with constant friction coefficient. It makes also clear that the angle between the rubbing structure and the moving plane plays a key role, pointing out the importance of the geometry and the variation of the normal force as a source of instability. However, expressing interaction between the friction force and the normal force may be achieved using other simple models and especially those that enable mode coupling instability to be demonstrated.

Mode coupling

Oden and Martins [32] introduced this notion of "Mode coupling" by observing the coupling between the normal and tangential directions in Tostoi's paper [33]. North is the first researcher to consider brake squeal as a self-excited vibration induced by friction forces with constant friction coefficient according to Kinkaid *et al.* [34]. To clarify the phenomenon, several academic models have been proposed in [1, 35, 36]. The mechanism needs at least two DOFs which makes it different from the two mechanisms of tribological origin.

To illustrate the mechanism, Hoffman used a two degree of freedom model (cf. Fig. 1.14). The mass m is maintained in position by two linear springs k_1 and k_2 on a linear contact spring k_3. A conveyor belt with constant velocity V is pushed, inducing a normal contact force R_n against the mass m. To take into account of sliding friction, a Coulomb-type friction force in sliding phase $R_t = \mu R_n$ with a constant friction coefficient μ, is assumed.

The equations of motion is written:

$$\mathbf{M}\ddot{\mathbf{U}} + \mathbf{K}\mathbf{U} = \mathbf{R} \tag{1.14}$$

where $\mathbf{U} = \begin{pmatrix} \ddot{U}_x \\ \ddot{U}_y \end{pmatrix}$ and $\mathbf{R} = \begin{pmatrix} R_t \\ R_n \end{pmatrix} = \begin{pmatrix} \mu R_n \\ R_n \end{pmatrix}$ are the nodal displacement and contact reaction vectors respectively. $\mathbf{M} = \begin{bmatrix} m & 0 \\ 0 & m \end{bmatrix}$ and $\mathbf{K} = \begin{bmatrix} k_{11} & k_{12} \\ k_{21} & k_{22} \end{bmatrix}$ are the mass and stiffness matrix respectively. The coefficients of the stiffness matrix can be obtained from elementary considerations as:

$$\begin{aligned} k_{11} &= k_1 \cos^2\alpha_1 + k_2 \cos^2\alpha_2 \\ k_{12} = k_{21} &= k_1 \sin\alpha_1 \cos\alpha_1 + k_2 \sin\alpha_2 \cos\alpha_2 \\ k_{22} &= k_1 \sin^2\alpha_1 + k_2 \sin^2\alpha_2 + k_3 \end{aligned} \tag{1.15}$$

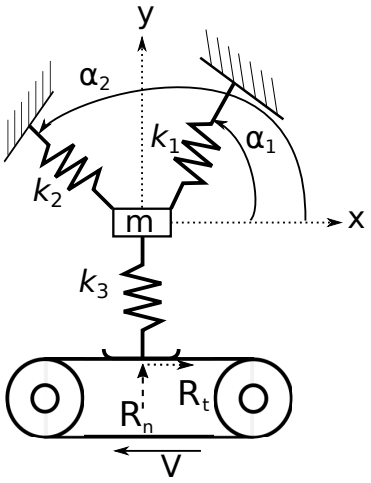

Figure 1.14: Hofmann's model [1]

Considering small perturbations $\tilde{\mathbf{U}}$ around the steady sliding state and approximating the friction force by $\tilde{R}_t = \mu k_3 \tilde{U}_y$, it leads to a non symmetric eigenvalues problem:

$$(\lambda^2 \mathbf{M} + \mathbf{K} + \mathbf{K_f})\tilde{\mathbf{U}} = 0 \tag{1.16}$$

where $\mathbf{K}_f = \begin{bmatrix} 0 & -\mu k_3 \\ 0 & 0 \end{bmatrix}$

Because of the non symmetry of matrix $\mathbf{K_f}$, complex eigenvalues λ may be obtained: $\lambda = D + i\omega$ where D, ω is the real and imaginary part of λ respectively. ω is the pulsation of the perturbation whereas D characterizes the damping or the divergence of the perturbation according to its sign. Indeed, if D is positive, the amplitude of the solution corresponding to eigenvalue λ increases exponentially around the quasi-static equilibrium. The system is consequently unstable.

With $m = 1$, $\alpha_1 = 150\,°$, $\alpha_2 = 30\,°$, $k_1 = 2/3(2-\sqrt{3})$, $k_1 = 2/3(2+\sqrt{3})$, $k_3 = 4/3$, the evolution of the pulsations and the real parts of the two eigenvalues of the system are represented in Fig. 1.15. The frequencies coalesce for a friction coefficient $\mu = 0.75$ (Fig. 1.15a) above which there is a mode with a positive real part, leading to the destabilization of the mechanical system (Fig. 1.15b).

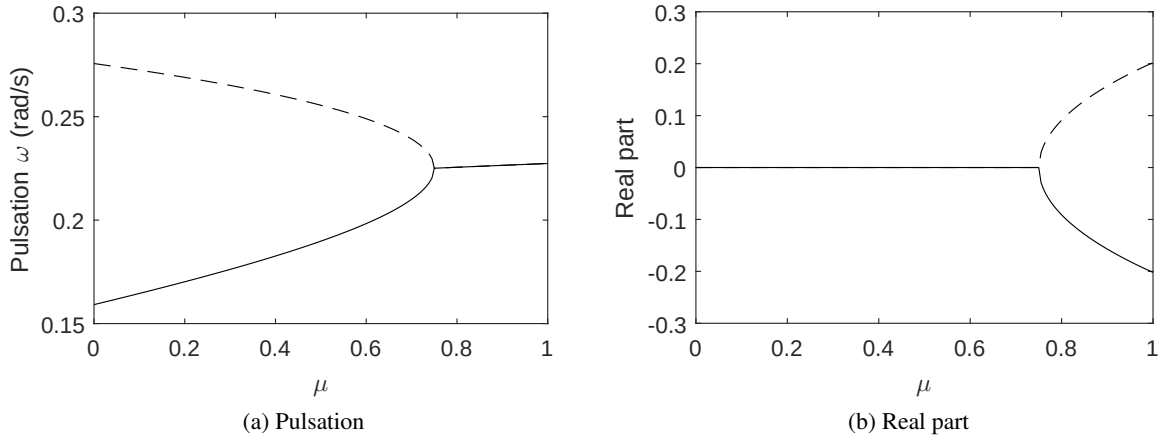

(a) Pulsation (b) Real part

Figure 1.15: Evolution of the pulsation and the real part of λ as a function of μ

In summary, among the four mechanisms described above, two mechanisms explain the occurrence of friction-induced vibrations through the stability analysis of the sliding equilibrium. This first mecha-

nism has a tribological origin and is characterized by negative damping introduced in the system by the decrease of the friction coefficient with the relative tangential velocity. The second mechanism has a geometric origin and is characterized by mode coupling with a constant friction coefficient. This phenomenon is mathematically due to the non symmetrical stiffness matrix induced by the coupling between the normal and tangential directions through friction. Both instability mechanisms may lead to self-sustained vibrations. Nonlinear limit cycles can then be obtained. This could be the slip/stick vibration as shown by the first mechanism but other kind of self-sustained vibrations are possible. In particular, loss of contact (separation) may occur in the contact zone leading to slip/separation or slip/stick/separation cycles (cf. [37, 38]). Nonlinear phenomena localized elsewhere in the structure (like in the sprag/slip mechanism) can also appear and be involved in self-sustained vibrations.

1.2.3 Stability analysis

In the previous sections, it has been showed how friction-induced vibrations may be the result of the instability of the sliding equilibrium, either by negative damping (1-dof system) or by mode coupling (2-dof system). In order to study friction-induced vibrations of mores complex systems, it is thus necessary to perform stability analysis in a more general way. In this subsection, we present the main definitions and tools concerning this notion.

1.2.3.1 General definitions and Liapounov's theorems

We consider a nonlinear dynamic system of the first order given by:

$$\dot{\mathbf{x}} = f(\mathbf{x}) \tag{1.17}$$

where $\mathbf{x}$ is a vector of $\mathbb{R}^N$ and f is a nonlinear function which is not explicitly expressed as a function of time t.

A point called "equilibrium" is a point $\mathbf{x}_e$ such that: $f(\mathbf{x}_e) = 0$. Two definitions are then introduced concerning the stability of the equilibrium [39]:

- Stability:

  The equilibrium $\mathbf{x}_e$ is simply stable if and only if :

$$\forall \varepsilon, \exists \delta / ||\mathbf{x}(0) - \mathbf{x}_e|| \leq \delta \rightarrow \forall t, ||\mathbf{x}(0) - \mathbf{x}_e|| \leq \varepsilon \tag{1.18}$$

- Asymptotic stability or stability in the sense of Liapounov:

  The equilibrium $\mathbf{x}_e$ is asymptoticly stable if and only if :

$$\exists p, \forall \varepsilon, \exists \delta / ||\mathbf{x}(0) - \mathbf{x}_e|| \leq \delta \rightarrow \forall t, ||\mathbf{x}(0) - \mathbf{x}_e|| \leq \varepsilon e^{-pt} \tag{1.19}$$

The simple stability allows the existence of self-sustained oscillations with weak amplitude around the equilibrium whereas the asymptotic stability characterizes a damped solution that returns to the equilibrium.

Stability analysis of the nonlinear system is base on the system linearized around a point. The Eq. (1.17) linearized around the equilibrium $\mathbf{x}_e$ is given by:

$$\dot{\mathbf{x}}_e + \dot{\varepsilon} = f(\mathbf{x}_e) + \mathbf{J_d} \mathbf{x}_e \varepsilon \tag{1.20}$$

where ε is the small perturbation around $\mathbf{x}_e$ and $\mathbf{J_d}$ is the Jacobian of the function f.

Stability analysis is simply studied according to Liapounov's theorems [39]:

- If the real parts of all eigenvalues of $\mathbf{J_d}(\mathbf{x}_e)$ are negative, so $\mathbf{x}_e$ is asymptoticly stable,

- If there are eigenvalues of $\mathbf{J_d}(\mathbf{x}_e)$ with positivie real part, so $\mathbf{x}_e$ is unstable.

In summary, the stability analysis consists in calculating the eigenvalues of the dynamic system, after its linearization around the equilibrium. This is what has been proposed for the 2-dof system presented for the description of mode-coupling instabilities. This could have been done for the 1-dof system where negative damping would also lead to a positive real part.

It should also be noted that there is two general ways for a equilibrium point to be unstable :

– when the imaginary part of the eigenvalue is non null, the instability will give rise to exponentially growing oscillations ; this is generally called periodic exponential instability or oscillatory instability (sometimes known also as flutter but this term often refers to mode coupling phenomena only) ,

– when the imaginary part is null the instability will give rise to a periodic exponentially growing motion ; this type of instability is called divergence.

Self-sustained vibrations are due to oscillatory instabilities, in both "negative damping" or "mode coupling" cases. The transitions from stable equilibrium points to oscillatory instabilities are called "Hopf bifurcations" and are explained in the next paragraph.

1.2.3.2 Hopf's bifurcation

In the previous paragraph, it is showed that Liapounov's theorems can be used to decide on the stability of an equilibrium of the nonlinear system. If the system is controlled by a scalar parameter μ, Eq. (1.17) can be written:

$$\dot{\mathbf{x}} = f(\mathbf{x}, \mu) \tag{1.21}$$

During variations of parameter μ, the behavior of the system changes. A point $\mathbf{x}_o, \mu_o$ is a Hopf's bifurcation if it verifies the three following conditions:

- $f(\mathbf{x}_o, \mu_o) = 0$,
- $\mathbf{J_d}(\mathbf{x}_o, \mu_o)$ admits a pair of conjugate pure imaginary eigenvalues ($\lambda = i\omega$, $\bar{\lambda} = -i\omega$) and no other eigenvalue has a null real part,
- $\frac{\partial \text{ Real}(\lambda(\mu))}{\partial \mu} \neq 0$ at $\mathbf{x}_o, \mu_o$

In the vicinity of the bifurcation, if it exists an eigenvalue with positive real part, there is a loss of stability of the equilibrium. Self-sustained vibrations can develop. The orbits grow exponentially until reaching a closed orbit with the period $T = 2\pi/\omega$ following the classical scheme in Fig. 1.16. For mode coupling instabilities, the friction coefficient is often considered as a control parameter. In the undamped case presented in Fig. 1.16, the Hopf bifurcation occurs for instance at the critical friction coefficient $\mu = 0.75$, when the two imaginary parts of the eigenvalues (pulsation) coalesce. However, other control parameters can be used.

1.2.3.3 Computational methods for stability analysis of friction destabilized systems

The finite element method is commonly used to perform stability analysis of frictional contact problem such as brake squeal [22, 40, 41]. By solving a complex eigenvalue problem [21, 42], they allow to determine the potential unstable modes and corresponding frequencies of the system and are useful to test the influence of the parameters on the onset of friction-induced vibrations.

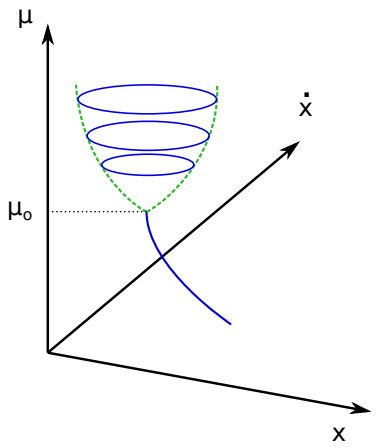

Figure 1.16: Illustration of a Hopf bifurcation with limit-cycle amplitude (blue)

With finite element models, stability analysis of systems with frictional contact generally leads to a constrained non symmetric eigenvalues problem:

$$(\lambda^2 \mathbf{M}_{stab} + i\lambda \mathbf{C}_{stab} + \mathbf{K}_{stab})\tilde{\mathbf{U}} = 0 \tag{1.22}$$

where $\mathbf{M}_{stab}, \mathbf{C}_{stab}, \mathbf{K}_{stab}$ are respectively the mass, damping and rigidity matrix of the system linearized around an equilibrium. λ and $\tilde{\mathbf{U}}$ are respectively complex eigenvalue and eigenvector of the eigenvalue problem.

In most cases, computing stability analysis thus requires to solve a non-symmetrical eigenvalue problem with very large size. Effective algorithms are classic in the symmetrical case but the non-symmetry makes things more difficult. Such a problem is often solved by using reduction methods. The principle of the reduction methods consists of searching a discrete solution of the form:

$$\tilde{\mathbf{U}} = \mathbf{B}\tilde{\mathbf{U}}_r \tag{1.23}$$

where $\mathbf{B}$ is the reduce base and $\tilde{\mathbf{U}}_r$ is the generalized coordinates.

The choose of the reduction basis $\mathbf{B}$ is crucial for the resolution of Eq. (1.22). In iterative algorithms based on Arnoldi process [43] or the residue iterative method [44], the reduction basis $\mathbf{B}$ are progressively enriched from a chosen initial basis until reaching the desired accuracy. However, in any case, they can be highly expensive.

To overcome the computational problem, reduction basis which are *a priori* determined are sometimes used. They can be separated in two types. The first type includes the normal (real) modes of the conservative corresponding system (undamped and without friction). This base can then be enriched by adding some static response to the friction forces [41] or to the load generated by the damping [45] in order to offer more precision in the non-conservative case. For a system composed of many substructures, component mode synthesis (CMS) [46, 47] offers the advantage of computing component modes separately. In the classical technique, the reduction basis are composed of component's normal modes and static boundary modes. In presence of friction, the static boundary modes may also include tangential attachment modes or more specific rubbing attachments modes [41]. Brizard *et al.* [41] showed that the two kind of enriched reduction bases provide errors about 10 times smaller than the no enriched bases. In addition, errors on the real part of the complex eigenvalues are reduced to about 0.01% in term of damping factor (or divergence rate) which is a reasonable precision.

1.2.4 Nonlinear self-sustained vibration

The temporal evolution of friction-induced vibrations is composed of three phases. In the vicinity of the sliding equilibrium point, the linear phase is controlled by the stability parameters and the temporal

solution is characterized by a superposition of harmonics oscillations at the frequencies of the unstable modes, with amplitudes increasing exponentially. Then, the transient phase follows with the occurrence of nonlinear phenomena , modal competition and new oscillations at harmonic frequencies. The last phase is called the steady state where the average amplitude and the full spectrum of the solution no longer change. The nonlinear self-sustained vibrations are then constituted by periodic or quasi-periodic limit cycles.

Stability may deal with the linear phase but may not provide sufficient information to assess the system full behavior. It can not introduce strong nonlinear phenomena such as stick-slip cycles or loss of contact (separation) [48] and therefore can not determine the amplitude and the full spectrum of self-sustained vibrations. In this subsection, an inventory of the methods used to determine these nonlinear self-sustained vibrations is presented, especially in the case of friction destabilized systems.

1.2.4.1 Time integration

The discretized equations of the non-linear system are formulated as a function of time t:

$$\begin{cases} \mathbf{M}\ddot{\mathbf{U}}(t)+\mathbf{C}\dot{\mathbf{U}}(t)+\mathbf{K}\mathbf{U}(t)=\mathbf{F_{ex}}(t)+\mathbf{F_{nl}}(\mathbf{U},\dot{\mathbf{U}},t) \\ \mathbf{U}(0),\dot{\mathbf{U}}(0),\ddot{\mathbf{U}}(0) \\ \text{B.C. on} \quad \mathbf{U},\dot{\mathbf{U}} \end{cases} \tag{1.24}$$

where $\mathbf{M},\mathbf{C},\mathbf{K}$ are respectively the mass, damping and stiffness matrix of the linear system. $\mathbf{U},\dot{\mathbf{U}},\ddot{\mathbf{U}}$ are respectively the vector of displacements, velocities and accelerations of the system. $\mathbf{F_{ex}}$ contains the linear external forces applied to the system. $\mathbf{F_{nl}}$ is the vector of nonlinear forces present in the system notably including contact and friction forces in the problems of friction-induced vibrations. .

By discretization of the time dimension, time integration schemes provide tools for computing a time dependent response from given initial conditions. Finite-differences schemes are based on numerical quadratures for a given time discretization. The time step at a given instant t_i is then function of the previous and following time steps. A scheme is called *explicit* if the solution at instant t_{i+1} only depends on the previous steps. On the contrary, it is called *implicit* if the solution at instant t_{i+1} depends on next time steps. For a implicit scheme, at each instant, a system has to be solved.

As indicated for instance in [49, 50], a time integration schemes is characterized by three quantities: consistence, stability and energy conservation. On a time interval $[t_i,t_{i+1}]$ of length h, a scheme is consistent if the approximate solution converges towards the continuous solution as the time step is decreased:

$$\lim_{h\to 0}\frac{\mathbf{U}_{i+1}-\mathbf{U}_i}{h}=\dot{\mathbf{U}}_i \tag{1.25}$$

A time integration scheme is stable if a finite variation of the state response at instant t_i induces a bounded variation of the state response calculated at a following instant t_{i+1}. A time integration is conservative if the system energy does not change from t_i to t_{i+1} (in case of conservative systems).

Some analysis about different time integration scheme are proposed by Vermot des Roches [51], A.Loyer [40] or L.Charroyer [52]. In the following, the time integration schemes will be distinguished according to their adaptation to the type of frictional contact laws.

Smooth frictional contact laws

By using smooth frictional contact laws, the contact and friction forces can be expressed in the form of regular functions of kinematic quantities $(\mathbf{U},\dot{\mathbf{U}},t)$. The laws can limit the occurrence of discontinuities in the solution and the acceleration can be defined at each instant. Second order time schemes are commonly used, especially: Newmark scheme introduced by Newmark [53] or Hilber-Hughes-Taylor scheme [54].

In a linear case, the Newmark scheme uses the numerical quadrature of the acceleration to calculate the displacement and the velocity:

$$\begin{aligned} \dot{\mathbf{U}}_{i+1} &= \dot{\mathbf{U}}_i + \int_{t_i}^{t_{i+1}} \ddot{\mathbf{U}}(\tau) d\tau \\ \mathbf{U}_{i+1} &= \mathbf{U}_i + h\dot{\mathbf{U}}_i + \int_{t_i}^{t_{i+1}} (t_{i+1} - \tau)\ddot{\mathbf{U}}(\tau) d\tau \end{aligned} \tag{1.26}$$

To approximate the two different integrals, the quadratures for the velocity and displacement are performed using two parameters γ_1 and γ_2 respectively:

$$\begin{aligned} \dot{\mathbf{U}}_{i+1} &= \dot{\mathbf{U}}_i + h(1-\gamma_1)\ddot{\mathbf{U}}_i + h\gamma_1\ddot{\mathbf{U}}_{i+1} \\ \mathbf{U}_{i+1} &= \mathbf{U}_i + h\dot{\mathbf{U}}_i + h^2\dot{\mathbf{U}}_i + h^2(\frac{1}{2} - \gamma_2)\ddot{\mathbf{U}}_i + h^2\gamma_1\ddot{\mathbf{U}}_{i+1} \end{aligned} \tag{1.27}$$

Knowing the solution in time step t_i, the resolution of Eq. (1.24) gives the system to be solved at time step t_{i+1}:

$$\begin{cases} \mathbf{J}\ddot{\mathbf{U}}_{i+1} = (h(1-\gamma_1)\mathbf{C} + h^2(\frac{1}{2} - \gamma_2)\mathbf{K})\ddot{\mathbf{U}}_i + (\mathbf{C} + h\mathbf{K})\dot{\mathbf{U}}_i + \mathbf{K}\mathbf{U}_i + \mathbf{F}_{\mathbf{ex}i+1} \\ \dot{\mathbf{U}}_{i+1} = \dot{\mathbf{U}}_i + h(1-\gamma_1)\ddot{\mathbf{U}}_i + h\gamma_1\ddot{\mathbf{U}}_{i+1} \\ \mathbf{U}_{i+1} = \mathbf{U}_i + h\dot{\mathbf{U}}_i + h^2\dot{\mathbf{U}}_i + h^2(\frac{1}{2} - \gamma_2)\ddot{\mathbf{U}}_i + h^2\gamma_1\ddot{\mathbf{U}}_{i+1} \end{cases} \tag{1.28}$$

where $\mathbf{J} = \mathbf{M} + h\gamma_1\mathbf{C} + h^2\gamma_1\mathbf{K}$. The scheme is unconditionally stable if $\gamma_1 = 1/2$ and $\gamma_2 = 1/4$ [49].

In a nonlinear case, the nonlinear forces generally depend on the displacement and the velocity. For the resolution of Eq. (1.28), one needs a prediction/correction algorithm. Assuming that the solution in time step t_i is given, the prediction is initialized by assuming a null acceleration at time step t_{i+1}.

The displacement corrections $\Delta\mathbf{U}$ are determined by a Newton-Raphson algorithm which first consists in computing the derivative of the residue of the dynamic equation as a function of the displacement correction:

$$\mathbf{J_d}(\mathbf{U}, \dot{\mathbf{U}})|_{\Delta\mathbf{U}} = \frac{\partial \mathbf{r}(\mathbf{U}, \dot{\mathbf{U}})}{\partial \Delta\mathbf{U}}|_{\Delta\mathbf{U}} = \frac{1}{\gamma_2 h^2}\mathbf{M} + \frac{\gamma_1}{\gamma_2 h}\mathbf{C} + \mathbf{K} + \frac{\partial \mathbf{F_{nl}}(\mathbf{U} + \Delta\mathbf{U}, \dot{\mathbf{U}} + \Delta\dot{\mathbf{U}})}{\partial \Delta\mathbf{U}} \tag{1.29}$$

The Jacobian matrix $\mathbf{J_d}$ depends clearly on the derivative of the nonlinear forces at the current state which is very expensive from a computational point of view, especially in dynamic transient simulations. Vermot Des Roches [55] proposes a fixed Jacobian to avoid repeating the factorization of the Jacobian. He uses a fixed stiffness matrix $\mathbf{K}_r$ approximating the terms relating to the contact forces the contact forces (Eq. (1.30)). He shows that the use of this fixed Jacobian does not change the solution but only the convergence properties of the scheme.

$$\mathbf{J_d}(\mathbf{U}, \dot{\mathbf{U}})|_{\Delta\mathbf{U}} = \frac{1}{\gamma_2 h^2}\mathbf{M} + \frac{\gamma_1}{\gamma_2 h}\mathbf{C} + \mathbf{K} + \mathbf{K}_r \tag{1.30}$$

Non-smooth frictional contact laws

Several special issues arise when non-smooth frictional contact laws are used. Indeed, non-smooth frictional contact laws such as Signorini's and Coulomb's laws are non-differentiable. The use of a resolution method using gradients could therefore become complex although generalized Newton methods exist. Another difficulty is the possible occurrence of impacts (or shocks) at the contact interface. These phenomena lead to velocity discontinuities and the acceleration are formally not defined during the

shocks. Finally non-smooth laws are not "one to one". Frictional contact reactions must be considered as unknowns of the system. That generally increases the size of the problem to be solved.

Different strategies are possible to deal with this the first and last problems. One can distinguish them in two types. Both types use Lagrange multipliers in order to impose contact and friction laws. In the first type of methods, the dynamic equations and the frictional contact equations are solve simultaneously using semi-smooth (or generalized) Newton methods. At each time step, algorithms proposed in [50, 56, 57] impose the status of the nodes present at the potential contact surface (stick, slip or loss of contact) until the verification of unilateral contact and friction laws. The friction contact relations become differentiable and Newton-Raphson algorithms can then be used for the resolution of the nonlinear problem as well as Newmark schemes for the time integration. At each change of status, a non symmetric Jacobian matrix has to be recalculated which can be expensive. Several approximations of the Jacobian have been proposed in order to make theses methods more performant (cf. [50]). The second type of methods dealing with non-smooth frictional contact laws includes methods of "Lagrangian augmented family" such as *Large Time INcrement* (LATIn) method proposed in [58–60] and methods using fixed-points algorithms on frictional contact reactions described for instance [50, 61–63]. An important characteristic of these methods is to decouple the resolution of contact equations from the dynamic equation resolution. LATIn method separates the equations of a nonlinear problem in two sets. The first one corresponds to the linear global equations. The second one corresponds to nonlinear local equations. In the case of systems with frictional contact , the first one is the principle of virtual power verifying kinematic constraints and behavior equations. The second one describes non-smooth Signorini-Coulomb's laws. Once this separation is performed, LATIn method consists in searching for the solution of each set starting from the solution of the other set and a search direction. The global step is a linear problem which can be solved by adapted time integration schemes. For the local step which is a nonlinear problem, a time integration scheme of first order such as Implicit Euler method is generally chosen. The search directions influence the convergence of the method towards the final solution. Fixed-point methods are also commonly used since formulations of Signorini/Coulomb in terms of nonlinear projections in Eqs. (1.5) and (1.7) naturally define a fixed point on frictional contact reactions. At each time step, an iterative resolution on the projections can then be performed until reaching the desired precision. The frictional contact reactions at a given iteration are defined by their projections at the previous iteration. The convergence is significantly slower than that of Newton methods but it does not need to recalculate the Jacobian. The method is also rather intuitive using only two augmentation parameters ρ_n and ρ_t. The determination of the optimal values of these parameters, which influences the convergence of the fixed point algorithm, is presented in [40, 50].

To deal with the second problem, i.e. discontinuities induced by shocks, several techniques exist. At this point it is important to detail some physical facts concerning with the shocks in dynamics. Indeed, ideal unilateral contact law Eq. (1.5) is formulated in terms of displacements. It excludes solid interpenetration at the contact state and imposes null repulsive contact forces if the contact is open. However, in dynamics, due to this unilateral contact law, non-smooth impacts phenomena occur when the normal gap reaches zero (contact) from a positive value (separation). In this case, an impact law on the velocity must be added since the velocity after the impact is undetermined. A classical assumption is to considered inelastic impact laws, i.e. null velocities after the shocks. In order to impose this condition, Khenous [64] propose a modification of the mass matrix. The mass of the nodes at contact interface are eliminated and redistributed in the rest of the volume. The objective is to avoid the rebound of the normal stress. The method looks like a penalization of contact. Another technique, the modified $\theta-$ method developed by Moireau and Jean [62] proves to be adapted to non-smooth dynamics. Assuming that the solution is known at time step t_i, by integrating Eq. (1.24) , one obtains:

$$\begin{cases} \mathbf{M}(\dot{\mathbf{U}}_{i+1} - \dot{\mathbf{U}}_i) = \int_{t_i}^{t_{i+1}} (\mathbf{F_{ex}}(\tau) + \mathbf{F_{nl}}(\mathbf{U}, \dot{\mathbf{U}}, \tau) - \mathbf{K}\mathbf{U}(\tau) - \mathbf{C}\dot{\mathbf{U}}(\tau)) d\tau \\ \dot{\mathbf{U}}_{i+1} = \dot{\mathbf{U}}_i + \int_{t_i}^{t_{i+1}} \ddot{\mathbf{U}}(\tau) d\tau \end{cases} \tag{1.31}$$

Since the irregularities can occur within a time step, the integral $\int_{t_i}^{t_{i+1}} \mathbf{F_{nl}}(\mathbf{U}, \dot{\mathbf{U}}, \tau) d\tau$ is computed using a mean impulse value, assuming the non-linear forces are known at time step t_{i+1}:

$$\frac{1}{h} \int_{t_i}^{t_{i+1}} \mathbf{F_{nl}}(\mathbf{U}, \dot{\mathbf{U}}, \tau) d\tau = \mathbf{F_{nl}}(\mathbf{U}, \dot{\mathbf{U}}, t_{i+1}) \tag{1.32}$$

The other integrals are computed using a numerical quadrature with the same parameter:

$$\int_{t_i}^{t_{i+1}} f(\tau) d\tau = h\theta f_{i+1} + h(1-\theta) f_i \tag{1.33}$$

The displacement is computed using a numerical quadrature introducing a parameter θ, giving:

$$\mathbf{U}_{i+1} = \mathbf{U}_i + h\theta \dot{\mathbf{U}}_{i+1} + h(1-\theta)\dot{\mathbf{U}}_i \tag{1.34}$$

The combination of Eqs. (1.31) to (1.34) gives:

$$\begin{cases} \mathbf{J}\dot{\mathbf{U}}_{i+1} = \mathbf{E}(\mathbf{U}_i, \dot{\mathbf{U}}_i) + h\mathbf{F_{nl}}(\mathbf{U}_{i+1}, \dot{\mathbf{U}}_{i+1}) \\ \mathbf{U}_{i+1} = \mathbf{U}_i + h\theta \dot{\mathbf{U}}_{i+1} + h(1-\theta)\dot{\mathbf{U}}_i \end{cases} \tag{1.35}$$

where

$$J = \mathbf{M} + h\theta\mathbf{C} + h^2\theta^2\mathbf{K}$$

,

$$\mathbf{E} = \left(\mathbf{M} - h^2\theta(1-\theta)\mathbf{K} - h(1-\theta)\mathbf{C}\right)\dot{\mathbf{U}}_i - h\mathbf{K}\mathbf{U}_i + h\theta\mathbf{F_{ex}}_{i+1} + h(1-\theta)\mathbf{F_{ex}}_i$$

In the original theta-method, a gap velocity $\dot{\mathbf{g}}_n^{i+1}$ in time step $t_{i+1}$is computed as:

$$\dot{\mathbf{g}}_n^{i+1} = \frac{1}{h\theta}(\mathbf{g}_n^{i+1} - \mathbf{g}_n^i) + \frac{\theta - 1}{\theta}\dot{\mathbf{g}}_n^i \tag{1.36}$$

If the contact happens at time step t_i and the gap does not change from t_i to t_{i+1}, $\dot{\mathbf{g}}_n^{i+1}$ is equal to $\frac{\theta-1}{\theta}\dot{\mathbf{g}}_n^i$ which is not null. Inelastic contact is thus non verified. To overcome this difficulty, Jean [62] propose to compute gaps with an offset of time. The new gap $\tilde{\mathbf{g}}_n^{i+1}$ is computed at time $t_{i+1} + h(1-\theta)$ assuming the velocity constant and equal to $\dot{\mathbf{g}}_n^{i+1}$ in the interval:

$$\tilde{\mathbf{g}}_n^{i+1} = \mathbf{g}_n^{i+1} + h(1-\theta)\dot{\mathbf{g}}_n^{i+1} \tag{1.37}$$

Since $\mathbf{g}_n^{i+1} = \mathbf{g}_n^i + h(1-\theta)\dot{\mathbf{g}}_n^i + h\theta\dot{\mathbf{g}}_n^{i+1}$, Eq. (1.37) yields:

$$\tilde{\mathbf{g}}_n^{i+1} = \tilde{\mathbf{g}}_n^i + h\dot{\mathbf{g}}_n^{i+1} \tag{1.38}$$

The new gap velocity at time step is then given by:

$$\dot{\mathbf{g}}_n^{i+1} = \frac{1}{h}(\tilde{\mathbf{g}}_n^{i+1} - \tilde{\mathbf{g}}_n^i) \tag{1.39}$$

This gap velocity is null if $\tilde{\mathbf{g}}_n^{i+1} = \tilde{\mathbf{g}}_n^i$ and inelastic contact is thus possible. The $\theta-$method is well adapted for non-smooth frictional contact laws. This scheme is unconditionally stable and conservative for $\theta = 1/2$ as presented by Vola [63]. On the other hand, this scheme is implicit because it needs a resolution of Eq. (1.31) at each time step. This scheme has been used in several recent works [21, 38, 42, 52] dealing with brake squeal problems.

1.2.4.2 Other methods for limit cycle computation

By using time integration of the non-linear dynamic equations, a time-history response can be obtained and transient or steady-state vibrations can be analyzed. However the procedure is time consuming. Alternative methods have been developed in order to determine directly the steady-state responses of the system. A number of approximations are used to estimate the nonlinear response. Some of the most fondamental and common ones (center manifold and constrained harmonic balance) are briefly presented below. However, others methods exist and can be just as effective like the shooting method (cf. [52]), the orthogonal collocation [65] or the complex nonlinear modal analysis [66], depending on the application.

Center manifold method

The center manifold method is a reduction of the solution of a non-linear dynamic system in the vicinity of a Hopf bifurcation. It is based on the center manifold theorem which states that all solutions of the system staying in the neighborhood of the Hopf bifurcation tend exponentially quickly to some solution on a reduced subspace called center manifold. Moreover, this center manifold is an invariant manifold tangent to the hyperplane of linear modes with null real parts at the bifurcation. This method is described in [66].

By considering the nonlinear dynamic system Eq. (1.21) as a general formulatinon of Eq. (1.24),

$$\dot{\mathbf{x}} = f(\mathbf{x}, \mu) \tag{1.40}$$

the Taylor development of the function f then gives:

$$\dot{\mathbf{x}} = \mathbf{A}\mathbf{x} + f_2(\mathbf{x}) + \cdots + f_i(\mathbf{x}) + o(||\mathbf{x}||^i) \tag{1.41}$$

where $\mathbf{A}$ is the Jacobian of f on $\mathbf{x} = 0$ (supposed here as the equilibrium point). .

It is assumed that the Hopf bifurcation is in $\mu = \mu_o$ and there is no unstable mode at the bifurcation. Writing the variable $\mathbf{x} = \mathbf{P_{cs}}\mathbf{v} = \mathbf{P_{cs}}\begin{bmatrix}\mathbf{v_c}\\ \mathbf{v_s}\end{bmatrix}$, where $\mathbf{v_c}, \mathbf{v_s}$ are respectively center and stable manifolds of the system.

In the vicinity of the bifurcation, $\mu = \mu_o(1+\varepsilon)$ with $\varepsilon << 1$ and system Eq. (1.41) can be split in two equations corresponding to stable and center manifolds. In addition, each manifold may be written as a combination of a linear part and a purely nonlinear part:

$$\begin{cases} \dot{\mathbf{v}}_\mathbf{s} = \mathbf{A_s}\mathbf{v_s} + \mathcal{F}(\mathbf{v_s}, \mathbf{v_c}) \\ \dot{\mathbf{v}}_\mathbf{c} = \mathbf{A_c}\mathbf{v_c} + \mathcal{G}(\mathbf{v_s}, \mathbf{v_c}) \end{cases} \tag{1.42}$$

The key point of the theory is the invariance property of the manifold. In order to determine the center manifold, it is sufficient to impose that the dynamics of the stable manifold follows the dynamics of the center manifold :

$$\mathbf{v_s} = f_h(\mathbf{v_c}, \varepsilon) \tag{1.43}$$

where f_h verifies the following conditions:

$$\begin{aligned} f_h(0,0) &= 0 \\ \frac{\partial f_h}{\partial \mathbf{v_c}}(0,0) &= 0 \\ \frac{\partial f_h}{\partial \varepsilon} &= 0 \end{aligned} \tag{1.44}$$

Using Eqs. (1.42) and (1.43) and noting that $\dot{\mathbf{v}}_\mathbf{s} = \dot{\mathbf{v}}_\mathbf{c}\frac{df_h}{d\mathbf{v_c}}$, one obtains:

$$(\mathbf{A_c v_c} + \mathcal{G}(\mathbf{v_s}, \mathbf{v_c}))\frac{df_h}{d\mathbf{v_c}} = \mathbf{A_s v_s} + \mathcal{F}(f_h(\mathbf{v_c}, \varepsilon), \mathbf{v_c}) \tag{1.45}$$

Polynomial expansions of the non-linear terms of $\mathcal{G}$, $\mathcal{F}$ and f_h leads to the identification of the coefficients of f_h in Eq. (1.45). The reduced expression of the center manifold finally becomes:

$$\dot{\mathbf{v}}_\mathbf{c} = \mathbf{A_c v_c} + \mathcal{G}(f_h(\mathbf{v_c}, \varepsilon), \mathbf{v_c}) \tag{1.46}$$

Eq. (1.46) describes the dynamics of the system on its center manifold thus considerably reducing its size. However, the major drawback of the method is that it only gives good approximations in the vicinity of the studied bifurcation. Moreover the choice of the order of the polynomial approximation of the stable manifold may have a great influence on the quality of the solution.

Constrained harmonic Balance Method (CHBM)

The harmonic balance method (HBM) is a widely used method to approximate the non-linear solution as a Fourier development truncated at order n_F of harmonics of a given frequency ω:

$$\mathbf{U}(t) = a_o + \sum_{k=1}^{n_F} (a_k \cos(k\omega t) + b_k \sin(k\omega t)) \tag{1.47}$$

The displacement is thus described by the Fourier coefficients s_k, b_k. Applying Eq. (1.47) in Eq. (1.24), the nonlinear system can be written:

$$\sum_{k=0}^{n_F} A_k \cos(k\omega t) + \sum_{k=1}^{n_F} B_k sin(k\omega t) = \mathbf{F_{ex}}(t) + \mathbf{F_{nl}}(a_k, b_k) \tag{1.48}$$

where

$$A_k = (\mathbf{K} - (k\omega)^2\mathbf{M})a_k + k\omega\mathbf{C}b_k$$

and

$$B_k = (\mathbf{K} - (k\omega)^2\mathbf{M})b_k + k\omega\mathbf{C}a_k$$

.

Projecting the equation on sine and cosine orthonormal bases, and writing the multi-harmonics vector $\tilde{\mathbf{U}}$ such that:

$$\tilde{\mathbf{U}} = [a_0 \quad a_1 \quad b_1 \quad \cdots \quad a_{n_F} \quad b_{n_F}]$$

leads to $n_f + 1$ independent systems of 2 equations:

$$\Lambda\tilde{\mathbf{U}} = \mathbf{F_{ex}} + \mathbf{F_{nl}}(\tilde{\mathbf{U}}) \tag{1.49}$$

where

$$\Lambda = \begin{bmatrix} \mathbf{K} & & & \\ & \Lambda_1 & & \\ & & \cdots & \\ & & & \Lambda_{n_F} \end{bmatrix}$$

and

$$\Lambda_k = \begin{bmatrix} (\mathbf{K} - (k\omega)^2\mathbf{M}) & k\omega\mathbf{C} \\ -k\omega\mathbf{C} & (\mathbf{K} - (k\omega)^2\mathbf{M}) \end{bmatrix}$$

In the case of the non-linear forces which can not be expressed easily by Fourier series, an iterative time-frequency algorithm must be introduced [67]. The procedure is as follows:

$$\tilde{\mathbf{U}} \xrightarrow{IFFT} \mathbf{U}(t) \rightarrow \mathbf{F_{nl}}(\mathbf{U}(t)) \xrightarrow{FFT} \mathbf{F_{nl}}(\tilde{\mathbf{U}}) \tag{1.50}$$

For a given state of the Fourier coefficients, the temporal displacement is recovered by an inverse FFT (IFFT). The corresponding temporal non-linear forces are then computed for each instant. The Fourier coefficients of the non-linear force are then obtained by the FFT of its transient expression.

One defines the residue from Eq. (1.49):

$$rsd = \Lambda\tilde{\mathbf{U}} - \mathbf{F_{ex}} - \mathbf{F_{nl}}(\tilde{\mathbf{U}}) \tag{1.51}$$

The search for a steady solution consists in finding the Fourier coefficients a_k and b_k minimizing residues *rsd*. For this purpose, a Newton-Raphson algorithm is generally used. In the case of autonomous systems (for instance for friction-induced vibrations), $\mathbf{F_{ex}}$ is constant and the algorithm naturally gives the trivial solution which is the unstable equilibrium [68]. Moreover, the pulsation ω of the nonlinear response is not known a priori. The constrained harmonic balance method [69] has thus be proposed by Coudeyras *et al.* in order to solves theses issues : a set of additional equations is included to Eq. (1.50) so that the algorithm converges to the non trivial solution.

This method makes it possible to obtain periodic and quasi-periodic limit cycles far from the bifurcations. However, if the system is large, the numerical computation may be expensive.

1.2.4.3 Reduction methods

Dealing with the size of the numerical models, another tool is useful to overcome this common issue. As for the stability analysis, the principle of the reduction methods in nonlinear time calculation consists of searching a discrete solution of the form:

$$\mathbf{U} = \mathbf{B}\mathbf{U}_r \tag{1.52}$$

where $\mathbf{B}$ is the reduce base and $\mathbf{U}_r$ includes the corresponding generalized coordinates.

The choice of the reduction basis $\mathbf{B}$ must optimize the compromise between the reduced size and the precision of the resolution of Eq. (1.22). The classical Component mode synthesis (CMS) bases [46, 47] offer the advantage of computing component modes separately. In the technique, the reduction bases are composed of component's normal modes completed by some static boundary or attachment modes on the contact zone. This technique give good results in linear systems when the external forces oscillate at frequencies inferior to $2/3$ of the highest frequency of the normal modes [70].

In the case of nonlinear systems, the evolution of the modes may depend on the evolution of the solution. To determine relevant reduction bases, it is possible to use singular value decomposition (SVD) of Proper Orthogonal Decomposition [71] of some representative sets of the non reduced (full) temporal solution to extract the major shapes. However, the calculation of the solution of the full model makes this technique expensive in computation time. The concept of nonlinear modes [72] was developed in recent years and proves to be efficient in some applications [73–75]. However, this technique still requires considerable computational effort. In addition, for autonomous systems with mono-instabilities (only one unstable mode), the searched periodic limit cycles are precisely the nonlinear modes.

Consequently, the use of *a priori* reduction bases remains a commonly used technique for industrial systems but the performance of the bases depends on the application. For a simplified brake squeal application, Lorang [22] showed a strong participation of the unstable complex mode shapes determined by stability analysis in the nonlinear solution. However, Sinou [48] observed that the contributions of the harmonic components and the combination of frequency components can not be neglected. Loyer *et al.* [21] performed intensive simulations in order to test two types of bases. The degrees of freedom at contact interface are kept in these bases based on the complex modes resulting from the stability analysis. The study notably shows that an accurate model reduction for friction destabilized system is possible but requires great care. In particular, all the stable modes in the frequency range must be included to ensure an accurate prediction of the nonlinear response. In addition, if separation at the interface is present, the reduction basis must also contain corresponding static boundary modes.

1.3 Wheel/rail rolling contact

This section outlines the main phenomena at wheel/rail contact surface as reported in the literature. An overview of existing wheel/rail contact models is presented.

1.3.1 Description of the problem

A wheel/rail rolling contact is considered, as shown in Fig. 1.17. The $z-$axis is chosen to coincide with the common normal to the two surfaces in contact. The longitudinal $x-$axis corresponds to the rolling direction and the $y-$axis refers to the lateral direction. The wheel rolling speed is V in a direction parallel to $x-$axis . In case of curving, wheel/rail relative lateral velocities ΔV_y and longitudinal velocities ΔV_x have to be considered as discussed in sectiin section 1.1.2. The wheel may also have a relative angular velocity $\Delta\Omega_z$ around their common normal (or spin).

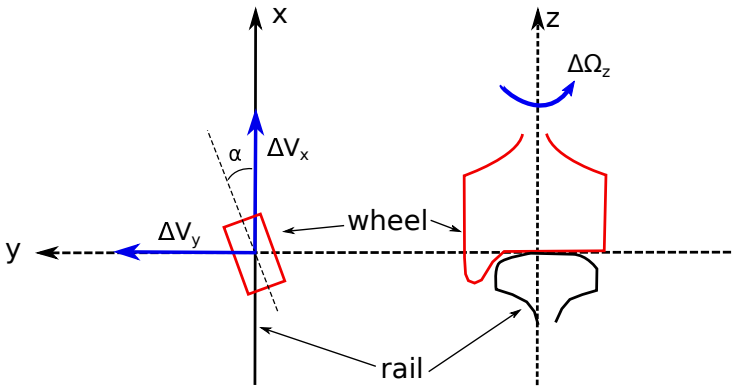

Figure 1.17: Coordinate system, kinetic variables

According to [76], in the Eulerian frame which moves with the point of contact, the instantaneous creepage between the wheel and the rail at a fixed point of the potential contact interface are given by:

$$\begin{aligned} s_x &= \frac{v_x^W - v_x^R}{V} = \frac{\Delta V_x}{V} - \frac{\Delta\Omega_z}{V}y - \left(\frac{\partial u_x^W}{\partial x} - \frac{\partial u_x^R}{\partial x}\right) + \frac{(\dot{u}_x^W - \dot{u}_x^R)}{V} \\ s_y &= \frac{v_y^W - v_y^R}{V} = \frac{\Delta V_y}{V} + \frac{\Delta\Omega_z}{V}x - \left(\frac{\partial u_y^W}{\partial x} - \frac{\partial u_y^R}{\partial x}\right) + \frac{(\dot{u}_y^W - \dot{u}_y^R)}{V} \end{aligned} \tag{1.53}$$

where R, W denote respectively the rail and the wheel. $\mathbf{u}(x,y,z,t)$ and $\mathbf{v}(x,y,z,t)$ denote respectively the displacement and velocity fields of the structure in the Eulerian frame. The terms involving $V\frac{\partial u}{\partial x}$ represent the deformation contributions due to rolling in the Eulerian frame whereas the terms involving $\dot{u}$ simply represent the dynamic contributions.

Combining with Eq. (1.1), Eq. (1.53) can be re-written as:

$$\begin{aligned} s_x &= s_{xo} - s_{wo}y - \left(\frac{\partial u_x^W}{\partial x} - \frac{\partial u_x^R}{\partial x}\right) + \frac{(\dot{u}_x^W - \dot{u}_x^R)}{V} \\ s_y &= s_{yo} + s_{wo}x - \left(\frac{\partial u_y^W}{\partial x} - \frac{\partial u_y^R}{\partial x}\right) + \frac{(\dot{u}_y^W - \dot{u}_y^R)}{V} \end{aligned} \tag{1.54}$$

where s_{xo}, s_{yo} and s_{wo} are the imposed creepages. If the transient term $\dot{u}$ in Eq. (1.54) is neglected, one obtains a steady case and steady creepages are given by:

$$\begin{aligned} s_{xs} &= s_{xo} - s_{wo}y - \left(\frac{\partial u_x^W}{\partial x} - \frac{\partial u_x^R}{\partial x}\right) \\ s_{ys} &= s_{yo} + s_{wo}x - \left(\frac{\partial u_y^W}{\partial x} - \frac{\partial u_y^R}{\partial x}\right) \end{aligned} \tag{1.55}$$

Wheel/rail contact models can be distinguished between point-contact models, surface-contact models based on influence functions and full finite element models presented in the following subsections.

1.3.2 Point-contact models

Point-contact models are simple models, which attempt to describe the phenomena at a global contact level. Both normal and tangential problems can be considered as point contacts. The relationship between creepages and contact forces is represented by analytical formulas. This modeling approach leads to very fast computation because of its simplicity.

1.3.2.1 Normal contact: Hertz's theory

Hertz's theory [20] is introduced by Hertz in 1882 and widely used for the resolution of normal contact problems. Details about Hertz's theory can be found in [3, 76, 77]. The theory is based on the following assumptions:

- elastic, homogeneous and isotropic material behavior,
- contact surfaces are continuous and non-conforming implying that the area of contact is much smaller than the characteristic dimensions of the contacting bodies,
- each solid is considered as an elastic half-space,
- contact surfaces are frictionless.

The wheel undergoes a normal load F_n. R_w and R_{wt} are the radii of curvature of the wheel in the rolling direction and in the transverse direction (Fig. 1.18). R_r and R_{rt} are the radii of curvature of the rail in the rolling direction and in the transverse direction (Fig. 1.18). R_r is usually infinite.

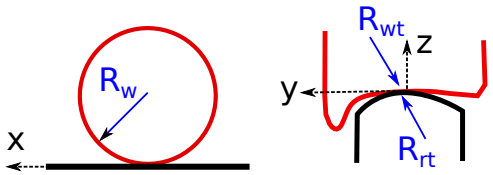

Figure 1.18: Rayons of the wheel (red) and the rail in contact (black)

R_o is an effective radius of curvature of the surfaces in contact given by:

$$\frac{1}{R_o} = \frac{1}{2}\left(\frac{1}{R_w} + \frac{1}{R_{wt}} + \frac{1}{R_r} + \frac{1}{R_{rt}}\right) \tag{1.56}$$

If the assumptions of Hertz's theory are respected, the contact surface is an ellipse of semi-axes a in the rolling direction and b in the transverse direction given by:

$$\begin{aligned} a &= \sigma_1 \left(\frac{3F_n R_o}{2E'}\right)^{1/3} \\ b &= \sigma_2 \left(\frac{3F_n R_o}{2E'}\right)^{1/3} \end{aligned} \tag{1.57}$$

where $E' = E/(1-\nu^2)$ is the plane elastic modulus and E is Young's modulus.

The distribution of normal pressure along this surface is defined by an ellipsoid:

$$p_n(x,y) = p_{max}\sqrt{1-\left(\frac{x}{a}\right)^2-\left(\frac{y}{b}\right)^2} \tag{1.58}$$

where p_{max} is the maximal pressure given by:

$$p_{max} = \frac{3F_n}{2\pi ab} \tag{1.59}$$

The static penetration of the two bodies δ, due to the load F_n, is given by:

$$\delta = \frac{\xi}{2R_o}\left(\frac{3F_nR_o}{2E'}\right)^{2/3} \tag{1.60}$$

The parameters σ_i in Eq. (1.57) and ξ in Eq. (1.58) are listed in tables in [3] as a function of θ defined by:

$$\cos\theta = -\frac{R_o}{2}\left(\frac{1}{R_w}-\frac{1}{R_{wt}}+\frac{1}{R_r}-\frac{1}{R_{rt}}\right) \tag{1.61}$$

Despite the elastic half-space and frictionless assumptions, this theory gives good results in many cases and is therefore commonly used in wheel/rail contact problems as long as the contact is conforming.

1.3.2.2 Tangential contact

Tangential contact models attempt to provide the relationship between creepages and resulting tangential contact forces. The main theories can be found in [78] and are examined in the following.

Carter's theory

Carter [79] found the solution for the 2D case of a cylinder rolling on a plane. The relationship between the imposed longitudinal creepage and the resulting tangential force F_x in the longitudinal direction is non-linear and given by:

$$\frac{F_x}{\mu F_n} = \begin{cases} -\frac{4R_w}{\mu a}s_{xo} + 4\left(\frac{4R_w}{\mu a}\right)^2 s_{xo}|s_{xo}| & \text{if} \quad \frac{4R_w}{\mu a}|s_{xo}| \le 2 \\ -\frac{s_{xo}}{|s_{xo}|} & \text{if} \quad \frac{4R_w}{\mu a}|s_{xo}| \ge 2 \end{cases} \tag{1.62}$$

where R_w is the rayon of the cylinder, μ is the friction coefficient and a is the contact half-width.

This non-linear equation highlights the three typical wheel/rail contact cases : full stick, partial slip and full slip as showed in Fig. 1.19. Full stick or "pure rolling" is in fact only possible when the creepage is null. Partial slip occurs when the creepage is relatively small whereas full slip is obtained for high creepages, depending on the curvature radii, the friction coefficient and the dimension of the contact zone.

Kalker's linear theory

The linear theory [77] was developed by linearizing Carter's solution. Neglecting the quadratic term in the relationship Eq. (1.62) for $\frac{4R_w}{\mu a}|s_{xo}| \le 2$, the linear relationship between the imposed creepage s_{xo} and the resulting contact force is obtained:

$$\frac{F_x}{\mu F_n} = -\frac{4R_w}{\mu a}s_x \tag{1.63}$$

According to Pater [80], this linear theory gives an asymptotic solution of the tangential-contact problem for the case of full stick in the contact area. In other words, the imposed creepage s_{xo} has to

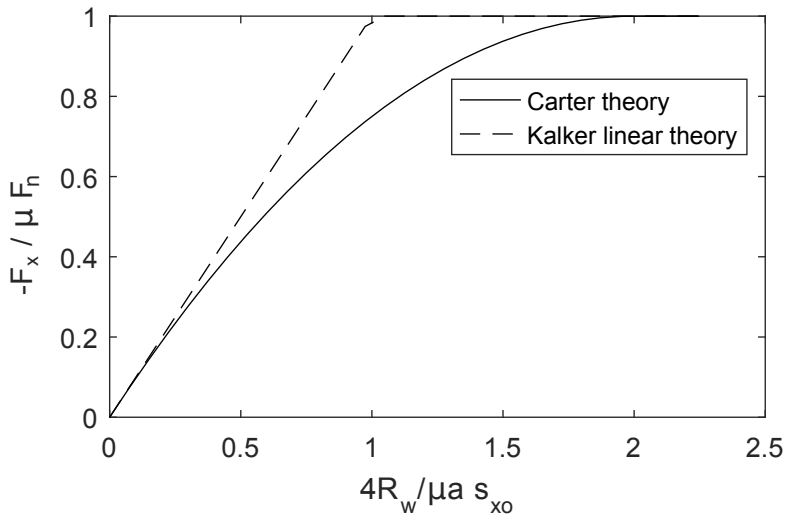

Figure 1.19: Imposed creepage - force relationship according to Carter's theory and Kalker's linear theory

be very small. Kalker [77] proposed the generalization of Eq. (1.63) in the 3D case where the imposed creepages are very small or the coefficient of friction tends forward infinity. For these conditions and in the case of steady rolling, creepages defined in Eq. (1.55) vanish. Eq. (1.55) becomes:

$$\begin{aligned} 0 &= s_{xo} - s_{wo}y - \left(\frac{\partial u_x^W}{\partial x} - \frac{\partial u_x^R}{\partial x}\right) \\ 0 &= s_{yo} + s_{wo}x - \left(\frac{\partial u_y^W}{\partial x} - \frac{\partial u_y^R}{\partial x}\right) \end{aligned} \tag{1.64}$$

By integrating Eq. (1.64) over the entire contact zone and by assuming that each solid is considered as an elastic half-space, the following relationships between the imposed creepages and the contact forces and spin moment are obtained:

$$\begin{aligned} F_x &= -GabC_{11}s_{x_o} \\ F_y &= -GabC_{22}s_{y_o} - G(ab)^{3/2}C_{23}s_{w_o} \\ M_z &= -G(ab)^{3/2}C_{32}s_{y_o} - G(ab)^2C_{33}s_{w_o} \end{aligned} \tag{1.65}$$

where F_x, F_y and M_z are the longitudinal and lateral resulting contact forces and the spin moment about the vertical axis respectively. a, b are the semi-axes of the elliptic contact zone. The Kalker coefficient C_{ij} depend on the ration a/b of the contact ellipse and the Poisson coefficient. Creepage coefficients are tabulated in [77]. G is the shear modulus of the material.

However, the linear theory does not consider any interaction between longitudinal and lateral forces [76]. Moreover, as stated above, this theory is limited to small values of imposed creep velocities. When imposed creep velocitys are important, a non vanishing slip zone is developed in the contact area and this linear theory is not valid anymore.

Vermeulen and Johnson's model

To overcome this difficulty, it is possible to use the Vermeulen and Johnson's model [2] which is a 3D nonlinear model. They assumed that the stick area was also bounded by an ellipse with the same axial ratio and the same orientation of the contact ellipse (see Fig. 1.20). In addition, spin is neglected

in the model. They proposed a relationship between longitudinal and transverse creep velocity and the tangential contact force in polynomial form. A good correlation between the results from this model and measurements is generally found in quasi-static (steady) cases [2].

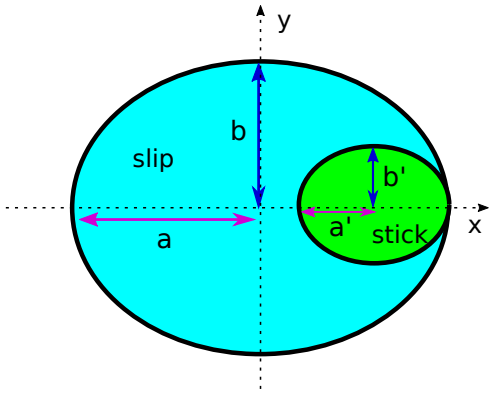

Figure 1.20: Slip and stick areas according to Vermeulen and Johnson's model [2]

Other models and saturation curves

Many attempts to improve these wheel/rail contact laws can be found in the literature, taking into account several parameters like spin, surface roughness or other tribological effects. Validation of the proposed models with measurements or other models are often presented in the form of the curve in Fig. 1.19 in each direction of the creep force. An alternative consists in using the modulus of the friction force. Thus, saturation curves represent the relationship between the imposed creepages and the modules of the creep force combining the resulting lateral and longitudinal contact forces.

For Kalker's linear theory, this relationship is given by :

$$\begin{aligned} |F_t| &= \sqrt{F_x^2 + F_y^2} \quad \text{if} \quad |s_{to}| \leq 1 \\ F_t &= \mu F_n \quad \text{if} \quad |s_{to}| > 1 \end{aligned} \tag{1.66}$$

where:

$$s_{to} = \frac{1}{\mu F_n} \sqrt{\left(GabC_{11}s_{x_o}\right)^2 + \left(GabC_{22}s_{y_o} + G(ab)^{3/2}C_{23}s_{w_o}\right)^2} \tag{1.67}$$

For Vermeulen and Johnson's model, this relationship is given by :

$$\begin{aligned} |F_t| &= \left(1 - (1 - s_{to})^3\right) \mu F_n \quad \text{if} \quad |s_{to}| \leq 1 \\ F_t &= \mu F_n \quad \text{if} \quad |s_{to}| > 1 \end{aligned} \tag{1.68}$$

where

$$s_{to} = \frac{4Gab}{3\pi\mu F_n} \sqrt{(c_{11}s_{xo})^2 + (c_{22}s_{yo})^2}$$

To take into account the spin, Shen, Hedrick and Elkins [81] extended the Vermeulen and Johnson's model by using the expression s_{to} in Eq. (1.67) , due to Kalker's linear theory, to determine the resulting tangential force in Eq. (1.68). This model is considered suitable only for small spin calculations [77].

As an example, a similar but different law is proposed by Ayasse , Chollet and Pascal [82] from forces measurement in field conditions:

$$|F_t| = \left(1 - e^{-s_{to}}\right) \mu F_n \tag{1.69}$$

where

$$s_{to} = \frac{Gab}{3\mu F_n}\sqrt{(c_{11}s_{xo})^2 + (c_{22}s_{yo})^2}$$

Transient case

All models presented above are valid in the steady case. At high frequencies, Other phenomena appear due to the instantaneous terms in Eq. (1.54) and models have to be adapted. According to Knoth and Gross-Thebing [83], transient contact models should be used when the ratio of the characteristic motion wavelength L (related to frequency and depending on dynamic properties of wheel and rail) and the contact length a_1 in the rolling direction drops below ten. Knoth and Gross-Thebing [83] proposed frequency-dependent creepage coefficients by studying non-steady rolling contact in the case of small creepages (linear theory). For the lateral force, Thompson [3] showed that the frequency-dependence law is equivalent to a simple model which combines a contact stiffness at high frequency with a damper at low frequency. It is important to note that, in this case, the damper traduces the creep due to the Kalker linear theory whereas the stiffness corresponds to the lateral stiffness propose by Mindlin [84] to model the lateral force in Hertzian (non rolling) contact at high frequencies. This model is notably commonly used in rolling noise problems when creepages are small. However, a "nonlinear version" does not exist: no point contact model is adapted to problems combining high-frequency dynamics and high creepages.

1.3.3 Surface-contact models based on elastic half-space assumption

Like the finite element models presented in the following section, surface-contact models use a discretization of contact zone and calculations are performed at a local level (contact level). However, the general idea adopted in this type of models is that in the end, it is the average quantities (resulting forces) that are applied to the structures.

Hertz's hypothesis are not applicable when the contact curvature is not elliptic. A discretization of the contact is thus necessary to determine better contact variables. Piotrowski and Chollet [85], Piotrowski and Kik [86] and Ayasse and Chollet [87] developed semi-Hertzian contact models which can handle non-Hertzian cases where the curvature may vary in the transverse direction. These models are based on the virtual inter-penetration of the two bodies in the undeformed state. The distribution of the normal pressure is assumed semi-elliptical in the rolling direction. These models can take into account non-Hertzian conditions in the lateral direction. However, they only concern only the normal contact problem.

FASTSIM

Kalker [88] developed a simplified theory named FASTSIM which introduces a bedding of independent springs in the contact zone. The deformation of one point in the contact area is proportional to the traction at that the same point:

$$\begin{cases} u_x = u_x^W - u_x^R = L_x p_x \\ u_y = u_y^W - u_y^R = L_y p_y \end{cases} \tag{1.70}$$

where L_x, L_y are the flexibilities in $x-$ and $y-$ axis directions respectively. p_x and p_y are contact shear stresses in $x-$ and $y-$ axis directions respectively.

These flexibilities are identified by Kalker's linear theory. By combining Eqs. (1.55) and (1.70) and assuming that the contact zone is fully sticking: $s_{xs} = 0$; $s_{ys} = 0$, one has:

$$\begin{aligned} 0 &= s_{xo}/L_x - s_{wo}y/L_x - (\frac{\partial p_x^W}{\partial x}) \\ 0 &= s_{yo}/L_y + s_{wo}x/L_y - (\frac{\partial p_y^W}{\partial x}) \end{aligned} \tag{1.71}$$

By integrating Eq. (1.71) over the entire contact zone, the tangential forces F_x, F_y can be obtained and by comparing these forces with those in Eq. (1.65), L_1, L_2, L_3 will be identified for the three imposed creepages.

$$\begin{aligned} L_1 &= \frac{8a}{3C_{11}G} \\ L_1 &= \frac{8a}{3C_{22}G} \\ L_1 &= \frac{\pi a^2}{4G\sqrt{ab}C_{23}} \end{aligned} \tag{1.72}$$

The final system to be solved in the steady case is:

$$\begin{aligned} s_{xs}/L &= s_{xo}/L_1 - s_{wo}y/L_3 - (\frac{\partial p_x^W}{\partial x}) \\ s_{ys}/L &= s_{yo}/L_2 + s_{wo}x/L_3 - (\frac{\partial p_y^W}{\partial x}) \end{aligned} \tag{1.73}$$

where L is the averaged flexibility given by:

$$L = \frac{s_{xo}L_1 + s_{yo}L_2 + \sqrt{ab}s_{wo}L_3}{\sqrt{s_{xo}^2 + s_{yo}^2 + abs_{wo}^2}} \tag{1.74}$$

This approach is implemented in the algorithm FASTSIM developed by Kalker. The contact area is discretized in several trips parallel to the rolling direction. Each trip is then divided in several elements. Tangential stresses are assumed constant in each element and then evaluated by using Eq. (1.73).

This model is 1000 times faster but less accurate by at least 10% than the program CONTACT presented in the following paragraph. The main disadvantage is that FASTSIM is a steady-state model. Shen and Li [89], Alonso and Giménez [90] and Guiral [91] extended this theory to transient processes by including the transient term in the kinematic equation of the simplified model. Shen and Li used Kalker's flexibility coefficient for both steady-state and transient terms whereas Alonso and Giménez [90] and Guiral [91] used the dynamic flexibility coefficient by minimizing, for a range of wavelengths, the difference between the non-stationary Linear Theory of Knothe and Groß-Thebing [83] and the non-stationary FastSim of Alonso and Giménez [90]. These models proved to be in good agreement with CONTACT except in the case of significant spin.

Kalker's variational method and program CONTACT

Kalker proposed a theory which is a generalization of the principle of the virtual work for the resolution of the contact problem. The theory is detailed in [92]. The proposed approach is based on a variational formulation of the frictional contact problem and uses non-smooth frictional contact laws: Signorini's unilateral contact law and Coulomb's law. This theory is called "exact" because it is based on two basic conclusions of Fichera [93] and Duvaut and Lions [23]. Fichera [93] demonstrated the existence and uniqueness of the normal contact problem without friction by using the principle of virtual works. Duvaut and Lions [23] also uses the principle of virtual works to demonstrate the existence and the uniqueness of the tangent problem.

The contact problem can be solved with the variational approach which is based on the two inequalities, one of which derives from the principle of virtual works and the other from its dual, the principle of complementary virtual works [94, 95]. By introducing the equations of continuum mechanics, reducing the problem to the surface and satisfying the boundary conditions defined by Coulomb's law and the

principle of complementarity, the contact problem can be expressed as a minimization of the potential energy of the system or a maximization of the complementary energy of the system.

The relationship between contact forces and displacements due to linear elasticity in solids the following surface integral:

$$u_i(x) = \int\int_{S_c} G^{ij}(x,y)p_i(y)dS \tag{1.75}$$

where $i,j = x,y,z$ and $G^{ij}(x,y)$ is the influence (flexibility) function. This function represents the (quasi-static) displacement in x due to a load applied in y. It can be calculated explicitly in the case of the infinite elastic half-space approximation from the Boussinesq-Cerruti solutions.

The potential contact area is discretized into rectangular elements in which pressure and tractions are constant. The NORM algorithm solves the normal contact problem (without friction) and determines the contact shape and size, along with the normal pressure distribution. The solution of this normal contact problem is then used to solve the tangential contact problem and to determine tangential contact forces by using the TANG algorithm. "Active sets" algorithms are used in order to solve the complementary problems.

This theory can describe both hertzian and non-hertzian contact. It can be applied for steady-state or transient processes. The drawback is that the price of computation is high for the resolution of the tangential contact problem.

Hybrid model

In order to reduce this computation time, Zenzerovic *et al.* [96, 97] developed a point-contact model for the tangential problem by disregarding the spatial derivative $\frac{\partial u}{\partial x}$. The instantaneous contact displacement u_τ (defined as a mean quantity over the contact area) is obtained as:

$$u_\tau = A_\tau F_\tau, \quad \tau = x,y \tag{1.76}$$

The contact compliances A_τ are obtained by using the solution of the normal contact problem and the elastic half-space assumption and assuming the contact is in full-slip.

The tangential contact forces are finally obtained as:

$$F_t = -\mu_{RF}(s)F_n\frac{s_\tau}{s}, \quad \tau = x,y \tag{1.77}$$

where $s_\tau = \sqrt{s_x^2 + s_y^2}$ is the absolute slip creep velocity (also defined here as a mean quantity). The regularized friction model $\mu_{RF}(s)$ is the ratio between the resulting tangential force and the resulting normal force obtained by CONTACT program as a function of lateral creepage and contact position in steady conditions.

The global consideration of the contact avoids the discretization needed for the determination of the deformation term due to rolling $\frac{\partial u}{\partial x}$ and significantly improves computational efficiency. However the price for improved efficiency is the steady-state nature of the point-contact model [98].

1.3.4 Full finite element models

The common point of the wheel/rail contact models presented above is the use of the elastic half-space assumption, the decoupling of the normal contact problem and the tangential contact problem as well as the Eulerian frame in which equations are developed. The fact is that the effects of the elastic half-space assumption and the normal/tangential decoupling, especially in the case of high frequency dynamics have been little studied. Moreover, the use of the elastic half-space assumption does not allow to introduce the non-elastic material behavior. All theses difficulties can be overcome by using finite element models. Works dealing with wheel/rail contact analysis by FE methods exist but are quite recent. Bogdansky *et al.* [99] solved the normal problem of static elastic wheel–rail contact in three dimensions

with the FE method. The normal problem of contact of elastic-plastic material was investigated by Wiest *et al.* [100] with a 3D static FE model. Other solutions of the normal problem with FE can be found but the treatment of the tangential problem of wheel–rail rolling contact with FE is still rare. Interesting results are given in the study of Toumi [101] as well as the work of Zhao and Li [102] who treated wheel–rail rolling contact with an explicit FE method. By approaching a quasi-static state, the FE model is notably validated against Hertz theory and CONTACT in both normal and tangential solutions, for the case of wheel tread–rail head contact.

In these models, unlike those presented in the previous sections, dynamics and contact equations are solved in a Lagrangian frame. All the potential contact area in the rolling direction needs to be meshed with elements of sufficient small size to insure the desired precision. In addition, the meshes of the two potential contact surfaces are not compatible. As a consequence, the treatment of the contact is not straightforward. For instance, Wiest [100] and Toumi [101] used FE software ABAQUS/Standard where contact between the two bodies is defined using a strict "master–slave" algorithm. Between the two surfaces, a "master" surface and a "slave" surface have to be defined. There are then two types of contact discretization (node-to-surface and surface-to-surface) and the results differ depending on the user choice. The contact discretization "surface-to-surface" gives better results than contact discretization "node-to-surface" [103]. To deal with the unilateral contact and friction problems, both non-smooth and smooth frictional contact laws can be used. For the resolution of the nonlinear problem, the Lagrange multipliers method is generally used when the non-smooth frictional contact laws are chosen. Efficient algorithms exist for both formulations but, in any case, nonlinear transient FE simulations with frictional contact still remain very expensive in terms of CPU time and memory size.

Finally, the main disadvantage of the FE method is its computation cost. However, this cost seems to be due, to a large extent, to the choice of the Lagrangian frame. Indeed, this choice imposes significant constraints on the FE mesh which increases the size of the problem.

1.3.5 Inclusion of falling friction laws in wheel/rail models

As stated in section 1.1.2, the falling of the saturation curve is suspected to play a crucial role in the squeal generation mechanisms. Wheel/rail contact models presented above do not take into account this feature. Several works can be found on the subject but, for the most part, these studies are related to squeal problems. Therefore, in this review, they are presented within the part dedicated to squeal models.

However, it is worth noting that friction coefficient decreasing with the creepage s defined in Eq. (1.54) can be included simply in wheel/rail contact models presented above by changing μ in the equations of this section by $\mu(s)$.

1.4 Review and classification of curve squeal models

This section aims to review and classify existing curve squeal models on the basis of the following main criteria : Wheel and rail dynamics, Wheel/rail contact models including friction characteristic and Dynamics interaction combined with solution computation. This criteria correspond to the general structure of a curve squeal model as shown in Fig. 1.21. To be complete, it should be noted that some of the models are also extended with a stage dedicated to sound radiation computation that is not treated here.

1.4.1 Wheel and rail dynamics

1.4.1.1 Wheel dynamics

As most wheels have a strong modal behavior, the wheel dynamics are generally represented by a modal basis including a series of mode shapes, natural frequencies and modal damping factors. Boundary

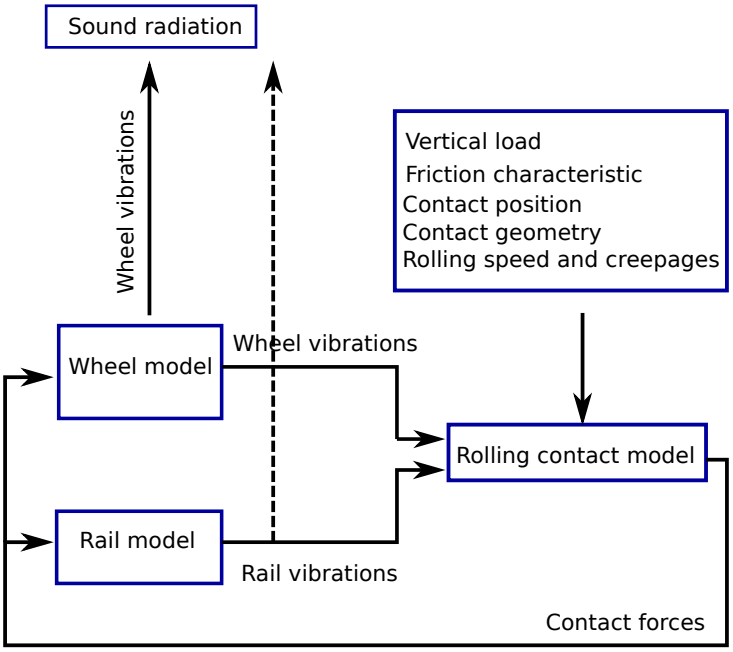

Figure 1.21: General structure of curve squeal models

conditions used to obtain the basis can vary concerning the connection with the axle and the rest of the vehicle but are always free with regard to the potential contact surface with the rail.

In the models of Rudd and Van Ruiten [6, 104], the wheel dynamics are represented by 1-DOF model with a modal mass m, a modal stiffness k and a damping c depending of the wheel motion during squeal. m is defined by the ratio between the mean kinetic energy of vibration and the mean square velocity of vibration at the contact point. k is defined by the ratio between the mean bending energy of vibration and the mean square displacement of vibration at the contact point. For a axial wheel mode, Rudd estimates that m lies between the third and the half of the mass of the wheel and k will vary approximately as the fourth power of the mode frequency. c is given by the sum of the internal and acoustic dampings, which can be neglected in most of the cases. :

$$c = \eta_{int} m\omega + \phi\rho_{co}A$$

where η_{int} is the internal loss factor, ϕ denotes the radiation efficiency , ρ_{co} represents the characteristic impedance of air and A is the surface of wheel.

In more recent models, the wheel dynamics is taken into account by contact mobilities obtained from the TWINS software [105], for instance in Debeer *et al.* [9], Xie *et al.* [106], Hsu *et al.* [107] and Squicciarini's models [108]. The vertical, lateral and vertical-lateral dynamics coupling is considered leading to mobility matrices rather than algebraic mobilities. In order to compute the mobilities, a modal basis is first determined by using the finite element method. The frequency responses of the wheel are then predicted in TWINS by using a modal summation including the effects of wheel rotation, since the coupling with the rail is considered in an Eulerian frame (cf. section 1.4.3).

Schneider *et al.* [109], Fingberg [110], Periard [111], Chiello *et al.* [112], Glocker *et .al* [12], Pieringer [113], Zenzerovic *et al.* [96] and Ding *et al.* [19] also modeled the wheel by using the FE method. The wheel is then represented by a modal basis in the whole model. The wheel displacement discretized response $\mathbf{U}$ is approximated by an expansion on the modal basis Φ :

$$\mathbf{U} = \Phi\mathbf{q} \tag{1.78}$$

where $\mathbf{q}$ denotes the unknown generalized coordinates vector.

Heckl *et al.* [114] used an analytical wheel model represented by a annular disc clamped the center edge. Only the lateral dynamics was considered. Modal superposition and truncation is also performed but with analytically calculated modes.

Brunel [115, 116] also used a wheel model characterized by wheel modes determined by the finite element method. In [115] a three-dimensional finite element model is used. In [116], in order to reduce the computation times, a two-dimensional axi-symmetric model is proposed. The third dimension (circumferential coordinate) is then added by using a Fourier transformation to define displacements and contact forces.

To deal with boundary conditions of the wheel in finite element models, a rigid constraint is applied on the hub in most of the models. However, in order to correctly represent the low-frequency behavior, a rigid body mode of the complete wheelset including the primary suspension is sometimes considered (cf. [97, 113] for instance).

1.4.1.2 Rail dynamics

Unlike the wheel, the rail is an infinite structure in the longitudinal direction. This fundamental property induces some advantages but also some drawbacks. The main advantage is that the rail can be modeled using beam-like structures in a wide frequency range, for which analytical or semi-analytical solutions exist. Cross-sectional deformations have to be taken into account only at high frequencies at which numerical (discretization) methods have to be used. The drawback is that the vibratory behavior is not modal but is essentially the result of waves propagating in the longitudinal direction. This is not a problem in the case of equations formulated in terms of point mobilities in the frequency domain but this can be unfavorable to other methods like time-domain modeling or model reduction.

Considering that the effects of the rail could be neglected due to the high flexibility of the wheel at squeal frequencies, the rail dynamics was not included in Rudd [6], Van Ruiten [15], Schneider *et al.* [109], Heckl *et al.* [114, 117], Chiello *et al.* [112], Brunel *et al.* [116] or Glocker *et al.* [12].

The rail vertical and lateral dynamics was included through point mobilities obtained from the TWINS software [105] in Debeer *et al.* [9], Xie *et al.* [106], Hsu *et al.* [107] and Squicciarini [108]'s models. There are three available modules in TWINS for the track dynamics. In case of ballasted tracks, the first two modules use analytical models of a Timoshenko beam in vertical and lateral bending, mounted on a two-layer continuous (Rodel) or periodic support. Pads and ballast are modeled by springs whereas sleepers are considered as rigid masses. The damping of the pads and ballast is taken into account by structural loss factors rather than viscous dampers. The third module allows the track to be modeled as a continuously-supported rail but in addition it allows deformation of the rail cross-section to be included. This is particularly important at high frequencies (above 1 or 2 kHz). A short length of rail, modeled using finite elements, is joined end to end to form an infinite model using periodic structure or transfer matrix theory. As well as the rail, the pad, sleeper and ballast are also included using finite element matrices [118]. However, since the support is continuous , this last model can not predict the behavior associated with the "pinned- pinned" effect. Indeed, depending on the location of the excitation, resonances or anti-resonances occur at frequencies when the half of the wavelengths of the propagating waves in the rail are close to the length of the sleeper span.

In Fingberg's model [110], the rail is described using Timoshenko beam models on a two -layer continuous support. Lateral (bending) and longitudinal dynamics are taken into account. However, a modal rail model is finally used in the squeal simulation. Parameters of the modal model are identified using least-squared approximations. In Périard's model [111] a discretely supported rail is included. The rail modal parameters are obtained from a finite FE model.

In Pieringer [113] and Zenzerovic *et al.* [96, 97]'s models, the lateral, vertical and longitudinal rail dynamics are modeled using waveguide finite elements (WFE) [119]. Considering that the rail has a constant cross-section in $x-$direction, a wave-type solution is assumed along the rail. For an harmonic time dependence $e^{i\omega t}$ with ω is a given frequency and a point force at $x = 0$, the amplitude of the

displacement of the rail can be formulated as a superposition of waves:

$$\begin{bmatrix} u_x \\ u_y \\ u_z \end{bmatrix} = \mathbf{N}(y,z)\hat{\mathbf{U}}(x) = \mathbf{N}(y,z)\sum_n A_n(\mathbf{F_o})\tilde{\mathbf{U}}_n e^{-ik_n x} \tag{1.79}$$

where $\hat{\mathbf{U}}(x)$ is the vector of nodal displacements and $\mathbf{N}(y,z)$ are two-dimensional FE shape functions. The eigenvectors $\tilde{\mathbf{U}}_n$ correspond to cross-sectional wave shapes. k_n is the complex wavenumber and includes propagation and decay characteristics of the waves along the rail. $\mathbf{F_o}$ is the force vector formulated in the wavenumber domain and $A_n(\mathbf{F_o})$ is given in [119]. The model takes into account the cross-sectional deformations of the rail. However, in this model, the support is continuous. It can not predict the behavior associated with the "pinned- pinned" effect.

Finally, Ding *et al.* [19] uses both analytical and modal track models with updated parameters. In the analytical model, the vertical mobility is determined by using a beam on two-layer support. The lateral mobility of railway track is computed by using the multi-beam model developed by Wu and Thompson [120]. Torsional motion of the rail is also modeled by using a Timoshenko beam model [121]. The analytical models are used for the stability analysis (frequency domain) but are not suitable to the step-by step integration in the time domain. An equivalent modal track model is adopted instead, which is based on a multi-degree of freedom mass-spring system. In addition, structural damping has also to be forsaked and replaced by a viscous damping in the modal model. According to Thompson [3], a viscous damping coefficient C can be chosen by equaling it to the required structural damping value at the corresponding rail/pad cut on frequency:

$$C = \frac{k\eta_s}{\omega_o} \tag{1.80}$$

where k is the stiffness, η_s is the structural damping factor and ω_o is the modal frequency. The resulting modal model is not in good agreement with the analytical model at high frequencies because of the reflexions provided by the modal model. For a better match, an "virtual" extra mode is added. Using this mode, the modal model match well with the analytical model for lateral and vertical bending but not for torsional vibration.

1.4.2 Contact models and friction characteristics

In most of curve squeal models, point and surface contact models presented in sections 1.3.2 and 1.3.3 are used in order to take into account the effects of wheel/rail contact. However, dynamic formulations are obtained by adapting quasi-static formulations at a global level. Dynamic laws are simply derived by using dynamic creepage s in spite of quasi-static ones s_0 by adding a global velocity term due to the vibration of the structures. In many models, a decreasing friction coefficient is also considered in order to model the instabilities leading to squeal as explained in section 1.2.2.1. In the models of Rudd [6] and Van Ruiten [104], only lateral dynamic is considered. F_n is the load on the wheel and is maintained constant. The vertical force F_n and lateral force F_t are coupled by using a simplified creep curve:: $F_t = \mu(s)F_n$ where $\mu(s_y)$ is an apparent global friction coefficient taking into account the main features of the creep curve through an analytical expression. For the small lateral creepage s, friction coefficient is proportional to creepage. It reaches a maximum μ_o after which it decreases:

$$\mu = \mu_o\,(s/s_o)\exp(1-s/s_o) \tag{1.81}$$

where s_o is the creepage such that $\mu = \mu_o$.

In the contact models of Heckl *et al.* [114, 117], only lateral degree of freedom is considered. The normal contact force is maintained constant. In the tangential problem, two friction characteristics are

considered expressed in terms of creep velocities rather than creepages. A linear friction characteristic [114] is assumed for the stability analysis:

$$F_t = F_0 + \gamma \Delta V_y$$

and a piecewise linear friction characteristic [114, 117] for the nonlinear simulation::

$$F_t = \begin{cases} F_0 + \gamma \Delta V_y \text{ for } \Delta V_y < V_{crab} - \Delta V \text{ and } \Delta V_y > V + \Delta V \quad \text{(slip)} \\ \Gamma(\Delta V_y - V) \text{ for } \Delta V_y \in (V_{crab} - \Delta V, V_{crab} + \Delta V) \quad \text{(stick)} \end{cases} \tag{1.82}$$

where γ is slope of the curve in the slip section, Γ is the slope of the curve in the creep section. V_{crab} is the crabbing speed representing sticking and ΔV is the the narrow velocity interval which encloses the stick section of the friction characteristic. ΔV_y is the wheel lateral velocity. F_o is equal to the vertical force applied at the contact point by the weight of the disc.

Schneider *et al.* [109] also considers the lateral degree of freedom. and the normal contact force is maintained constant. In the tangential problem, the friction is described by Kraft's falling friction model [122] given by:

$$\mu(s) = \mu_{\text{ statique}} \{1 - 0.5e^{-0.138/|\Delta V_y|} - 0.5e^{-6.9/|\Delta V_y|}\} \tag{1.83}$$

where $\mu_{\text{ statique}}$ is the static coefficient of friction and ΔV_y is the lateral creep velocity.

Brunel *et al.* [115, 116] considers only the lateral degree of freedom at contact level and the normal contact force is maintained constant. In the tangential problem, two types of friction–velocity relation are considered from experimental measurements performed by Kooijman [14]. One friction law shows negative friction–velocity slope whereas the other shows positive friction–velocity slope.

Fingberg [110] considers lateral and longitudinal degrees of freedom at contact. The normal force is assumed constant. Kalker's linear theory extended with the dynamic first-order corrections proposed by Knothe and Grob-Thebing [83] is used to take into account transient contact conditions during squeal. However, the details of the time-domain implementation are not provided. The friction law of Kraft Eq. (1.83) is included.

Debeer *et al.* [110] considers vertical and lateral dynamics at contact. Hertz's theory is assumed for the normal problem. Kalker's linear theory is used for the tangential problem. In the slip zone, the friction law of Kraft Eq. (1.83) is included. Hsu [107] applied de Beer's model [110] in the case of a constant normal contact force.

Chiello *et al.* [112] consider lateral and vertical degrees of freedom at contact. In the normal contact problem, a nonlinear Hertzian dynamic vertical force is used. The nonlinear dynamic normal and tangential contact forces are coupled by using the creep-friction curve proposed by Chollet *et al.* [82] (Eq. (1.69)) but with a friction coefficient decreasing linearly with the dynamic lateral creepage.

$$\mu(s) = \mu_o + \gamma V |s_{yo} + \frac{\Delta V_y(t)}{V}| \tag{1.84}$$

where $\gamma < 0$ is the slope of the friction coefficient with the lateral creepage.

Périard [111] considers lateral, vertical, longitudinal and spin degrees of freedom at contact. For the normal problem, Hertz's theory is used whereas for the tangential problem, FASTSIM and Vermeulen and Johnson's models are used.

For curving behavior simulations, the model proposed by Xie *et al.* [106] uses Kalker's FASTSIM program to solve the contact problem. The model considers lateral, longitudinal and vertical degrees of freedom at contact. A linear falling friction model is used to reduce the computational effort:

$$\mu = \begin{cases} \mu_s \text{ if } s = 0 \\ \mu_s - \dfrac{\mu_s - \mu_d}{s_c}|s| \text{ if } 0 < s < s_c \\ \mu_d \text{ if } |s| > s_c \end{cases} \tag{1.85}$$

where μ_s, μ_d are the static and sliding friction coefficients respectively and s_c denotes the critical creepage.

Huang *et al.* [123] consider the lateral, vertical, longitudinal and spin degrees of freedom at contact. To calculate the contact force, the FASTSIM algorithm is adopted for values of creepage up to saturation. After saturation, the following heuristic expression is adopted:

$$\mu(s) = \left(1 - c_{mu} e^{\kappa/|s|}\right) \mu_s \tag{1.86}$$

where c_{mu} is the falling ratio and κ is the saturation coefficient.

Glocker *et al.* [12] consider the lateral, vertical and longitudinal degrees of freedom at contact. The wheel–rail contact is modeled as a hard unilateral constraint with spatial Coulomb friction and constant friction coefficient μ. The contact law does not take into account any elasticity. It may theoretically allow loss of wheel/rail contact but such events do not occur in the simulations. As a result, the used normal contact model traduces a bilateral contact law.

Squicciarini [108] extends Hsu's model to account for two-point contact in the case of flange contact between the outer wheel and the rail. The model takes into account displacements in lateral, vertical, longitudinal and spin directions. Hertz's theory is used for the normal contact problem. Kalker's FASTSIM is used for the tangential problem. Friction law is chosen from Huang's model [123].

Ding *et al.* 's model [19] consider the lateral, longitudinal, vertical and spin dynamics determined by using FASTSIM at contact. Friction law is chosen from Huang's model [123]. The model includes both falling friction law and constant friction law.

Pieringer [113] considers the longitudinal, lateral and vertical dynamics at contact. The Kalker variational theory is used for the contact problem. Friction coefficient is assumed constant. There is a loop between the contact calculation and the global calculation but in the end, resulting contact forces are applied to the structures.

Zenzerovic's work [96, 97] is based on Pieringer's model [113]. However, a point-contact model is used for the resolution of the tangential contact problem to reduce the computational effort. Friction coefficient is also constant. In [97], the effects of the contact angle of the wheel/rail system about the vertical axis can be included. In this case, the contact coordinate system in which the contact problem is solved and the wheel/rail coordinate system in which the wheel and rail displacements are determined are not the same. The origins of the two systems are coincident and the vertical z-axes are the same.

Finally, Brunel [124] uses a FE model with discretization of the contact zone. Friction coefficient is supposed to be constant. Penalty method which is a linear regularization of the frictional contact laws is used to solve the contact problem. In this model, the lateral, vertical and longitudinal degrees of freedom are considered.

1.4.3 Dynamic interaction and solution computation

Combining the wheel and rail dynamics with the wheel/rail contact models, a full dynamic interaction model is obtained. A main characteristic of the whole model is the coupling type at the contact described in the previous section. In some models, by maintaining the constant normal contact force, there is only lateral dynamic [6, 104, 107, 109, 114–117] or the coupling between lateral and longitudinal dynamics [110]. The coupling between lateral and vertical dynamics are present in [9, 112]. The common point of these models is the used of point-contact models. The coupling among lateral, vertical and longitudinal dynamics in [12, 96, 97, 106, 111, 113, 124] and coupling among lateral, vertical, longitudinal and spin dynamics in [19, 108, 123] are applied when contact models are more complex such as FASTSIM, Kalker's variational method, Zenzerovic's hybrid model or full finite element models. Except for full finite element model, the dynamic coupling is performed among the resulting contact forces. It means that the dynamic coupling occurs among maximum 4 degrees of freedom of contact : lateral, vertical, longitudinal and spin. This small number allows some authors to condense the problem on these contact degrees of freedom to solve the problem (cf. Nyquist's criterion in stability or convolution in time domain in the next sections).

Another characteristic of the interaction model is the type of frame reference. Almost models are performed in the Eulerian frame except Brunel's finite element model [124] which is derived in a Lagrangian frame. A major consequence of the Eulerian frame is to induce convective terms in the equations of motion by wheel rotation. These terms are only significant in the case where the rotational speed is in the order of magnitude of the natural pulsations. This is generally not the case in squeal situations ([3,125]). Thus, the majority of models neglect the convective effects. The other characteristics of the interaction model are the kind of solutions sought and the resolution methods used. In particular, frequency-domain linear solutions corresponding to stability analysis and time-domain nonlinear solutions can be distinguished.

1.4.3.1 Stability analysis and frequency-domain solutions

In curve squeal models, stability analysis is performed by linearizing the non-linear equations induced by wheel/rail contact. This approach provides unstable modes and corresponding frequencies. In existing models, this analysis is generally proposed only in the case of point-contact models.

Firstly, all nonlinear contact variables need to be linearized. For the normal problem, except for some models [6,104,117] considering a constant contact force, Hertz's theory is used for point-contact models. The linerization of the non-linear relation between the dynamic penetration $\delta + u_n(t)$ and the dynamic normal contact force $F_n + f_n(t)$ in Eq. (1.60) gives Hertz contact spring k_H :

$$\frac{1}{k_H} = \frac{du_n}{df_n}|_{u_n=0} = \frac{\xi}{2}\left(\frac{2}{3E'^2 F_o R_o}\right)^{1/3} \tag{1.87}$$

For the tangential problem, coefficient of friction μ depending on creepage s must be linearized:

$$\mu(s_o + \frac{v(t)}{V}) = \mu(s_o) + \frac{\partial \mu}{\partial s}|_{s_o}\frac{v(t)}{V} \tag{1.88}$$

where $v(t)$ is the transient creep velocity. This term leads to a equivalent (positive or negative) damping since it relies the dynamic tangential force to the dynamic tangential velocity.

Finally, the linerization of the relation between the dynamic tangential contact force $F_t + f_t(t)$ and the dynamic penetration $\delta + u_n(t)$ gives a contact spring:

$$k_{tn} = \frac{\partial f_t}{\partial u_n} = k_H \frac{\partial f_t}{\partial f_n} \tag{1.89}$$

The spring is called the vertical/lateral cross-stiffness [112] and induces a stiffness matrix asymmetry in the system. This stiffness depends on the contact state. In the case of full sliding contact, this tangential contact spring is equal to $\mu(s)k_H$. However, in the case of creep contact, it is more complicated because Kalker's creep coefficients also depend on the dynamic normal contact force $F_n + f_n(t)$.

The linearized contact variables are then substituted in the equations governing the mechanical system. There are two main approaches to solve the problem.

Modal approach

Some models [6, 16, 104, 112] use the modal approach in the case where the rail dynamics is not included or identified in a modal form. The wheel model can also be represented by using a reduction basis Φ which can include one normal mode [6,104,112], 2 normal modes [16] or several normal modes [12,112]. By using the modal approach, the overall linearized equation of motion can then be formulated:

$$\mathbf{I}\ddot{\mathbf{q}} + (\Xi - C_f)\dot{\mathbf{q}} + \left([\omega_i^2] + K_f\right)\mathbf{q} = 0 \tag{1.90}$$

where $\mathbf{I}, \Xi, [\omega_i^2]$ are the generalized mass, damping and stiffness matrices. $\mathbf{I}$ is an identity matrix when Φ is normalized with respect to mass. $[\omega_i^2]$ is a diagonal matrix where the diagonal are squared natural

frequency ω_i. $\mathbf{q}$ are unknown generalized coordinates vector. C_f is the matrix resulting from the linearization of friction force with dynamic creep [6, 16, 104, 112] or the direction of the friction force [12]. It can be non positive in case of sliding equilibrium in the falling friction zone. $\mathbf{K_f}$ is a (potentially non symmetric) stiffness matrix induced by cross-stiffness. If the reduction basis includes only a wheel mode, $\mathbf{K_f}$ is then a real positive scalar and can not be a factor of instability.

The stability can be deduced from a complex eigenvalue analysis of system Eq. (1.90). A complex mode is then unstable if and only if the real part of the corresponding complex eigenvalue is positive. If the reduction basis includes only a wheel mode [6, 104, 112], the stability may be found by comparing the wheel mode damping Ξ with the negative damping C_f due to the falling friction law.

Nyquist criterion

Other models [9, 19, 106–108, 112, 117, 123] performed stability analysis in the frequency domain by applying the Nyquist criterion [3]. By combining the wheel dynamics, rail dynamics and contact dynamics, a linearized self-excited vibration loop can be obtained (Fig. 1.22). Matrix $\mathbf{H_1}$ gives the linearized effect from the fluctuation of normal force on the friction forces whereas matrix $\mathbf{H_2}$ gives the linearized effect from the fluctuation of creep velocities on the friction forces. Stability analysis can be studied using the open loop transfer function of the self-excited vibration loop $\mathbf{H_{loop}} = \mathbf{H_1} + \mathbf{H_2}$. The system is unstable for frequencies where the Nyquist contour $\mathbf{H_{loop}}$ passes the real axis at the right-hand side of 1.

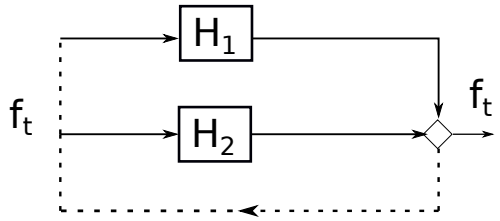

Figure 1.22: Linearized self-excited vibration loop of the wheel/rail contact system

1.4.3.2 Time-domain solutions

Time-domain models have the ability to include non-linearities present in the wheel/rail system and to determine the amplitudes of the self-sustained vibrations leading to squeal noise. Full harmonic components in the system response can also be
determined.Two methods have been used in order to determine these solutions for curve squeal: time numerical integrations and temporal convolution using Green functions. Details on these methods are given below.

Time integration schemes

Schneider *et al.* [109], Huang *et al.* [123], Ding *et al.* [16, 19] and Chiello [112] apply modal transformation techniques to determine the temporal solution. Time integration is performed by using the Runge-Kutta schemes for the modal degrees of freedom.

Fingberg [110] uses modal transformation techniques leading to a set of differential equations for rail and wheel which are coupled by the non-linear lateral and longitudinal creep forces. A integrator of Adams-Moulton [126] is used for the time integration of the equations.

Périard [111] extends Fingberg's model [110] including simulations of the vehicle curving behavior. The integrator of Adams-Moulton [126] is used to integrate the set of differential equations governing the dynamics of the vehicle whereas the inegrator of Newmark-beta is used to the equations governing the vibrations of the wheelset and the waves in the track.

Glocker *et al.* [12] also use modal transformation techniques to determine the temporal solution. By considering non-smooth frictional contact laws, Moreau's first order time integration scheme [127] is applied consisting of of a midpoint rule for the positions and an Euler backwards step for the velocities.

The initial conditions in transient simulations are not detailed in Huang *et al.* [123], Ding at al [16, 19], Fingberg [110] and Périard [111] 's work. In Schneider *et al.* 's work [109], the initial velocities are set to zero and the initial displacement are equal to the quasi-static displacement multiplied by a factor. In Chiello *et al.* work [112], the initial displacements are zero and the initial lateral velocity represents 10% of the sliding velocity ΔV_y with the same contributions of modes (a,0,n_d). Glocker *et al.* [12] use the unstable quasi-static equilibrium as initial conditions.

Temporal convolution using Green functions

Green's functions and convolution are used byHeckl *et al.* [114], Pieringer [113] and Zenzerovic *et al.* [96, 97] in order to determine the time solution. The displacements at the contact point are calculated by convoluting the contact forces with Green's functions:

$$u_c^j(t) = \int_0^t \sum_i F_i(\tau) g_{ij}(t-\tau) d\tau, \quad i,j = x,y,z \tag{1.91}$$

where g_{ij} are the impulse response functions (or Green's functions). g_{ij} is defined as the time response of the system at i-DOF due to the unit point forcing at at j-DOF. To include the motion of the nominal contact point along the rail, these functions describe the response at a point $x + V\tau$ moving with the rolling velocity V along the rail away from the excitation at x. These functions may be obtained by inverse Fourier transform from the wheel or rail receptances [96, 97, 113].

The use of Green's functions and convolution gives a significant advantage in computation time over numerical integration techniques in the case of a low number of degree of freedom in the contact zone. Thus, this approach shows only the advantage for point-contact models or surface contact models where the contact forces applied in the structures are the resulting forces.

1.4.4 Synthesis

Curve squeal models are summarized in Tab. 1.1 according to the above criteria and the frame in which equations are solved. The wheel dynamics are taken into account in all models whereas the rail dynamics are ignored in some models. Contact models are diverse including point-contact models, surface-contact models based on elastic half-space assumption or finite element method. Concerning the friction characteristics, some models considered only falling friction, only constant friction or both friction models. Solution computations were performed in time or frequency domain or both domain. The majority of models solve equations in the Eulerian frame whereas only FEM model [124] is performed in a Lagrangian frame.

1.5 Main results of curve squeal models

The results provided by the curve squeal models presented above are numerous. This section is an attempt to summarize the main results in order to perform a critical analysis and suggest improvements.

1.5.1 Instability mechanisms and characteristics of the unstable modes

An important point is the difference between the results according to the focused instability mechanism. All the models [6, 9, 19, 104, 109–112, 114, 117] show that a falling friction law can generate instabilities of wheel/rail contact. The unstable frequencies found are generally close to axial wheel modes with 0 nodal circle.

Models	Rail dyn.	Wheel dyn.	Contact model	Friction coef.		Domain		Ref. frame	
Rudd [6]		×	PC	falling			Freq	El	
Van Ruiten [104]		×	PC	falling			Freq	El	
Fingberg *et al.* [110]	×	×	PC	falling		Time		El	
Debeer *et al.* [9]	×	×	PC	falling			Freq	El	
Xie *et al.* [106]	×	×	FASTSIM	falling			Freq	El	
Hsu *et al.* [107]	×	×	PC	falling			Freq	El	
Heckl *et al.* [114]		×	PC	falling		Time		El	
Heckl *et al.* [117]		×	PC	falling			Freq	El	
Huang *et al.* [123]	×	×	FASTSIM	falling		Time		El	
Chiello *et al.* [112]		×	PC	falling		Time	Freq	El	
Brunel *et al.* [116]		×	PC	falling		Time		El	
Brunel *et al.* [115]		×	PC	falling		Time		El	
Brunel [124]	×	×	FEM		cst	Time			Lg
Glocker *et al.* [12]		×	PC		cst	Time	Freq	El	
Pieringer [113]	×	×	KKVT		cst	Time		El	
Zenzerovic *et al.* [96]	×	×	KKVT-PC		cst	Time		El	
Zenzerovic *et al.* [97]	×	×	KKVT-PC		cst	Time		El	
Ding *et al.* [19]	×	×	FASTSIM	falling	cst	Time		El	
Ding *et al.* [16]		×	PC	falling		Time	Freq	El	
Navarro *et al.* [128]	×	×	KKVT		cst	Time		El	

Table 1.1: Classification of curve squeal modes (PC: point-contact model, KKVT: Kalker's variational theory, KKVT-PC: Kalker's variational theory for the normal contact and point-contact model for the tangential contact, Freq: frequency, El: Eulerian, Lg: Lagrangian)

However, Brunel [116] obtained squeal even if the friction law is positive. He concluded that squeal is due to the coupling of the normal and lateral dynamics by the Poisson ratio of the wheel material (sprag-slip phenomena).

In the case of constant friction coefficient and rigid rail, Glocker *et al.* [12] found that squeal occurs with a number of wheel modes which has to be present with closely spaced natural frequencies: one axial mode with zero nodal circles and two radial modes of the wheel. Ding *et al.* [16] also demonstrated that a mode-coupling instability can occurs and there is a difference between the squealing frequency and the natural frequency of the wheel modes.

In the case of constant friction coefficient and flexible rail, Pieringer [113], Zenzerovic [96, 97] showed that curve squeal can occur due to coupling of the normal and lateral dynamics of a single wheel mode.

Finally, Ding *et al.* [19] found out that the dynamic rail plays an important goal by suddently changing the stability of the system in the case of constant friction coefficient. If the rail dynamics is not included, the unstable frequencies seem to be caused by the coupling of some wheel modes. Otherwise, almost unstable frequencies get close to axial wheel modes with 0 nodal circle. Ding *et al.* concluded that this is due to coupling of the normal and lateral component of the single wheel mode, when the flexibility of normal contact is changed by the rail dynamics.

1.5.2 Characteristics of the self-sustained vibration

Another major point is the type of vibration obtained with the nonlinear time-domain models. All time-domain models [12, 16, 19, 109–112, 116, 123, 124] showed that the self-sustained vibration converges to a periodic limit cycle. The wheel lateral vibration velocity amplitude at the contact does not exceed the imposed lateral creep velocity ΔV_y [112, 114]. Because of nonlinearities, the full spectrum of the limit cycle includes not only the unstable frequencies but also their harmonic frequencies.

According to Chiello [112], three phases can be distinguished in the time solution:

- In the linear phase, the lateral velocity increases until it reaches approximately the imposed lateral creep velocity ΔV_y,
- In the case of several unstable modes, the modes are in competition in a transient phase until one mode becomes dominant,
- In the stationary phase, the solution converges to a periodic creep/slip limit cycle.

However according to [96, 113], several unstable frequencies may co-exist in the final solution.

1.5.3 Effect of main parameters on stability and self-sustained vibration

Other results concern the effects of the main parameters. In existing models, three kind of key parameters can be identified: kinematics parameters, friction characteristics and wheel modal damping factors.

The imposed lateral creep velocity ΔV_y, the angle of attack α and the contact position are the three most investigated local parameters. By stability analysis [10, 112] or by transient analysis [96, 97, 113], a critical angle of attack α above which squeal occurs is obtained. Xie *et al.* [106] showed that the front inner and outer wheels whose the angle of attack is greater than other wheels are prone to squeal. The critical angle of attack is 15 (mrad) according to Chiello *et al.* [112] and 8 (mrad) according to Liu et al. [10]. Van Ruiten [104] and Hsu et al. [107] found that an increase of the angle of attack means a growth of the amplitude of the vibration. Pieringer [113] and Zenzerovic et al. [96] also found the strong influence of the angle of attack on squeal noise level. However, the direction of the angle of attack is also important. In their models, squeal almost occurred in the inner wheel/rail contact. The wheel lateral vibration velocity amplitude at the contact does not exceed the imposed lateral creep velocity

ΔV_y [112, 114]. Thus, this imposed lateral creep velocity decides the sound level of curve squeal. The contact position was investigated by Debeer *et al.* [9], Pieringer et al. [113] and Zenzerovic *et al.* [96]. Debeer et al. found that squeal can occur when the contact position is more toward to the wheel flange whereas Pieringer and Zenzerovic et al. obtained a contrary result.

Several models [16,96,107,113] showed a strong influence of the friction coefficient. In the majority cases, an increase of this coefficient means an increase of the occurrence of squeal. However, in [96,113], il exists some simulations showing that an increase of this coefficient may reduce the squeal noise level. In case of falling friction law, a key parameter is the negative slope of the law. An increase of the slope amplitude make the system more unstable et favors the squeal occurrence.

Rudd [6], Chiello et al. [112] and Huang *et al.* [123] studied the wheel damping modal factor which can eliminate curve squeal. This factors is about 6% according to Rudd [6], 2% according to Chiello *et al.* [112] and 0.5% according to Huang *et al.* [123]. Huang *et al.* [123] considered that the value can be greater in practice (above 1.3%).

1.6 Strategy of the thesis

In this chapter, curve squeal phenomenon and models able to simulate these phenomenon have been presented. Although longitudinal wheel slip and wheel flange contact have originally been cited as a cause of curve squeal, most of mechanisms proposed in literature put forward the high lateral slip of the wheel on the rail-head as the main input origin of curve squeal. The curve squeal can be then developed due to instabilities linked to friction leading self-sustaining vibrations.

1.6.1 Main issues

Two major questions stand out from the literature review concerning the instability mechanism and the modeling of the wheel/rail rolling contact.

Instability mechanisms

In the case of friction coefficient decreasing with creep velocities, the phenomena are rather straightforward. Instability is caused by the negative damping introduced by the slope of creep/friction curve for large creepages. The results of the models correspond well to experimental observations such as instabilities of axial modes with zero nodal circle and creep/slip limit cycles. However, the slope of the friction coefficient is not really proved in experimental terms. In dynamics, it is difficult to measure the dynamic creep quantities (especially contact forces) and the dynamic curve is not accessible. So one may wonder whether the addition of this slope is not artificial but not physical means to bring out the instability.

In the case of constant friction coefficient and providing that the rail dynamics is taken into account, one can also find results consistent with experimental observations such as instabilities of axial modes with zero nodal circle and creep/slip limit cycles [19, 96, 97, 113]. However, the mechanisms behind this instability are not clear. It seems that there is no mode coupling and that the influence of the rail is crucial. These mechanisms should therefore be studied more closely.

Modeling of the wheel/rail rolling contact

For the modeling of the wheel/rail rolling contact, equivalent point-contact models can theoretically only be used in quasi-static computations with smooth surfaces, even in the case of large slips. In other cases, including large slips and high-frequency dynamics, surface contact models are more adapted. However, some simplifications are generally performed in these models, especially in the semi-analytical computation of the local contact flexibilities or influence functions (Boussinesq and Cerruti elastic half-space assumptions, contact/friction decoupling). The impact of these simplifications is rather unknown

in the case of friction-induced vibrations in curves characterized by large slips, high frequency dynamics and very fast evolutions in the contact zone. On the other hand, the finite element method can deal with several different wheel/rail profiles and can take into account many effects. However, existing FE models are actually performed in a Lagrangian reference frame, which greatly limits their performance. As a consequence, they are rarely used in the case of high frequency dynamics.

1.6.2 Objectives

Considering these two main issues, the objectives of the thesis are the following:

- Develop models allowing to analyze and to understand the instability mechanisms responsible for curve squeal.
- Develop models allowing to take into account the wheel/rail contact in a discretized way with a strong dynamic coupling with the structures without simplifying assumptions. The models will be able to validate the existing models, to analyze the characteristics of self-sustained vibrations and eventually take into account more phenomena (non-Hertzian contact, plasticity, macro roughness).

1.6.3 Main assumptions

In this thesis, some general assumptions are made as follows:

- The local friction coefficient is assumed to be constant.
- The cases with the highest occurrence probability of curve squeal will be studied. With regards to the surface geometry, non-conformal contact which occurs in wheel tread/rail head contact is considered. In this case, flange rubbing is naturally excluded. For stability analysis, the case of full sliding in the effective contact zone is considered.

1.6.4 Methodology and structure of the thesis

The thesis is divided into two main parts corresponding to the two above objectives.

Part 1

Part I is dedicated to the clarification of the mechanism responsible of curve squeal noise in wheel/rail frictional rolling contact. By using a point-contact model and wheel/rail modal bases, a stability analysis is performed around the equilibrium state. The normal contact problem is assumed to be Hertzian. A constant Coulomb's friction law is used in the tangential problem. Only full sliding equilibrium states are assumed. Chapter 2 presents a stability analysis of wheel/rail contact in curve with wheel/rail finite element models including longitudinal,lateral and vertical dynamics. Potential instabilities are analyzed and distinguished through the use of bifurcation curves. The effects of damping, rail dynamics, structural and kinetic parameters are also studied. In order to examine in detail one kind of instability, Chapter 3 proposes a simple semi-analytical 1-dof model which is based on the results provided by Chapter 2. The contact model is similar but the wheel dynamic is represented by only one free-interface normal mode. The rail dynamics is modeled by a complex stiffness which is determined by an analytical model. Due to the simplicity of the model, the parameter study can be performed analytically. This is useful to clarify outstanding issues of chapter 2.

Part 2

The point-contact model developed in Part 1 can predict unstable modes of the wheel/rail system in curve. However, it does not allow to compute nonlinear self-sustained vibrations. For this purpose, a full finite element model of wheel/rail contact is developed in part II. This model is useful to calculate reference solutions and verify the simplifications of point-contact models, especially in the case of strongly nonlinear high-frequency creep behaviors. A rolling contact model between two elastic bodies using the finite element method and a discretized contact surface is developed in Chapter 4. The approach is performed around the stationary position in an Eulerian reference frame. Non-smooth unilateral Signorini's and Coulomb's friction laws with constant friction coefficient are used. A weak Lagrangian formulation and a resolution by a fixed-point algorithm allows reasonable computation times. In dynamic conditions, a modified θ method able to impose inelastic shock is used. In order to reduce the computational cost, reduction strategies are proposed. Both stability and transient analyses are performed around the sliding equilibrium position. They allow the determination of unstable modes and corresponding frequencies but also the determination of nonlinear friction-induced vibrations. The validation of the approach in quasi-static and dynamic conditions is carried out by comparison with CONTACT software and some analytical laws. Reduction strategies are validated by comparison with the full method. The developed method is then applied to a wheel/rail rolling system in curve in Chapter 5. The obtained results are compared with those provided by the point-contact model in order to verify the impact of the discretization of the contact zone.

Finally, conclusions and prospects are given at the end of the thesis.

Part I

Stability analysis of wheel/rail contact systems on curve by point-contact model

Stability analysis of wheel/rail systems on curve by point-contact model and modal bases

Contents

2.1 Introduction

In the previous chapter, curve squeal phenomena and a literature review of existing curve squeal models have been presented. In most models, the lateral creep velocity of the wheel on the rail head, due to the fact that the wheel motion does not align with the rolling direction, is considered as a main cause of curve squeal. The creepage can show unstable stick–slip behavior, causing the wheel to oscillate and radiate loud annoying noise.

In the case of constant friction coefficient and the rail dynamics included, one can find results consistent with experimental observations such as instabilities of axial modes with zero nodal circle and creep/slip limit cycles [19, 96, 97, 113]. However, the mechanisms behind this instability is not always clear and the influence of the rail has to be detailed.

The aim of this chapter is to investigate the instability mechanisms through the stability analysis of wheel/rail contact in curve. The contact is managed by using Hertz's theory combined with an hypothesis of full slip in the effective contact area and constant friction coefficient. The wheel and the rail is modeled by using the finite element method. The wheel and rail dynamics are then reduced by using the modal bases. This model is quite similar to Chiello's model [112] but with the influence of rail dynamics.

2.2 Wheel/Rail interaction model

2.2.1 Statement of the problem

The wheel/rail interaction model is represented in the figure 2.1. The rolling direction along the rail is the $x-$ direction. The lateral direction is the $y-$ direction. The vertical direction is the $z-$direction. (n,t,b) and (n',t',b') are respectively the local frames of the wheel and the rail such that:

$$n' = -n = 0Z$$

$$t' = -t = -0Y$$

$$b' = -b = 0X$$

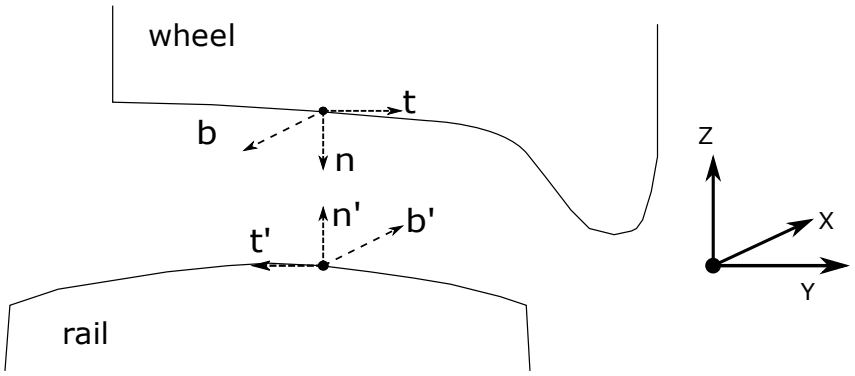

Figure 2.1: Reference frame of the wheel/rail interaction.

The following assumptions are made:

- The normal contact is Hertzian so that the normal contact force can be analytically determined,
- The lateral friction force verifies the Coulomb law in the sliding phase with a constant friction coefficient μ,
- There is no longitudinal interaction,
- Wheel rotation is neglected,
- Calculations are made in the Eulerian frame.

A loaded wheel with constant rolling speed V and angle of attack α is considered (see Fig. 1.17). The resulting sliding velocity is noted $\Delta V_y \approx V\alpha$. In the case with only imposed lateral creepage $s_{yo} = \frac{\Delta V_y}{V}$, the mean dynamic lateral creepage s_y at the contact point is defined by Eq. (1.54):

$$s_y = s_{yo} + \frac{(\dot{u}_y^W - \dot{u}_y^R)}{V} \tag{2.1}$$

2.2.2 Wheel/Rail dynamics

It is assumed that the wheel and the rail are represented by normal modal bases. These bases are supposed to be normalized with respect to mass.

At the contact point on the wheel, wheel vertical and lateral displacements can be written as:

$$\begin{aligned} u_z^w &= \Phi_{zw}\mathbf{q} \\ u_y^w &= \Phi_{yw}\mathbf{q} \end{aligned} \tag{2.2}$$

where Φ_{zw} and Φ_{yw} are the vectors of vertical and lateral modal amplitudes at the contact point on the wheel. At the contact point on the rail, wheel vertical and lateral displacements can be written as:

$$\begin{aligned} u_z^r &= \Phi_{zr}\mathbf{q} \\ u_y^r &= \Phi_{yr}\mathbf{q} \end{aligned} \tag{2.3}$$

where Φ_{zr} and Φ_{yr} are the vectors of vertical and lateral modal amplitudes at the contact point on the rail and $\mathbf{q}$ denotes the unknown generalized coordinates vector.

2.2.3 Contact mechanics

In the normal direction n, a linearized Hertz's stiffness (see Eq. (1.87)) can be applied for small amplitudes of displacement:

$$k_H = \frac{3}{2}\frac{F_n}{\delta} \tag{2.4}$$

where F_n is the static normal contact force and δ is the static penetration caused by the load F_n at the contact point. The dynamic perturbation f_n of the normal force can be expressed through the contact stiffness as:

$$f_n = -k_H u_n \tag{2.5}$$

where $u_n = u_z^r - u_z^w = (-\Phi_{zw} + \Phi_{zr})\mathbf{q}$ is the dynamic relative displacement between the wheel and the rail in the normal direction n.

In tangential direction t, a Coulomb's friction law is assumed and a full sliding contact state is considered. Friction coefficient μ is supposed to be constant. The relation between the dynamic perturbation f_t of the tangential contact force and the dynamic perturbation of the normal contact force f_n is then given by:

$$f_t = \mu f_n \text{sign}(s_y) \tag{2.6}$$

where $\text{sign}(\bullet)$ denotes the sign of $(\bullet)$. In the full sliding state, $\text{sign}(s_y) = \text{sign}(s_{yo})$.

2.2.4 Stability analysis

Hence, combining with Eqs. (2.5) and (2.6), the linearized equation of motion around the total sliding equilibrium in the global frame is written:

$$\begin{aligned} \mathbf{I}\ddot{\mathbf{q}} + \mathbf{C_{red}}\dot{\mathbf{q}} + \mathbf{K_{red}}\mathbf{q} &= (-\Phi_{zw} + \Phi_{zr})^T f_n + (\Phi_{yw} - \Phi_{yr})^T f_t \\ f_n &= -k_H(-\Phi_{zw} + \Phi_{zr})\mathbf{q} \\ r_t &= \mu r_n \ \text{sign}(s_y) \end{aligned} \tag{2.7}$$

where $\mathbf{q}$ is the dynamic perturbation of generalized coordinates vector around the total sliding equilibrium. $\mathbf{M_{red}}$, $\mathbf{K_{red}}, \mathbf{C_{red}}$ are the reduced mass, stiffness and viscous damping matrix of the system respectively. Matrix $\mathbf{K_{red}}$ is generally a diagonal matrix containing the squared natural pulsations of the wheel and the rail. $\mathbf{C_{red}}$ depends on the chosen damping model and can be full in non proportional damping cases. $\mathbf{M_{red}}$ is an identity matrix $\mathbf{I}$ due to the normalization of the wheel/rail modes with respect to mass.

An eigenvalue problem can be obtained from Eq. (2.7) given by:

$$\mathbf{I}\ddot{\mathbf{q}} + \mathbf{C_{red}}\dot{\mathbf{q}} + (\mathbf{K_{red}} + \mathbf{K}_\mu)\,\mathbf{q} = 0 \tag{2.8}$$

where $\mathbf{K}_\mu = k_H \left((-\Phi_{zw} + \Phi_{zr})^T + \mu\, \mathrm{sign}(s_y)(\Phi_{yw} - \Phi_{yr})^T\right)(-\Phi_{zw} + \Phi_{zr})$. This matrix is not symmetric due to the coupling of the normal and tangential dynamics through friction coefficient μ.

The solution of Eq. (2.8) is sought in the form: $\mathbf{q} = \mathbf{q_o} e^{\lambda t}$ where $\mathbf{q_o}$ is the complex amplitude of $\mathbf{q}$ and λ is a complex number. The equation Eq. (2.8) becomes:

$$\left(\lambda^2 \mathbf{I} + \mathbf{C_{red}}\lambda + (\mathbf{K_{red}} + \mathbf{K}_\mu)\right)\mathbf{q_o} = 0 \tag{2.9}$$

If the real part of λ is positive , the system becomes unstable. A perturbation of the equilibrium leads to an increase vibrations with deformations and frequencies related to the the unstable modes. The divergence rate of a mode is defined as the ratio between the real and imaginary part of the complex mode:

$$DvR = \mathrm{Real}(\lambda)/\mathrm{Imag}(\lambda) \tag{2.10}$$

where $\mathrm{Real}(\lambda)$ and $\mathrm{Imag}(\lambda)$ are the real and imaginary parts of the associated complex mode.

2.3 Wheel and rail specific models for the numerical application

In this section, the finite element (FE) wheel/rail models and modal bases for the numerical application are presented.

2.3.1 Wheel FE model and modal basis

The considered wheel model in the CERVIFER project is a wheel of type "Vyksa BA005" with a nominal rolling diameter of 920 mm and a mass of 314 kg. The FE mesh (see Fig. 2.2) consists of 70300 tetra quadratic elements. The size of elements are has been refined until the eigenfrequencies converge in the frequency range of interest (see below). The material data of the wheel are listed in Tab. 2.1. A rigid constraint is applied at the inner face of the hub, where the wheel is connected to the axle. This boundary condition allows to have no rigid mode in the modal basis.

The 60 first natural frequencies and corresponding free-interface modes have been calculated up to 5000 Hz. Three types of mode may be distinguished: the radial modes (r, n_d), the axial modes (a, n_c, n_d) and the circumferential modes (c, n_c, n_d) where n_d is the number of nodal diameters and n_c is the number of nodal circles. The modes types and frequencies are listed in Tab. 2.2 where "double" means that there are two wheel modes of the same type and frequency due to the symmetry of the wheel. Some typical mode shapes are showed in Fig. 2.3.

Classical modal damping factors η_w are chosen depending on the nodal diameters [3]:

$$\begin{cases} \xi_w = 10^{-3} & \text{if} \quad n_d = 0 \\ \xi_w = 10^{-2} & \text{if} \quad n_d = 1 \\ \xi_w = 10^{-4} & \text{if} \quad n_d \geq 2 \end{cases} \tag{2.11}$$

This leads to diagonal reduced stiffness matrix $\mathbf{K_{red}}^w$ and diagonal viscous damping matrix $\mathbf{C_{red}}^w$ for the wheel.

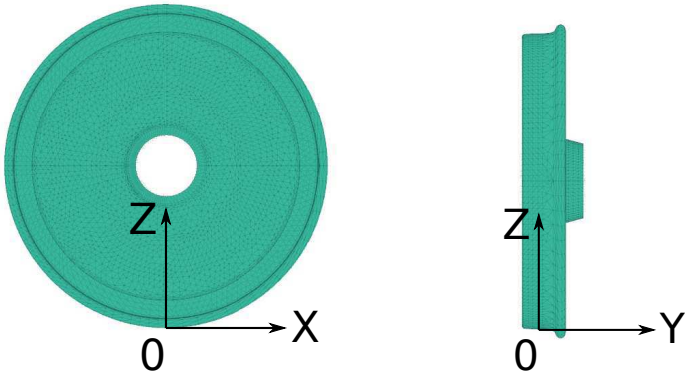

(a) XOZ plan (b) YOZ plan

Figure 2.2: Wheel FEM mesh

Data	Wheel	Rail
Young's modulus (GPa)	206.9	205
Poisson's ratio	0.288	0.3
Density (kg/m^3)	7800	7800

Table 2.1: Material data of the wheel and the rail

Mode	Type		Eigenfrequencies	Mode	Type		Eigenfrequencies
1	a.0.1	double	135	18	a,1,0		3238
2	a.0.0		226	19	r,5	double	3280
3	a.0.2	double	335	20	a,1,1	double	3356
4	c.0		445	21	a,0,6	double	3419
5	r.0	double	659	22	a,1,4	double	3541
6	a.0.3	double	920	23	a,1,2	double	3614
7	r,2	double	1155	24	r,6	double	4074
8	a,1,0	double	1494	25	a,1,3	double	4310
9	a,0,4	double	1671	26	c,2	double	4313
10	a,1,1	double	1709	27	a,0,7	double	4350
11	r,3	double	1833	28	a,1,5	double	4390
12	r,0		2059	29	a,2,0		4704
13	a,1,2	double	2152	30	a,2,1		4733
14	a,0,5		2519	31	a,3,0		4747
15	r,4	double	2543	32	a,2,2	double	4854
16	r,1	double	2683	33	r,7	double	4931
17	a,1,3	double	2774	34	a,2,4	double	5054

Table 2.2: Wheel FE modal basis

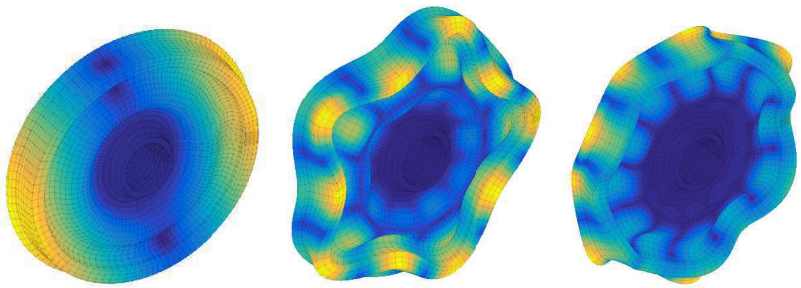

(a) (b) (c)

Figure 2.3: a: Mode axial of 135 Hz ($n_c = 0, n_d = 1$), b:Mode radial of 3280 Hz ($n_d = 5$) et c: Mode axial of 3419 Hz ($n_c = 0, n_d = 6$)

2.3.2 Track model

In most of the publications relating to railway noise, analytical models for the rail such as Euler beam or Timoshenko beam are widely used [83, 129–131]. The major advantage of the Euler model is its relative simplicity because it takes in account only the bending of the rail. The Timoshenko model includes however shear deformation and rotational inertia which play an important role in the bending of thick beams. These models can deal with continuous support or periodic support. However cross-sectional deformations of the rail are not taken into account in these models. Cross-sectional deformations can be taken into account by using waveguide finite elements WFE [119]. However the support in this model is continuous and can not describe the "pinned-pinned" effect due to the periodic support.

The limits of these models can be overcome by using FE track model. [105, 132]. Unlike the wheel which is finite structure, the track can be considered as an infinite structure because of its very high length in comparison with its dimensions in the cross-section. There is not reflection of the waves due to the free propagation along the rail. Thus, in order to avoid the reflexion of waves in a finite FE model, one gradually increases the rail damping at its termination , as proposed for instance in [132].

The track model consists of one periodically supported rail of type UIC60 (Fig. 2.4). This rail is 48 m long. The space between the sleepers (sleeper span) is 60 cm. The FE track model consists of 200000 quadratic elements and 600000 DOFs. As a first approach, the dynamics of the sleepers and the ballast is neglected because of its rather low frequency domain. The track support contains only elastic pads that connect the rail and each sleeper. They are modeled by 69 springs of longitudinal, lateral and vertical stiffnesses $(Kx = Ky = 36e6, Kz = 180e6)$N/m for each sleeper. The structural damping is set to $\eta_s = 1$.

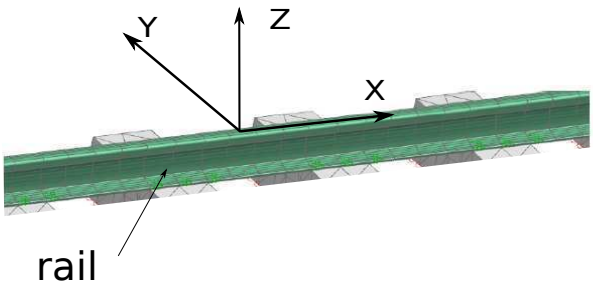

Figure 2.4: Track model

The contact position is in the center of the rail in the $x-$axis. The rail structural damping is $\eta = 0.02$. The rail ends with an anechoic termination of 6 meters which is composed of 5 subsections of length $L = (0.6, 0.6, 0.6, 1.2, 3.0)$ m which are associated with increasing structural damping $\eta = 0.1$ to 1 to avoid the return of waves . Finally, a complex stiffness matrix $\hat{\mathbf{K}}_\mathbf{r}$ is obtained including the real stiffness matrix $\mathbf{K_r}$ and the damping matrix $\mathbf{C_r}$, given by $\hat{\mathbf{K}}_\mathbf{r} = \mathbf{K_r} + \mathbf{jC_r}$ where $\mathbf{C_r}$ is piecewise proportional to

$\mathbf{K_r}$ according to the different structural damping factors. At this point, no viscous damping is introduced for the track.

The 1700 natural frequencies and corresponding free-interface modes Φ_r have been calculated up to 5000 Hz using only real stiffness matrix $\mathbf{K_r}$. The proposed track model is validated by calculating its dynamic mobilities and comparing these mobilities with the results obtained by a Timoschenko model. The dynamic mobilities at the contact point are computed by using the reduce basis including the free-interface modes Φ_r. For each frequency ω, the mobility at contact DOF i_1 due to a force at contact DOF i_2 is given by:

$$V_c^{i_1,i_2}(\omega) = j\omega\Phi_r(i_1,:)\left(-\omega^2\mathbf{M}_{red}^r + \hat{\mathbf{K}}_{red}^r\right)^{-1}\Phi_r(i_2,:)^T \tag{2.12}$$

where $\hat{\mathbf{K}}_{red}^r = \Phi_r^T\hat{\mathbf{K}}_\mathbf{r}\Phi_r$ and $\hat{\mathbf{M}}_{red}^r = \Phi_r^T\mathbf{M_r}\Phi_r$ the (non diagonal) reduced complex stiffness and the reduced mass matrix respectively.

The amplitude and phase of the track vertical and lateral mobilities at the center point between two sleepers are represented in Figs. 2.5 and 2.6. Two resonant frequencies $f = 1062$ Hz and $f = 502$ Hz are observed on the mobility curves respectively for the cases of lateral and vertical loads. These frequencies correspond to the pinned-pinned frequencies.

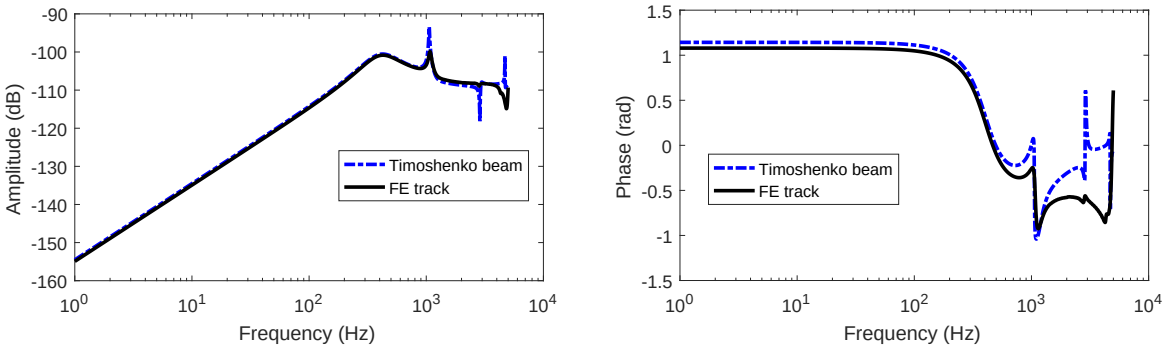

(a) Amplitude (b) Phase

Figure 2.5: Vertical mobility at contact point

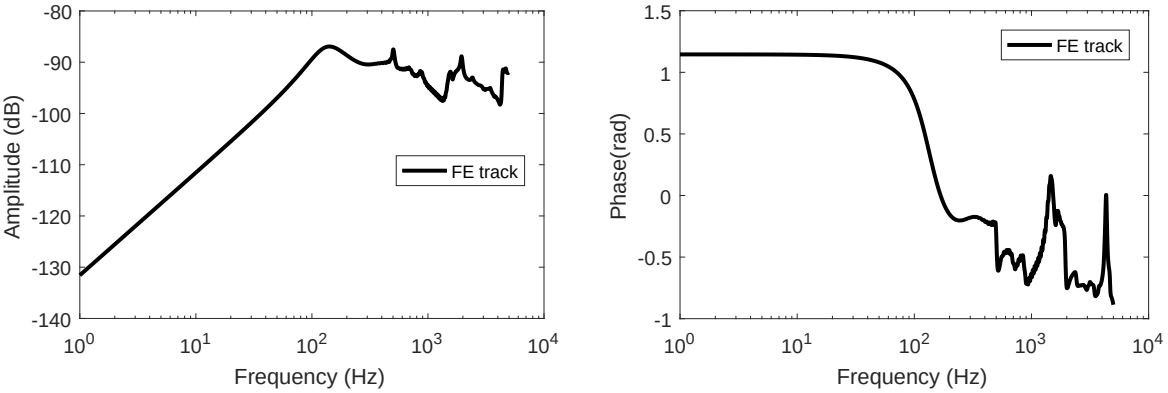

(a) Amplitude (b) Phase

Figure 2.6: Lateral mobility at contact point

One compares the dynamic response obtained by FEM with the dynamic response obtained with the analytical Timoshenko beam model [131] in vertical bending in Fig. 2.5. The frequencies of the peaks

are close. However the amplitudes are different at the resonance peak that are related to the distance between two sleepers. This difference results from the spreading of the springs that connect the rail and the sleepers in the FE model. In the Timoshenko beam, there is only one spring that connects the rail and the sleepers. The evolution of the curves for high frequencies ($> 3000Hz$) is also different. This is due to the cross-sectional deformations which are not taken into account in the Timoshenko beam. There is no analytical track model with periodic support for lateral vibration. For the lateral vibration, no comparison is proposed since a pertinent analytical model should include both bending and torsional deformations and is only valid at low frequencies.

Concerning the rail anechoic termination, the amplitude of the vertical mobility along the track caused by the impulsion at the contact point ($x = 0$) at some frequencies is represented in Fig. 2.7. The amplitude of this mobility decreases along the track and there is no wave reflection.

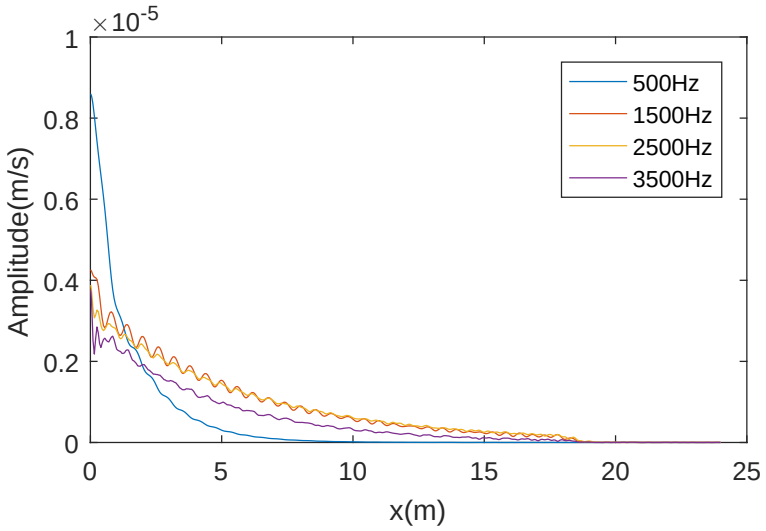

Figure 2.7: Vertical mobility along the track caused by the impulsion at the contact point ($x = 0$)

2.4 Numerical results

In this section, the results of stability analysis of the wheel/rail system for a reference case is firstly presented. The bifurcation curve (effect of friction coefficient) then allows to analyze the instability mechanism in both damped and undamped cases. The effects of some parameters whose the effects are strong on the occurrence of these unstable complex modes are then investigated such as the lateral contact position on the wheel, the wheel modal damping and the vertical pad stiffness.

2.4.1 Reference case analysis

The reference case with the kinematic parameters listed in Table 2.3 is considered. Both damped and undamped cases are tested. The undamped case is obtained by neglecting all damping (viscous damping for the wheel and structural damping for the rail) in the system.

Rolling velocity V (m/s)	10
Imposed lateral velocity of the wheel V_y (m/s)	0.1
Friction coefficient μ	0.3
Static vertical load N	70000 N

Table 2.3: Kinematic parameters of the wheel/rail rolling contact model

2.4.1.1 Undamped case

In this case, only one unstable mode (with positive real part) is obtained (cf. Fig. 2.8). The corresponding mode shape is illustrated in (Fig. 2.9). This shape gets close to the axial wheel "double" modes with 3 nodal diameters and 0 nodal circle. The corresponding unstable frequency is 918 Hz which gets close to the natural frequency of the same mode.

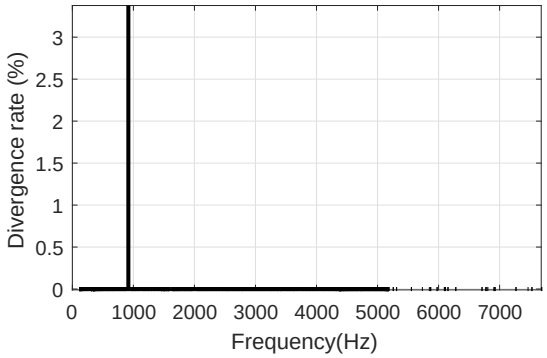

Figure 2.8: Divergence rate of the complex modes in the undamped reference case

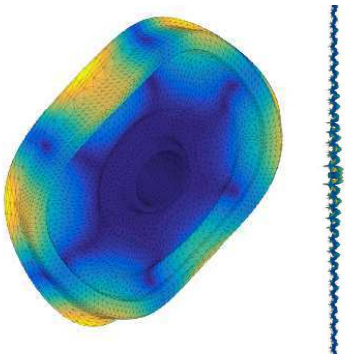

(a) Wheel (b) Rail

Figure 2.9: Unstable complex mode (a,0,3) in the undamped reference case

2.4.1.2 Damped case

In this case, 4 unstable modes (with positive real part) are obtained (cf. Fig. 2.10). The frequency of these unstable complex modes are 334, 918, 1670 and 3417 Hz respectively which get close to the frequencies of the 4 axial wheel modes with (2,3,4,6) nodal diameters and 0 nodal circle.

The corresponding unstable modes shapes are illustrated in Figs. 2.11 to 2.14. The first three modes shapes get close to the 3 axial wheel modes with (2,3,4) nodal diameters and 0 nodal circle respectively. This result is coherent with the experimental observation that the squeal fundamental frequencies correspond to axial wheel modes with zero nodal circles, according with the literature review [5, 8].

Even if the frequency of the fourth complex mode gets close to the axial wheel mode with 6 nodal diameters and 0 nodal circle, the mode shape is significantly different. In order to find the contributions of the free wheel modes in this unstable complex mode, the *Normalized Modal Assurance Criterion* (MAC) [41] between wheel normal modes and this unstable complex mode is calculated. The expression of the MAC used here is given by (2.13) in which $\Phi_{complex}$ is the unstable complex mode and Φ_w is a free normal wheel mode.

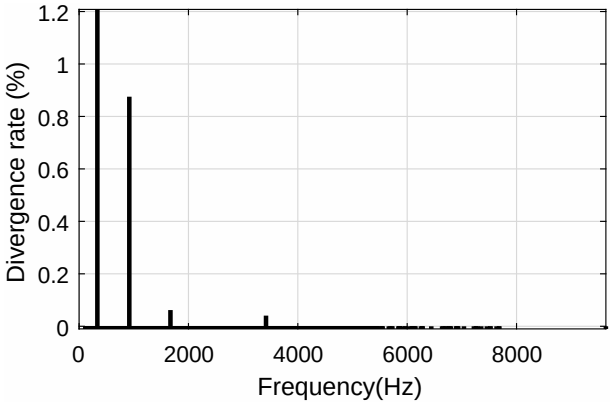

Figure 2.10: Divergence rate of the complex modes in the damped reference case

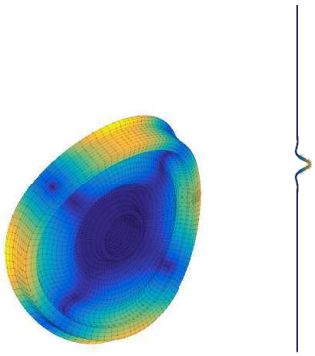

(a) Wheel (b) Rail (vertical)

Figure 2.11: Unstable mode shape (a,0,2) in the damped reference case

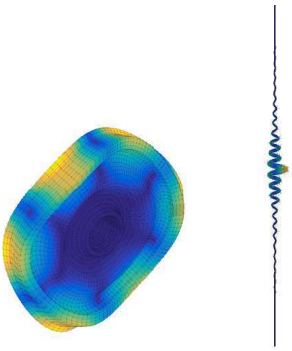

(a) Wheel (b) Rail (vertical)

Figure 2.12: Unstable mode shape (a,0,3) in the damped reference case

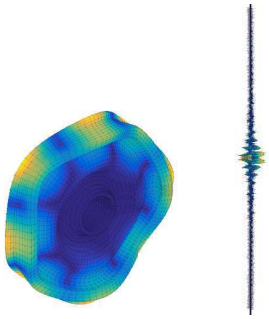

(a) Wheel (b) Rail (vertical)

Figure 2.13: Unstable mode shape (a,0,4) in the damped reference case

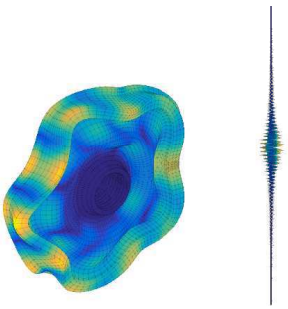

(a) Wheel (b) Rail (vertical)

Figure 2.14: Unstable mode shape (a,0,6) in the damped reference case

$$\mathbf{MAC}(\Phi_w, \Phi_{complex}) = \frac{|\Phi^T \mathbf{M}_w \Phi_{complex}|^2}{|\Phi_w^T \mathbf{M}_w \Phi_w||\Phi_{complex}^T \mathbf{M}_w \Phi_{complex}|} \tag{2.13}$$

Fig. 2.15 allows to identify five natural wheel modes involved in the fourth unstable complex mode: the radial mode (r,5) of frequency 3280 Hz, the "double" axial modes (a,1,1) of frequency 3356 Hz and the "double" axial modes (a,0,6) of frequency 3420 Hz. The contribution of the axial modes (a,0,6) is the greatest.

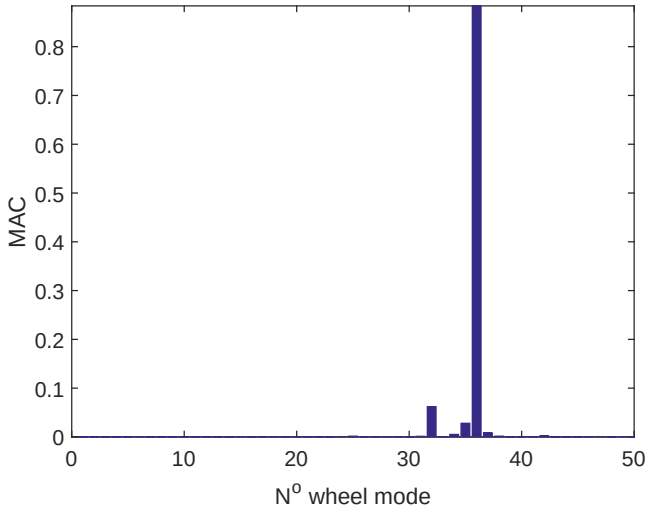

Figure 2.15: MAC between the wheel modes and the fourth unstable complex mode

The results in the undamped and damped cases are summarized in Tab. 2.4.

Undamped system			Damped system		
Unstable frequencies (Hz)	Divergent rate (%)	Wheel modes involved	Unstable frequencies (Hz)	Divergent rate (%)	Wheel modes involved
			334	1.2	335 Hz - (a,0,2)
917.5	3.3	920 Hz - (a,0,3)	918.3	0.87	920 Hz - (a,0,3)
			1671	0.06	1671 Hz - (a,0,4)
			3418	0.04	3419 Hz - (a,0,6), 3280 Hz - (r,5) and 3256- (a,1,1)

Table 2.4: Stability results in the reference case

2.4.2 Bifurcations curves

To analyze the instability mechanism, it is useful to compute the bifurcation curves representing the evolution of the unstable modes as a function of friction coefficient μ while the other parameters are maintained constant.

2.4.2.1 Undamped Case

For the undamped system, the bifurcation curves of the unstable complex modes are represented in Figs. 2.16 and 2.17. Besides the unstable mode (a,0,3) found in the reference case, by increasing

friction coefficient, a new unstable complex mode is obtained for high friction coefficients. Its mode shape is close to the (a,0,6) mode and similar to that of the fourth unstable mode in the damped case (cf. Fig. 2.14). The critical friction coefficient from which the complex modes frequencies coalesce and a mode becomes unstable are respectively 0.12 and 0.5 for the unstable complex modes (a,0,3) and (a,0,6). In this case, the instability mechanism is mode coupling with constant friction coefficient as presented in chapter 1.

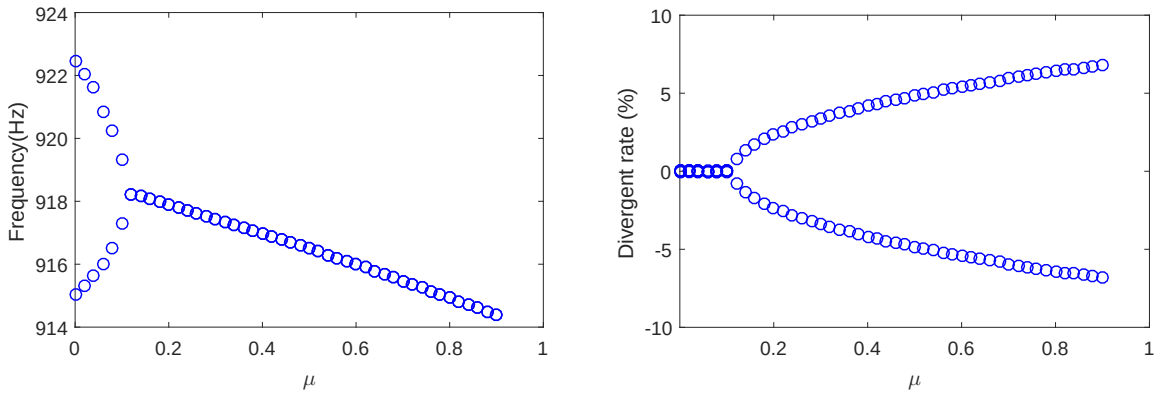

(a) Frequency (b) Divergence rate

Figure 2.16: Bifurcation curves of the unstable complex mode (a,0,3) for the undamped system

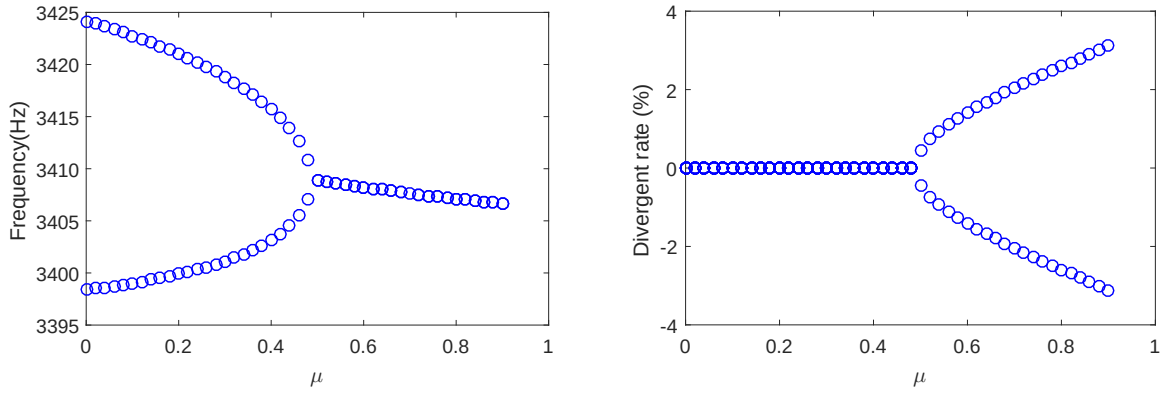

(a) Frequency (b) Divergence rate

Figure 2.17: Bifurcation curves of the unstable complex mode (a,0,6) for the undamped system

2.4.2.2 Damped Case

For the damped system, the bifurcation curves of the unstable complex modes are represented in Figs. 2.18 to 2.21. The critical friction from which the complex modes become unstable are respectively 0.06, 0.1, 0.22 and 0.3 for the unstable complex modes (a,0,2), (a,0,3), (a,0,4) and (a,0,6).

For the first three unstable modes (a,0,2), (a,0,3) and (a,0,4), the form of the bifurcation curves that seems to be linear is not the same as the form of the bifurcation curves for the undamped system. Moreover, the zoom near the unstable frequency (a,0,2) in Fig. 2.22 does not show the coalescence of any frequencies. Results similar for the unstable modes (a,0,3) and (a,0,4). Actually, one can imagine

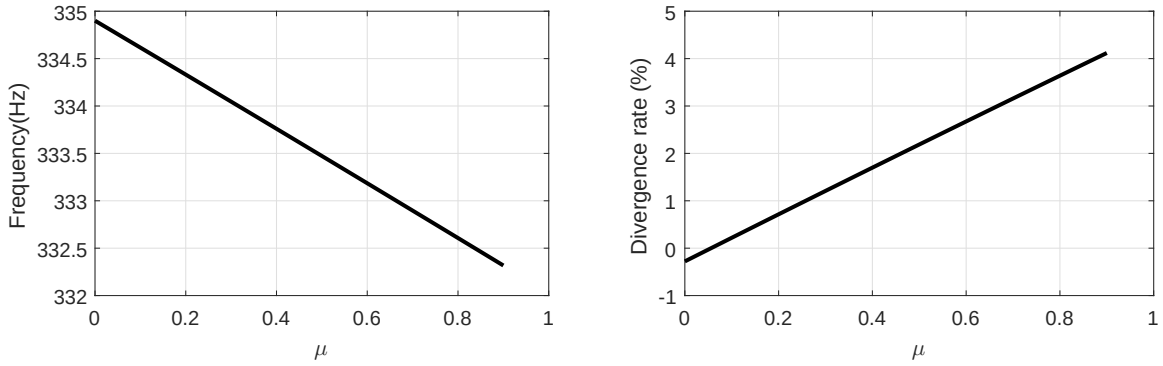

(a) Frequency (b) Divergence rate

Figure 2.18: Bifurcation curves of the unstable complex (a,0,2) for the damped system

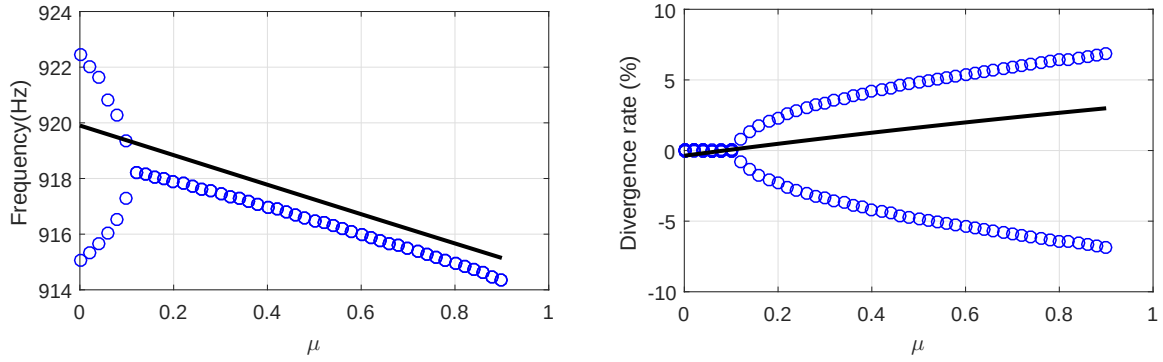

(a) Frequency (b) Divergence rate

Figure 2.19: Bifurcation curves of the unstable complex mode (a,0,3) for the undamped system (blue) and for the damped system (black)

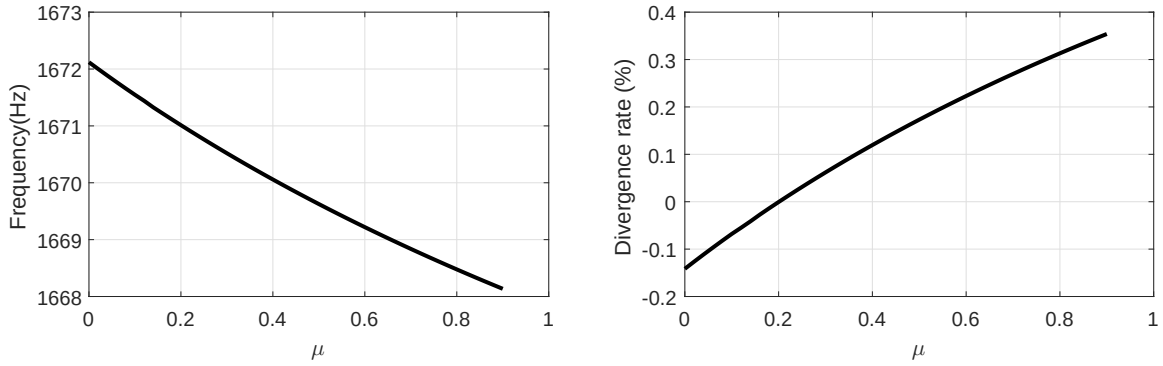

(a) Frequency (b) Divergence rate

Figure 2.20: Bifurcation curves of the unstable complex mode (a,0,4) for the damped system

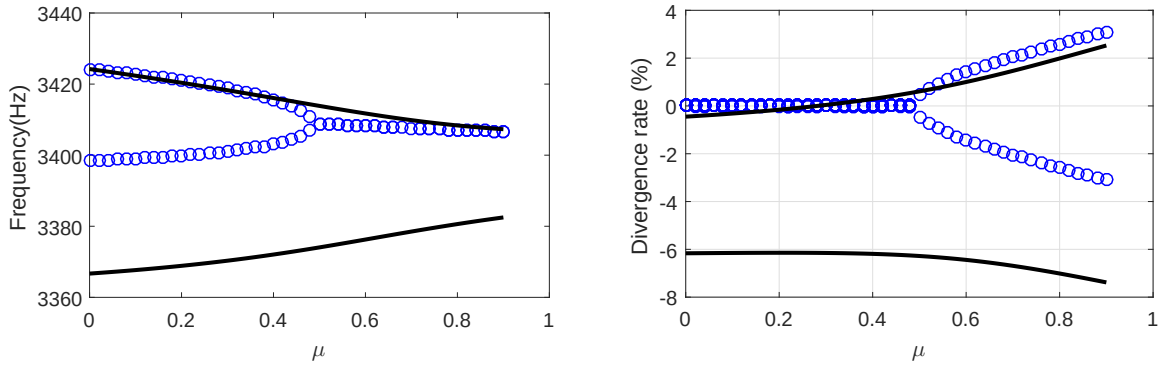

(a) Frequency (b) Divergence rate

Figure 2.21: Bifurcation curves of the unstable complex mode(a,0,6) for the undamped system (blue) and for the damped system (black)

that these instabilities are not due to mode coupling. According to Ding *et al.* [19], this instability is due to coupling between the normal and tangential components of the single wheel mode when the rail dynamics is included.

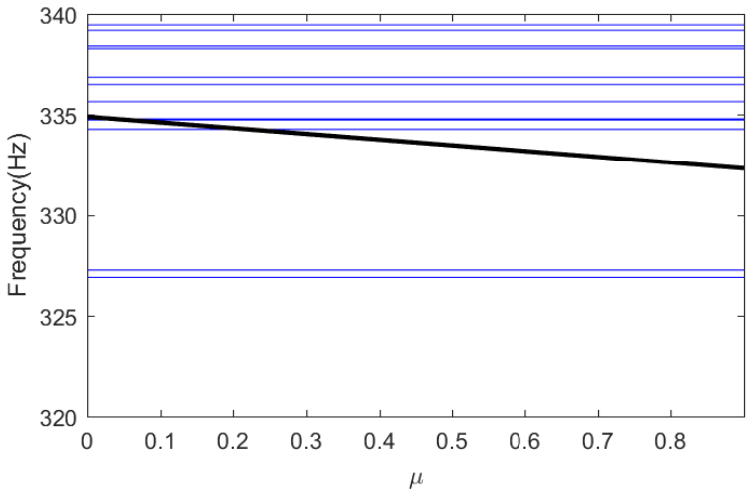

Figure 2.22: Zoom near the unstable mode (a,0,2) frequency (black)

On the other hand, the bifurcation curves of the unstable mode (a,0,6) for the damped system is not so far from the bifurcation curves of the unstable mode (a,0,6) for the undamped system (Fig. 2.21) although they are more distant. This damping effect is rather classical and one can conclude that this instability is due to mode coupling.

In brief, it is found that there is a difference between instability mechanisms for the two undamped and damped cases. For the undamped system, the instability mechanism is mode coupling whereas for the damped system, there are two instability mechanisms: mode coupling and coupling between the normal and tangential components of a single wheel mode can coexist.

In the following subsection, one focuses firstly on the effect of the rail global dynamics on the occurrence of instability. The role of the rail vertical and lateral dynamics is clarified.

2.4.3 Effect of the rail dynamics

2.4.3.1 Case without the rail dynamics

In some models [6, 16, 104, 109, 112, 114, 116, 117], the rail dynamics are neglected. In this model, the rail dynamics may be also neglected by eliminating all terms concerning the rail in Eq. (2.8). In this case, there is only one unstable complex mode (a,0,6), corresponding to the mode-coupling instability in the previous section. The bifurcation curves are represented in Fig. 2.23. The critical friction coefficient from which the complex modes frequencies coalesce and a mode becomes unstable is about $\mu = 0.95$ for the undamped system and $\mu = 0.8$ for the damped system. This critical friction coefficient is greater than the critical friction coefficients in the case taking into account the rail dynamics ($\mu = 0.3$ for the damped system and $\mu = 0.5$ for the undamped system). These results show the important role of the rail dynamics which can generate some specific kind of instability.

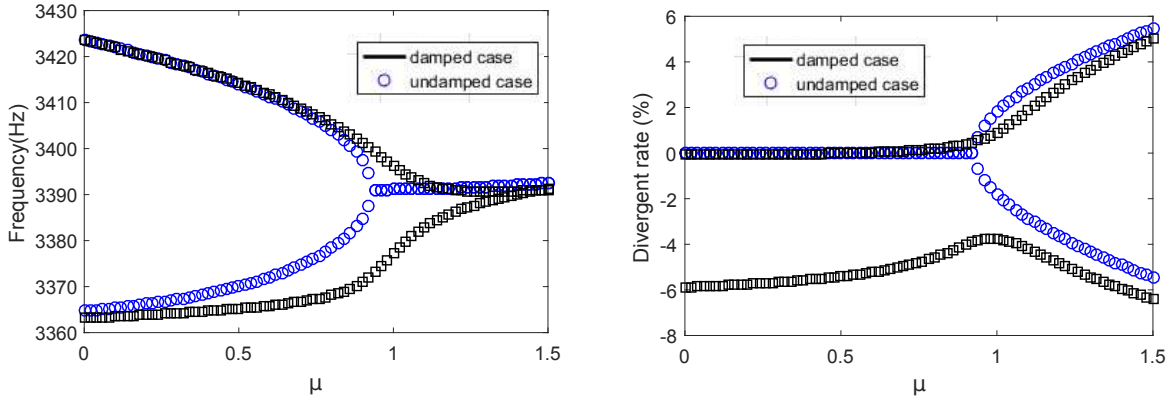

(a) Frequency

(b) Divergence rate

Figure 2.23: Bifurcation curves in the case without the rail dynamics (black: with wheel damping, blue: without wheel damping)

2.4.3.2 Effects of the rail vertical and lateral dynamics

In the case with the rail dynamics, one can determine separately the role of the rail vertical and lateral dynamics. In Eq. (2.8), the rail lateral dynamics can be neglected by eliminating the term Φ_{yr}.

With the data from the reference case, Fig. 2.24 shows that the instability does not depend on the lateral flexibility of the rail. The rail vertical dynamics is therefore the most important characteristic for the occurrence of instability. Ding *et al.* [19] stated that the rail dynamics can change the flexibility of the normal contact, which affects the level of coupling. With our results, one can also conclude more specifically that the rail vertical dynamics changes the flexibility of the normal contact.

2.4.4 Effect of the contact position on the wheel and creepage sign

In this study, as in De Beer *et al.* model [9], it is assumed that the contact position on the rail does not change. Only the $y-$ coordinate of the contact point on the wheel y_0 is varied. Two cases are tested:

- $\Delta V_y > 0$ corresponding to the sliding of the inner wheel,
- $\Delta V_y < 0$ corresponding to the sliding of the outer wheel.

Other the other parameters are maintained constant.

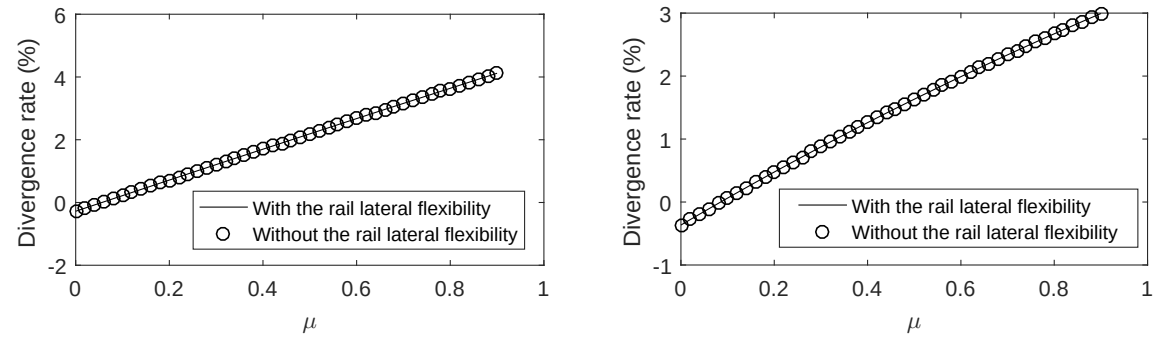

(a) Mode 1

(b) Mode 2

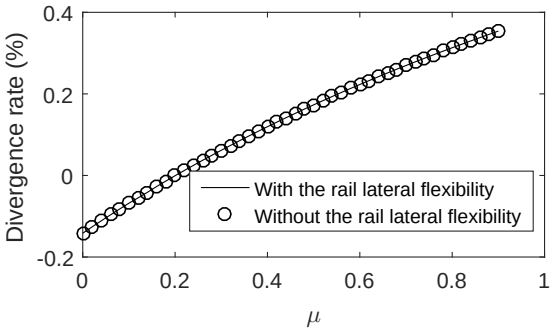

(c) Mode 3

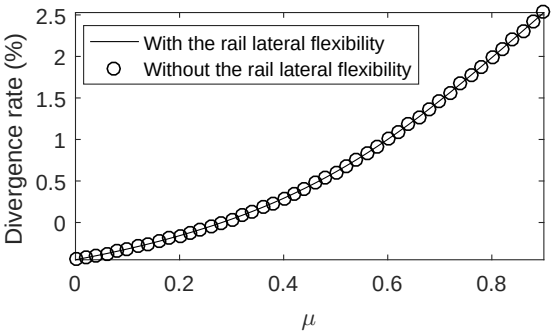

(d) Mode 4

Figure 2.24: Bifurcation curves of unstable complex modes for the damped system with the lateral flexibility of the rail (−) and without the lateral flexibility of the rail (○)

Fig. 2.25 shows the strong influence of the contact position on the wheel combined with the sign of ΔV_y. In the case of sliding inner wheel ($\Delta V_y > 0$), the divergence rates of the unstable complex modes (a,0,2), (a,0,3) and (a,0,4) increase when the contact position gets close to the flange (y_0 increases). This result is similar to the result of De Beer's model [9] but is opposed to the result of Pieringer's model [113]. On the other hand, the divergence rate of the unstable complex mode (a,0,6) decreases while the contact position gets close to the flange.

In the case of sliding outer wheel ($\Delta V_y < 0$), the results are contrary to the results corresponding to the sliding inner wheel. The unstable complex modes (a,0,2), (a,0,3) and (a,0,4) appear when the contact position is far from flange. By taking into account the behavior of railway bogies in curve, the contact position of the outer wheel is close to the flange. Thus, for the outer wheel, the occurrence probability of the unstable complex modes (a,0,2), (a,0,3) and (a,0,4) is lower than for the inner wheel.

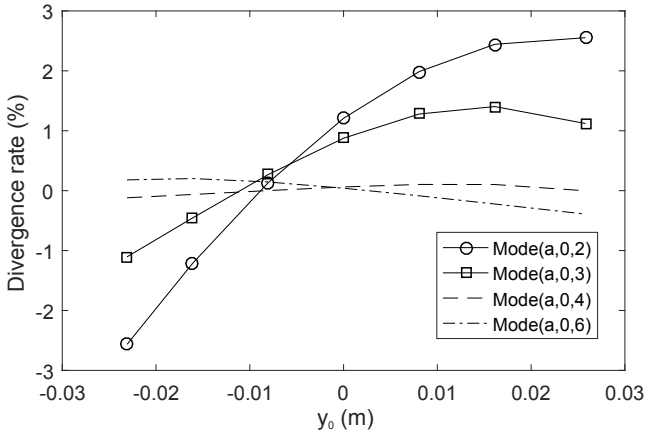

(a) $\Delta V_y > 0$

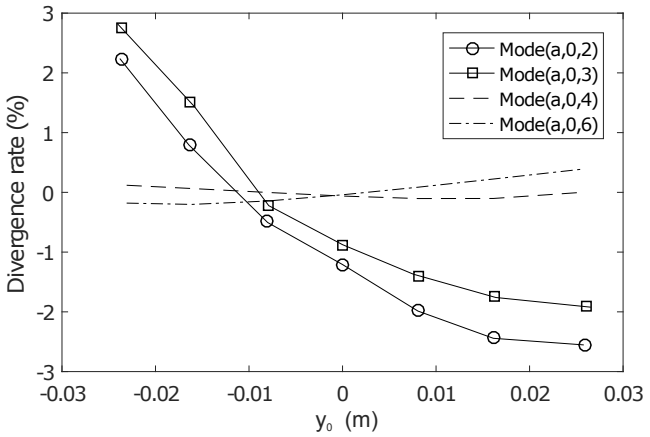

(b) $\Delta V_y < 0$

Figure 2.25: Divergence rate of unstable complex modes as a function of the contact position on the wheel

2.4.5 Effect of the wheel modal damping

The effect of the wheel modal damping factors are showed in (Fig. 2.26). We can observe that when the modal damping factor of the axial wheel modes (a,0,2), (a,0,3), (a,0,4) and (a,0,6) reach 0.2%, 0.15% , 0.02% and 0.1% respectively, the associated unstable complex modes become stable. Thus, squeal occurrence tends to reduce if the damping of the implicated axial wheel modal increases. The

modal damping factors do not agree with the $1.3 - 3\%$ range of critical damping factor needed to avoid squealing on the mode (a,0,2) founded experimentally by Koch *et al.* [8] on a $1/4$ scale test rig. Nothing can be concluded here because the two systems are not the same. The rail in Koch *et al.* 's test [8] is not a real rail and is represented by a wheel with a large diameter. In any case, the obtained critical damping factors are quite low compared with those generally observed in the literature. This point deserves to be further explored. A (too) law friction coefficient (equal to 0.3 here) might explain this difference.

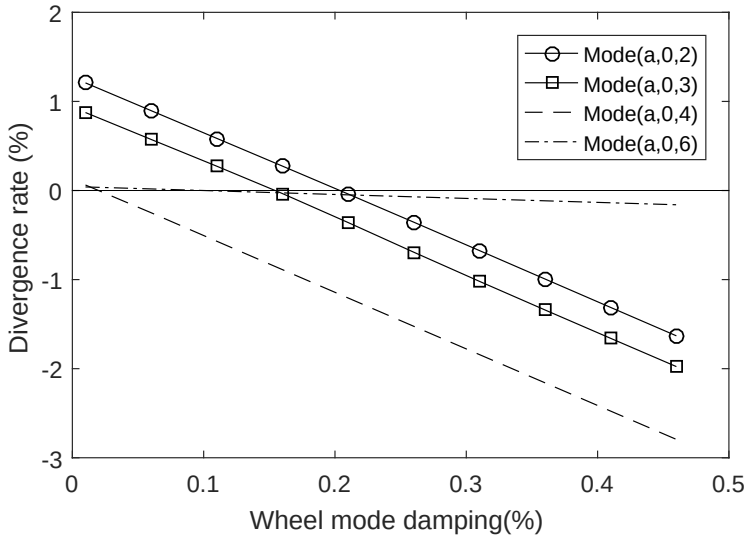

Figure 2.26: Divergence rate of unstable complex modes a a function of the associated axial wheel modes

2.4.6 Effect of vertical pad stiffness

While the parameters of the reference case are maintained constant, if the vertical pad stiffness k_{pad} increases, the divergence rate of the unstable modes (a,0,2) and (a,0,3) decreases greatly as shown in Fig. 2.27. The divergence rate of the unstable modes (a,0,4) firstly decreases and then increases. The divergence rate of the unstable mode (a,0,6) does not change. Chen [133] also found that an increase of the track vertical pad stiffness can reduce the instability of unstable mode. It can be explained by the fact that an increase of the vertical pad stiffness implies an decrease of the rail vertical flexibility, which decreases the level of coupling. However, the effect of the vertical pad stiffness is not straightforward and seem to depend on other parameters.

2.5 Conclusion

A frequency-domain model for curve squeal generation has been presented in this chapter. The model is composed of an Hertz'stiffness for the normal contact, a constant Coulomb's friction law for the tangential contact and modal wheel and rail dynamics calculated by using the finite element method. By performing the stability analysis in the case of the sliding of the system, two kinds of instability can be distinguished. The first kind of instability is due to the coupling between the tangential and normal components in one axial wheel mode with (2,3,4) nodal diameters and 0 nodal circle with the rail dynamic. This instability is not due to mode coupling. It is greatly influenced by the damping and the rail vertical dynamics. The second kind of instability is due to a mode coupling between the axial wheel mode (a,0,6) and other modes whose frequencies are close to the frequency of axial wheel mode (a,0,6). It is not significantly modified by either the damping or the rail dynamics. The influence of kinematic parameters on the occurrence of instability is also established. It is found that the occurrence

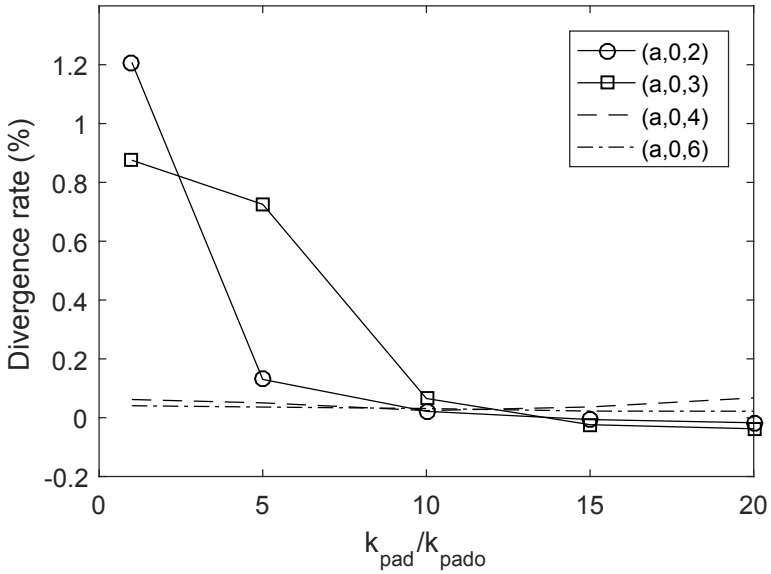

Figure 2.27: Influence of the pad vertical stiffness on the unstable complex modes (k_{pado}: vertical pad stiffness in the reference case)

of instability depends mainly on friction coefficient, contact position, lateral wheel modal damping and rail vertical pad stiffness.

Although the rail vertical flexibility is found to play an important role on the instability occurrence without "falling friction" nor without "mode-coupling" as showed in Ding's work [19], this role need to be clarified. In addition, the large number of track normal modes prevents us from a simple analysis of the stability. For this purpose, the track model needs to be simplified. That is the reason why, in the following chapter, a 1-DOF model taking into account one wheel mode and a simplified rail analytical dynamics is developed. The aim is to show how the vertical dynamics of the rail can a critical effect on curve squeal occurrence.

The critical effect of rail vertical phase response in railway curve squeal generation

Contents

3.1 Introduction

In the previous chapter, it is found that the coupling between a single wheel mode and the rail vertical dynamics can lead to instability. This instability occurs without falling friction nor mode coupling, that are the two mechanisms considered in most models. Thus, the role of the rail vertical dynamic on the instability needs to be clarified.

The aim of this chapter is to show how the vertical dynamics of the rail and especially its phase response has a critical effect. In order to explain this new mechanism, a one-mode model is proposed in which the rail is modeled as a constant complex stiffness near the natural frequency of the free wheel mode. For the numerical application, the modal parameters of the wheel are provided by the modal basis resulting from the finite element analysis of the wheel presented in the previous chapter. For the rail, a simple beam model in vertical bending is used in order to propose an analytical expression of the rail equivalent stiffness and damping.

3.2 A simplified wheel/rail model

The wheel/rail interaction model considered in this chapter is similar to that of the previous chapter with the same notations and assumptions. However, simplifications in this model are made concerning the wheel model and the rail model.

3.2.1 Simplified wheel model

The wheel is supposed to vibrate on only one mode of natural pulsation Ω and damping factor ξ_w. All wheel modes calculated by finite elements method in the previous chapter can be re-used in this chapter.

3.2.2 Simplified rail model

In the previous chapter, it is found that the instability does not depend on the rail lateral flexibility. Thus, in this chapter, one focuses on a simplified vertical model of the rail.

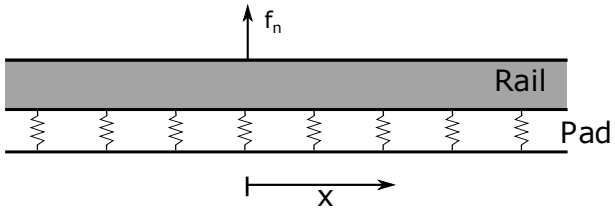

Figure 3.1: Continuous track model

The track model is illustrated in Fig. 3.1 with a rail on a foundation including pads. Sleepers and ballasts are supposed to be rigid. . This rail is excited by a dynamic normal contact force f_n in x, the vertical mobility of the rail $Z(\omega)$ is defined by a relation between the exciting force $f_n(\omega)$ and the vertical velocity $v_z^r(x,(\omega))$ in the frequency domain:

$$Z(x,\omega) = \frac{v_z^r(x,\omega)}{f_n(\omega)} \tag{3.1}$$

The rail dynamic complex stiffness is then given by:

$$k_r(x,\omega) = \frac{f_n(\omega)}{u_z^r(x,\omega)} = \frac{f_n(\omega)}{i\omega v_z^r(x,\omega)} = \frac{i\omega}{Z(x,\omega)} \tag{3.2}$$

In order to estimate the complex stiffness of the rail, an Euler/Bernouilli infinite beam model on continuous elastic foundation representing the rail pad has been used with parameters corresponding to a UIC60 rail profile (cf. Table 3.1). The point complex stiffness of the rail in vertical bending can then be written [3]:

$$k_r(0,\omega) = 2EIk_p^3(i-1) \tag{3.3}$$

where $k_p(\omega)$ is a complex wave number given by:

$$k_p^4 = \frac{m_r\omega^2 - k_s(1+i\eta_s)}{EI(1+i\eta)} \tag{3.4}$$

It is worth to note that the imaginary part of complex stiffness k_r is non null and represents a phase shift in the point receptance of the rail. This shift is mainly due to the $\pi/2$ shift of the propagating wave (the imaginary term in Eq. (3.3)) but also to structural damping effects (the imaginary terms in Eq. (3.4)).

The vertical mobility of the track is represented in Fig. 3.2. In comparison with the vertical mobility of the FE track model considered in the previous chapter, the mobility of the Euler beam model on continuous support is roughly similar but does not show the peaks due to the periodic support.

Rail mass per unit length	m_r	60	kg/m
Rail bending moment	EI	6.23	MN.m^2
Rail damping factor	η	0.02	–
Pad vertical stiffness per unit length	k_s	300	MN/m^2
Pad damping factor	η_s	1	–

Table 3.1: Track structural parameters

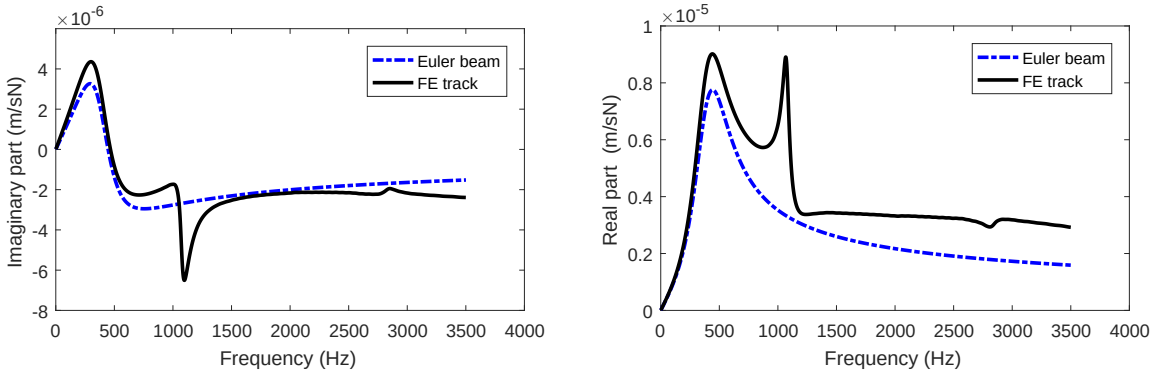

(a) Imaginay part (b) Real part

Figure 3.2: Comparison of the rail vertical mobility obtained with the FE model and the analytical beam model

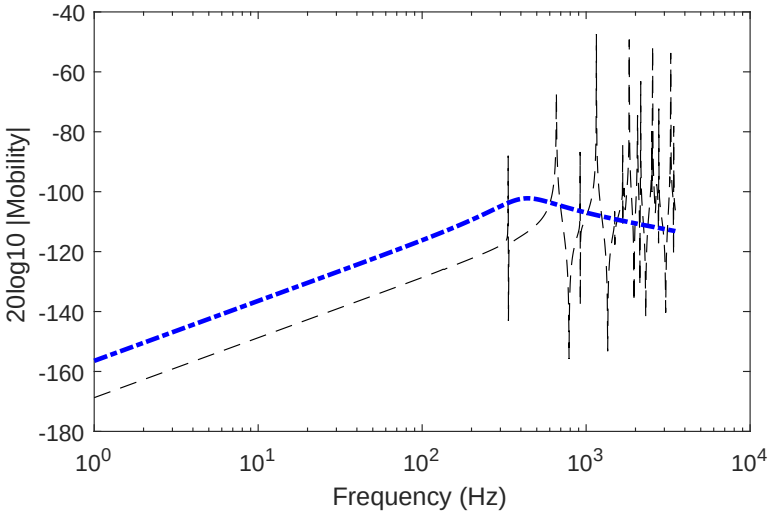

Figure 3.3: Comparison of rail and wheel vertical mobilities at the contact point (blue: track, black: wheel)

Fig. 3.3 shows the vertical mobility of the wheel and the track on the contact point ($x = 0$). The rail vertical mobility does not vary so much near the natural frequency of the wheel. The rail dynamic complex stiffness at the contact point is therefore supposed to be almost constant near the natural frequency of the wheel such that:

$$k_r(0,\omega) \simeq k_r(0,\Omega) \tag{3.5}$$

3.2.3 Stability analysis of the wheel/rail system in full sliding contact

Under the above assumptions, the mechanical system is represented by one wheel mode, coupling with an Hertz'stiffness k_H [3] and the rail complex stiffness k_r in series as shown in Fig. 3.4.

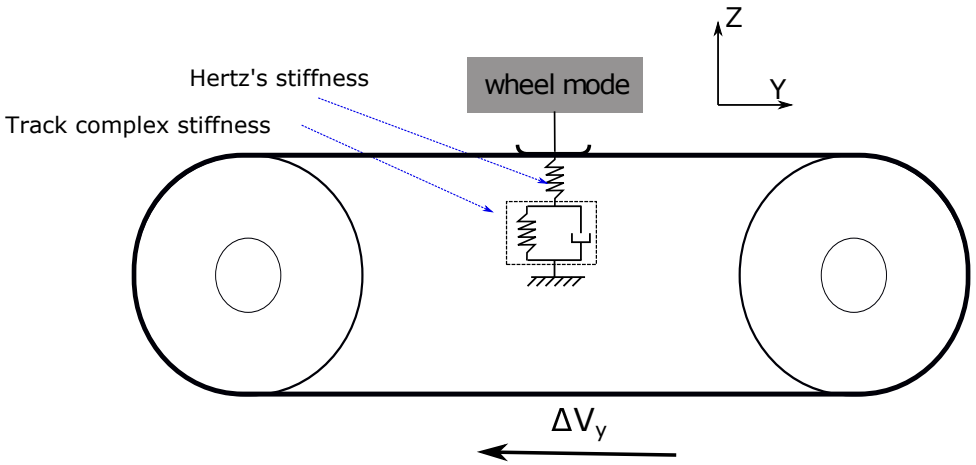

Figure 3.4: Simple 1-DOF model for instabilities due to the rail vertical phase response

By assuming a harmonic dependence for all dynamic variables X such that $X = X_o(\omega)e^{i\omega t}$, the linearized equations of the system become:

$$u_n^w = -\Phi_{zw} \times q \tag{3.6a}$$
$$(-\omega^2 + 2i\omega\xi_w\Omega + \Omega^2)q = -\Phi_{zw} f_n + \Phi_{yw} f_t \tag{3.6b}$$
$$f_n = -k_v u_n^w \tag{3.6c}$$
$$f_t = \mu f_n \times \mathrm{sign}(s_{yo}) \tag{3.6d}$$
$$\tag{3.6e}$$

where u_n^w is the vertical displacement at the contact point in the local frame of the wheel. q denotes the unknown generalized coordinate corresponding to the wheel mode. f_n, f_t are the dynamic vertical and lateral contact forces. s_y is the lateral creepage of the wheel. k_v is the stiffness of the series springs:

$$k_v = \frac{k_H k_r}{k_H + k_r} \tag{3.7}$$

Eq. (3.6) leads to an eigenvalue equation:

$$\left(-\omega^2 + 2i\omega\xi_w\Omega + \Omega^2 + K_c\right) q = 0 \tag{3.8}$$

where

$$K_c = \left(\Phi_{zw} - \mu \mathrm{sign}(s_{yo})\Phi_{yw}\right) k_v \Phi_{zw} \tag{3.9}$$

is the complex stiffness due to the contact, the friction, the wheel modal amplitudes and the rail vertical dynamics. The imaginary part of this complex stiffness K_c results from the imaginary part of the rail

stiffness. In others words, it results from the damping and the propagative waves of the rail. We can then introduce a equivalent viscous damping in the system defined by:

$$c_c(\omega) = \frac{\text{Imag}(K_c)}{\omega} \tag{3.10}$$

where Imag$(\bullet)$ denotes respectively the imaginary part of $(\bullet)$.

This damping can be expressed by a modal damping factor:

$$\eta_c(\omega) = \frac{c_c}{2\Omega} \tag{3.11}$$

In addition, near the natural frequency of the considered wheel mode, we have: $\eta_c(\omega) \approxeq \eta_c(\Omega)$ and Eq. (3.8) becomes:

$$\left(-\omega^2 + 2i\omega\xi_c\Omega + \Omega^2 + \text{Real}(K_c)\right) q = 0 \tag{3.12}$$

where the total damping factor ξ_c is thus given by:

$$\xi_c = \xi_w + \eta_c \tag{3.13}$$

Eq. (3.12) gives:

$$\omega = i\xi_c\Omega \pm \sqrt{-\xi_c^2\Omega^2 + \Omega^2 + \text{Real}(K_c)} \tag{3.14}$$

The unknown generalized coordinate corresponding to the wheel mode q is given by:

$$q = q_o e^{i\omega t} = q_o e^{-\xi_c\Omega t} e^{\pm i\sqrt{-\xi_c^2\Omega^2+\Omega^2+\text{Real}(K_c)}t} \tag{3.15}$$

where q_o is the amplitude of q.

The unstable frequency is given by:

$$f_{unstable} = \frac{\sqrt{-\xi_c^2\Omega^2 + \Omega^2 + \text{Real}(K_c)}}{2\pi} \tag{3.16}$$

The divergence rate of the coupled complex mode can be defined using the real and imaginary terms in Eq. (3.14):

$$DvR = \frac{-\xi_c\Omega}{\sqrt{-\xi_c^2\Omega^2 + \Omega^2 + \text{Real}(K_c)}} \tag{3.17}$$

3.2.3.1 Stability criterion

The sign of damping factor ξ_c is the key factor for the stability of the system. If this damping factor is negative, the divergence rate is positive and the wheel/rail system becomes unstable.

Looking at expression (3.9), it is clear that this may occur for sufficiently high value of $\mu > |\Phi_{zw}/\Phi_{yw}|$ in the case where the sign of (s_y) is the same that the sign of the product $\Phi_z\Phi_y$. However a numerical application has to be performed in order to evaluate if this negative damping is sufficient to destabilize the system in realistic cases, i.e. $-\eta_c > \xi_w$.

3.3 Numerical application

In this section, the results of stability analysis of the wheel/rail system for the reference case is firstly presented. The bifurcation curves (effect of friction coefficient) then allow to analyze the instability mechanism. A parameter study is also proposed. Due to the simplicity of the model, it can be performed analytically. This is useful to clarify outstanding issues of chapter 2.

3.3.1 Reference case analysis

The reference case with the kinematic parameters listed in Table 2.3 is considered. A divergent rate in Eq. (3.17) is calculated for all computed wheel modes using η_c values given by Eq. (3.11). Results given on Fig. 3.5a for $\Delta V_y > 0$, $k_H = 1260$ MN/m and $\mu = 0.3$ show that only three unstable modes are found ($\xi < 0$) which correspond to the three axial wheel modes without nodal circle (a,0,2), (a,0,3) and (a,0,4) with natural frequencies 334 Hz, 919 Hz and 1670 Hz respectively. The divergent rates corresponding to these three mode are 0.297%, 0.325% and 0.047%. These positive divergent rates traduce the fact that negative damping η_c added by the frictional contact with the rail is greater than the modal damping factor ($\xi = 0.01\%$ for these modes). As expected for this 1-DOF model, the unstable mode (a,0,6) found in previous chapter due to the modes coupling is not found here. This result is coherent with the fact that the fundamental frequencies correspond to axial wheel modes with zero nodal circles from literature review [5, 8] and the result of the previous chapter.

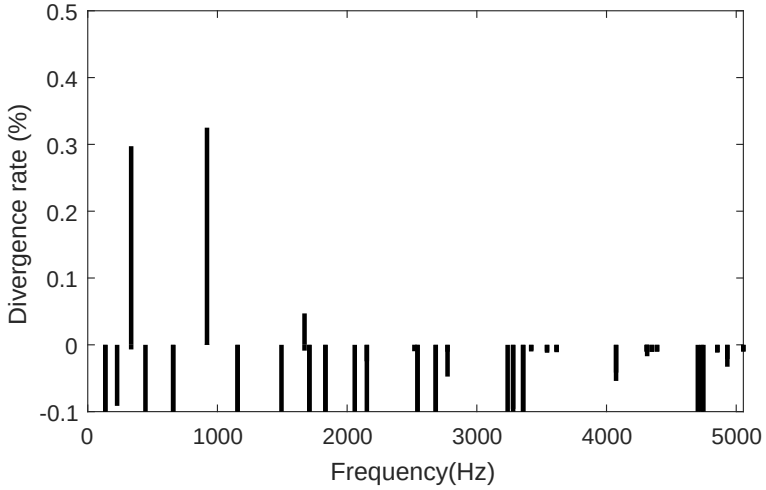

Figure 3.5: Divergence rates obtained with the 1-DOF model in the reference case

Fig. 3.6 shows the imaginary part of the complex rail vertical stiffness k_r, the stiffness of the series springs k_v and the complex stiffness due to the contact, the friction, the wheel modal amplitudes and the rail vertical dynamic K_c corresponding to the unstable modes. The imaginary parts of k_r and k_v are not negative. The imaginary parts of k_r and k_v do not therefore decide the sign of damping η_c. From Eq. (3.9), the sign of η_c then only depends on the sign of $\left(\Phi_{zw}^2 - \mu \text{sign}(s_{yo})\Phi_{yw}\Phi_{zw}\right)$.

3.3.2 Bifurcation curves

Since $\text{Imag}(k_v) > 0$, the analytical expression of the critical friction coefficient can be also deduced for $\xi_c < 0$ in Eq. (3.13):

$$\text{sign}(s_{yo})\Phi_{zw}\Phi_{yw}\mu > (\Phi_{zw})^2 + \frac{2\xi_w\Omega^2}{\text{Imag}(k_v)} \tag{3.18}$$

A necessary condition for the system to become unstable is :

$$\text{sign}(s_{yo})\Phi_{zw}\Phi_{yw} > 0 \tag{3.19}$$

In this case, the critical friction coefficient is then given by:

$$\mu = \frac{1}{\text{sign}(s_{yo})\Phi_{zw}\Phi_{yw}}\left(\Phi_{zw}^2 + \frac{2\xi_w\Omega^2}{\text{Imag}(k_v)}\right) \tag{3.20}$$

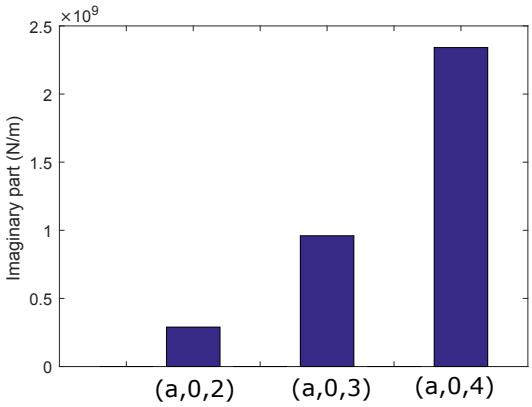

(a) k_r

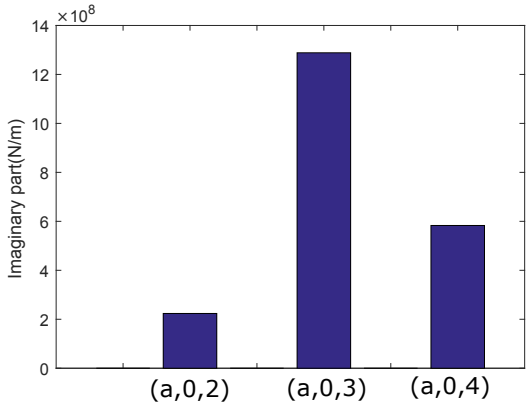

(b) k_v

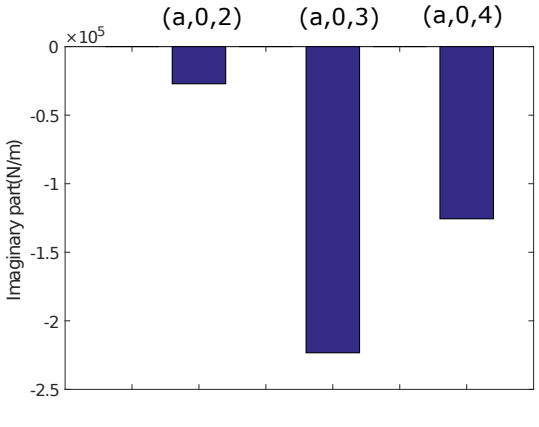

(c) K_c

Figure 3.6: Imaginary part of the complex stiffnesses k_r, k_v and K_c in the reference case

This equation shows that the critical friction coefficient is small for the high lateral modal amplitude Φ_{yw} corresponding to axial wheel modes.

While the other parameters are maintained constant, the bifurcation curves of the unstable modes are represented in Figs. 3.7 to 3.9. The critical friction coefficient from which the system becomes unstable are respectively 0.06, 0.08, 0.15 for the wheel modes (a,0,2) , (a,0,3) and (a,0,4). In comparison with the results of the previous chapter, the critical friction coefficients for the unstable modes are not so different ($\mu = 0.06$, $\mu = 0.09$ and $\mu = 0.22$ respectively).

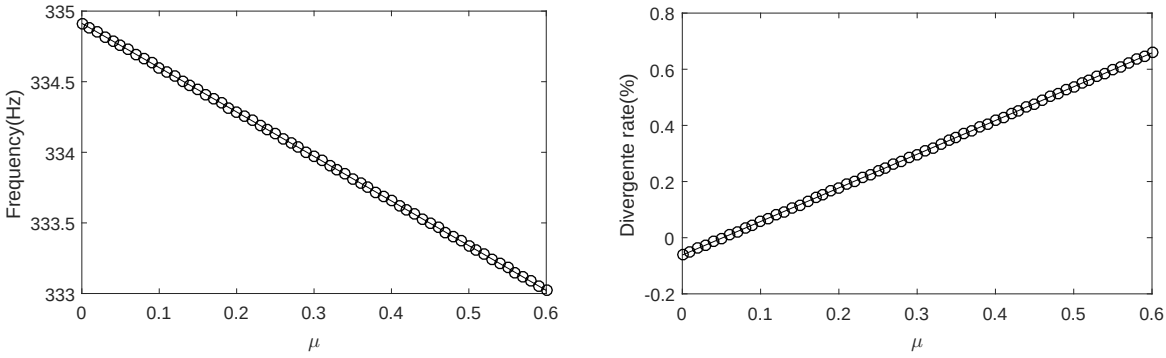

(a) Frequency (b) Divergence rate

Figure 3.7: Bifurcation curves of the unstable complex mode (a,0,2) for the 1-DOF model

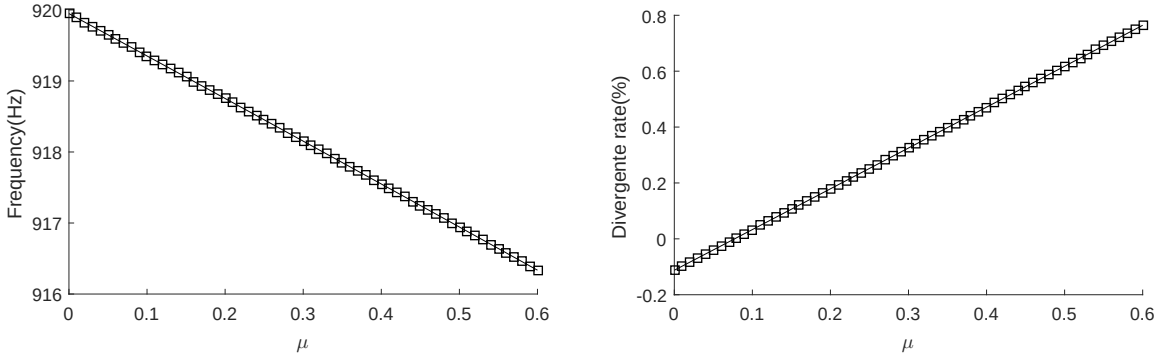

(a) Frequency (b) Divergence rate

Figure 3.8: Bifurcation curves of the unstable complex mode (a,0,3) for the 1-DOF model

Figs. 3.7 to 3.9 show the linear evolution of the divergence rate of the unstable modes since the relation between the imaginary part of K_c and μ is linear (Eq. (3.9)). The model in the previous chapter gives similar results.

3.3.3 Effect of the contact position on the wheel and creepage sign

Like in the previous chapter, one supposes that the lateral contact position on the rail does not change. Only the $y-$ coordinate of the contact point on the wheel is varied. Two cases are also tested:

- $\Delta V_y > 0$ corresponding to the sliding of the inner wheel,
- $\Delta V_y < 0$ corresponding to the sliding of the outer wheel.

The other parameters are maintained constant.

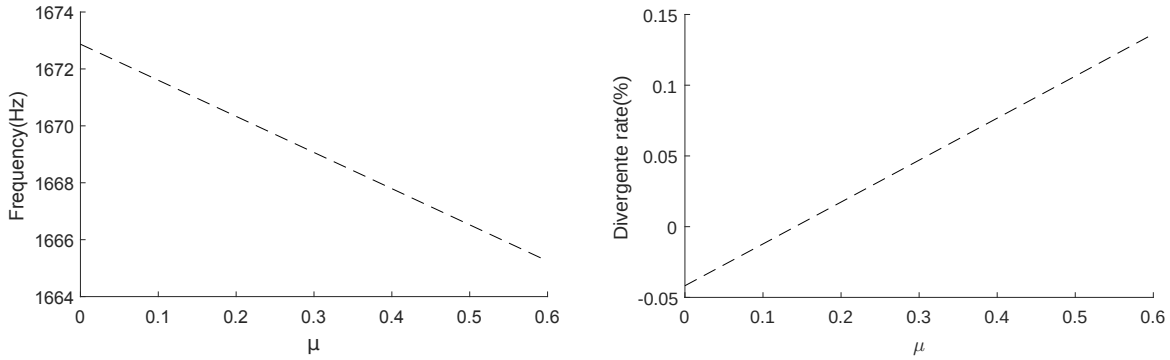

(a) Frequency (b) Divergence rate

Figure 3.9: Bifurcation curves of the unstable complex mode (a,0,4) for the 1-DOF model

Fig. 3.10 shows the contact amplitudes of the wheel modes as a function of the lateral contact position. Of course, the lateral amplitudes are greater than the vertical amplitudes. These lateral amplitudes are almost constant around 0.1 m whereas the vertical amplitudes increase and their sign change when the contact position moves towards the wheel flange.

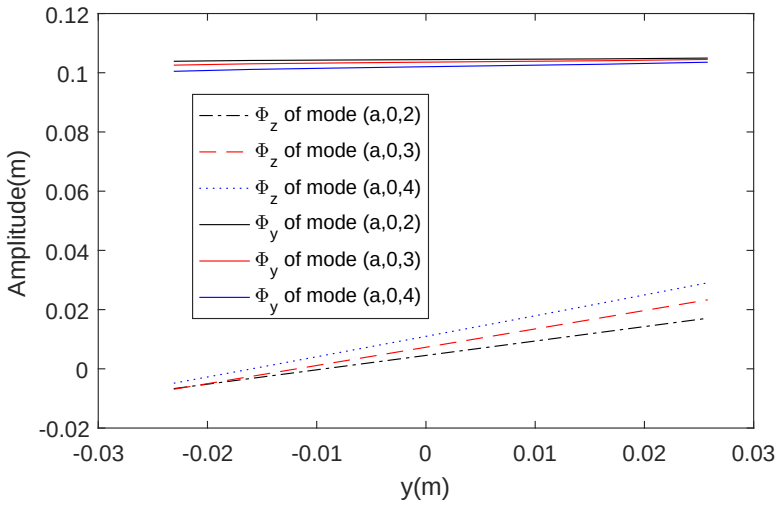

Figure 3.10: Modal amplitude of wheel modes in contact zone

Fig. 3.11 shows that the occurrence of instability depends on the lateral contact position y_0 and the lateral sliding direction of the wheel. In the case of sliding of the inner wheel which traduces that $\Delta V_y > 0$, there are more instability if the contact position is near the wheel flange. However, in the case of sliding of the outer wheel which traduces that $\Delta V_y < 0$, there are more instability if the contact position is far the wheel flange. The curves obtained in the previous chapter are very similar. These results get close to the ones of De Beer's model [9] where instability occurs only for $y_0 \times \text{sign}(sy) > 0$.

Fig. 3.11 verifies also the necessary condition for the unstable system $\text{sign}(s_{yo})\Phi_{zw}\Phi_{yw} > 0$ in Eq. (3.19). The lateral sliding direction combined with the local dynamics of the wheel therefore play an important role for the occurrence of instability.

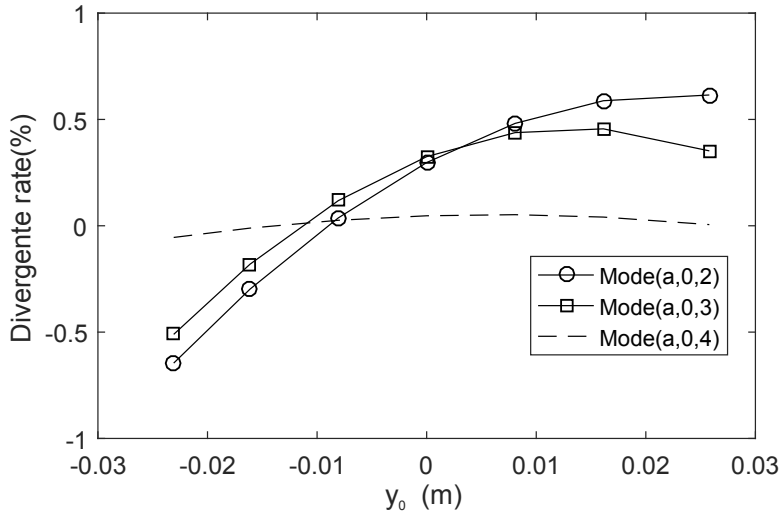

(a) $\Delta V_y > 0$

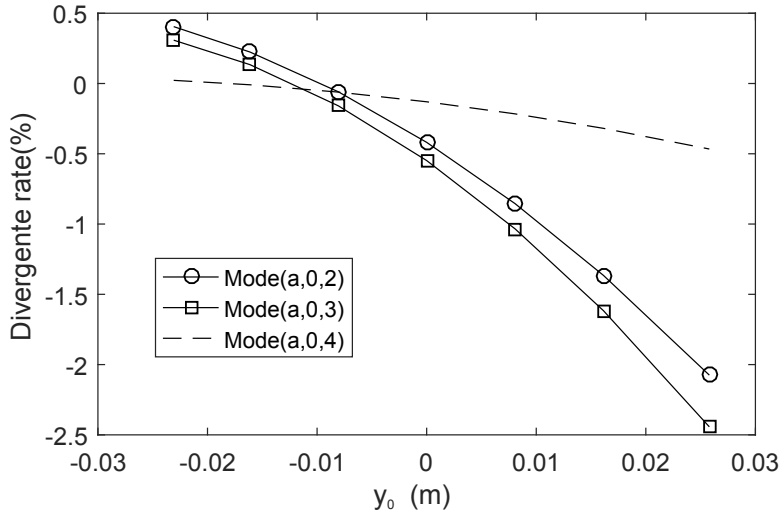

(b) $\Delta V_y < 0$

Figure 3.11: Divergence rates as a function of the lateral contact position on wheel for the 1-DOF model

3.3.4 Effect of the wheel modal damping

With the parameters of the reference case, there are four unstable modes corresponding to three axial wheel modes: (a,0,2) , (a,0,3) and (a,0,4). When $\xi_c > 0$ which traduces the fact that the modal damping of these axial wheel modes is superior than its associated negative damping η_c of 0.22, 0.17 and 0.06 % respectively, these modes become stable.

When the parameters of the reference case are maintained constant and the modal damping factors of the corresponding axial wheel modes (a,0,2), (a,0,3) and (a,0,4) reach 0.23%, 0.18% and 0.06% respectively, the associated complex modes become stable (Fig. 3.12). Thus, squeal reduces when the involved axial wheel modal damping increases. In comparison with the results of chapter 2, these critical damping are not so different (0.2%, 0.15% and 0.02% respectively).

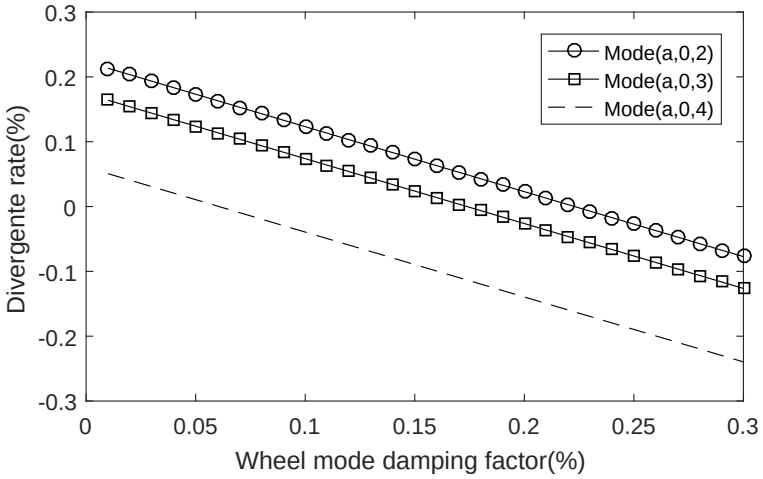

Figure 3.12: Divergence rates as a function of the modal damping factors of the free wheel for the 1-DOF model

3.3.5 Effect of the vertical pad stiffness

While the parameters of the reference case are maintained constant and the vertical pad stiffness increases, the divergence rates of the unstable modes (a,0,2) and (a,0,3) decrease greatly as shown in Fig. 3.13. The divergence rate of the unstable mode (a,0,4) firstly decreases then increases. These results are similar to those obtained in the previous chapter.

To clarify the results, Fig. 3.14 shows the imaginary part of rail stiffness k_r and stiffness k_v as a function of vertical pad stiffness k_{pad} at the frequencies of unstable axial wheel modes. An increase of the vertical pad stiffness implies a decrease of rail stiffness k_r but this is not the case for for k_v. A decrease of the imaginary part of k_r does not always imply that the imaginary of k_v decreases because of the nonlinear relation between k_v and k_r. Thus, although it is seems to be rather favorable for the stability, an increase of the vertical pad stiffness can not therefore eliminate all instabilities.

3.4 Conclusion

In this chapter, the stability analysis of a simple 1-DOF wheel/rail interaction model in curve is performed. The wheel is represented by only one free mode and the rail is modeled by a complex stiffness computed by using Euler beam model in vertical bending. Coulomb's friction law and linearized Hertzian normal contact are considered under the assumption of full sliding. Results show that instability may occur in the case of a constant friction coefficient without mode coupling. Wheel axial modes with $(2,3,4)$ nodal diameters and 0 nodal circle are found to be unstable in the numerical application. As in

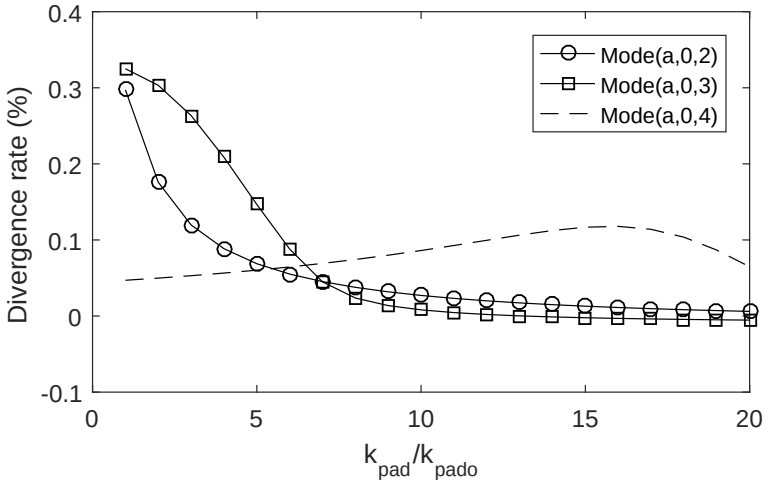

Figure 3.13: Influence of the pad vertical stiffness on the unstable complex modes

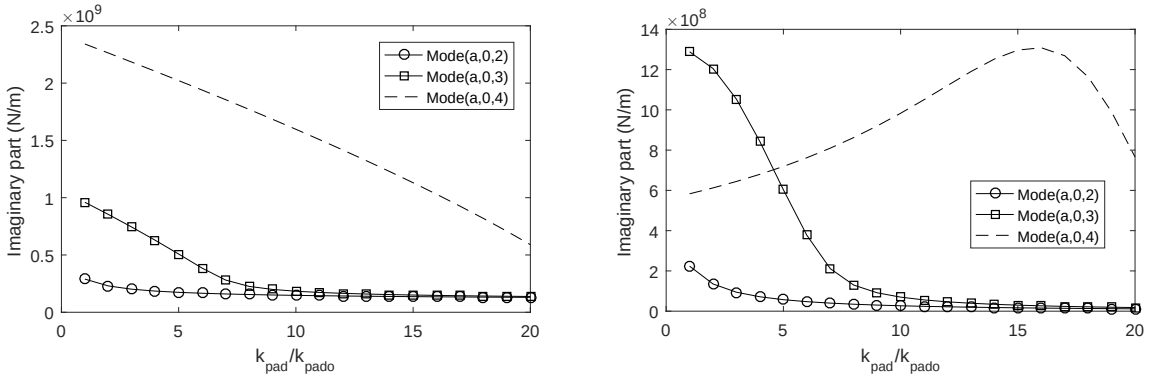

(a) k_r (b) k_v

Figure 3.14: Imaginary part of the rail stiffness k_r and of the stiffness k_v as a function of k_{pad}

chapter 2, the influence of kinematic parameters on the occurrence of instability is also established. It is found that the occurrence of instability depends greatly on friction coefficient, contact position, wheel modal damping and stiffness of the rail support. The results are very similar to those obtained by the model developed in chapter 2 for the instabilities without mode coupling.

Concerning instability mechanism, the role of the rail vertical dynamics on curve squeal occurrence is clarified. It is pointed out that the imaginary part of the complex stiffness of the rail, induced by the phase shift of the propagating wave but also by pad and rail damping plays an critical role in the instability mechanism since it is converted into negative damping by friction in some cases. This negative damping may then destabilize the system, leading to self-sustained vibration and squeal.

Part II

Development of a full FE frictional rolling contact model

FE models for friction-induced vibrations of rolling contact systems

Contents

4.1 Introduction

In the case of friction-induced vibrations in curves characterized by large slips, high frequency dynamics and very fast evolutions in the contact zone, the instability occurrence of instabilities in wheel/rail frictional rolling systems in curve can be predicted with a point contact model and proves to be qualitatively coherent with experimental observations. However, for the prediction of the self-sustained nonlinear vibrations resulting from the instabilities, point contact models are no longer sufficient. Indeed, average linear creep/friction laws are derived only under quasi-static assumptions. Therefore, surface contact models with discretization of the contact zone are more adapted. Surface-contact models which are used for instance in Pieringer's model [113] and Zenzerovic *et al.* [96,97] are based on the variational theory of Kalker [134]. The models use some simplifications, notably for the semi-analytical computation of the local contact flexibilities or influence functions (Boussinesq and Cerruti elastic half-space assumptions, contact/friction decoupling). The impact of these simplifications is however unknown. Actually, there is no full FE models able to simulate curve squeal in the literature although it would be useful to calculate reference solutions.

The aim of this chapter is to develop a full Finite Element (FE) computational method for the dynamics of frictional rolling contact systems, especially in order to calculate reference solutions for curve squeal models. Continuous equations of the problem are derived around the stationary position of rolling in an Eulerian reference frame. Local unilateral contact and Coulomb friction laws apply on the rolling interface. Weak formulation and FE discretization lead to a nonlinear discrete system which is solved in the time domain by a numerical integration and a fixed-point algorithm at each time step. In addition to the transient approach, a stability analysis performed around the sliding equilibrium position allows

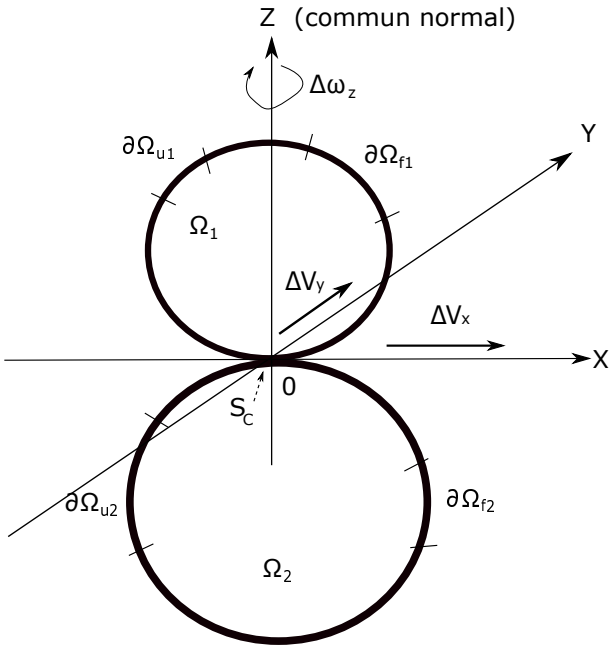

Figure 4.1: Two bodies in rolling contact

to determine unstable modes and frequencies. In order to obtain reasonable computation times, two reduction strategies are proposed. An application of the method to the frictional rolling contact between two annular cylinders is presented in both quasi-static and dynamic cases with and without mode coupling instabilities. The validation of the approach in quasi-static and dynamic conditions is carried out by comparison with CONTACT software. Reduction strategies are validated by comparison with the full method.

4.2 Finite Element (FE) formulation in the time-domain

4.2.1 Contact problem in the Eulerian frame

Two bodies in rolling contact are considered, as shown in Fig. 4.1. The conventions frequently used in rolling contact problems are adopted (cf. for instance [76]). The $z-$axis is chosen to coincide with the common normal to the two surfaces in contact, the longitudinal $x-$axis corresponds to the rolling direction and the $y-$axis refers to the lateral direction. The whole structure is decomposed into two subdomains $\Omega = \Omega_1 \cup \Omega_2$ where subscripts 1 et 2 stand for the upper and the lower bodies respectively. In the absence of deformation and sliding, material particles of each surface move through the contact region in a direction parallel to $x-$axis with rolling speed V. In case of sliding, relative lateral velocities $\Delta V_y = V_{y1} - V_{y2}$ and longitudinal velocities $\Delta V_x = V_{x1} - V_{x2}$ have to be considered. The bodies may also have a relative angular velocity $\Delta\Omega_z = \omega_{z1} - \omega_{z2}$ around their common normal (or spin).

According to [76], in the Eulerian frame which moves with the point of contact, the relative sliding instantaneous creepages between the two deformable bodies at a fixed point of the potential contact interface S_c are given by:

$$\begin{aligned} s_x &= \frac{v_{x1} - v_{x2}}{V} = s_{xo} - s_{wo} y - \left(\frac{\partial u_{x1}}{\partial x} - \frac{\partial u_{x2}}{\partial x}\right) + \frac{(\dot{u}_{x1} - \dot{u}_{x2})}{V} \\ s_y &= \frac{v_{y1} - v_{y2}}{V} = s_{yo} + s_{wo} x - \left(\frac{\partial u_{y1}}{\partial x} - \frac{\partial u_{y2}}{\partial x}\right) + \frac{(\dot{u}_{y1} - \dot{u}_{y2})}{V} \end{aligned} \tag{4.1}$$

where $\mathbf{u}(x,y,z,t)$ and $\mathbf{v}(x,y,z,t)$ denote respectively the displacement and velocity fields of the structure in the Eulerian frame, subscripts x and y stand for the spatial components of the fields and the notation

$\dot{u} = \frac{\partial u}{\partial t}$ refers to the time partial derivative. The terms involving $V\frac{\partial u}{\partial x}$ represent the deformation contributions due to rolling in the Eulerian frame whereas the terms involving $\dot{u}$ simply represent the dynamic contributions. s_{xo}, s_{yo} and s_{wo} are the imposed creepages as defined in Eq. (1.1).

In addition, a displacement $\mathbf{u_d}$ is prescribed on the part of the boundary of the domain $\delta\Omega_u = \delta\Omega_{u1} \cup \delta\Omega_{u2}$ and a surface load $\mathbf{f_s}$ is applied on the part $\delta\Omega_f = \delta\Omega_{f1} \cup \delta\Omega_{f2}$. In Ω, a volume load $\mathbf{f_d}$ can be also considered.

4.2.2 Frictional contact laws

To deal with contact and friction between the two bodies, non-smooth unilateral contact Signorini's law (Eqs. (1.4) and (1.5)) and Coulomb's friction law (Eqs. (1.6) and (1.7)) are respectively chosen.

4.2.3 Dynamics equations and FE discretization

A major consequence of the Eulerian reference frame is to induce convective terms in the equations of motion. These terms are only significant in the case where the rotational speed is in the order of magnitude of the eigenfrequencies ([125]). It is assumed that it is not the case in the present application and the effects of the convective terms are neglected in the following developments.

The displacement field $\mathbf{u}$ must verify the equations of continuum mechanics [135] together with the local formulations of contact equations Eqs. (1.5) and (1.7). In order to introduce FE approximations, the principle of virtual power is used for the system dynamics and the contact laws are written in weak forms [136]:

$$\begin{aligned} &\text{Find } \mathbf{u} \in \mathcal{U} \text{ and } \mathbf{r} \text{ such as } \forall \mathbf{u}^* \in \mathcal{U}^o \text{ and } \forall \mathbf{r}^* \\ &\int_\Omega \rho \mathbf{u}^*.\ddot{\mathbf{u}} d\Omega + \int_\Omega \varepsilon(\mathbf{u}^*) : \sigma(\mathbf{u}) d\Omega = \int_\Omega \mathbf{u}^*.\mathbf{f}_s d\Omega + \int_{\partial\Omega_F} \mathbf{u}^*.\mathbf{f}_d ds + \int_{S_c} \mathbf{u}^*.\mathbf{r} ds \\ &\int_{S_c} r_n^* r_n ds = \int_{S_c} r_n^* \text{Proj}_{\mathbb{R}^-}(r_n - \rho_n \Delta u_n) ds \\ &\int_{S_c} \mathbf{r}_t^* \mathbf{r}_t ds = \int_{S_c} \mathbf{r}_t^* \text{Proj}_C(\mathbf{r}_t - \rho_t V \mathbf{s_t}) ds \end{aligned} \tag{4.2}$$

where $\varepsilon(\mathbf{u})$ and $\sigma(\mathbf{u})$ stand respectively for the symmetric gradient and the stress tensor corresponding to any displacement field $\mathbf{u}$, the notation $\ddot{\mathbf{u}} = \frac{\partial^2 \mathbf{u}}{\partial t^2}$ refers to the double time partial derivative, $\mathcal{U} = \{\mathbf{u} | \mathbf{u} = \mathbf{u}_d \text{ on } \partial\Omega_u\}$ and $\mathcal{U}^0 = \{\mathbf{u} | \mathbf{u} = \mathbf{0} \text{ on } \partial\Omega_u\}$. $\mathbf{s_t}$ denote the tangential creepage defined in Eq. (4.1)

By using appropriate shape interpolation functions for unknown and test displacement and reaction fields $(\mathbf{u}, \mathbf{r}, \mathbf{u}^*, \mathbf{r}^*)$, finite element discretization of Eq. (4.2) directly gives:

$$\begin{aligned} &\mathbf{M}\ddot{\mathbf{U}} + \mathbf{C}\dot{\mathbf{U}} + \mathbf{K}\mathbf{U} = \mathbf{F} + \mathbf{P_n}^T \mathbf{R_n} + \mathbf{P_t}^T \mathbf{R_t} \\ &\mathbf{R_n} = \int_{S_c} \mathbf{N_n}^T \text{Proj}_{\mathbb{R}^-}(\mathbf{N_n}(\mathbf{H_n^{-1}} \mathbf{R_n} - \rho_n(\mathbf{P_n}\mathbf{U} - \mathbf{G})) ds \\ &\mathbf{R_t} = \int_{S_c} \mathbf{N_t}^T \text{Proj}_C(\mathbf{N_t}(\mathbf{H_t^{-1}} \mathbf{R_t} - \rho_t V \mathbf{S_t}(\mathbf{P_t}\mathbf{U}, \mathbf{P_t}\dot{\mathbf{U}}))) ds \end{aligned} \tag{4.3}$$

where $\mathbf{U}$, $\mathbf{R_n}$ and $\mathbf{R_t}$ denote respectively the vectors of nodal displacements, equivalent normal reactions and equivalent friction forces, $\mathbf{M}, \mathbf{C}, \mathbf{K}$ are respectively the mass, damping and stiffness matrices of the structure without contact, $\mathbf{G}$ is the vector of nodal initial gaps and $\mathbf{N_n}, \mathbf{N_t}$ are the shape function vectors on the contact interface. In addition, $\mathbf{P_n}, \mathbf{P_n}$ are matrices allowing to pass the contact reactions from the local relative frame to the global frame whereas $\mathbf{H_n} = \int_{S_c} \mathbf{N_n}^T \mathbf{N_n} ds$ and $\mathbf{H_t} = \int_{S_c} \mathbf{N_t}^T \mathbf{N_t} ds$ are transformation matrices from nodal to equivalent forces. Finally, $\mathbf{S_t}(\mathbf{P_t}\mathbf{U}, \mathbf{P_t}\dot{\mathbf{U}})$ denotes the vector of nodal creepages which can be determined linearly from local displacement and velocity vectors, taking into account quasi-static creep velocities (cf. Eq. (4.1)).

4.3 Reduction strategies

As the size of the system is often large and the nonlinear solving process implies several resolutions of a linear system at each time step, reducing the size of the system is necessary to obtain reasonable computation times. The principle is to search an approximated solution $\mathbf{U} = \mathbf{B}\mathbf{q_r}$ of the problem spanned by a reduced basis $\mathbf{B}$ which leads to a reduced dynamics equation:

$$\mathbf{M_r}\ddot{\mathbf{q}}_\mathbf{r} + \mathbf{C_r}\dot{\mathbf{q}}_\mathbf{r} + \mathbf{K_r}\mathbf{q_r} = \mathbf{B}^T(\mathbf{F} + \mathbf{P_n}^T\mathbf{R_n} + \mathbf{P_t}^T\mathbf{R_t}) \tag{4.4}$$

where $\mathbf{M_r}, \mathbf{C_r}, \mathbf{K_r} = \mathbf{B}^T(\mathbf{M_r}, \mathbf{C_r}, \mathbf{K_r})\mathbf{B}$ and the size of the system is reduced to the number of modes in basis $\mathbf{B}$.

In the context of nonlinear dynamics, many reduction methods have been developed in recent years like using for instance the concept of nonlinear modes [72] or proper orthogonal decomposition POD [137]. However these techniques required considerable computational effort. In this paper, the proposed basis is rather classical and is based on an *a priori* selection of free-interface normal modes enriched by static local modes.

4.3.1 Component Mode Synthesis (CMS) with free-interface modes

A first reduction basis includes free-interface normal modes of the structure and static attachment modes $\mathbf{B} = [\Phi \quad \Phi_s]$. Matrix Φ contains the real solutions of the free and undamped system:

$$(\mathbf{K} - \omega^2\mathbf{M})\mathbf{U} = \mathbf{0} \tag{4.5}$$

whereas Φ_s make the base statically complete by adding static solutions to unitary forces (normal and tangential) on the contact interface:

$$\mathbf{K}\Phi_s = \mathbf{P_c}^T \tag{4.6}$$

where $\mathbf{P_c}^T = [\mathbf{P_n}^T \quad \mathbf{P_t}^T]$. In order to improve the numerical efficiency, the basis is then orthogonalized in relation to stiffness matrix $\mathbf{K}$ before use. It is well-known that static attachment modes are useful to provide a better approximation of the dynamics by comparison with normal modes alone. It is also worth noticing that the size of the basis is $n_m + 3n_c$ where n_m is the number of normal modes taken into account in the frequency range of interest and n_c is the number of facing nodes on the interface.

4.3.2 Contact static approximation

A stronger approximation consists in neglecting the dynamic terms in the reduced equations corresponding to attachment modes. However, bases Φ and Φ_s are not orthogonal which is a necessary condition in order to separate the contributions of normal modes and attachments modes. This can be fixed by using residual attachment modes defined by:

$$\tilde{\Phi}_s = \Phi_s - \Phi(\Phi^T\mathbf{K}\Phi)^{-1}\Phi^T\mathbf{P_c}^T \tag{4.7}$$

These modes are the static displacement responses to unit contact reactions after the elimination of the contribution of normal modes. It can be easily verified that $\tilde{\Phi}_s^T\mathbf{K}\Phi = \mathbf{0}$.

The use of basis $\mathbf{B} = [\Phi \quad \tilde{\Phi}_s]$ in Eq. (4.4) together with the elimination of the dynamic terms relating to attachments modes gives:

$$\begin{aligned} \Phi^T\mathbf{M}\Phi\ddot{\mathbf{q}} + \Phi^T\mathbf{C}\Phi\dot{\mathbf{q}} + \Phi^T\mathbf{K}\Phi\mathbf{q} &= \Phi^T(\mathbf{F} + \mathbf{P_n}^T\mathbf{R_n} + \mathbf{P_t}^T\mathbf{R_t}) \\ \tilde{\Phi}_s^T\mathbf{K}\tilde{\Phi}_s\mathbf{q_s} &= \tilde{\Phi}_s^T(\mathbf{F} + \mathbf{P_n}^T\mathbf{R_n} + \mathbf{P_t}^T\mathbf{R_t}) \end{aligned} \tag{4.8}$$

where $\mathbf{q}$ and $\mathbf{q_s}$ are the generalized coordinate vectors corresponding respectively to normal modes and residual attachment modes such that $\mathbf{U} = \Phi\mathbf{q} + \tilde{\Phi}_s\mathbf{q_s}$. A total decoupling between the generalized equations corresponding to free-interface normal modes and residual static attachment modes is obtained.

In addition, noticing that:

$$\begin{aligned}\tilde{\Phi}_s^T \mathbf{K} \tilde{\Phi}_s \mathbf{q_s} &= (\Phi_s^T - \mathbf{P_c}\Phi(\Phi^T\mathbf{K}\Phi)^{-1}\Phi^T)\mathbf{K}(\Phi_s - \Phi(\Phi^T\mathbf{K}\Phi)^{-1}\Phi^T{\mathbf{P_c}}^T)\mathbf{q_s} \\ &= (\mathbf{P_c}\Phi_s - \mathbf{P_c}\Phi(\Phi^T\mathbf{K}\Phi)^{-1}\Phi^T{\mathbf{P_c}}^T)\mathbf{q_s} \\ &= \mathbf{P_c}\tilde{\Phi}_s\mathbf{q_s} \\ &= \mathbf{P_c}(\mathbf{U} - \Phi\mathbf{q})\end{aligned} \tag{4.9}$$

and including the above expression in Eq. (4.4) gives:

$$\begin{aligned}\Phi^T\mathbf{M}\Phi\ddot{\mathbf{q}} + \Phi^T\mathbf{C}\Phi\dot{\mathbf{q}} + \Phi^T\mathbf{K}\Phi\mathbf{q} &= \Phi^T(\mathbf{F} + {\mathbf{P_n}}^T\mathbf{R_n} + {\mathbf{P_t}}^T\mathbf{R_t}) \\ \mathbf{P_c}\mathbf{U} &= \tilde{\Phi}_s^T(\mathbf{F} + {\mathbf{P_n}}^T\mathbf{R_n} + {\mathbf{P_t}}^T\mathbf{R_t}) + \mathbf{P_c}\Phi\mathbf{q}\end{aligned} \tag{4.10}$$

It must be emphasized that, with this formulation, contact displacements $\mathbf{P_c}\mathbf{U}$ can be directly calculated from expanded forces and normal modes coordinates.

This reduction strategy consists in solving the global dynamics using free-interface normal modes and adding a local static residual flexibility controlled by matrix $\tilde{\Phi}_s^T$ in the expression of the contact displacements. This allows to determine the contact displacements with a high precision level which is needed to solve the frictional contact laws and calculate the reaction forces. This method gets very close to models such as Pieringer's one [113] combining modal dynamics and static local resolutions of the kind of CONTACT software. However, in the proposed method, the local flexibility is calculated numerically by finite elements instead of using semi-analytical influence functions derived from Boussinesq's approximations. In particular, it takes into account the static normal/tangential coupling in the contact zone. It also depends on the number of free-interface modes in the basis since it corresponds to a residual flexibility.

4.4 Stability analysis

The aim of the stability analysis is to address the mechanism of self-excited vibration due to frictional contact through the determination of the evolution of small perturbations around the steady sliding equilibrium. In stable cases, the perturbations vanish and no vibration occurs. In unstable cases, some perturbations tend to diverge which can lead to self-sustained vibrations. Such an analysis is performed by a linearization of the non-linear equations around the equilibrium.

4.4.1 Quasi-static equilibrium

The quasi-static or steady sliding equilibrium is first obtained by neglecting the dynamic terms in Eqs. (4.1) and (4.3):

$$\begin{aligned}\mathbf{K}\mathbf{U^e} &= \mathbf{F} + \mathbf{P_n^T}\mathbf{R_n^e} + \mathbf{P_t^T}\mathbf{R_t^e} \\ \mathbf{R_n^e} &= \int_{S_c} \mathbf{N_n^T}\mathrm{Proj}_{\mathbb{R}^-}(\mathbf{N_n}(\mathbf{H_n^{-1}}\mathbf{R_n^e} - \rho_n(\mathbf{P_n}\mathbf{U^e} - \mathbf{G})))ds \\ \mathbf{R_t^e} &= \int_{S_c} \mathbf{N_t^T}\mathrm{Proj}_C(\mathbf{N_t}(\mathbf{H_t^{-1}}\mathbf{R_t} - \rho_t\mathbf{S_t^e})ds\end{aligned} \tag{4.11}$$

where $\mathbf{S_t^e} = \mathbf{S_t}(\mathbf{P_t}\mathbf{U^e}, \mathbf{0})$ is the vector of nodal quasi-static creepages.

Assuming that some solutions of Eq. (4.11) exist and can be calculated, it notably provides the status of the nodes on the contact interface as a function of the equivalent normal reactions r_n^e and friction forces $\mathbf{r}_t^e$:

- if $r_n^e = 0$, the facing nodes are not in contact,
- if $r_n^e \neq 0$ and $\|\mathbf{r_t^e}\| < -\mu r_n^e$ the facing nodes are sticking,

- if $r_n^e \neq 0$ and $\|\mathbf{r}_t^e\| = -\mu r_n^e$ the facing nodes are sliding ; the sliding direction of the friction force is then given by $\mathbf{t} = \mathbf{r}_t^e / \|\mathbf{r}_t^e\|$.

4.4.2 Complex Eigenvalue Analysis (CEA) in case of full steady sliding

In this paper, stability analysis is only carried out in the case of full steady sliding (no sticking region) and maintained contact configuration: it is thus assumed that for each node in contact at equilibrium, bilateral contact and sliding Coulomb friction laws apply. In order to perform the stability analysis, these laws have to be linearized. On effective contact region, the linearized forms of Eqs. (1.5) and (1.7) with the above assumptions can be written (cf. for instance [41]):

$$\begin{aligned} \Delta u_n &= 0 \\ \mathbf{r}_t &= -\mu r_n \mathbf{t} - c_b \dot{u}_b \mathbf{b} \end{aligned} \tag{4.12}$$

where $c_b = -\mu r_n^e / \|\mathbf{S}_t^e\|$ is a damping term due to the linearisation of the sliding direction of the friction force and $\mathbf{b}$ is the tangential direction orthogonal to $\mathbf{t}$.

Searching a discrete solution of the form $\mathbf{U^e} + \tilde{\mathbf{U}}\exp(\lambda t)$ where $\tilde{\mathbf{U}}$ stands for the complex displacement vector corresponding to small harmonic perturbations around the equilibrium, the linearized form of equation (4.3) leads to a constrained non symmetric eigenvalues problem:

$$\begin{aligned} (\lambda^2 \mathbf{M} + \lambda(\mathbf{C} + \mathbf{C_b}) + \mathbf{K})\tilde{\mathbf{U}} &= (\tilde{\mathbf{P}}_\mathbf{n}^T + \mu \tilde{\mathbf{P}}_\mathbf{t}^T)\tilde{\mathbf{R}}_\mathbf{n} \\ \tilde{\mathbf{P}}_\mathbf{n}\tilde{\mathbf{U}} &= 0 \end{aligned} \tag{4.13}$$

where $\mathbf{C_b}$ is the damping matrix provided by the linearisation of the sliding direction of friction force [21, 22, 41] and $\tilde{\mathbf{P}}_\mathbf{n}, \tilde{\mathbf{P}}_\mathbf{t}$ are new projections matrices such that $\tilde{\mathbf{P}}_\mathbf{n}$ is the restriction of $\mathbf{P_n}$ on nodes in the effective contact region at equilibrium whereas $\tilde{\mathbf{P}}_\mathbf{t}$ is the restriction of $\mathbf{P_t}$ on components in direction $\mathbf{t}$ on nodes in the effective contact region.

Complex modes and eigenvalues of the problem are then calculated. Modes corresponding to eigenvalues with positive real part are unstable. The divergence rate of a mode is notably defined as $\mathrm{Re}(\lambda)/\mathrm{Im}(\lambda)$ where $(\mathrm{Re}(\lambda), \mathrm{Im}(\lambda))$ are respectively the real and imaginary parts (pulsation) of the mode. This rate corresponds to a negative damping rate.

4.4.3 Reduced CEA formulations

Solving such a large non-symmetric eigenvalue problem needs model reduction. Several reduction bases have been notably tested by following the methodology proposed by Brizard [41]. The two reductions strategies proposed in the nonlinear case (section 4.3) are adapted here for the stability analysis.

4.4.3.1 Component Mode Synthesis with free-interface modes

The first reduced basis includes free-interface normal modes of the structure and static attachment modes $\mathbf{B} = [\Phi \quad \Phi_s]$ as proposed in section 4.3 but defined on effective contact region by using $\tilde{\mathbf{P}}_\mathbf{n}$ and $\tilde{\mathbf{P}}_\mathbf{t}$ instead of $\mathbf{P_n}$ and $\mathbf{P_t}$. In order to solve the eigenvalue problem with this reduced basis, the constraints are directly added to the generalized coordinates associated to the modes (cf. [46, 47] for symmetric normal problems and [21, 41] for non-symmetric friction problems)

4.4.3.2 Contact static approximation

The stronger approximation consisting in neglecting the dynamic part of the attachments modes is also tested for the stability analysis. The same technique used in section 4.3 is applied. The reduction is first performed with basis $\mathbf{B} = [\Phi \quad \tilde{\Phi}_s]$ composed of free-interface component modes Φ and static

attachment residual modes $\tilde{\Phi}_s$ defined on effective contact region. The dynamic effects corresponding the residual attachment modes are then neglected leading to the following constrained eigenvalue problem:

$$\begin{aligned}(\lambda^2\Phi^T\mathbf{M}\Phi+\lambda\Phi^T(\mathbf{C}+\mathbf{C_b})\Phi+\Phi^T\mathbf{K}\Phi)\tilde{\mathbf{q}} &= \Phi^T(\tilde{\mathbf{P}}_\mathbf{n}^T+\mu\tilde{\mathbf{P}}_\mathbf{t}^T)\tilde{\mathbf{R}}_\mathbf{n}\\ \tilde{\mathbf{P}}_\mathbf{c}\tilde{\mathbf{U}} &= \tilde{\Phi}_s^T(\tilde{\mathbf{P}}_\mathbf{n}^T+\mu\tilde{\mathbf{P}}_\mathbf{t}^T)\tilde{\mathbf{R}}_\mathbf{n}+\tilde{\mathbf{P}}_\mathbf{c}\Phi\tilde{\mathbf{q}}\\ \tilde{\mathbf{P}}_\mathbf{n}\tilde{\mathbf{U}} &= \mathbf{0}\end{aligned} \tag{4.14}$$

where $\tilde{\mathbf{q}}$ is the generalized vector corresponding to free-interface normal modes.

From the two last lines of Eq. (4.14), normal reactions $\tilde{\mathbf{R}}_\mathbf{n}$ can be expressed as a function of the generalized vector $\tilde{\mathbf{q}}$:

$$\tilde{\mathbf{R}}_\mathbf{n} = -(\mathbf{I}_n\tilde{\Phi}_s^T(\tilde{\mathbf{P}}_\mathbf{n}^T+\mu\tilde{\mathbf{P}}_\mathbf{t}^T))^{-1}\tilde{\mathbf{P}}_\mathbf{c}\Phi\tilde{\mathbf{q}} \tag{4.15}$$

where $\mathbf{I}_n$ is the boolean localization matrix such that $\tilde{\mathbf{P}}_\mathbf{n}=\mathbf{I}_n\tilde{\mathbf{P}}_\mathbf{c}$. Finally, using the above expression in the reduced eigenvalue problem gives:

$$(\lambda^2\Phi^T\mathbf{M}\Phi+\lambda\Phi^T(\mathbf{C}+\mathbf{C_b})\Phi+\Phi^T(\mathbf{K}+\mathbf{K_c})\Phi)\tilde{\mathbf{q}}=\mathbf{0} \tag{4.16}$$

where $\mathbf{K_c}$ is a non-symmetric stiffness matrix taking account the effect of the local residual flexibility of the structure due to normal and friction forces:

$$\mathbf{K_c} = (\tilde{\mathbf{P}}_\mathbf{n}^T+\mu\tilde{\mathbf{P}}_\mathbf{t}^T)(\mathbf{I}_n\tilde{\Phi}_s^T(\tilde{\mathbf{P}}_\mathbf{n}^T+\mu\tilde{\mathbf{P}}_\mathbf{t}^T))^{-1}\tilde{\mathbf{P}}_\mathbf{n} \tag{4.17}$$

This reduction strategy consists in solving the global dynamics using free-interface normal modes and adding a local static residual stiffness controlled by matrix $\mathbf{K_c}$. This matrix plays the same role than the 2-DOF Hertzian stiffness/Coulomb friction relations in the case on equivalent point contact models but is calculated by finite elements.

4.5 Numerical methods for nonlinear simulations

For the determination of quasi-static and transient solutions from Eqs. (4.3) and (4.11), with or without reduction, the following numerical methods are used.

4.5.1 Integration scheme for the dynamics

For the computation of the transient solution, the chosen time integration method is a modified θ-method. This is a first-order scheme developed by Jean [62] and appropriate to unilateral contact dynamics. It notably allows to compute quasi-inelastic shocks. A value $\theta = 0.5$ is chosen to avoid numerical damping. The detail of the scheme with an application to friction-induced vibrations can be found for instance in Loyer's work [21].

4.5.2 Non-linear resolution

For the computation of the quasi-static solution and dynamics solutions at each time step, an iterative fixed point algorithm on equivalent contact reactions and friction forces is used with a stop criterion based on forces convergence [21]. This algorithm is appropriate to the formulation of the frictional contact laws as nonlinear projections. The main advantage of the fixed point algorithm is that the integrator matrix remains constant at each iteration. In the simulations presented in this paper, the augmented parameters ρ_n, ρ_t are chosen as the smallest eigenvalue of the integrator matrix condensed on the contact degrees of freedom [138]. More optimized parameters can be found in [21] but have not been used.

Table 4.1: Material and geometrical parameters of the cylinders

Young's modulus	205 GPa
Poisson's ratio	0.3
Density	7800 kg/m^3
Rayleigh's damping coefficients (α, β)	$(0.1, 10^{-5})$
Internal rayon	0.1 m
External rayon	0.5 m
Thickness	0.05 m

4.6 Application to contact between 2 annular cylinders

A rolling contact between two same annular cylinders is considered, as shown in Fig. 4.2. The material behavior is assumed to be linearly elastic, isotropic and undergoing small deformations. A Rayleigh damping with coefficients α and β is introduced in the model. The material and geometrical parameters of the cylinders are listed in Tab. 4.1.

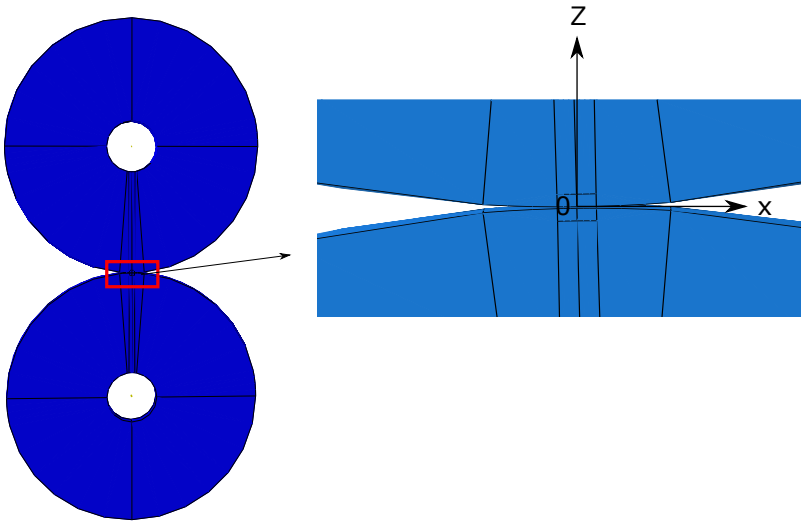

Figure 4.2: Contact between two annular cylinders

A vertical displacement u_{z0} is applied at the hub of the upper cylinder whereas a rigid constraint is applied at the lower cylinder. For the discretization by finite elements, compatible meshes on the interface are considered: facing nodes of the two cylinders in potential contact have identical tangential coordinates y and y. The potential contact area is meshed with elements of length 1 mm as shown in Fig. 4.3.

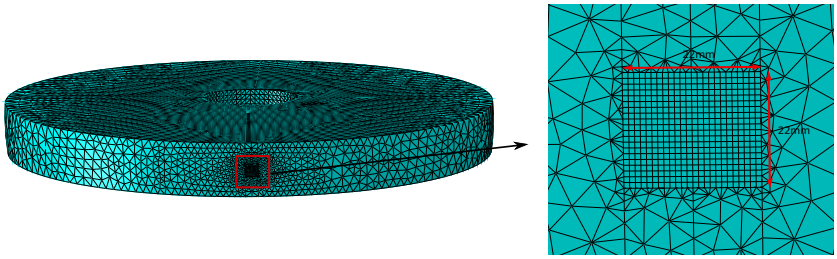

Figure 4.3: FE model of a cylinder with fine mesh on the contact zone

4.6.1 Free-interface normal modes

The 75 first natural frequencies and corresponding free-interface modes have been calculated up to 7310 Hz. The eigenmodes are classified according to their predominant deformations (axial, radial or circumferential) and their numbers (n,m) of nodal diameters and nodal circles. Two modes are represented in Fig. 4.4. This classification is necessary to obtain a convergence of eigenvalues depending on the model mesh.

(a) Axial mode (0,2) (316 Hz) (b) Radial mode (0,3)(3695 Hz)

Figure 4.4: Examples of free eigenmodes of a cylinder

4.6.2 Reduced bases

The two reduction strategies presented in section 4.3 are tested using 150 free-interface normal modes in the frequency range up to 7310 Hz and 1323 residual attachment modes corresponding to 1323 degrees of freedom on the potential contact interface. For the classical CMS method, a reduced integrator matrix of size 1473×1473 is then obtained while the size of the initial matrix is 239358×239358. This reduced matrix is full but may be factorized before the iterative computation. The problem is therefore reduced. For the contact static approximation, the size of the integrator matrix is reduced to 150×150 which induces a high gain in computation times and in memory.

4.7 Quasi-static results

In this section the quasi-static rolling contact of the two cylinders with lateral creepage is considered. The contact zone is supposed to be laterally centered. As shown in Fig. 4.5, the geometry of the lateral profiles of the two cylinders has been curved in order to obtain an effective 3-dimensional contact. For each cylinder the applied radius of curvature is 0.5 m. The rolling is performed in the $-x$ direction with $V = 10$ m/s. An vertical displacement $u_{z0} = 0.1$ mm is applied leading to a resultant vertical contact force of about 75 kN. A friction coefficient $\mu = 0.3$ is considered.

Three cases of longitudinal, lateral and spin creepages are performed and compared with CONTACT software in the following subsections.

4.7.1 Longitudinal creepage

For an imposed lateral creepage $\Delta V_x/V = 0.3\%$ and other creepages set to zero, the longitudinal distributions of the normal contact stresses and frictional stresses on the center line of the contact zone

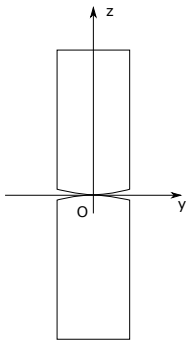

Figure 4.5: Lateral curvatures of the cylinders and contact point in center

($y = 0$) are presented in Fig. 4.7. As expected, a stick zone occurs at the leading edge of the contact and a slip zone occurs at the trailing edge of the contact (Fig. 4.6). The comparison of the results obtained with the proposed full FE method and the results provided by CONTACT software shows a good agreement with some small differences for the tangential stresses in the transition between the stick zone and the slip zone Fig. 4.7. The difference is 3% in terms of maximal normal contact reaction. The dimensions of effective contact zone are 5mmx5mm by FE model against 4.5mmx4.5mm by CONTACT software.

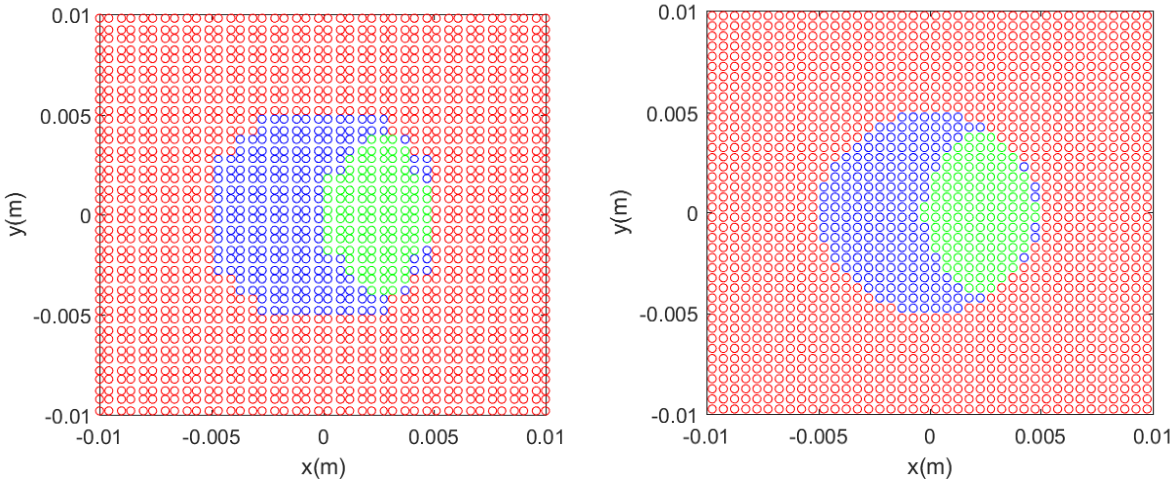

(a) FEM (b) CONTACT

Figure 4.6: Status of nodes in the potential contact zone: no contact zone (red), slip zone (blue) and stick zone (green) for $\Delta V_x/V = 0.3\%$ and $\mu = 0.3$

4.7.2 Lateral creepage

For an imposed lateral creepage $\Delta V_y/V = 0.3\%$ and other creepages set to zero, the longitudinal distributions of the normal contact stresses and frictional stresses on the center line of the contact zone ($y = 0$) are presented in Fig. 4.9. As expected, a stick zone occurs at the leading edge of the contact and a slip zone occurs at the trailing edge of the contact (Fig. 4.8). Like in the case of longitudinal creepage, the comparison of the results obtained with the proposed full FE method and the results provided by CONTACT software shows a good agreement with some small differences for the tangential stresses in the transition between the stick zone and the slip zone.

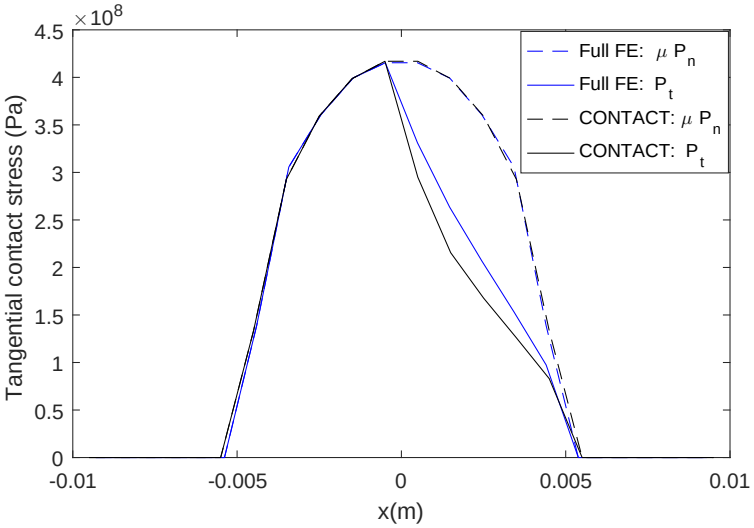

Figure 4.7: Quasi-static frictional stresses on a line $y = 0$ for $\Delta V_x/V = 0.3\%$ and $\mu = 0.3$

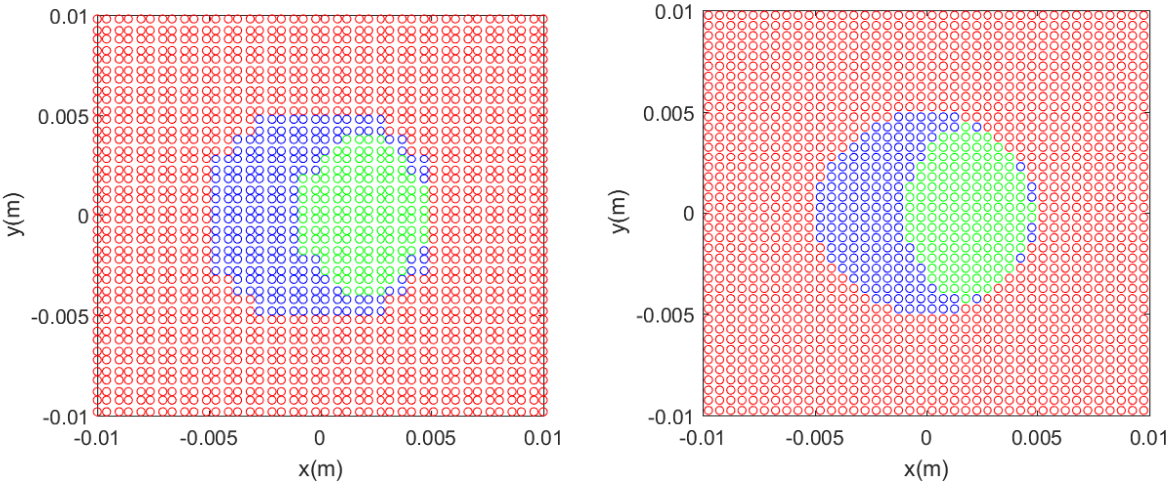

(a) FEM (b) CONTACT

Figure 4.8: Status of nodes in the potential contact zone: no contact zone (red), slip zone (blue) and stick zone (green) for $\Delta V_y/V = 0.3\%$ and $\mu = 0.3$

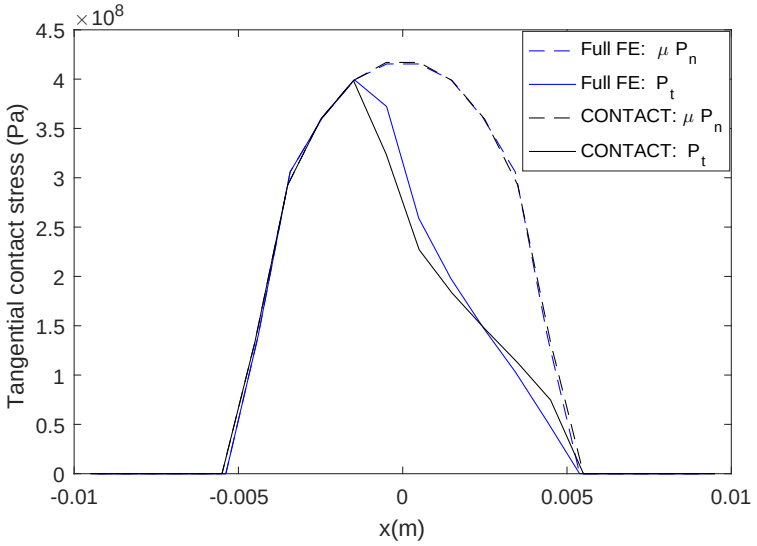

Figure 4.9: Quasi-static frictional stresses on a line $y = 0$ for $\Delta V_y/V = 0.3\%$ and $\mu = 0.3$

4.7.3 Spin creepage

For an imposed lateral creepage $\Delta\Omega_z/V = 0.5$ and other creepages set to zero, the longitudinal distributions of the normal contact reactions and frictional reactions on the center line of the contact zone ($y = 0$) are presented in Fig. 4.11. The status of the nodes in the potential contact zone is represented in (Fig. 4.10). The comparison of the results obtained with the proposed full FE method and the results provided by CONTACT software shows more differences in comparison to the two lateral and longitudinal creepages. For the moment, no simple explanation can be given for these differences. It does not call into question the proposed formulation but will need to be studied in more detail.

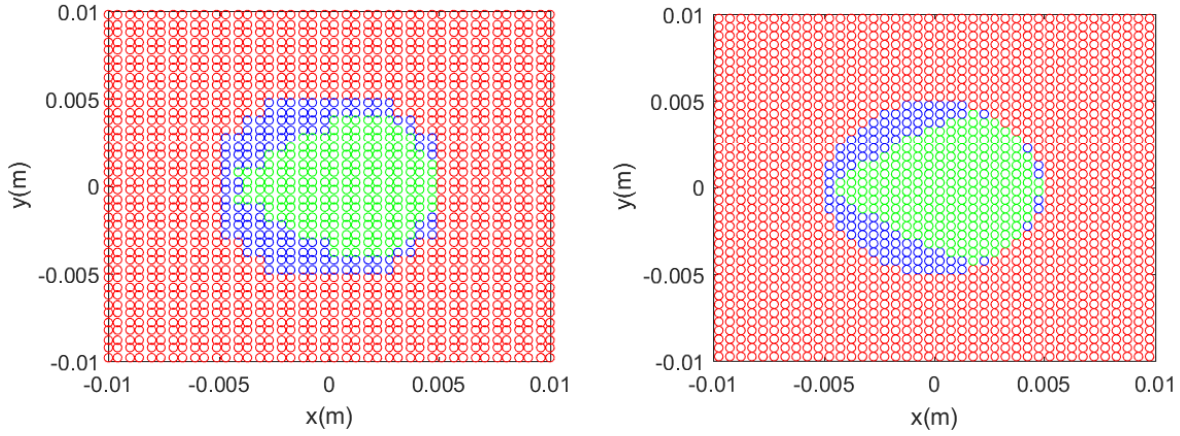

(a) FEM (b) CONTACT

Figure 4.10: Status of nodes in the potential contact zone: no contact zone (red), slip zone (blue) and stick zone (green) for $\Delta V_y/V = 0.3\%$ and $\mu = 0.3$

4.7.4 Saturation curve

Figs. 4.12 to 4.14 show the relation between tangential contact resulting force and longitudinal, lateral and spin creepage respectively. The curves corresponding to FE model, CONTACT software and

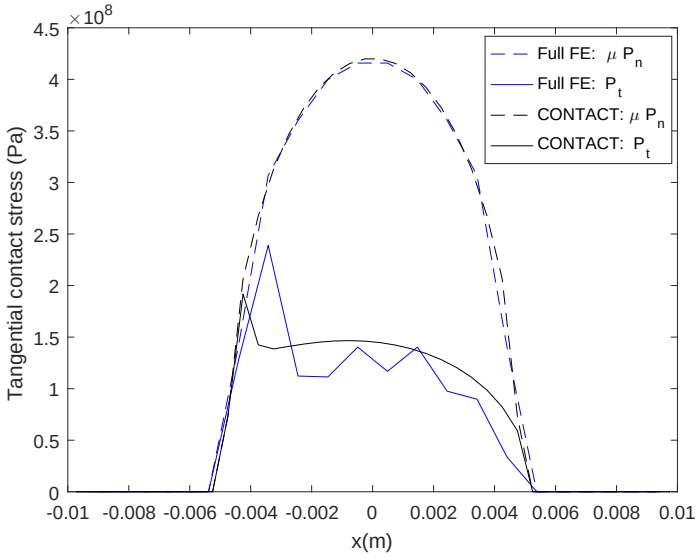

Figure 4.11: Quasi-static frictional stresses on a line $y = 0$ for $\Delta\Omega_z/V = 0.5$ and $\mu = 0.3$

Vermeulen-Johnson's model are close.

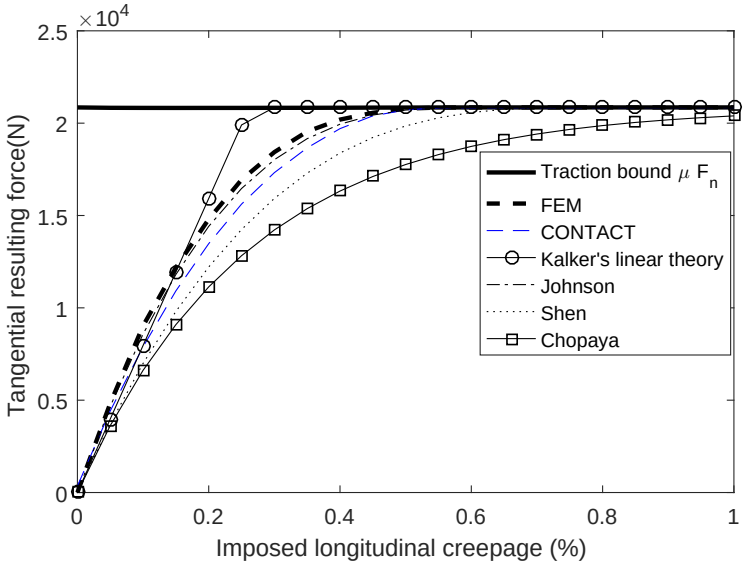

Figure 4.12: Saturation curve for longitudinal creepage

In this section, the quasi-static solution of the rolling contact between two cylinders is calculated and compared with the solution obtained with CONTACT software. There are no significant differences between these two models. In the following section, the transient calculation in the case without instability is going to be performed and also compared with the quasi-static solution obtained with CONTACT software.

4.8 Transient results in the stable case

In the case where the contact point is centered (Fig. 4.9), no instability is found. Transient calculations are performed and the results are discussed and compared with the quasi-static solution obtained with CONTACT software.

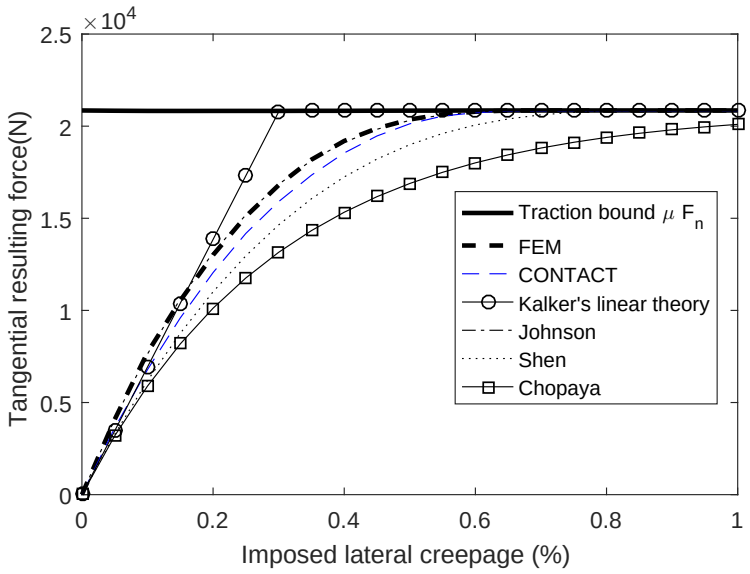

Figure 4.13: Saturation curve for lateral creepage

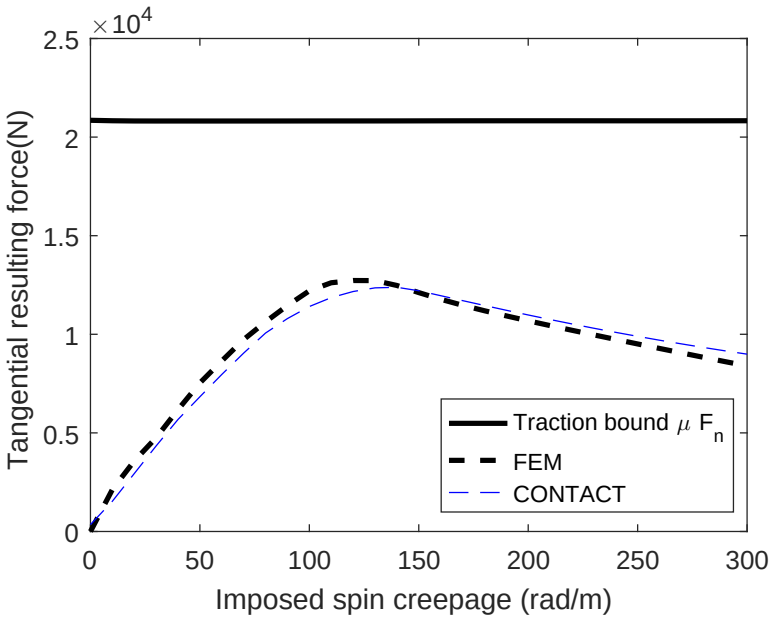

Figure 4.14: Saturation curve for spin creepage

The initial displacements are the displacements obtained from the quasi-static solution in the case of pure rolling ($\Delta V_x = \Delta V_y = \Delta\Omega_z = 0$) and the initial velocities are null. The parameters $V = 10$m/s, $\mu = 0.3$ are used. The time step for the integration is $\Delta t = 10^{-5}$ s. As in the quasi-static case, three cases of longitudinal, lateral and spin creepages are also performed. Results obtained with the full FE model and reduced solutions are then discussed.

4.8.1 Lateral creepage

In the case of lateral creepage $\Delta V_y/V = 0.3\%$ and other creepages set to zero, Fig. 4.15 shows the temporal evolution of the tangential contact resulting forces obtained by the full FE model and reduced models. These forces increase until a an almost constant value. The results obtained with both reduction bases is close to the one obtained with the full model.

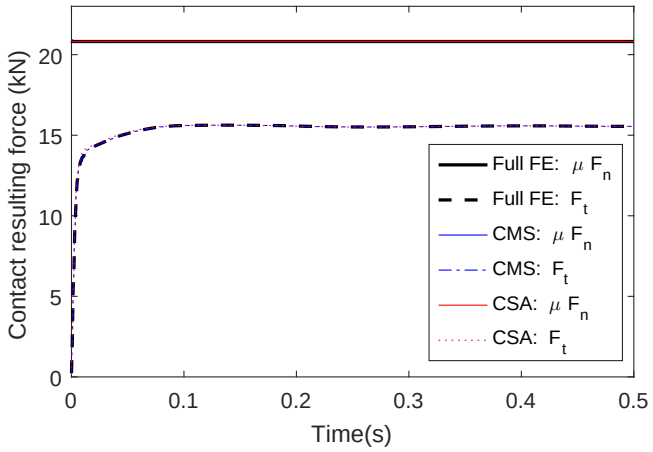

Figure 4.15: Evolution of the tangential contact resulting force for $\Delta V_y/V = 0.3\%$ and $\mu = 0.3$

The longitudinal distributions of the normal contact reactions and frictional reactions on the center line of the contact zone ($y = 0$) are presented in Fig. 4.16. In comparison to the solution obtained by CONTACT software , the dynamic solution shows a light different in the stick zone, probably due to the slow dynamic convergence of the solution.

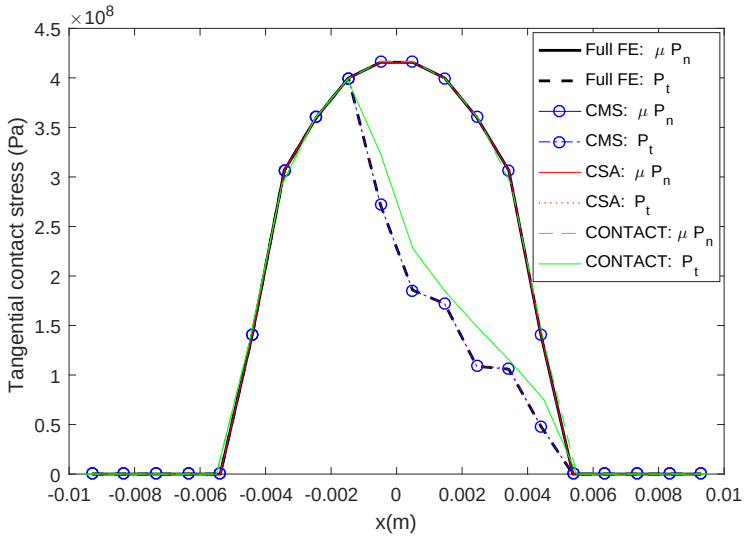

Figure 4.16: Dynamic frictional stresses on a line $y = 0$ for $\Delta V_y/V = 0.3\%$ and $\mu = 0.3$

As in the quasi-static case, a stick zone occurs at the leading edge of the contact and a slip zone occurs at the trailing edge of the contact (Fig. 4.17). The results obtained with the full FE method, the two proposed reduced basis and by CONTACT software shows a good agreement in the status of nodes in the potential contact zone. Fig. 4.18 shows the temporal evolution of the tangential velocity at a point outside the contact zone. The results obtained with the reduction bases are similar to those obtained with the full model.

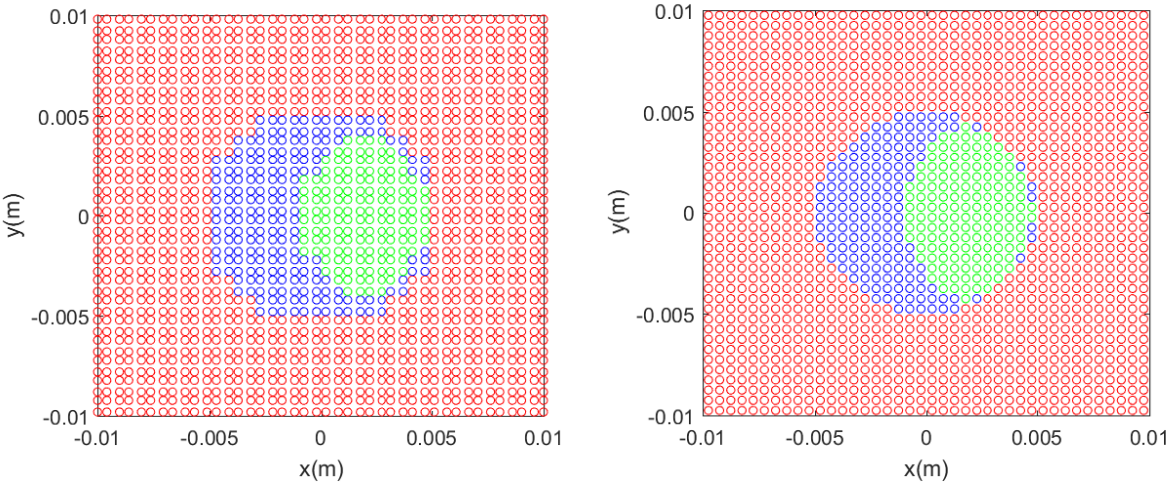

(a) Full FE, CMS and CSA (b) CONTACT

Figure 4.17: Status of nodes in the potential contact zone: no contact zone (red), slip zone (blue) and stick zone (green) for $\Delta V_y/V = 0.3\%$ and $\mu = 0.3$

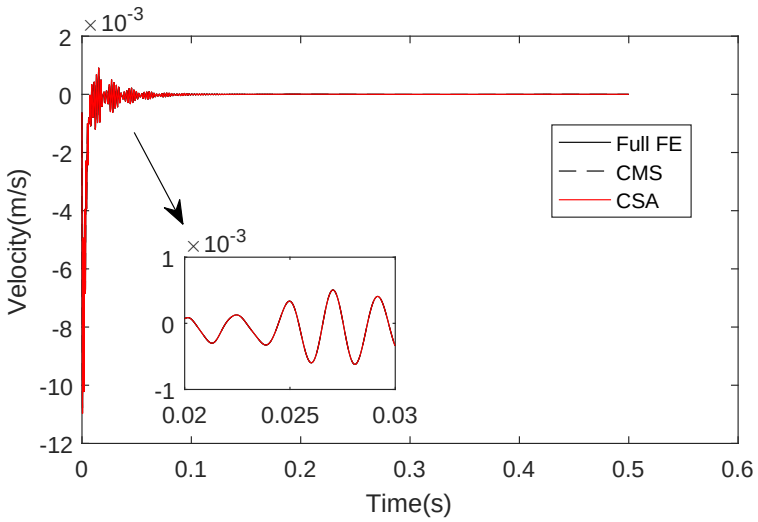

Figure 4.18: Temporal evolution of the tangential velocity at a point outside the contact zone for $\Delta V_y/V = 0.3\%$ and $\mu = 0.3$

4.8.2 Longitudinal creepage

In the case of a longitudinal creepage $\Delta V_x/V = 0.3\%$ and other creepages set to zero, as for the case of lateral creepage, the dynamic results obtained with the reduction bases are also similar to those

obtained with the full model in Figs. 4.19 to 4.21. The results obtained with the full FE method, the two proposed reduction bases and with CONTACT software shows a good agreement in Figs. 4.20 and 4.21.

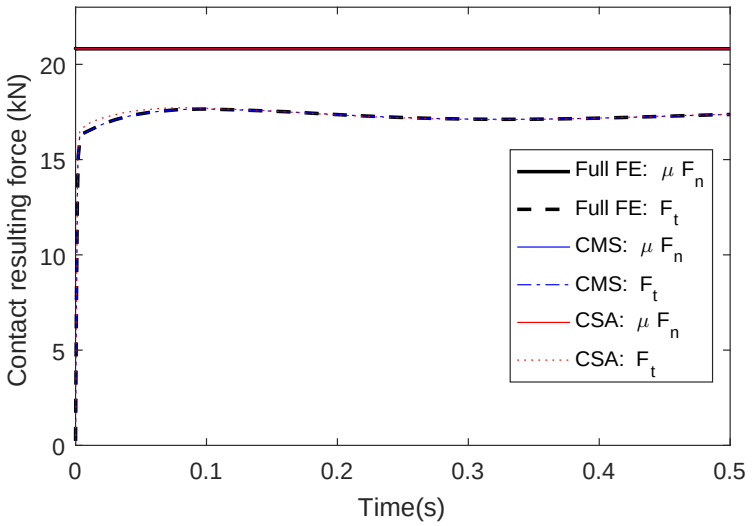

Figure 4.19: Evolution of the tangential contact resulting force for $\Delta V_x/V = 0.3\%$ and $\mu = 0.3$

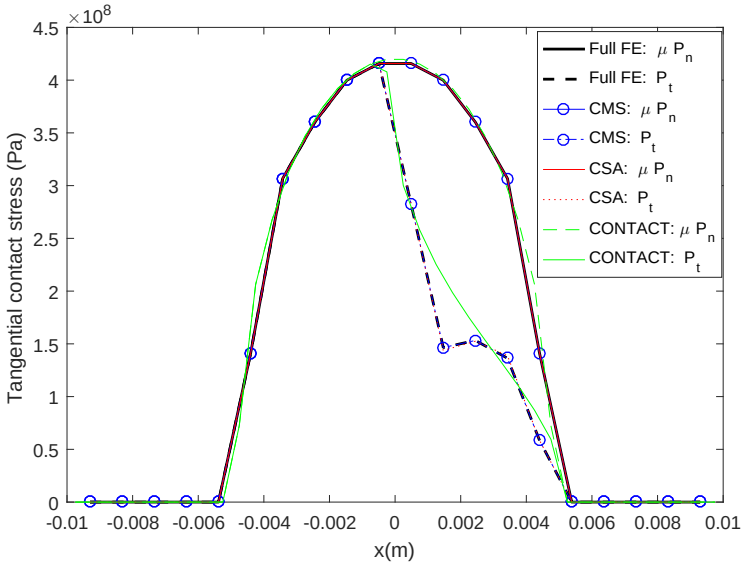

Figure 4.20: Dynamic frictional stresses on a line $y = 0$ for $\Delta V_x/V = 0.3\%$ and $\mu = 0.3$

4.8.3 Spin creepage

In the case of spin creepage $\Delta\Omega_z/V = 0.5$ rad/m and other creepages set to zero, as in the quasi-static case, the FE results shows the largest difference with the result of CONTACT among the three creepages (cf. Figs. 4.23 and 4.24).

In conclusion, the above results show that the proposed dynamic full FE model is able to simulate the frictional rolling systems with a good precision in the stable case, even through the use of the proposed reduction bases. In the following section, this model is tested in the case of instability.

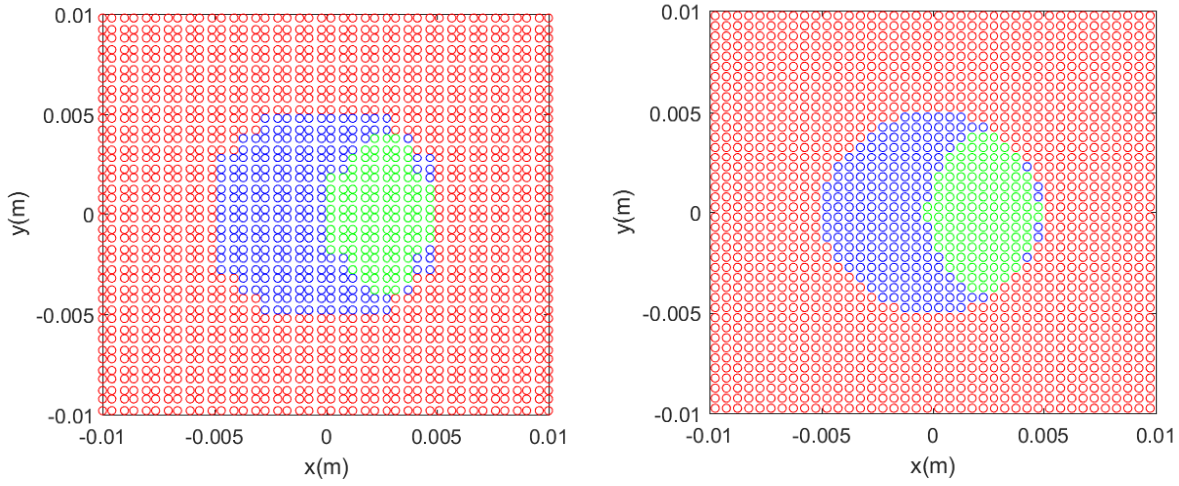

(a) Full FE, CMS and CSA (b) CONTACT

Figure 4.21: Status of nodes in the potential contact zone: no contact zone (red), slip zone (blue) and stick zone (green) for $\Delta V_x/V = 0.3\%$ and $\mu = 0.3$

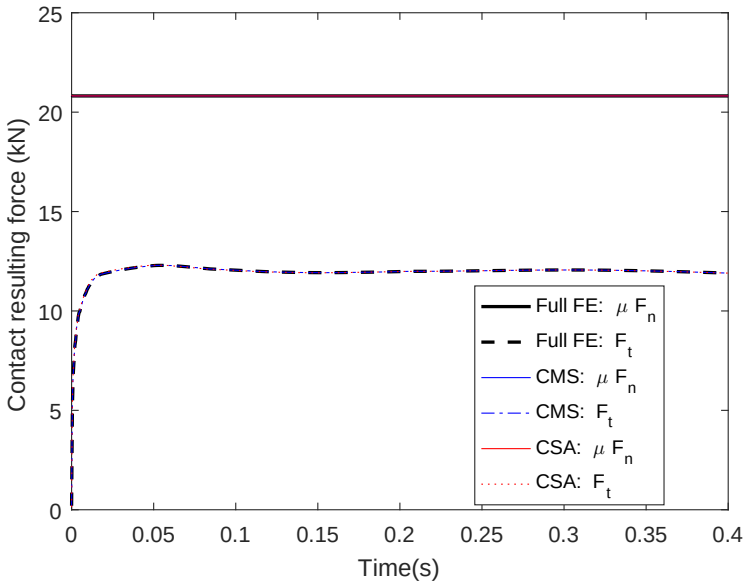

Figure 4.22: Evolution of the tangential contact resulting force for $\Delta\Omega_z/V = 0.5$ and $\mu = 0.3$

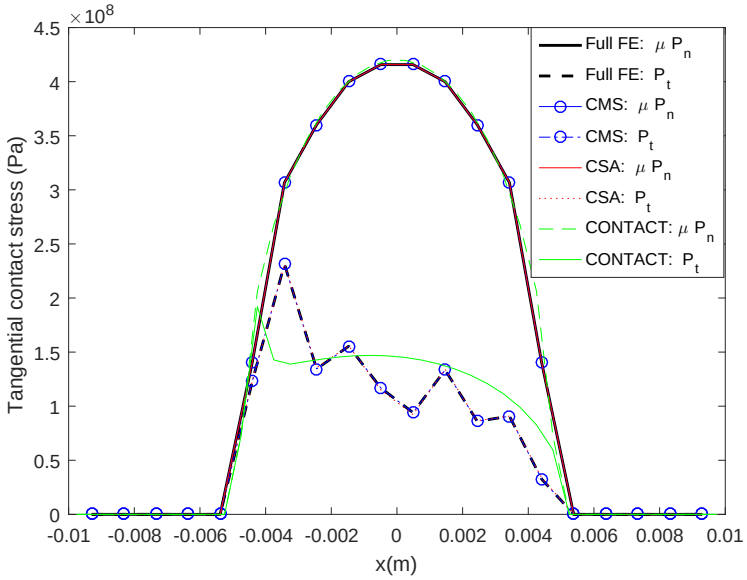

Figure 4.23: Dynamic frictional stresses on a line $y = 0$ for $\Delta\Omega_z/V = 0.5$ and $\mu = 0.3$

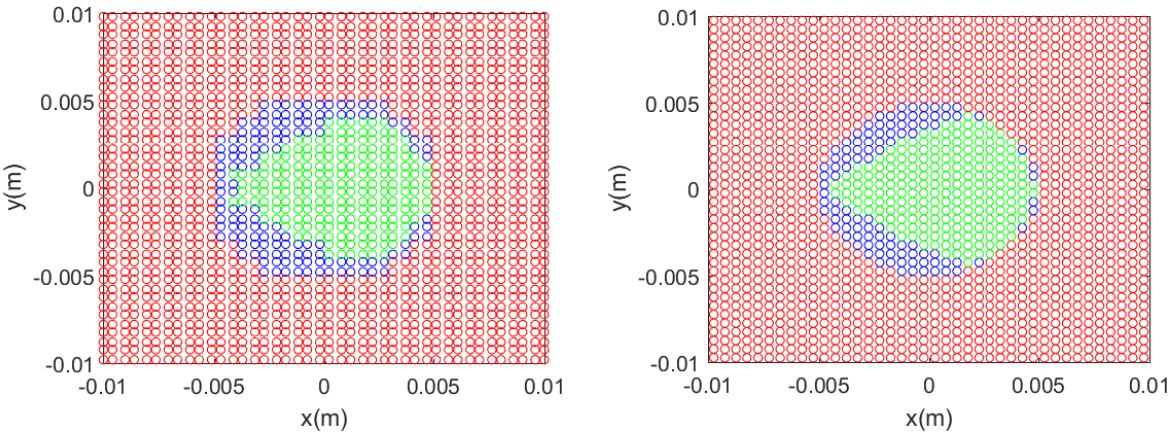

(a) Full FE, CMS and CSA

(b) CONTACT

Figure 4.24: Status of nodes in the potential contact zone: no contact zone (red), slip zone (blue) and stick zone (green) for $\Delta\Omega_z/V = 0.5$ and $\mu = 0.3$

4.9 Stability and transient results in the unstable case

In order to obtain instabilities, the contact point is laterally shifted, as shown in Fig. 4.25. This offset increases the lateral/vertical coupling which is a necessary condition to obtain mode-coupling instabilities.

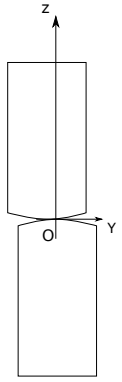

Figure 4.25: Lateral offset of the contact point

4.9.1 Stability results

Stability analysis is carried out in case of full sliding using a higher creepage $\Delta V_y/V = 1\%$ by using 150 free-interface normal modes (75 for each cylinder). In order to solve the non symmetric eigenvalue problem, the two reduction strategies presented in section 4.4.3 (classical CMS and contact static approximation) are tested. A third reduction basis called "enriched coupled modes" founded as very efficient by Brizard [41] is used as a reference.

With an lateral offset $u_{y0} = 4$ cm, one mode is founded to be unstable. Results obtained with $\mu = 0.3$ are shown in Fig. 4.26. The real part of a complex mode at frequency 1612 Hz is positive. The corresponding mode shape is presented in Fig. 4.27.

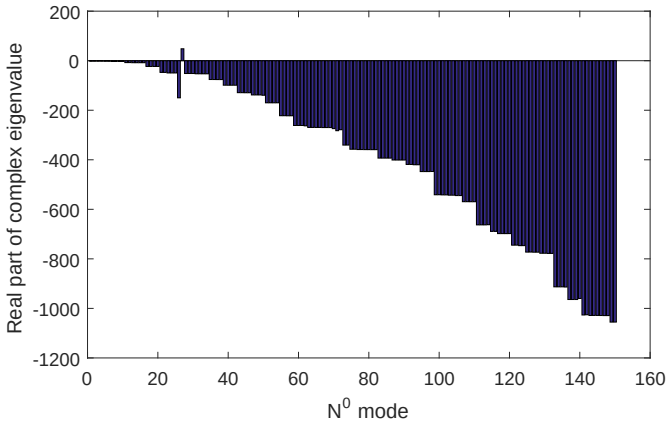

Figure 4.26: Real part of complex eigenvalues as a function of frequencies redfor $\Delta V_y/V = 1\%$ and $\mu = 0.3$

In order to confirm the mode-coupling instability and to test the behavior of the reduced basis presented in section 4.4.3, the evolution of the eigenvalues corresponding to the two complex modes involved in the instability (i.e. the bifurcation curves) are represented in Fig. 4.28 without damping and in Fig. 4.29 with damping. As expected, the increase of the friction coefficient brings the two modes closer until their frequencies coalesce and one mode becomes unstable. With regard to reduction strategies, it

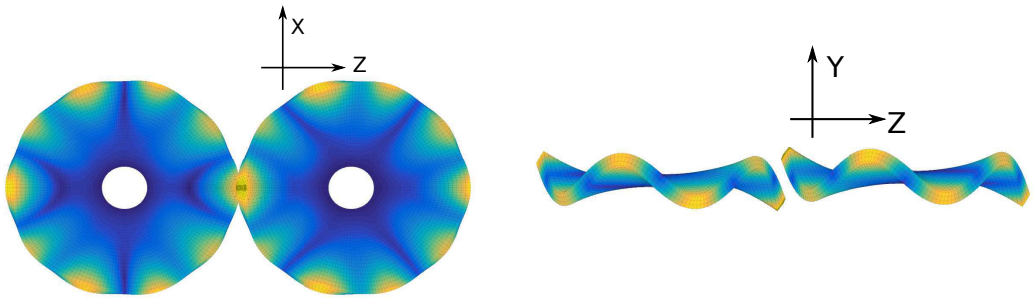

Figure 4.27: Unstable mode for $\Delta V_y/V = 1\%$ and $\mu = 0.3$

is observed that bifurcation curves obtained with the different techniques are very close to each other. In particular, the contact static approximation gives accurate results which means that the inertial effect of local attachments modes is negligible in the stability analysis.

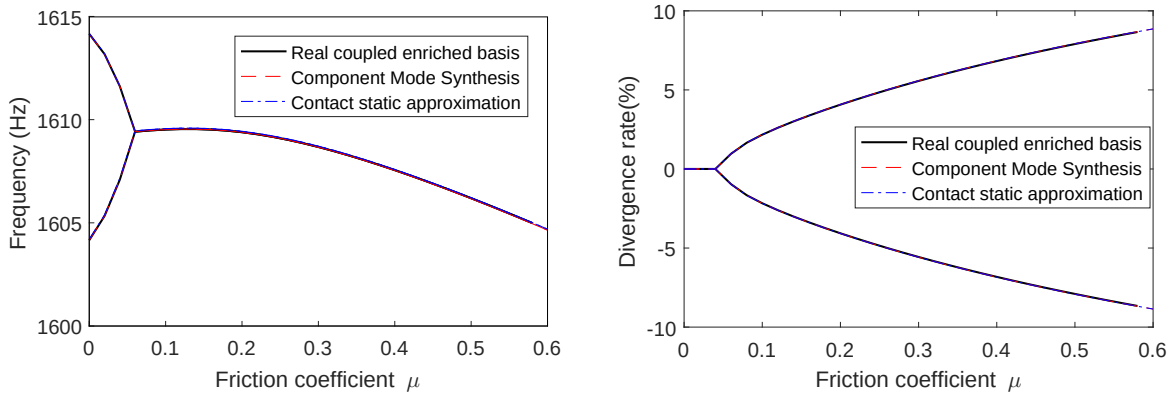

(a) Frequency (b) Divergence rate

Figure 4.28: Bifurcation of complex modes without damping for $\Delta V_y/V = 1\%$ and $\mu = 0.3$

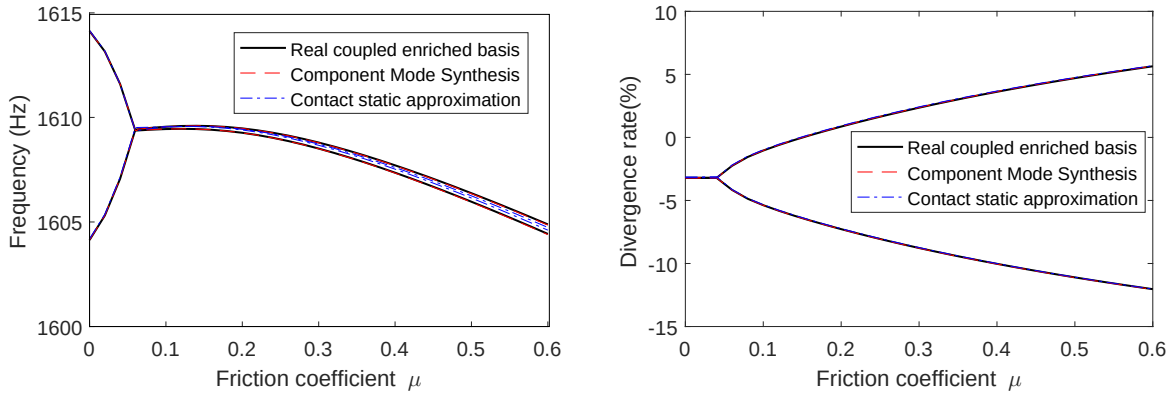

(a) Frequency (b) Divergence rate

Figure 4.29: Bifurcation of complex modes with damping for $\Delta V_y/V = 1\%$ and $\mu = 0.3$

4.9.2 Transient results

Transient results corresponding to the unstable case founded in the previous section are determined using a numerical time integration from given initial conditions. In all the following results, the integration starts from the equilibrium i.e. the initial displacements are the displacements obtained from the quasi-static solution and the initial velocities are null. The parameters $V_x = 10$ m/s, $\mu = 0.3$ and $\Delta V_y/V = 1\%$ are used. The time step for the integration is $\Delta t = 1\mu$s. Results obtained with the full non-reduced mode are first discussed. Reduced solutions are then presented.

4.9.2.1 Full model

Figs. 4.30 and 4.31 show the time series of the normal and lateral contact resultant forces F_n and F_t. The tangential resultant force increases until a pronounced stick/slip oscillation builds up as shown in Fig. 4.32. When the tangential contact resultant force is smaller than the traction bound μF_n, a transient stick zone appears at the leading edge of the effective contact region as shown in Fig. 4.33.

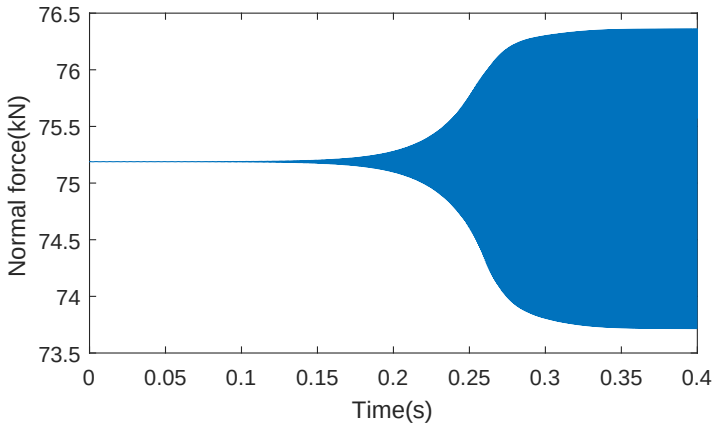

Figure 4.30: Evolution of the normal contact resultant force

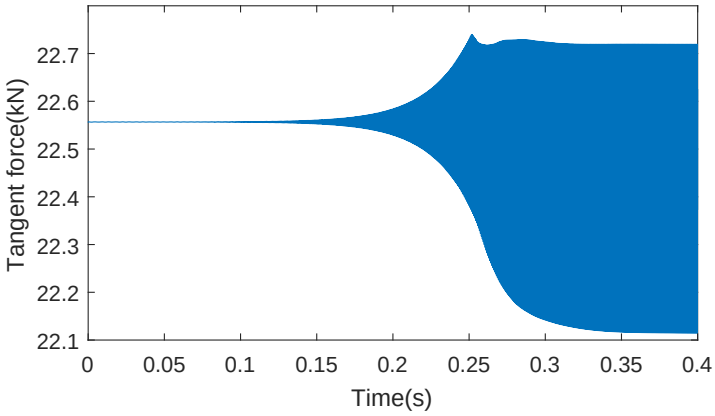

Figure 4.31: Evolution of the tangential contact resultant force

The time series of the lateral velocity of a point outside the contact zone is presented in the Figure 4.34a. The spectrogram in Fig. 4.34b allows to observe the frequencies which are present in the solution and when they appear. A fundamental frequency is founded at $f_0 = 1611$ Hz which gets very close to the natural frequency of the unstable complex mode provided by stability analysis. In the stationary step, harmonic frequencies $f_k = k f_0$ appear.

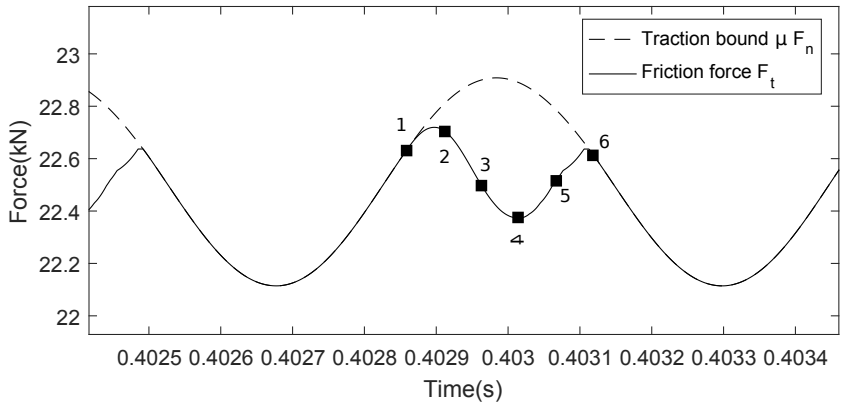

Figure 4.32: Zoom on time series of the contact resultant forces ; the status of the contact points at the time steps marked with Arabic numerals is represented Fig. 4.33

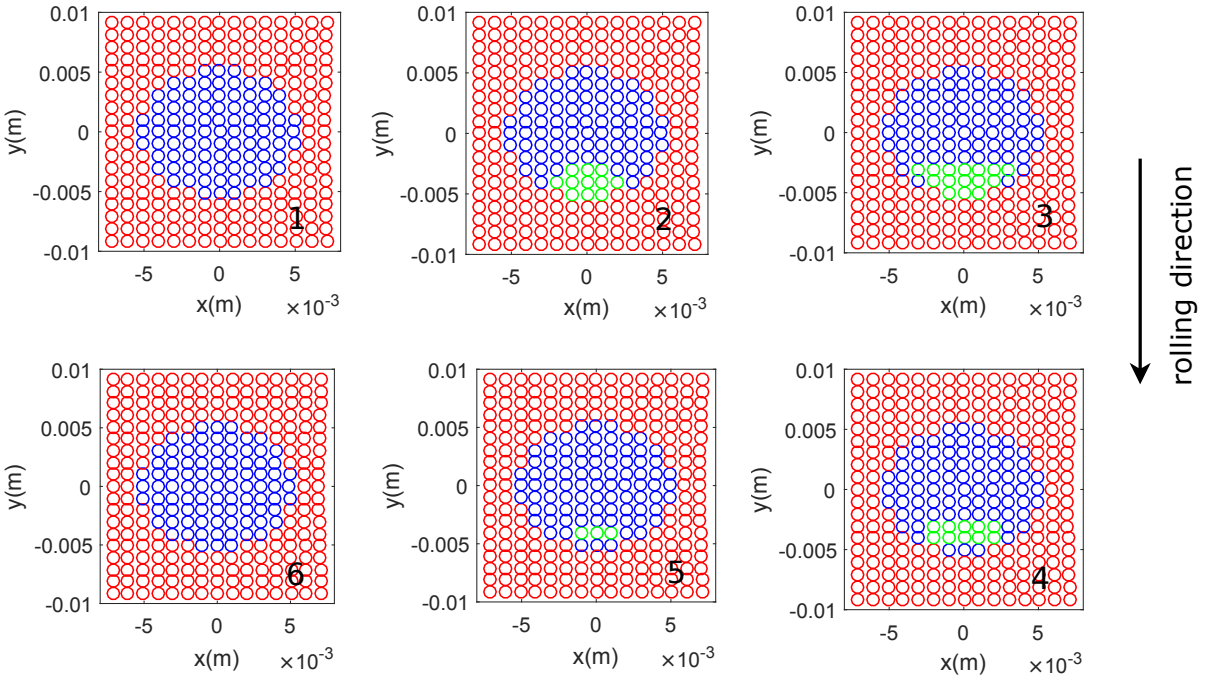

Figure 4.33: Status of nodes in the potential contact zone: no contact zone (red), slip zone (blue) and stick zone (green)

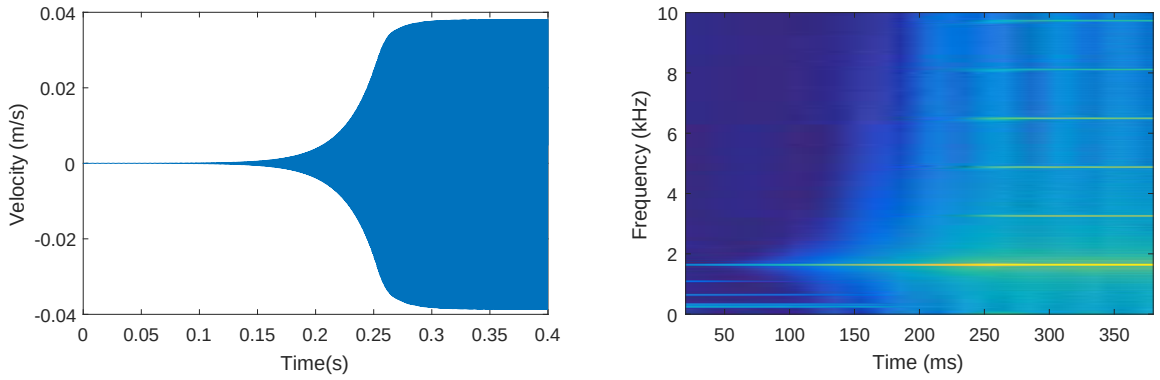

(a) Temporal evolution (b) Spectrogram (time-frequency)

Figure 4.34: Tangent velocity of a point outside the contact zone

4.9.2.2 Reduced models

Concerning the precision of the reduced models, the lateral velocity of the point outside the contact zone, obtained with the reduction bases are presented in Figs. 4.35 and 4.36 in comparison with the full solution. The fundamental frequencies of the three solutions are very close to each other. In the linear step, the amplitudes of the reduced solutions are slightly greater than the complete solution. It seems that, with the reduction bases, the divergent transient phase of the solution is slightly faster than with the full model. This phenomenon agrees with the conclusion of Loyer *et al.* [21] concerning the impact of the reduction on transient nonlinear solutions of friction-destabilized systems. However, in the stationary step, the amplitude of the three solutions are very similar. The corresponding spectra in the stationary part of the transient solution are also given in Fig. 4.37 showing a good agreement. In addition, it should be noted that the computation times resulting from the use of the reduction bases CMS and CSA are respectively ten and fifteen times faster than for the computation of the full solution.

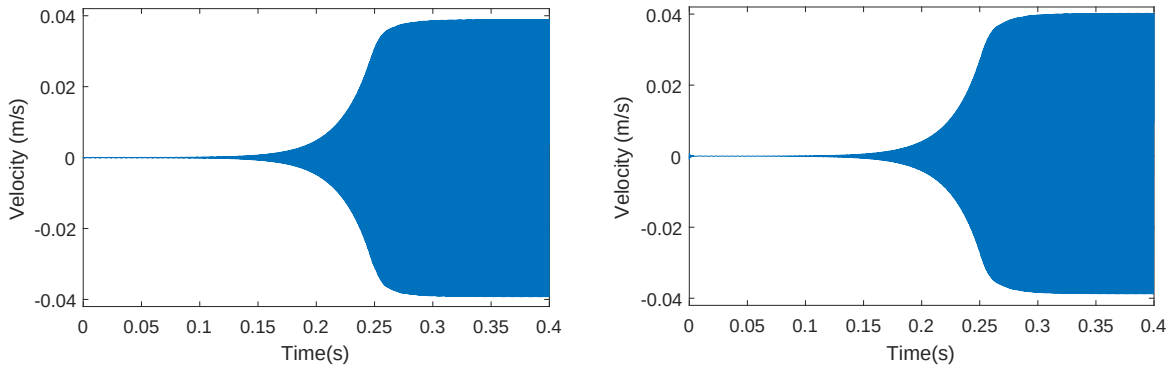

(a) Component Mode Synthesis (b) Contact static approximation

Figure 4.35: Lateral velocity in a point outside the contact zone obtained with the reduced basis

4.10 Conclusion

In this chapter, a method is proposed for the modeling and analysis of the high-frequency friction-induced instabilities of two structures in rolling contact in time and frequency domains. A full finite

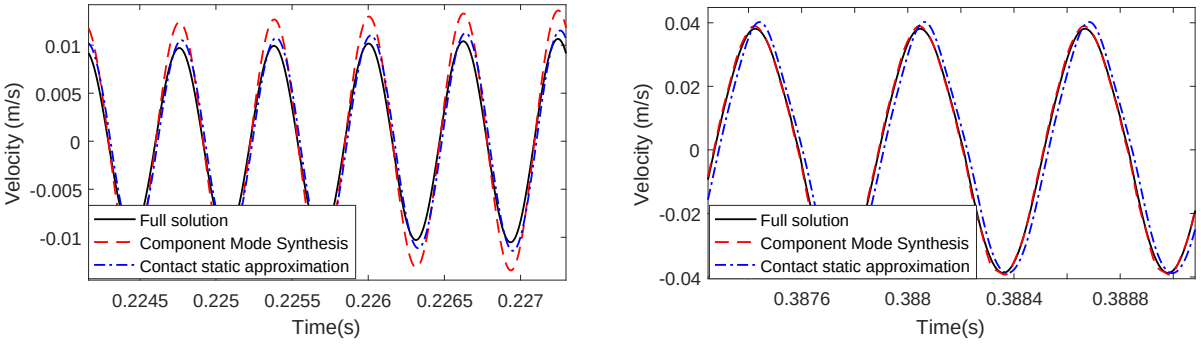

(a) In the linear step

(b) In the stationary step

Figure 4.36: Zoom on time series of the lateral velocity in a point outside the contact zone obtained with the reduced basis

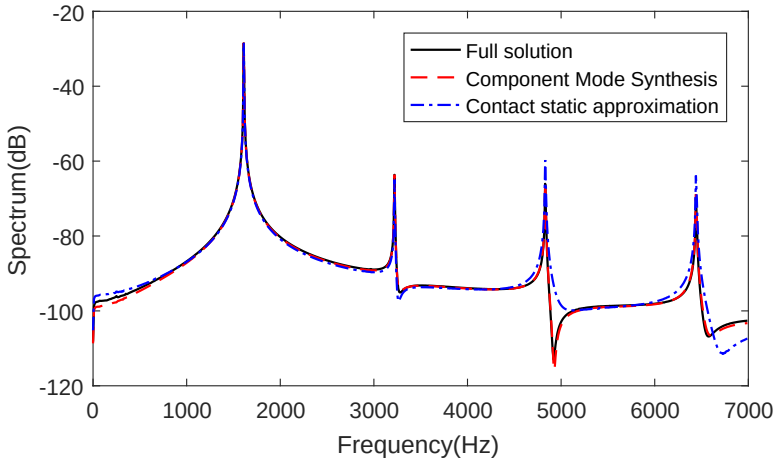

Figure 4.37: Spectrum of the stationary lateral velocity in a point outside the contact zone obtained with the reduced basis

element formulation around the stationary position in an Eulerian reference frame is derived with a fine discretization of the contact surface combined with Signorini's unilateral contact and Coulomb's friction laws with a constant friction coefficient. Appropriate numerical techniques are used in order to solve the nonlinear discrete equations in quasi-static or dynamic conditions. In addition to the transient approach, a stability analysis performed around the full sliding equilibrium position allows to determine unstable modes and frequencies.

In order to reduce the computational effort, reduction strategies are proposed for both domains. The first technique uses a classical CMS reduced basis including free-interface normal modes and static attachments modes. A second technique has been proposed, consisting in adding a residual static contact flexibility to the free-interface normal modes when solving the frictional contact equations (contact static approximation).

The method has been tested in the case of frictional rolling contact between two annular cylinders. The quasi-static results show a good agreement with the ones obtained with Kalker's CONTACT software. In case of full sliding, the stability analysis brings out a mode coupling instability when the contact zone is laterally shifted from the center of the cylinders. In the unstable configuration, the numerical integration provides solutions in the time domain which are coherent with the stability results. In particular, the unstable frequency determined by this analysis is very close to the fundamental frequency observed in the transient solution. The status of the contact nodes in the self-sustained vibrations clearly shows slip-stick limit cycles.

Concerning the performance of the reduction strategies, the approximate results obtained for the stability analysis show a good agreement with the reference ones. In the time domain, the amplitudes of the reduced solutions are slightly greater than the full solution in the linear phase. However in the stationary phase, solutions are very similar. This allows to considerably reduce the computational times, especially when the contact static approximation is used.

This methodology may be used later in a large variety of friction-mechanical system, especially curve squeal in the next chapter.

FE modeling of wheel/rail systems with discretization of the contact surface

Contents

5.1 Introduction

In the previous chapter, a full FE model for frictional rolling contact systems in the Eulerian frame is developed in time and frequency domains. Through a numerical application to the rolling contact between two cylinders, this model proves to be able to predict the instability of the system but also to determine the full spectrum and the amplitude of the friction-induced vibrations. In addition, the two reduction bases are proposed and show a good agreement with the full FE model leading to a considerable reduction of the computational cost.

The aim of this chapter is to apply the full finite element method proposed in previous chapter for the simulation of friction induced vibrations of the wheel-rail system in curves. For this purpose, the wheel-rail contact is simulated by using a discretization of the contact zone combined with non-smooth frictional contact laws. Simulations are performed in the Eulerian reference frame. Instabilities are analyzed through two types of analysis: stability analysis to predict unstable modes assuming a full steady steading in the contact zone, and a transient analysis which allows to introduce nonlinearities and to determine the amplitude of the vibrations. The most performant reduction basis including free-interface modes and residual static attachment modes (CSA) is used to reduce the computational times. The results are discussed and compared with those obtained with the point-contact model for the stability analysis.

5.2 Wheel/Rail interaction model

5.2.1 Statement of the problem

The wheel/rail interaction model considered in this chapter is the same model as considered in chapter 2 (Fig. 1.17). However the contact zone is discretized. For the discretization by finite elements, compatible meshes on the interface are considered: facing nodes of the wheel and the rail in potential

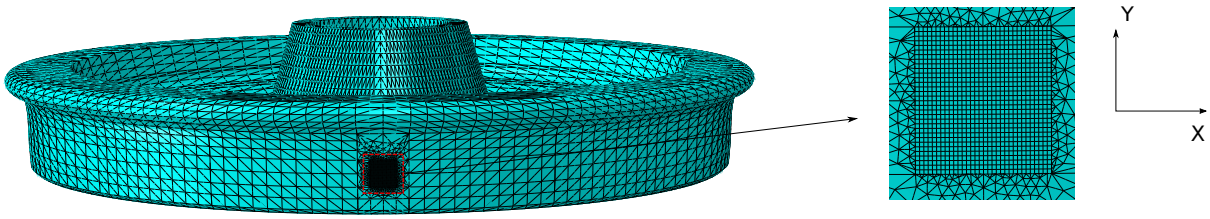

Figure 5.1: FE model of the wheel with fine mesh on the contact zone

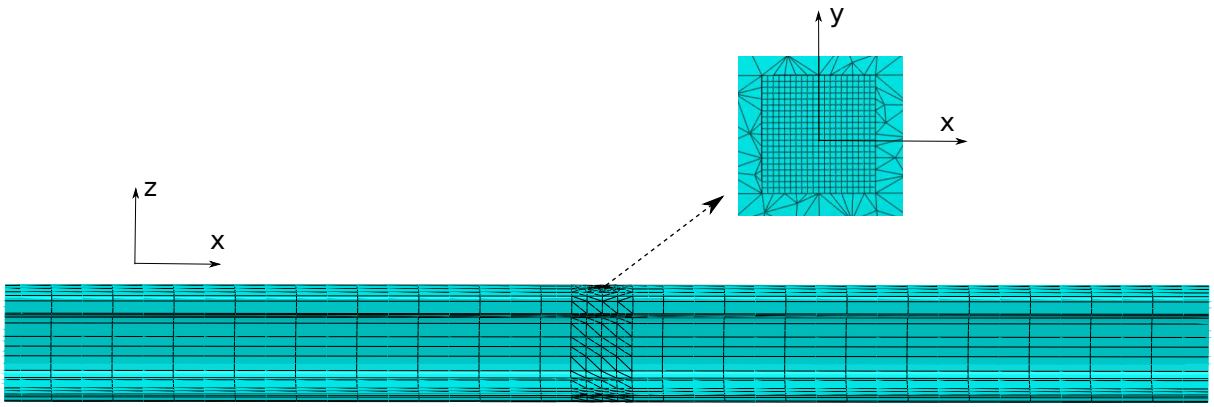

Figure 5.2: FE model of the rail with fine mesh on the contact zone

contact have identical tangential coordinates x and y. The potential contact area is meshed with elements of length 1 mm as shown in Figs. 5.1 and 5.2.

A vertical displacement u_{z0} is applied at the hub of the wheel for an equivalence normal force of 70kN. The other displacements at the hub are set to zero.

5.2.2 Wheel model

The wheel model considered in chapter 2 is retaken in this chapter. However, the contact zone is discretized (Fig. 5.1). By using the modal transformation, the dynamic response obtained by this wheel model is calculated and compared with the dynamic response obtained by the point-contact wheel model. The amplitude of the wheel vertical mobilities at the contact is represented in Fig. 5.3. The vertical and lateral mobilities obtained with the two models are very close.

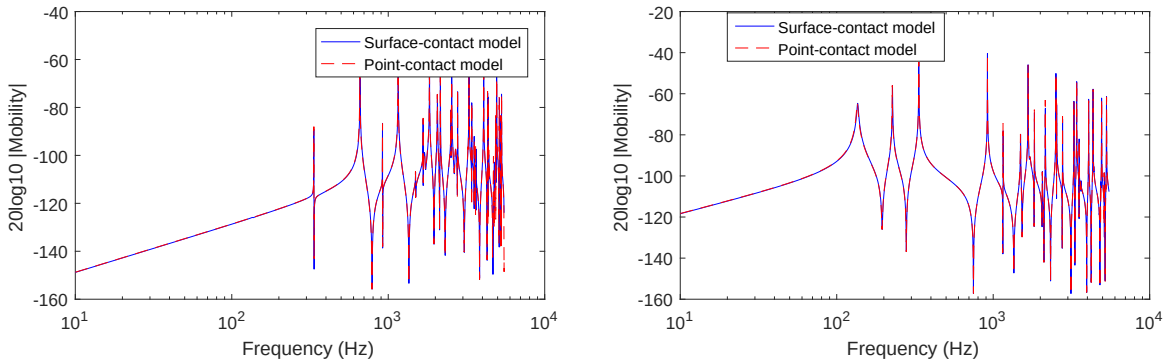

(a) Vertical mobility (b) Lateral mobility

Figure 5.3: Wheel mobility

5.2.3 Track model

As for the point-contact model in chapter 2, the track model consists of one periodically supported rail of type UIC60 (Fig. 2.4) with the same material, length and periodic pad stiffness. However in the track model, the contact zone is discretized. The dynamic response obtained by this track model is compared with the dynamic response obtained by the point-contact track model. The track vertical and lateral mobilities at the contact point are represented in Figs. 5.4 and 5.5. The lateral mobilities obtained by the two models are also close.

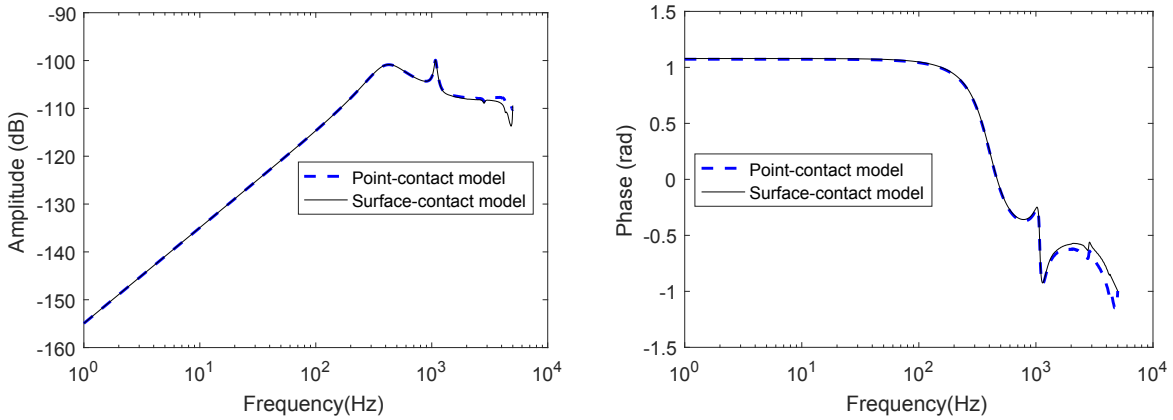

(a) Amplitude (b) Phase

Figure 5.4: Comparison of point-contact and surface-contact track vertical mobility

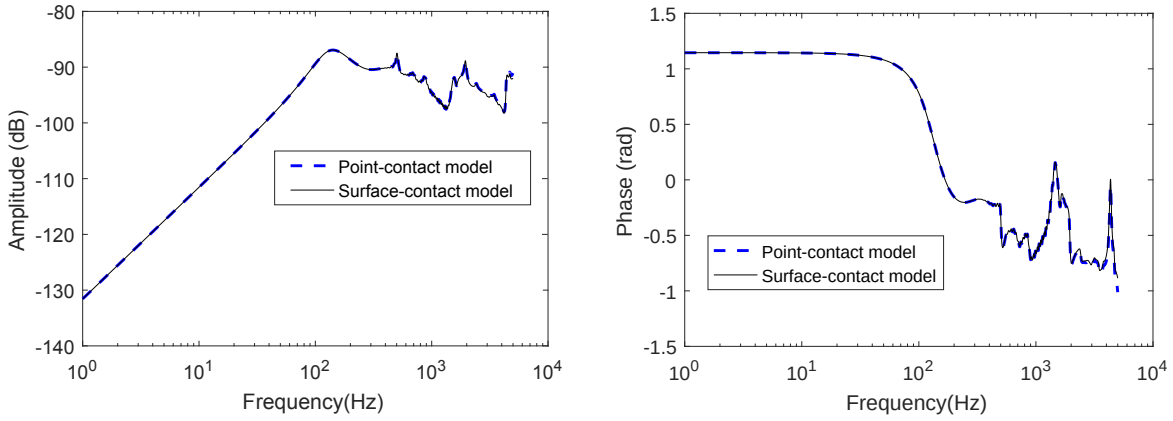

(a) Amplitude (b) Phase

Figure 5.5: Comparison of point-contact and surface-contact track lateral mobility

Track damping models

For the track, two damping models are proposed: a structural damping model as in chapter 2 and a viscous damping model. The structural damping model can only be used for stability analysis in a frequency-domain approach. On the other hand, the viscous damping model can be used in both time-domain and frequency-domain approaches [3, 19]. In this equivalent viscous damping model, a viscous damping coefficient C_{pad} of the track pad is chosen by equating it to the required structural damping value at the corresponding cut on frequency:

$$C_{pad} = \frac{k\eta_s}{\omega_o} \tag{5.1}$$

where k is the pad stiffness, η_s is the structural damping factor and ω_o is the cut on frequency.

In addition, assuming that the pad structural damping is equal to the rail structural damping $\eta = 0.02$, modal damping factors can be set to $\eta/2$ leading to a diagonal reduced damping matrix $\mathbf{C^r_{redo}}$. The diagonal terms of this matrix are thus equal to $\eta\Omega_r^i$ where Ω_r^i is the track natural pulsations. By taking into account the residual pad viscous damping $C_{pad} = k(\eta_s - \eta)/\omega_0$ and the anechoic terminations stocked in matrix $\mathbf{C_r}$, the final reduced damping stiffness finally becomes non diagonal and is given by:

$$\mathbf{C^r_{red}} = \mathbf{C^r_{redo}} + \Phi_r^T \mathbf{C_r} \Phi_r \tag{5.2}$$

where Φ_r is the track modal basis.

The track vertical and lateral mobilities at the contact point obtained by the two damping models are represented in Figs. 5.6 and 5.7. Both vertical and lateral mobilities obtained with the two different damping models are close at high frequencies. At low frequencies below the pad cut-on frequency, the differences between the phases are larger.

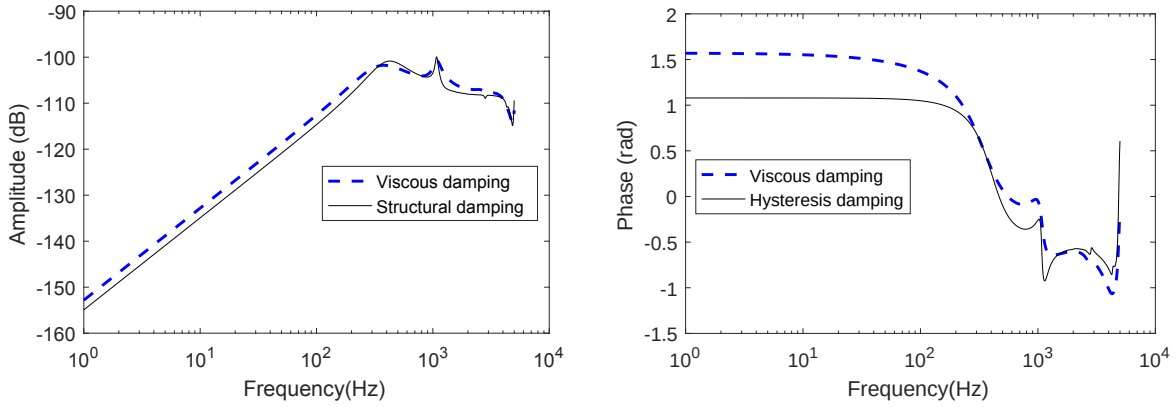

(a) Amplitude (b) Phase

Figure 5.6: Comparison of track vertical mobility for structural and equivalent viscous damping models

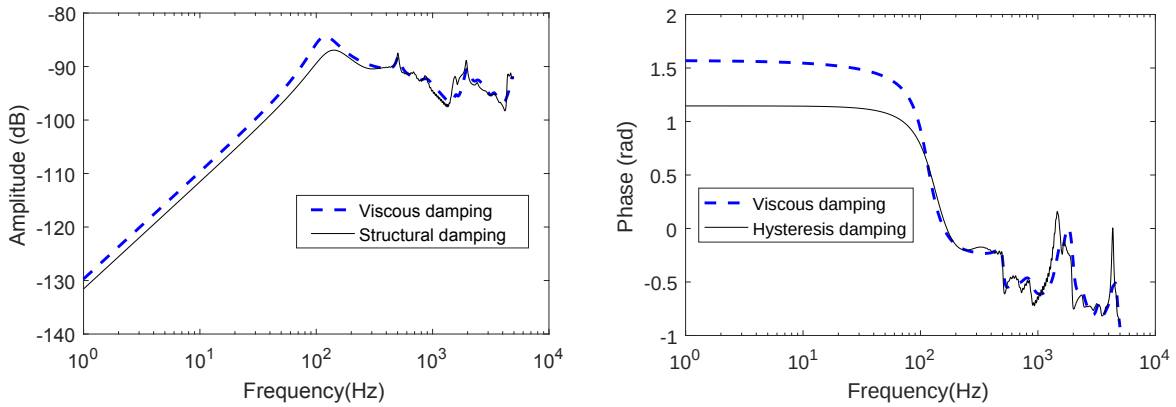

(a) Amplitude (b) Phase

Figure 5.7: Comparison of lateral mobility for structural and equivalent viscous damping models

5.2.4 Stability and transient analysis of the wheel/rail contact system

Considering that the size of the problem is very large (900000 DOFs), it is necessary to use the reduced methods. The reduction basis called Contact static approximation (CSA) in the previous chapter which proves to be efficient to reduce the computational times but still ensure the precision is used in this model. The formulations of the stability and transient analysis are found in the previous chapter.

5.3 Quasi-static results

In this section, the wheel/rail quasi-static contact in curve is considered. The rolling is performed in the $-x$ direction with $V = 10$ m/s. A vertical displacement $u_{z0} = 0.35$ mm is applied leading to a resultant vertical contact force of about 70 kN. A friction coefficient $\mu = 0.3$ is considered. Longitudinal and spin creepages are set to zero ($\Delta V_x = \Delta\omega_z = 0$).

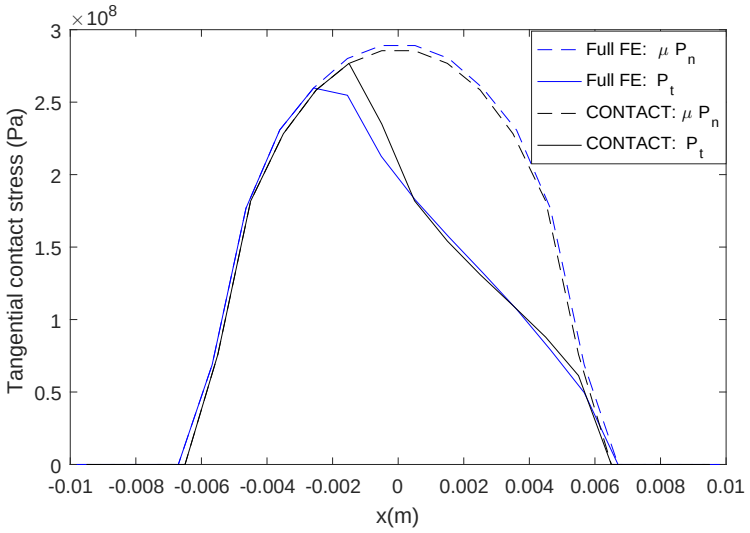

Figure 5.8: Quasi-static frictional stresses on a line $y = 0$ for $\Delta V_y/V = 0.2\%$ and $\mu = 0.3$

For an imposed lateral creepage $\Delta V_y/V = 0.2\%$, the longitudinal distributions of the normal contact stresses and frictional stresses on the center line of the contact zone ($y = 0$) are presented in Fig. 5.8. As expected, a stick zone occurs at the leading edge of the contact and a slip zone occurs at the trailing edge of the contact (Fig. 5.9). The comparison of the results obtained with the proposed full FE method and the results provided by CONTACT software shows a good agreement.

5.4 Stability results with the track structural damping model

The aim of this section is to perform a stability analysis of the system considering the track structural damping model and to compare it with the results obtained with the point-contact model, notably in order to show the influence of the discretization of the contact zone.

The results of the stability analysis of the wheel/rail system for the reference case is firstly presented. The bifurcation curves (effect of friction coefficient) then allow to analyze the instability mechanism. The effects of some parameters are then investigated such as creepage sign, wheel modal damping and vertical pad stiffness. The contact position on the wheel has not yet been investigated since it requires a different mesh of the wheel.

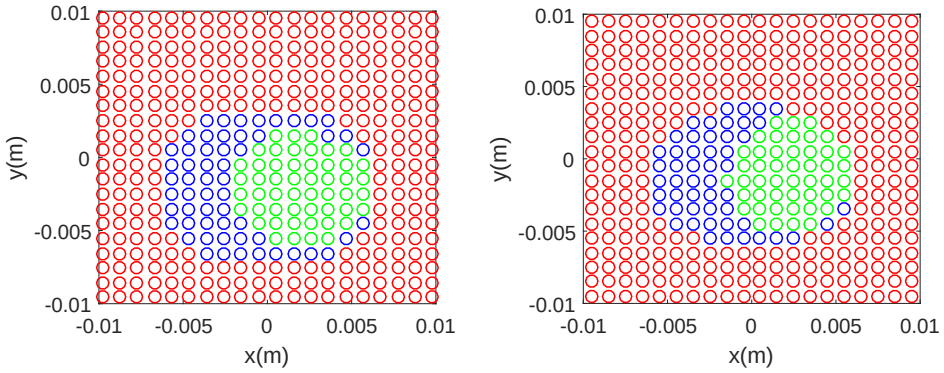

(a) MEF (b) CONTACT

Figure 5.9: Status of nodes in the wheel/rail potential contact zone: no contact zone (red), slip zone (blue) and stick zone (green) for $\Delta V_y/V = 0.2\%$ and $\mu = 0.3$

5.4.1 Reference case analysis

The reference case with the kinematic parameters listed in Table 2.3 is considered in this section. Stability analysis is carried out in case of full sliding using a higher creepage $\Delta V_y/V = 1\%$. In order to solve the non symmetric eigenvalue problem, the reduction strategy presented in section 4.4.3 (contact static approximation) is performed. Four unstable modes with positive real part are obtained as shown in Fig. 5.10. The divergent rates and the corresponding unstable mode shapes are listed in Tab. 5.1. As for the point-contact model, there are 3 axial wheel modes with (2,3,4) nodal diameters and zero nodal circle involved in the first three unstable modes and some axial and radial wheel modes involved in the fourth unstable mode. The corresponding frequencies are almost the same between the two models whereas the divergence rates are higher for the surface-contact model.

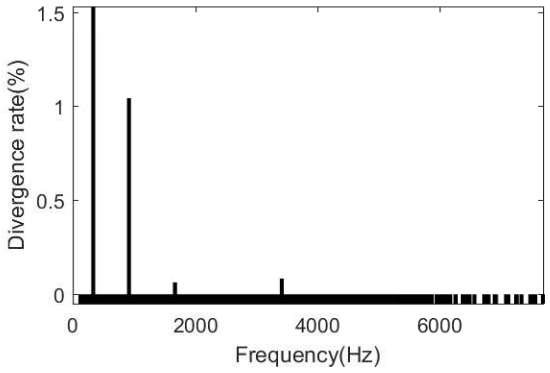

Figure 5.10: Divergence rate of the complex modes obtained by the surface-contact model in the reference case

5.4.2 Bifurcation curves

The bifurcation curves of the unstable complex modes are represented in Figs. 5.11 to 5.14 in comparison with the results obtained with the point-contact model. The critical friction coefficients above which the complex modes become unstable are respectively equal to 0.06, 0.1, 0.22 and 0.3.

Figs. 5.11 to 5.14 show also that with or without discretization of the contact area, the unstable frequencies are almost identical (difference <2Hz). However, the divergence rates of the unstable modes are higher for the surface contact model than for the point contact model due to the difference between

Point-contact model			Surface-contact model		
Unstable frequencies (Hz)	Divergence rate (%)	Wheel modes involved	Unstable frequencies (Hz)	Divergence rate (%)	Wheel modes involved
334	1.2	335 Hz - (a,0,2)	334	1.53	335 Hz - (a,0,2)
918.3	0.87	920 Hz - (a,0,3)	917.9	1.04	920 Hz - (a,0,3)
1671	0.06	1671 Hz - (a,0,4)	1670	0.06	1671 Hz - (a,0,4)
3418	0.04	3419 Hz - (a,0,6), 3280 Hz - (r,5) and 3256- (a,1,1)	3417	0.08	3419Hz - (a,0,6), 3280 Hz - (r,5) and 3256- (a,1,1)

Table 5.1: Stability results obtained with both point-contact and surface-contact models in the reference case

the Hertz's stiffness k_H in Eq. (2.4) and the FE local stiffness matrix $(\mathbf{I_n}\tilde{\Phi}_{sn}^T(\tilde{\mathbf{P}}_\mathbf{n}^T+\mu\tilde{\mathbf{P}}_\mathbf{t}^T))^{-1}$ in Eq. (4.15). An "equivalent" average FE stiffness k_{fe} can be calculated, equal to the sum of all terms of $(\mathbf{I_n}\tilde{\Phi}_s^T(\tilde{\mathbf{P}}_\mathbf{n}^T+\mu\tilde{\mathbf{P}}_\mathbf{t}^T))^{-1}$. . Stiffness k_{fe} is found to be 1.19 times larger than Hertz's stiffness k_H.

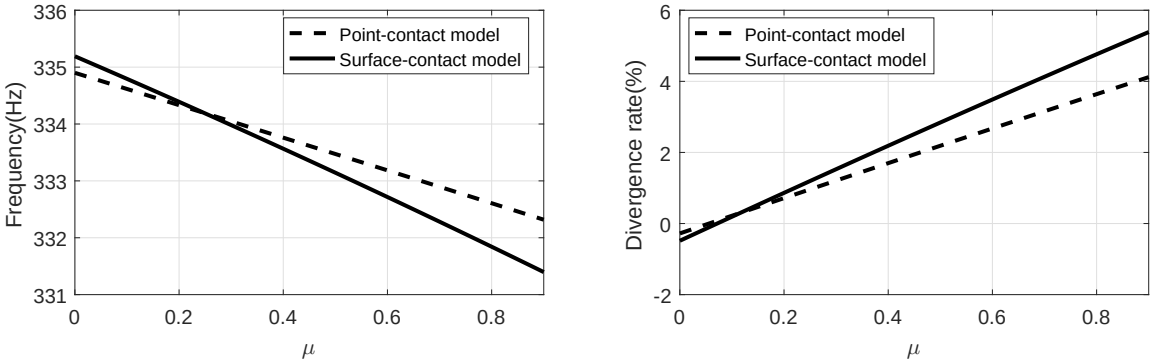

(a) Frequency (b) Divergence rate

Figure 5.11: Bifurcation curves of the unstable mode (a,0,2)

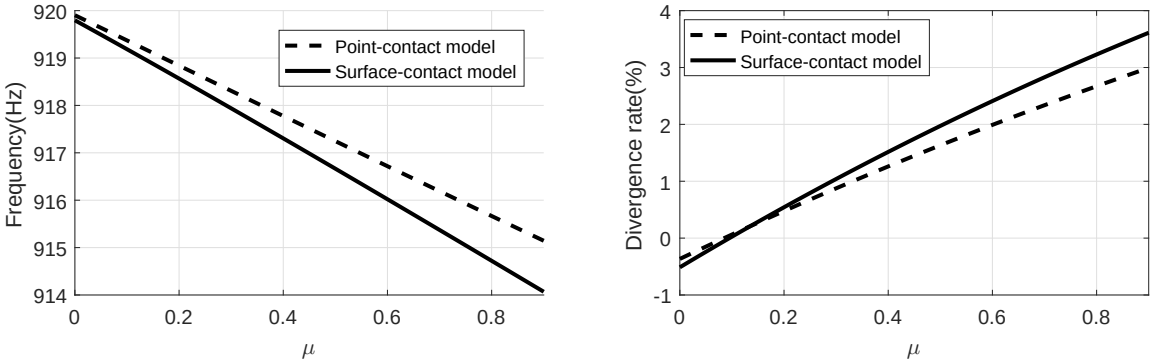

(a) Frequency (b) Divergence rate

Figure 5.12: Bifurcation curves of the unstable mode (a,0,3)

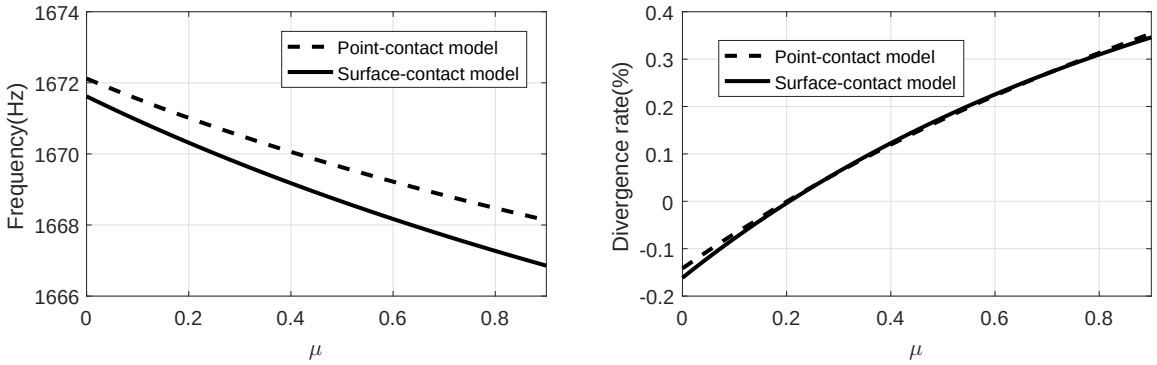

(a) Frequency (b) Divergence rate

Figure 5.13: Bifurcation curves of the unstable mode (a,0,4)

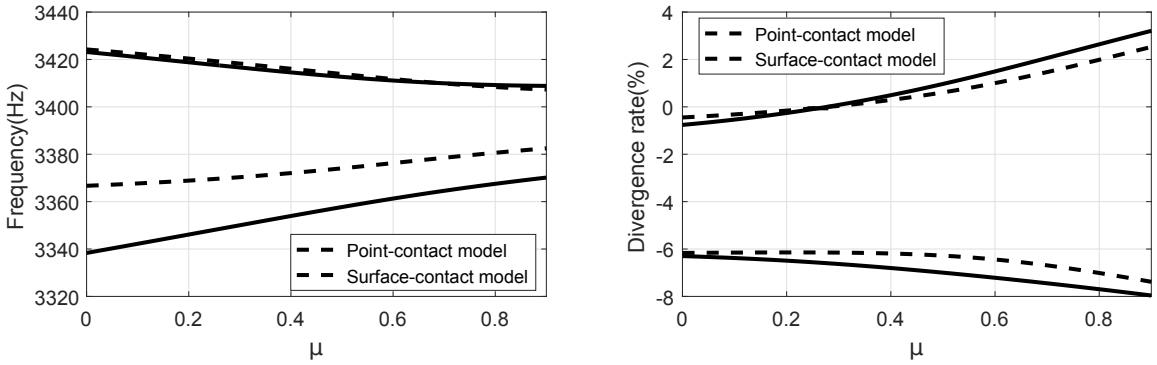

(a) Frequency (b) Frequency

Figure 5.14: Bifurcation curves of the unstable mode (a,0,6)

However, the form of the bifurcation curves of each unstable mode obtained with the point-contact model is similar to that obtained with the surface contact model. It can be conclude that the instability mechanisms are similar for the two models. Thus, the first three unstable modes are due to the negative damping effect related to the rail vertical phase response whereas the fourth unstable mode results from a mode coupling instability.

5.4.3 Effects of main parameters

For the creepage sign, as for the point-contact model, the lateral sliding of both inner and outer wheels has been tested. Instabilities only occur in the case of the inner wheel/ rail contact. This result is similar to the result obtained with the point-contact model.

The critical modal damping factors of the axial wheel modes (a,0,2), (a,0,3), (a,0,4) and (a,0,6) reach 0.28%, 0.18% , 0.02% and 0.15% respectively. These modal damping factors are significantly higher than the damping factors for the point-contact model (0.2%, 0.15% , 0.02% and 0.1% respectively) because of the higher divergence rates (Tab. 5.1).

Fig. 5.15 shows the effect of the vertical pad stiffness in comparison with the result obtained with the point-contact model. The evolution of the divergence rates are almost identical. The divergence rates of the unstable modes (a,0,2) and (a,0,3) decreases greatly while the vertical pad stiffness increases. The divergence rates of the unstable modes (a,0,4) and (a,0,6) do not change so much.

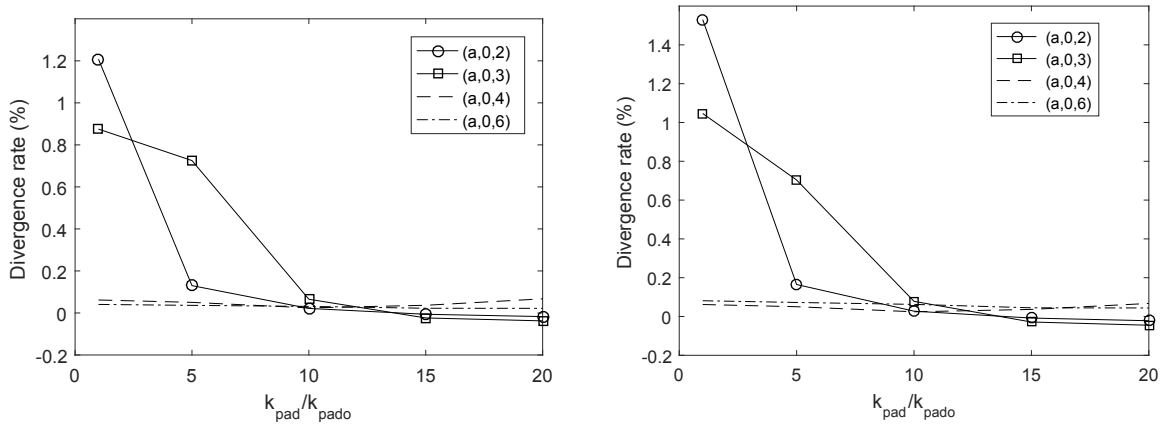

(a) Point-contact model (b) Surface-contact model

Figure 5.15: Influence of the pad vertical stiffness on the unstable complex modes for the surface contact model in comparison with the result obtained with the point-contact model

The above results show that for stability analysis, the discretization of the contact zone does not modify substantially the instability mechanisms. However due to a stronger coupling between the normal contact DOFs, the divergence rates of the unstable modes are greater for the surface-contact model than for the point-contact model.

5.5 Stability and transient results with the track viscous damping model

Through the stability analysis of the wheel/rail contact performed in the previous section, four unstable modes are obtained. However, the stability analysis does not allow to introduce nonlinearities and determine the amplitude and full spectrum of the friction-induced vibration. Moreover, the track structural damping model does not allow to perform transient calculations. The aim of this section is to perform both stability and transient analysis with track viscous damping model in order to compare these analyses, especially in the case of several unstable modes.

5.5.1 Stability results

The divergent rates and the corresponding unstable modes shapes are listed in Tab. 5.2 in comparison with the results obtained with the track structural damping model. The unstable frequencies and the critical friction coefficient are almost the same whereas the divergences rates are significantly different because of the difference between the track damping models.

5.5.2 Transient results

Transient results corresponding to the unstable case founded in the previous section are determined using a numerical time integration from given initial conditions. In all the following results, the integration starts from the equilibrium i.e. the initial displacements are the displacements obtained from the quasi-static solution and the initial velocities are null. The parameters $V = 10$ m/s, $\mu = 0.3$ and $\Delta V_y/V = 1\%$ are used. The time step for the integration is $\Delta t = 1\mu$s. Fig. 5.16a shows the time series of the lateral contact resultant forces F_t. The tangential resultant force increases until a pronounced creep/slip oscillation builds up as shown in Fig. 5.16b. When the tangential contact resultant force is smaller than the traction bound μF_n, a transient stick zone appears at the leading edge of the effective contact region as shown in Fig. 5.17.

Track structural damping model				Track viscous damping model			
Unstable frequencies (Hz) for ($\mu = 0.3$)	Divergence rate (%) for ($\mu = 0.3$)	Wheel modes	μ critical	Unstable frequencies (Hz) for ($\mu = 0.3$)	Divergence rate (%) for ($\mu = 0.3$)	Wheel modes	μ critical
334	1.53	(a,0,2)	0.06	334	1.51	(a,0,2)	0.08
917.9	1.04	(a,0,3)	0.1	917.9	0.77	(a,0,3)	0.1
1670	0.06	(a,0,4)	0.22	1670	0.09	(a,0,4)	0.2
3417	0.08	(a,0,6), (r,5), (a,1,1)	0.3	3417	0.107	(a,0,6), (r,5), (a,1,1)	0.28

Table 5.2: Stability results obtained with both track hysteresis and viscous damping models for the reference case

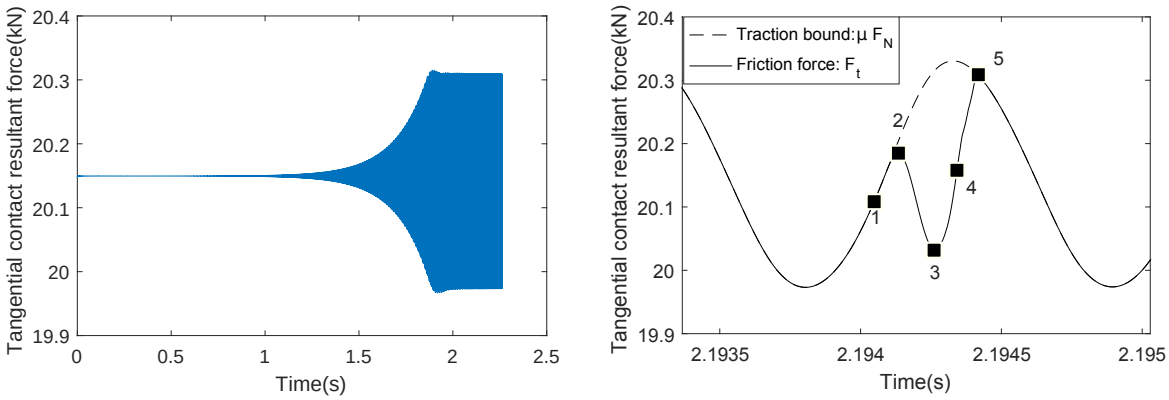

(a) (b)

Figure 5.16: a: Evolution of the tangential contact resultant force. b: Zoom on time series of the contact resultant forces. The status of the contact points at the time steps marked with Arabic numerals is represented Fig. 5.17

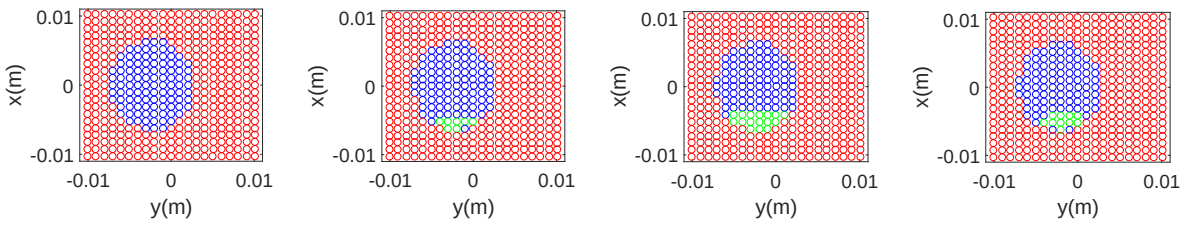

(a) 1&5 (b) 2 (c) 3 (d) 4

Figure 5.17: Status of nodes in the potential contact zone: no contact zone (red), slip zone (blue) and stick zone (green)

The time series of the lateral velocity of a point outside the contact zone is presented in Fig. 5.18a. The spectrogram in Fig. 5.18b allows to observe which frequencies are present in the solution and when they appear. At the beginning of the simulation, there are two major frequencies: 334 and 919 Hz which are very close to the natural frequencies of the two first unstable modes provided by stability analysis. In the stationary step, where nonlinear events happen, the dominant frequency is $f_o = 919$ Hz and its harmonic frequencies $f_k = kf_o$ appear. The corresponding spectra in the stationary part of the transient solution are also given in Fig. 5.19.

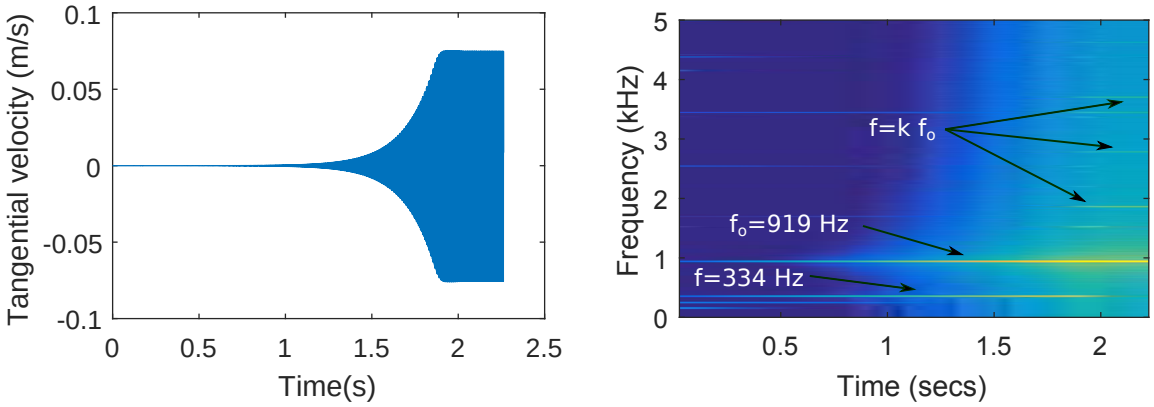

(a) Temporal evolution

(b) Spectrogram (time-frequency)

Figure 5.18: Tangential velocity of a point outside the contact zone

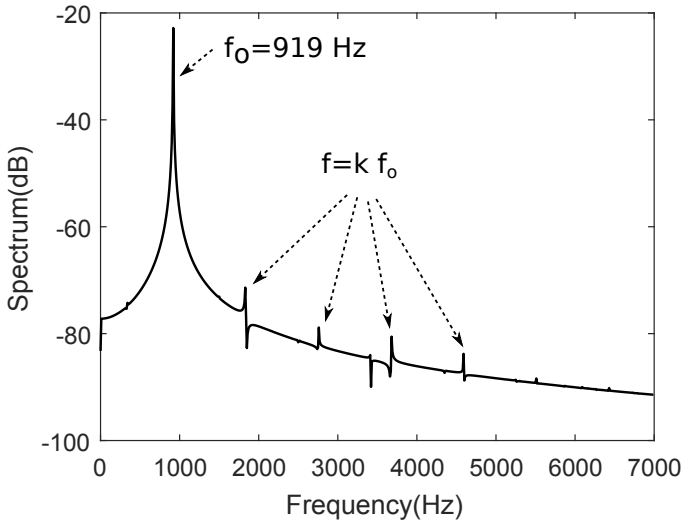

Figure 5.19: Spectrum of the stationary tangential velocity of a point outside the contact zone

The time series of the lateral velocity of a point inside the contact zone is presented in the Figure Fig. 5.20. This velocity does not exceed the imposed lateral velocity $Vs_{yo} = 0.1$ m/s. This conclusion is also drawn in [112, 114].

The apparent global friction coefficient which is defined as a ratio between the resulting tangential and normal contact force is represented in Fig. 5.21. This coefficient varies between 0.2958 corresponding to a partial slip state and 0.3 corresponding to the full slip state. It is clear that the average global friction coefficient during these stick-slip cycles is lightly smaller than the constant local friction coefficient. Thus, the decrease of the global friction coefficient could be interpreted as a consequence (and not

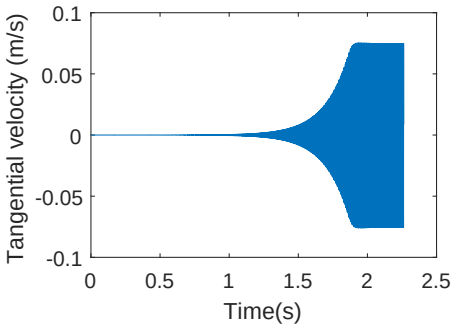

Figure 5.20: Tangential velocity of a point inside the contact zone

a cause) of the friction-induced vibrations.

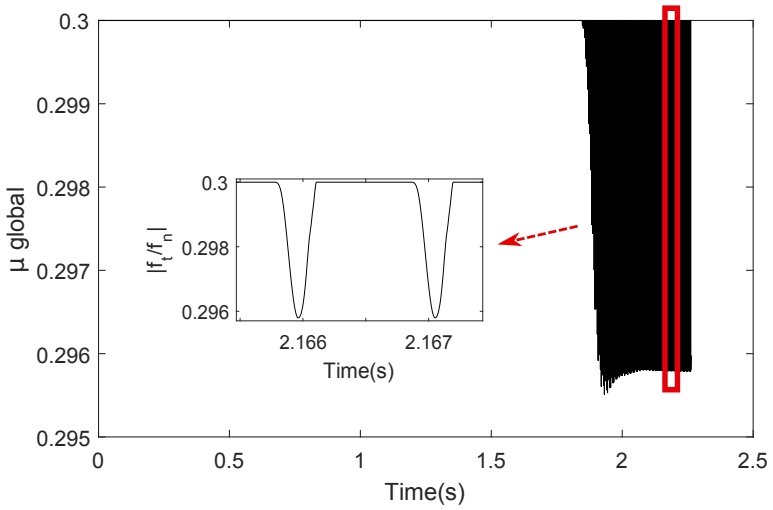

Figure 5.21: Apparent global friction coefficient

By neglecting the term $\frac{\partial u}{\partial x}$ in Eq. (1.54) representing the deformation contributions due to rolling in the Eulerian frame, the global dynamic lateral creepage can be defined as:

$$s_{yd} = s_{yo} + \frac{1}{V}\overline{\frac{\partial u_y}{\partial t}} \tag{5.3}$$

where $\overline{\frac{\partial u_y}{\partial t}}$ is the averaged lateral dynamic velocity in the effective contact zone.

The dynamic saturation curve is defined as the relation between the dynamic tangential resulting contact force and the global dynamic lateral creepage. The curve is represented in Fig. 5.22 in comparison with some quasi-static point-contact models. An hysteresis curve is obtained with the full FE model. This curve is considerably different of quasi-static point-contact saturation curves. A possible explanation is that the quasi-static point-contact models do not take in account the lateral contact stiffness which is a key parameter at high frequencies [3, 83].

Mindlin [84] showed that the contact between two static bodies has a lateral stiffness in the transverse direction which is approximately the same as for the vertical case and given by:

$$k_L = \chi k_H \tag{5.4}$$

where χ varies between about 0.7 and 1.

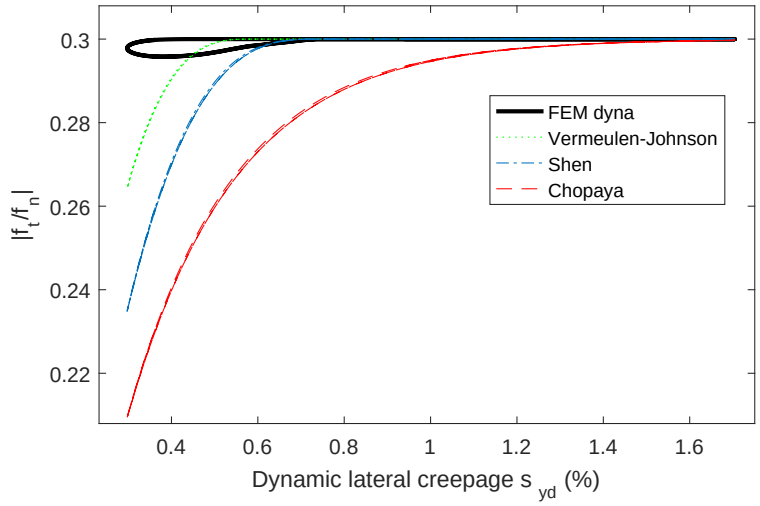

Figure 5.22: Dynamic saturation curve

The FE average dynamic lateral stiffness during limit cycles defined as the ratio between the average tangential contact force and the average tangential contact displacements and corresponding to the residual attachment modes is equal to $0.82k_H = 0.68k_{fe}$. This dynamic lateral stiffness is close to the interval of $[0.7 \quad 1]k_{fe}$, which is similar to the lateral stiffness found by Mindlin Eq. (5.4).

5.5.3 Calculation of sound radiation from a railway wheel/rail

By considering that the sound radiated from the rail is very smaller than the sound radiated from the wheel in the squeal phenomenon [5], most of curve squeal models only calculate the noise radiated from the wheel [96, 97, 109–111, 123]. Schneider and Popp [109] evaluated the radiated sound using the Rayleigh integral for a baffled plate. Fingberg [110], Huang [123] and Zenzerovic [96, 97] used a combination of the boundary element method (BEM) and modal expansion techniques. By using this technique, the sound power at a frequency is evaluated as a sum of contributions from wheel modes with the same number of nodal diameters.

In this thesis, the methodology for the calculation of sound radiation from both wheel and track is developed by ESI-Group in the CERVIFER project. If the resulting contact forces are known at a given frequency, the sound power radiated from the wheel and by the track can be evaluated by a simple expression:

$$\mathbf{P_i^a} = [\mathbf{f_t} \quad \mathbf{f_n}] \begin{bmatrix} \mathbf{H^i_{ayy}} & \mathbf{H^i_{ayz}} \\ \mathbf{H^i_{azy}} & \mathbf{H^i_{azz}} \end{bmatrix} [\mathbf{f_t} \quad \mathbf{f_n}]^{\mathbf{T}} \quad \text{(i=1,2,3...: wheel, rail, sleeper...)} \tag{5.5}$$

where $\mathbf{H_a^i}$ is the acoustic transfer function previously computed by using the boundary element method (BEM), with unit (W / N ^{2}). In this study, the extra-diagonal terms of the acoustic transfer matrix that represent the interaction effects are neglected. Thus, the total sound power is the summation of the power due to the lateral force with that due to the vertical component.

For the reference case, Fig. 5.23 shows the power spectral density (PSD) of the tangential and normal resulting contact force. Fig. 5.24 shows the sound power radiated from the track and wheel, as well as the contribution of each element separately in 1/3 octave. The radiated power may reach 118.1 dBA at the frequency 919Hz which is equal to the fundamental frequency of the limit cycle. (919Hz). It is clear that the sound power radiated from the wheel is dominant at this peak.

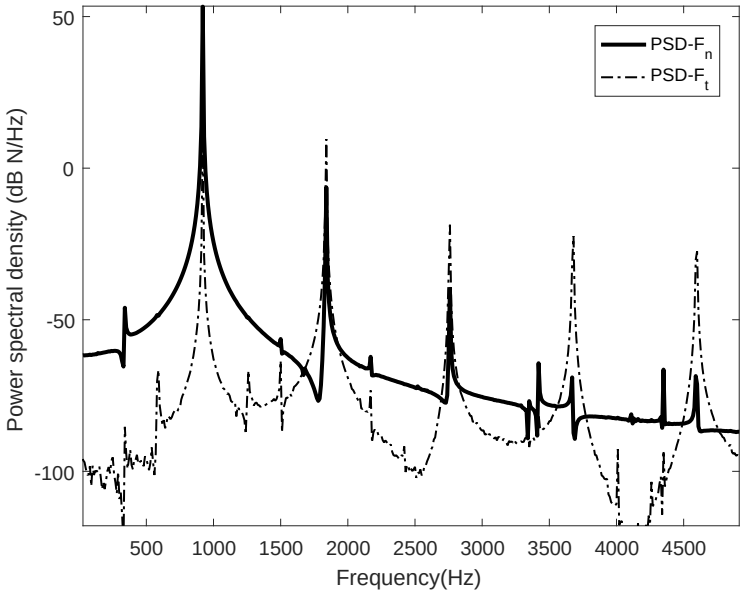

Figure 5.23: Power spectral density of the tangential and normal resulting contact force (Benchmark Bruit de Roulement Work Package 4 (Tâche 4.1))

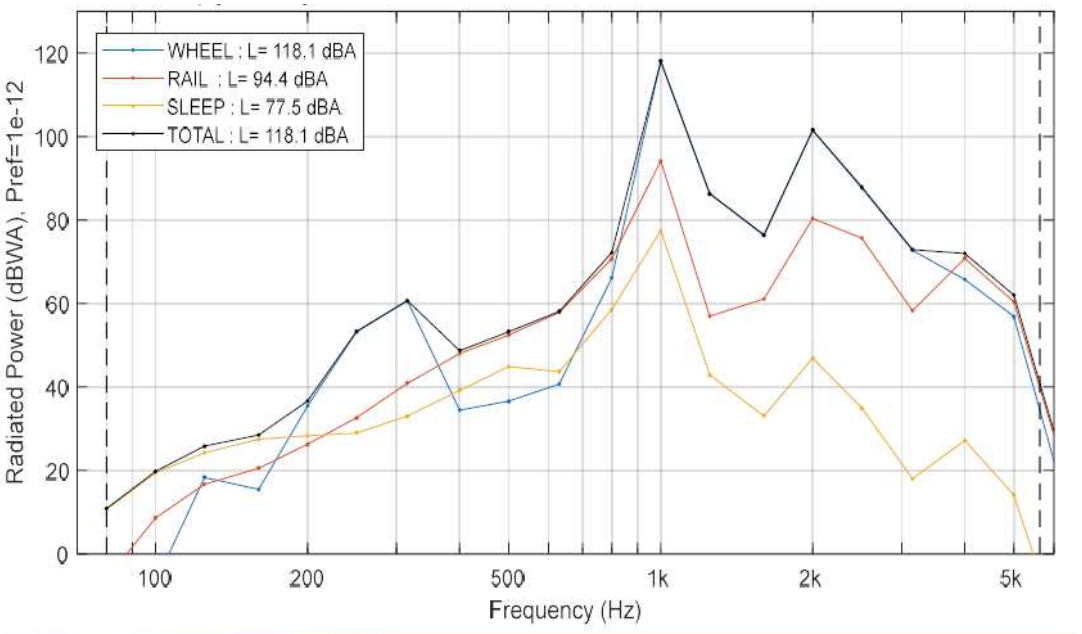

Figure 5.24: Sound power radiated from the track and wheel (Benchmark Bruit de Roulement Work Package 4 (Tâche 4.1))

5.6 Conclusion

In this chapter, the full FE model for rolling contact systems developed and validated in Chapter 4 is applied in the case of wheel/rail frictional rolling contact. The reduction basis including free-interface modes and static residual flexibility modes is used in order to reduce the computation loads and times. Stability analysis is performed in the case of the track structural damping model in comparison with the results obtained with the point-contact model in order to highlight the influence of the discretization of the contact zone on the instability mechanism and intensity. Both stability and transient analysis are performed in the case of the track viscous damping model in order to predict unstable modes and to determine the amplitude and full spectrum of the self-sustained vibrations in curve.

The stability results show that the discretization of the contact zone does not modify the instability mechanisms. However due to a stronger coupling between the normal contact DOFs, the divergence rates of the unstable modes are greater for the surface-contact model than for the point-contact model.

The results of the transient calculation are consistent with the stability analysis and exhibit localized stick/slip oscillations in the contact zone. The apparent global friction coefficient during stick-slip cycles is slightly smaller than the constant local friction coefficient. Thus, the decrease of the apparent global friction coefficient could be considered as a consequence of the friction-induced vibrations. The dynamic saturation curve with hysteresis obtained by the full FE model is considerably different of the quasi-static curves. This is probably due to the lateral wheel/rail contact stiffness at high frequencies. Thus, it is necessary for the curve squeal point-contact models to take into account this lateral stiffness.

In the case of several unstable modes, although the unstable mode (a,0,2) has the highest divergence rate among the four unstable modes, the fundamental frequency in the stationary solution is close to the frequency of wheel mode (a,0,3). Thus, the divergence rate is not a indicator to predict the dominant unstable mode in the final solution. The real part may be also a candidate but many factors can influence the dominant unstable mode as concluded is Loyer's work [21]. For instance, fundamental frequency of the limit cycles may be influenced by initial conditions. In future works, it will be necessary to test the effects of the kinematic and structural parameters as well as initial conditions on the limit cycles.

Conclusion

The present works dealt with the problematic of curve squeal of railway systems. The aim was to make a contribution to the study of instability mechanisms leading to curve squeal and to develop a full finite element model for wheel/rail contact in order to validate or to propose an enrichment of the existing models. Both stability and transient analyses have been performed. In stability analysis, by linearizing the equations of motion, unstable modes and frequencies can be predicted. In transient analysis, the nonlinearities are introduced in the model and the characteristics (amplitude, full spectrum) of self-sustained vibrations can be determined.

Main results

In Part I, a stability analysis of wheel/rail rolling contact in the case of lateral full sliding was proposed in order to investigate the instability mechanisms. A point contact model with linearized Hertzian normal law and Coulomb's friction law is used in all the part. In Chapter 2, the interaction model uses wheel and rail modal bases. It was found that even with a constant Coulomb friction, instabilities can occur because of the coupling between normal and tangential dynamics in wheel/rail systems. This coupling can involve two wheel modes (mode coupling) or only one wheel mode (among axial modes with 2 to 4 nodal diameters and 0 nodal circle) when the rail dynamics is included. It has been showed that the last case corresponds to a specific and original mechanism. These results are coherent with experimental observations (modal shapes, frequencies, parametric influences, etc.). The rail vertical flexibility is found to play an important role in the instability occurrence without "falling friction" nor without "mode-coupling". This role has been clarified by the simple model proposed in chapter 3. With this model, it was found that the imaginary part of the complex stiffness of the rail, induced by the phase shift of the propagating wave but also by pad and rail damping plays an critical role in the instability mechanism. The combination of friction and phase shift induces a negative damping which may then destabilize the system, leading to self-sustained vibration and squeal noise. A study on the influence of kinematic and structural parameters with both models shows that the instability occurrence depends greatly on the friction coefficient, the contact position (combined with the local wheel dynamics), the wheel modal damping and the stiffness of the rail pad.

The point-contact model developed in Part 1 can predict unstable modes of the wheel/rail system in curve. However the model does not allow to compute nonlinear friction-induced vibrations. For this purpose, a full finite element model of wheel/rail contact is developed in part II notably in order to calculate reference solutions and to verify the simplifications made in part I. In chapter 4, a rolling contact model between two elastic bodies is developed using the finite element method with a discretized contact surface to develop the numerical method and validate it on a reference case. The approach has been performed around the stationary position in an Eulerian reference frame. Non-smooth unilateral Signorini's and Coulomb's friction laws with constant friction coefficient are used. A weak Lagrangian formulation and a resolution by a fixed-point algorithm allows reasonable computation times. In dynamic conditions, a modified $\theta-$ method, able to impose inelastic shock, is used. In order to reduce the computational

costs, reduction strategies are proposed for both domains. The first proposed reduction basis includes free-interface modes and static contact attachments modes. A total decoupling between the generalized equations corresponding to free-interface modes and static attachments modes equations can be obtained if the dynamic associated to the static attachments modes is neglected. The result of an application of the rolling contact between two cylinders in 3D showed a good agreement in comparison with Kalker's theory implementation (CONTACT software) in the quasi-static case. A stability analysis performed around the sliding equilibrium position allows the determination of unstable modes and corresponding frequencies. The fundamental frequency in the transient solution is very close to the unstable frequency determined in the stability analysis. The stick-slip cycles are localized in some contact point at the trailing edge of the contact zone. Concerning the reduction method, the result obtained with the reduction bases shows a good agreement with some other proven methods in the stability analysis. In the transient domain, the amplitude of the reduced solutions is slightly greater than the complete solution in the linear step. However in the stationary step, there is no large difference between the amplitude of the solutions.

In chapter 5, the developed method has been then applied to a wheel/rail rolling system in curve. In stability analysis, the unstable axial modes are similar to those obtained with the point-contact model. It means that the discretization of the contact zone does not essentially change the instability mechanisms. However, the divergence rates of the FE unstable modes are more important, due to a stronger normal coupling with the discretized surface. The transients results are then analyzed. Despite the four unstable modes provided by the stability analysis, there is only one dominant frequency in the final stationary solution. The results also exhibit localized stick/slip oscillations in the contact zone. In addition, the average global friction coefficient during stick-slip cycles is lightly smaller than the constant local friction coefficient. Thus, the decrease of the global friction coefficient could be considered as a consequence of the friction-induced vibrations in the final solution. The dynamic saturation curve with an hysteresis obtained with the full FE model is also considerably different from the quasi-static curves. An exploitation of the results of the transient simulation is the quantification of the noise level via a vibro-acoustic simulation of the wheel-track system.

In comparison with existing models, the thesis work has given two major originalities. Firstly, a specific mechanism has been found and explained by proposing a appropriate simple 1-DOF model. This mechanism shows the crucial role of the rail on the stability of wheel/rail system in curve. It opens mitigation solutions which are not only concentrated on the wheel but also on the rail and its support. Secondly, a original finite element contact model with discretization of the contact surface in the Eulerian frame combined with the reduction bases is developed and validated for the study of friction-induced vibration of rolling contact systems. The first results obtained in the application to wheel/rail contact in curve have shown differences between the full FE model and the point-contact models especially concerning the global contact stiffness and creep saturation curve, both in linear and non linear analyses.

Future works

In short term, the stability analysis, even if it makes the total full sliding assumption of the contact zone, can be performed for a parametric analysis of the wheel and track parameters. Parametric analysis of the rail internal damping, the rail support damping and the wheel/rail angle of inclination can be performed to propose and quantify technological mitigation solutions.

The second group of prospects concerns the transient nonlinear analysis. Parametric analysis could also be performed in order to estimate the effects of the kinematic and structural parameters on the amplitude and the spectrum of the self-sustained vibrations. In the case of several unstable modes, a question stands out about how to predict the fundamental frequency in the stationary solution. Thus, transient calculations with different initial conditions have to be performed in order to test their impact on the stationary solution.

The improvement of point contact models may be another prospect. Indeed, in order to reduce the computational cost, point-contact models are preferred. However, these models need to be enriched by

the results obtained with surface-contact models to being more adapted in the case of large slip, high dynamics and very fast evolutions in the contact zone. The full model developed here can be used to define an enrichment of point-contact models.

The full FE model could be used to study other wheel/rail noise sources. In particular, rolling noise and curve squeal noise can coexist. A combination between the models dealing with the two types of noise is therefore necessary in order to determine the sound radiation of rolling noise in curve. For this purpose, a modification of the contact surface such as plastic behavior, wheel geometries or macro roughness could be taken into account in the combined model.

Finally, in order to validate the instability mechanism "negative damping introduced by the imaginary part of the track vertical complex stiffness", by considering the track as an infinite structure, the test rigs [8,9] in which the track is represented by a finite structure (cf. 3D cylinder) are not adapted anymore. A realistic wheel/rail test rig is required.

Bibliography

[1] N. Hoffmann, M. Fischer, R. Allgaier, L. Gaul. A minimal model for studying properties of the mode-coupling type instability in friction induced oscillations. Mechanics Research Communications, 29 (4) (2002).

[2] P. Vermeulen, K. Johnson. Contact of nonspherical elastic bodies transmitting tangential forces. Journal of Applied Mechanics, 31 (2) (1964).

[3] D. Thompson, Railway noise and vibration: mechanisms, modelling and means of control, Elsevier, 2008.

[4] D. Eadie, M. Santoro. Top-of-rail friction control for curve noise mitigation and corrugation rate reduction. Journal of Sound and Vibration, 293 (3-5) (2006).

[5] N. Vincent, J. Koch, H. Chollet, J. Guerder. Curve squeal of urban rolling stock—part 1: State of the art and field measurements. Journal of sound and vibration, 293 (3) (2006).

[6] M. Rudd. Wheel/rail noise-part ii: Wheel squeal. Journal of Sound and Vibration, 46 (3) (1976).

[7] P. Remington. Wheel/rail squeal and impact noise: What do we know? what don't we know? where do we go from here? Journal of Sound and Vibration, 116 (2) (1987).

[8] J. Koch, N. Vincent, H. Chollet, O. Chiello. Curve squeal of urban rolling stock—part 2: Parametric study on a 1/4 scale test rig. Journal of sound and vibration, 293 (3) (2006).

[9] F. De Beer, M. Janssens, P. Kooijman. Squeal noise of rail-bound vehicles influenced by lateral contact position. Journal of Sound and Vibration, 267 (3) (2003).

[10] X. Liu, P. A. Meehan. Investigation of the effect of lateral adhesion and rolling speed on wheel squeal noise. Proceedings of the Institution of Mechanical Engineers, Part F: Journal of Rail and Rapid Transit, 227 (5) (2013).

[11] L. Kurzweil. Wheel/rail noise—means for control. Journal of Sound and Vibration, 87 (2) (1983).

[12] C. Glocker, E. Cataldi-Spinola, R. Leine. Curve squealing of trains: Measurement, modelling and simulation. Journal of Sound and Vibration, 324 (1) (2009).

[13] P. Remington. Acoustic performance of incramute wheels. Bolt Beranek and Newman Inc. Report, (3342) (1976).

[14] P. Kooijman, W. Van Vliet, M. Janssens, F. de Beer. Curve squeal of railbound vehicles (part 2): set-up for measurement of creepage dependent friction coefficient. Proceedings of Internoise, Nice, France, 3 (2000).

[15] C. Van Ruiten. Mechanism of squeal noise generated by trams. Journal of Sound and Vibration, 120 (2) (1988).

[16] B. Ding, G. Squicciarini, D. Thompson, R. Corradi. An assessment of mode-coupling and falling-friction mechanisms in railway curve squeal through a simplified approach. Journal of Sound and Vibration, 423 (2018).

[17] D. J. Fourie, P. J. Gräbe, P. S. Heyns, R. D. Fröhling. Experimental characterisation of railway wheel squeal occurring in large-radius curves. Proceedings of the Institution of Mechanical Engineers, Part F: Journal of Rail and Rapid Transit, 230 (6) (2016).

[18] J. Jiang, R. Dwight, D. Anderson, Field verification of curving noise mechanisms, in: Noise and Vibration Mitigation for Rail Transportation Systems, Springer, 2012, pp. 349–356.

[19] B. Ding, G. Squicciarini, D. Thompson, Effects of rail dynamics and friction characteristics on curve squeal, in: Journal of Physics: Conference Series, Vol. 744, IOP Publishing, 2016, p. 012146.

[20] H. Hertz. Über die berührung fester elastischer körper. Journal für die reine und angewandte Mathematik, 92 (1882).

[21] A. Loyer, J.-J. Sinou, O. Chiello, X. Lorang. Study of nonlinear behaviors and modal reductions for friction destabilized systems. application to an elastic layer. Journal of Sound and Vibration, 331 (5) (2012).

[22] X. Lorang, F. Foy-Margiocchi, Q. S. Nguyen, P.-E. Gautier. Tgv disc brake squeal. Journal of Sound and Vibration, 293 (3-5) (2006).

[23] G. Duvaut, J. L. Lions. Les inéquations en mécanique et en physique (1972).

[24] J. Oden, J. Martins. Models and computational methods for dynamic friction phenomena. Computer methods in applied mechanics and engineering, 52 (1) (1985).

[25] G. Amonton. 1699,"on the resistance originating in machines,". Proc. French R. Acad. Sci. A, 12.

[26] R. Stribeck, M. Schröter, Die wesentlichen Eigenschaften der Gleit-und Rollenlager: Untersuchung einer Tandem-Verbundmaschine von 1000 PS, Springer, 1903.

[27] P. R. Dahl. Solid friction damping of mechanical vibrations. AIAA journal, 14 (12) (1976).

[28] R. Ibrahim. Friction-induced vibration, chatter, squeal, and chaos—part i: mechanics of contact and friction. Applied Mechanics Reviews, 47 (7) (1994).

[29] R. Ibrahim. Friction-induced vibration, chatter, squeal, and chaos—part ii: dynamics and modeling. Applied Mechanics Reviews, 47 (7) (1994).

[30] P. Stelter, et al. Stick-slip vibrations and chaos. Phil. Trans. R. Soc. Lond. A, 332 (1624) (1990).

[31] R. T. Spurr. A theory of brake squeal. Proceedings of the Institution of Mechanical Engineers: Automobile Division, 15 (1) (1961).

[32] J. Oden, J. Martins. Models and computational methods for dynamic friction phenomena. Computer methods in applied mechanics and engineering, 52 (1-3) (1985).

[33] D. Tolstoi. Significance of the normal degree of freedom and natural normal vibrations in contact friction. Wear, 10 (3) (1967).

[34] N. Kinkaid, O. M. O'Reilly, P. Papadopoulos. Automotive disc brake squeal. Journal of sound and vibration, 267 (1) (2003).

[35] J.-J. Sinou, L. Jezequel. Mode coupling instability in friction-induced vibrations and its dependency on system parameters including damping. European Journal of Mechanics-A/Solids, 26 (1) (2007).

[36] U. von Wagner, D. Hochlenert, P. Hagedorn. Minimal models for disk brake squeal. Journal of Sound and Vibration, 302 (3) (2007).

[37] Z. Li, H. Ouyang, Z. Guan. Nonlinear friction-induced vibration of a slider–belt system. Journal of Vibration and Acoustics, 138 (4) (2016).

[38] L. Charroyer, O. Chiello, J. Sinou. Self-excited vibrations of a non-smooth contact dynamical system with planar friction based on the shooting method. International Journal of Mechanical Sciences (2018).

[39] Q. S. Nguyen, Stabilité des structures élastiques, Vol. 18, Springer Science & Business Media, 1995.

[40] A. Loyer, Etude numérique et expérimentale du crissement des systemes de freinage ferroviaires, Ph.D. thesis, Ecully, Ecole centrale de Lyon (2012).

[41] D. Brizard, O. Chiello, J.-J. Sinou, X. Lorang. Performances of some reduced bases for the stability analysis of a disc/pads system in sliding contact. Journal of Sound and Vibration, 330 (4) (2011).

[42] X. Lorang, F. Foy-Margiocchi, Q. Nguyen, P. Gautier. {TGV} disc brake squeal. Journal of Sound and Vibration, 293 (3–5) (2006). Proceedings of the Eigth International Workshop on Railway NoiseProceedings of the Eighth International Workshop on Railway Noise. doi:http://dx.doi.org/10.1016/j.jsv.2005.12.006.

[43] Y. Saad, Iterative methods for sparse linear systems, SIAM, 2003.

[44] A. Bobillot, Méthodes de réduction pour le recalage application au cas d'ariane 5, Ph.D. thesis, Ecole Centrale Paris (2002).

[45] A.-S. Plouin, E. Balmès, Steel/viscoelastic/steel sandwich shells computational methods and experimental validations, in: International Modal Analysis Conference, Vol. 4062, 2000, pp. 384–390.

[46] R. R. Craig Jr, C.-j. Chang. On the use of attachment modes in substructure coupling for dynamic analysis. transformation, 10 (4) (1977).

[47] R. R. Craig Jr. A review of time-domain and frequency-domain component mode synthesis method (1985).

[48] J.-J. Sinou. Transient non-linear dynamic analysis of automotive disc brake squeal–on the need to consider both stability and non-linear analysis. Mechanics Research Communications, 37 (1) (2010).

[49] M. Géradin, D. J. Rixen, Mechanical vibrations: theory and application to structural dynamics, John Wiley & Sons, 2014.

[50] H. B. Khenous, Problèmes de contact unilatéral avec frottement de coulomb en élastostatique et élastodynamique. etude mathématique et résolution numérique., Ph.D. thesis, INSA Toulouse (2006).

[51] G. Vermot des Roches, Frequency and time simulation of squeal instabilities. application to the design of industrial automotive brakes., Ph.D. thesis, Châtenay-Malabry, Ecole centrale de Paris (2011).

[52] L. Charroyer, Méthodes numériques pour le calcul des vibrations auto-entretenues liées au frottement: Application au bruit de crissement ferroviaire, Ph.D. thesis, Lyon (2017).

[53] N. M. Newmark. A method of computation for structural dynamics. Journal of the engineering mechanics division, 85 (3) (1959).

[54] H. M. Hilber, T. J. Hughes, R. L. Taylor. Improved numerical dissipation for time integration algorithms in structural dynamics. Earthquake Engineering & Structural Dynamics, 5 (3) (1977).

[55] G. Vermot Des Roches, E. Balmes, T. Pasquet, R. Lemaire, Time/frequency analysis of contact-friction instabilities. application to automotive brake squeal., ISMA, 2010.

[56] P. Alart, A. Curnier. A mixed formulation for frictional contact problems prone to newton like solution methods. Computer methods in applied mechanics and engineering, 92 (3) (1991).

[57] D. Kudawoo, F. Lebon, M. Abbas, T. De Soza, I. Rosu, Two algorithms based on stabilized lagrangian formulation to solve frictional contact problems, in: 2nd International Conference on Computational Contact Mechanics, 2011.

[58] L. Champaney, J. Cognard, P. Ladeveze. Modular analysis of assemblages of three-dimensional structures with unilateral contact conditions. Computers & Structures, 73 (1-5) (1999).

[59] H. Lemoussu, P.-A. Boucard, P. Ladevèze. A 3d shock computational strategy for real assembly and shock attenuator. Advances in Engineering Software, 33 (7-10) (2002).

[60] C. Royer, Une approche des problémes de dynamique non-lineaires par la méthode à grand incrément de temps, Ph.D. thesis, Paris 6 (1990).

[61] P. Laborde, Y. Renard. Fixed point strategies for elastostatic frictional contact problems. Mathematical Methods in the Applied Sciences, 31 (4) (2008).

[62] M. Jean. The non-smooth contact dynamics method. Computer methods in applied mechanics and engineering, 177 (3) (1999).

[63] D. Vola, E. Pratt, M. Jean, M. Raous. Consistent time discretisation for a dynamical frictional problem and complementarity techniques. Revue Européenne des éléments finis, 7 (1-3) (1998).

[64] H. B. Khenous, P. Laborde, Y. Renard. Mass redistribution method for finite element contact problems in elastodynamics. European Journal of Mechanics-A/Solids, 27 (5) (2009).

[65] L. Renson, G. Kerschen, B. Cochelin. Numerical computation of nonlinear normal modes in mechanical engineering. Journal of Sound and Vibration, 364 (2016).

[66] J. Carr, Applications of centre manifold theory, Vol. 35, Springer Science & Business Media, 2012.

[67] T. Cameron, J. Griffin. An alternating frequency/time domain method for calculating the steady-state response of nonlinear dynamic systems. Journal of applied mechanics, 56 (1) (1989).

[68] N. Coudeyras, S. Nacivet, J.-J. Sinou. Periodic and quasi-periodic solutions for multi-instabilities involved in brake squeal. Journal of Sound and Vibration, 328 (4-5) (2009).

[69] N. Coudeyras, J.-J. Sinou, S. Nacivet. A new treatment for predicting the self-excited vibrations of nonlinear systems with frictional interfaces: The constrained harmonic balance method, with application to disc brake squeal. Journal of sound and vibration, 319 (3) (2009).

[70] E. Balmès. Modèles expérimentaux complets et modèles analytiques réduits en dynamique des structures. Mémoire d'habilitation à diriger les recherches (1997).

[71] K. Kunisch, S. Volkwein. Galerkin proper orthogonal decomposition methods for parabolic problems. Numerische mathematik, 90 (1) (2001).

[72] G. Kerschen, M. Peeters, J.-C. Golinval, A. F. Vakakis. Nonlinear normal modes, part i: A useful framework for the structural dynamicist. Mechanical Systems and Signal Processing, 23 (1) (2009).

[73] M. Peeters, R. Viguié, G. Sérandour, G. Kerschen, J.-C. Golinval. Nonlinear normal modes, part ii: Toward a practical computation using numerical continuation techniques. Mechanical systems and signal processing, 23 (1) (2009).

[74] C. Touzé, O. Thomas, A. Chaigne. Hardening/softening behaviour in non-linear oscillations of structural systems using non-linear normal modes. Journal of Sound and Vibration, 273 (1-2) (2004).

[75] C. Villa, J.-J. Sinou, F. Thouverez. The invariant manifold approach applied to nonlinear dynamics of a rotor-bearing system. arXiv preprint arXiv:0801.3020 (2008).

[76] K. L. Johnson, K. L. Johnson, Contact mechanics, Cambridge university press, 1987.

[77] J. Kalker, Wheel–rail rolling contact theory, in: Mechanics and Fatigue in Wheel/Rail Contact, Elsevier, 1991, pp. 243–261.

[78] B. Jacobson, J. J. Kalker, Rolling contact phenomena, Vol. 411, springer, 2014.

[79] F. Carter, On the action of a locomotive driving wheel, in: Proceedings of the Royal Society of London A: Mathematical, Physical and Engineering Sciences, Vol. 112, The Royal Society, 1926, pp. 151–157.

[80] A. De Pater, On the reciprocal pressure between two bodies, in: Proc. Symp. Rolling Contact Phenomena, Vol. 6, Elsevier, New York, 1962.

[81] Z. Shen, J. Hedrick, J. Elkins. A comparison of alternative creep force models for rail vehicle dynamic analysis. Vehicle System Dynamics, 12 (1-3) (1983).

[82] J.-B. Ayasse, H. Chollet. 4 wheel–rail contact. Handbook of railway vehicle dynamics (2006).

[83] K. Knothe, S. Grassie. Modelling of railway track and vehicle/track interaction at high frequencies. Vehicle system dynamics, 22 (3-4) (1993).

[84] R. Mindlin. Compliance of elastic bodies in contact. J. Appl. Mech. Trans. ASME, 16 (1949).

[85] J. Piotrowski, H. Chollet. Wheel–rail contact models for vehicle system dynamics including multipoint contact. Vehicle System Dynamics, 43 (6-7) (2005).

[86] J. Piotrowski, W. Kik. A simplified model of wheel/rail contact mechanics for non-hertzian problems and its application in rail vehicle dynamic simulations. Vehicle System Dynamics, 46 (1-2) (2008).

[87] J. B. Ayasse, H. Chollet. Determination of the wheel rail contact patch in semi-hertzian conditions. Vehicle System Dynamics, 43 (3) (2005).

[88] J. Kalker. Simplified theory of rolling contact. Delft Progress Rep., 1 (1) (1973).

[89] Z. Shen, Z. Li. A fast non-steady state creep force model based on the simplified theory. Wear, 191 (1) (1996).

[90] A. Alonso, J. Giménez. Non-steady state modelling of wheel-rail contact problem for the dynamic simulation of railway vehicles. Vehicle System Dynamics, 46 (3) (2008).

[91] A. Guiral, A. Alonso, L. Baeza, J. Giménez. Non-steady state modelling of wheel–rail contact problem. Vehicle System Dynamics, 51 (1) (2013).

[92] J. J. Kalker, Three-dimensional elastic bodies in rolling contact, Vol. 2, Springer Science & Business Media, 2013.

[93] G. Fichera, Problemi elastostatici con vincoli unilaterali: il problema di Signorini con ambigue condizioni al contorno, Accademia nazionale dei Lincei, 1964.

[94] J. Kalker. Variational principles of contact elastostatics. IMA Journal of Applied Mathematics, 20 (2) (1977).

[95] J. Kalker. The principle of virtual work and its dual for contact problems. Ingenieur-Archiv, 56 (6) (1986).

[96] I. Zenzerovic, W. Kropp, A. Pieringer. An engineering time-domain model for curve squeal: Tangential point-contact model and green's functions approach. Journal of Sound and Vibration, 376 (2016).

[97] I. Zenzerovic, W. Kropp, A. Pieringer. Influence of spin creepage and contact angle on curve squeal: A numerical approach. Journal of Sound and Vibration, 419 (2018).

[98] K. Knothe, A. Groß-Thebing. Short wavelength rail corrugation and non-steady-state contact mechanics. Vehicle system dynamics, 46 (1-2) (2008).

[99] S. Bogdanski, M. Olzak, J. Stupnicki. Numerical stress analysis of rail rolling contact fatigue cracks. Wear, 191 (1-2) (1996).

[100] M. Wiest, E. Kassa, W. Daves, J. C. Nielsen, H. Ossberger. Assessment of methods for calculating contact pressure in wheel-rail/switch contact. Wear, 265 (9-10) (2008).

[101] M. Toumi, H. Chollet, H. Yin. Finite element analysis of the frictional wheel-rail rolling contact using explicit and implicit methods. Wear, 366 (2016).

[102] X. Zhao, Z. Li. The solution of frictional wheel–rail rolling contact with a 3d transient finite element model: Validation and error analysis. Wear, 271 (1-2) (2011).

[103] U. M. ABAQUS. Version 6.12. Dassault Systemes Simulia Corp, Rhode Island, USA (2012).

[104] C. Van Ruiten. Mechanism of squeal noise generated by trams. Journal of Sound and Vibration, 120 (2) (1988).

[105] D. Thompson, B. Hemsworth, N. Vincent. Experimental validation of the twins prediction program for rolling noise, part 1: description of the model and method. Journal of sound and vibration, 193 (1) (1996).

[106] G. Xie, P. Allen, S. D. Iwnicki, A. Alonso, D. J. Thompson, C. J. Jones, Z. Huang. Introduction of falling friction coefficients into curving calculations for studying curve squeal noise. Vehicle system dynamics, 44 (sup1) (2006).

[107] S. S. Hsu, Z. Huang, S. D. Iwnicki, D. J. Thompson, C. J. Jones, G. Xie, P. Allen. Experimental and theoretical investigation of railway wheel squeal. Proceedings of the Institution of Mechanical Engineers, Part F: Journal of Rail and Rapid Transit, 221 (1) (2007).

[108] G. Squicciarini, S. Usberti, D. Thompson, R. Corradi, A. Barbera, Curve squeal in the presence of two wheel/rail contact points, in: Noise and Vibration Mitigation for Rail Transportation Systems, Springer, 2015, pp. 603–610.

[109] E. Schneider, K. Popp, H. Irretier. Noise generation in railway wheels due to rail-wheel contact forces. Journal of Sound and Vibration, 120 (2) (1988).

[110] U. Fingberg. A model of wheel-rail squealing noise. Journal of Sound and Vibration, 143 (3) (1990).

[111] F. J. Périard, Wheel-rail noise generation: curve squealing by trams, TU Delft, Delft University of Technology, 1998.

[112] O. Chiello, J.-B. Ayasse, N. Vincent, J.-R. Koch. Curve squeal of urban rolling stock—part 3: Theoretical model. Journal of sound and vibration, 293 (3) (2006).

[113] A. Pieringer. A numerical investigation of curve squeal in the case of constant wheel/rail friction. Journal of Sound and Vibration, 333 (18) (2014).

[114] M. A. Heckl, I. Abrahams. Curve squeal of train wheels, part 1: mathematical model for its generation. Journal of Sound and Vibration, 229 (3) (2000).

[115] J.-F. Brunel, P. Dufrénoy, F. Demilly. Modelling of squeal noise attenuation of ring damped wheels. Applied Acoustics, 65 (5) (2004).

[116] J.-F. Brunel, P. Dufrénoy, M. Naït, J.-L. Muñoz, F. Demilly. Transient models for curve squeal noise. Journal of sound and vibration, 293 (3) (2006).

[117] M. A. Heckl. Curve squeal of train wheels, part 2: Which wheel modes are prone to squeal? Journal of Sound and Vibration, 229 (3) (2000).

[118] L. Gry. Dynamic modelling of railway track based on wave propagation. Journal of sound and vibration, 195 (3) (1996).

[119] C.-M. Nilsson, C. Jones, D. Thompson, J. Ryue. A waveguide finite element and boundary element approach to calculating the sound radiated by railway and tram rails. Journal of Sound and Vibration, 321 (3-5) (2009).

[120] T. Wu, D. Thompson. Analysis of lateral vibration behavior of railway track at high frequencies using a continuously supported multiple beam model. The Journal of the Acoustical Society of America, 106 (3) (1999).

[121] Z. Huang, Theoretical modelling of railway curve squeal, Ph.D. thesis, University of Southampton (2007).

[122] K. Kraft. Der einfluß der fahrgeschwindigkeit auf den haftwert zwischen rad und schiene. Archiv für Eisenbahntechnik, 22 (1967).

[123] Z. Huang, D. Thompson, C. Jones, Squeal prediction for a bogied vehicle in a curve, in: Noise and Vibration Mitigation for Rail Transportation Systems, Springer, 2008, pp. 313–319.

[124] J.-F. Brunel, Étude vibro-acoustique du crissement des roues ferroviaires et de son atténuation par insertion d'éléments métalliques, Ph.D. thesis, Lille 1 (2004).

[125] P. Chambrette, L. Jezequel. Stability of a beam rubbed against a rotating disc. European journal of mechanics. A. Solids, 11 (1) (1992).

[126] G. Engeln-Müllges, F. Reutter, Formelsammlung zur numerischen Mathematik mit Standard-FORTRAN-77-Programmen, BI-Wiss.-Verlag, 1988.

[127] J. J. Moreau. Numerical aspects of the sweeping process. Computer methods in applied mechanics and engineering, 177 (1998).

[128] J. Giner-Navarro, J. Martínez-Casas, F. Denia, L. Baeza. Study of railway curve squeal in the time domain using a high-frequency vehicle/track interaction model. Journal of Sound and Vibration, 431 (2018).

[129] D. J. Thompson, N. Vincent. Track dynamic behaviour at high frequencies. part 1: theoretical models and laboratory measurements. Vehicle System Dynamics, 24 (sup1) (1995).

[130] A. Nordborg, Vertical rail vibrations: noise and structure-borne sound generation, Tech. rep. (1995).

[131] J.-F. Hamet. Railway noise: use of the timoshenko model in rail vibration studies. Acta Acustica united with Acustica, 85 (1) (1999).

[132] B. Betgen, G. Squicciarini, D. J. Thompson, On the prediction of rail cross mobility and track decay rates using finite element models, in: Proceedings of the In Proceedings of the 10th European Congress and Exposition on Noise Control Engineering, 2015, p. 2019.

[133] G. Chen, J. Xiao, Q. Liu, Z. Zhou, Complex eigenvalue analysis of railway curve squeal, in: Noise and Vibration Mitigation for Rail Transportation Systems, Springer, 2008, pp. 433–439.

[134] J. Kalker, Wheel–rail rolling contact theory, in: Mechanics and Fatigue in Wheel/Rail Contact, Elsevier, 1991, pp. 243–261.

[135] M. Raous, S. Barbarin, D. Vola, Numerical characterization and computation of dynamic instabilities for frictional contact problems, in: Friction and Instabilities, Springer, 2002, pp. 233–291.

[136] A. D. Kudawoo, Problèmes industriels de grande dimension en mécanique numérique du contact: performance, fiabilité et robustesse., Ph.D. thesis, Aix-Marseille (2012).

[137] A. Steindl, H. Troger. Methods for dimension reduction and their application in nonlinear dynamics. International Journal of Solids and Structures, 38 (10-13) (2001).

[138] H. B. Khenous, J. Pommier, Y. Renard. Hybrid discretization of the signorini problem with coulomb friction. theoretical aspects and comparison of some numerical solvers. Applied Numerical Mathematics, 56 (2) (2006).